Effects of Thermal Annealing and Ion Irradiation on the Properties and Microstructures of Copper Alloys

Steven John Zinkle

May 1985

UWFDM-642

Ph.D. thesis.

FUSION TECHNOLOGY INSTITUTE

UNIVERSITY OF WISCONSIN

MADISON WISCONSIN

Effects of Thermal Annealing and Ion Irradiation on the Properties and Microstructures of Copper Alloys

Steven John Zinkle

Fusion Technology Institute
University of Wisconsin
1500 Engineering Drive
Madison, WI 53706

http://fti.neep.wisc.edu

May 1985

UWFDM-642

Ph.D. thesis.

EFFECTS OF THERMAL ANNEALING AND ION IRRADIATION ON THE PROPERTIES AND MICROSTRUCTURES OF COPPER ALLOYS

by

Steven John Zinkle

A thesis submitted in partial fulfillment of the
requirements for the degree of

DOCTOR OF PHILOSOPHY

(Nuclear Engineering)

at the

UNIVERSITY OF WISCONSIN-MADISON

May 1985

EFFECTS OF THERMAL ANNEALING AND ION IRRADIATION ON THE PROPERTIES AND MICROSTRUCTURES OF COPPER ALLOYS

Steven John Zinkle

Under the Supervision of Professor Gerald L. Kulcinski

High-strength, high conductivity copper alloys have recently been developed for a variety of technologically challenging applications, including proposed nuclear fusion reactors. The purpose of this thesis research is to examine the effects of high temperatures and radiation levels on the microstructural stability of two commercial high-strength, high conductivity copper alloys, AMZIRC (Cu-Zr) and AMAX-MZC (Cu-Cr-Zr-Mg).

The recrystallization temperature of both AMZIRC and AMAX-MZC was measured to be 475°C for a 1 hour anneal, and was estimated to be 320°C for a 20 year anneal which corresponds to a recrystallization energy of 3.0 eV. The yield strength of AMZIRC and AMAX-MZC decreased by at least a factor of two upon recrystallization. Therefore, it is important to ensure that these alloys are not subjected to conditions that would allow recrystallization to occur.

No significant void formation was observed in pure copper or in the AMZIRC and MZC copper alloys following ion irradiation at temperatures of 100-500°C (0.28-0.59 T_M) to peak damage levels of 40 dpa. Instead, stacking fault tetrahedra (SFT) were detected. The absence of voids following ion irradiation is attributed to the low oxygen

content of the copper and copper alloys (< 5 ppm). A vacancy cluster stability model has been developed that predicts that SFT in pure copper are energetically favorable compared to voids. Small amounts (0.01-10 appm) of He and O are predicted to stabilize void formation.

Ion irradiation of cold-worked plus aged AMZIRC and AMAX-MZC caused an effective shift in the recrystallization temperature to a lower value by 75 to 150°C compared with thermal anneal results. A simple model based on radiation-enhanced diffusion predicts a radiation-enhanced recrystallization temperature of 150°C for these alloys for a 2 year neutron irradiation. This effect may limit AMZIRC and MZC to low temperature (< 100°C) applications in fusion devices, since much of their strength is lost when recrystallization occurs.

Displacement damage in the form of "black spot" defect clusters was observed at depths well beyond that expected from ion damage range calculations. This difference is probably due to the use of too high of electronic stopping power values in the range calculations.

APPROVED:

May 16, 1985
Date

Professor Gerald L. Kulcinski
Nuclear Engineering Department

ACKNOWLEDGEMENTS

There are a number of people who have provided encouragement and assistance during the course of this thesis study. This work is dedicated to my parents, A.P. and Katie Zinkle, and to my brothers and sisters and their spouses for their steadfast support of my studies.

The advice and comments of my advisor, Professor G.L. Kulcinski served as a mold for my scientific development. Special thanks are also due to Professor W.G. Wolfer for innumerable stimulating conversations. The assistance of Professors R.A. Dodd and J.H. Perepezko was also appreciated. I would like to thank Dr. P. Wilkes for expertly introducing me to the fields of materials science and radiation effects and Professor H.H. Barschall for his continued interest in my research career.

Excellent technical support with the ion irradiations was provided by R.C. Schmidt, Dr. J.H. Billen and the Nuclear Physics group. I would like to thank Dr. A. West for her training on the proper way to utilize the electron microscope, and R. Casper for providing additional training along with constantly keeping the microscopes in perfect operating condition. I would like to thank Dr. K.T. Hartwig for providing the equipment for the resistivity measurements. Acknowledgements are also due to Dr. R.C. Haight and Dr. M.W. Guinan of LLNL, for helping to show me what experimental research is all about.

I am grateful to Ms. Beth Brown for the long hours spent typing this manuscript. I would also like to thank Ms. Brown and Mrs. Pat Caliva for typing the many reports with countless tables that were generated during my graduate studies.

Finally, I would like to express my appreciation to the past and present members of the Radiation Effects group for their valuable discussions, suggestions, and assistance. These include Dr. R.W. Knoll for paving the way for all of the copper ion irradiation studies, and R.L. Sindelar, Dr. S.K. McLaurin and Dr. D.B. Bullen for their experimental assistance and comments. D.H. Plantz provided capable assistance during the thermal anneal study, and performed many of the tedious measurements. I would also like to acknowledge J.J. Kai, D.J. Pertzborn, L.E. Seitzman, L.M. Wang, C.D. Croessmann and J.H. Liang for their assistance, and D.L. Plumton for providing computer calculations on several occasions.

This work was supported by a Magnetic Fusion Energy Technology Fellowship and with funds supplied by the U.S. Department of Energy.

TABLE OF CONTENTS

LIST OF FIGURES

LIST OF TABLES

CHAPTER I. INTRODUCTION

Neutrons produced in fast breeder reactors and in proposed fusion reactor designs can interact deleteriously with the surrounding structural material. The effects caused by radiation damage from neutrons have been called "the second most serious obstacle to the commercialization of fusion reactors."[1] Neutron irradiation can cause substantial macroscopic swelling as a result of the formation of voids and irradiation generally causes a degradation of material properties, e.g. a loss of ductility. Microstructural phase changes in alloys can also be enhanced or induced by irradiation (see Section III.C).

There are currently no 14-MeV neutron sources that can approach the intensity that will be present in a commercial fusion reactor. Therefore, high-dose neutron irradiation effects must be studied by using fission neutrons, or high-energy electrons or ions. Accelerator-based light-ion or heavy-ion irradiations can produce damage structures similar to that of high-energy neutrons at rates up to several orders of magnitude higher than can be achieved with neutron sources. Therefore, ion irradiation experiments are useful for performing scoping studies on candidate fusion reactor materials since high-dose experimental results can be obtained in very short time periods. Unfortunately, ion irradiation does not produce hydrogen and helium during irradiation, while neutron irradiation produces these gases via transmutation reactions. These gases are known to

exert a considerable effect on void nucleation and growth (see Chapters II, IV.B). This shortcoming can be overcome to a certain degree through the use of gas preinjection or by dual ion irradiation.

The objective of this thesis research is to examine the microstructural stability of copper and two high-strength, high-conductivity copper alloys following thermal annealing and ion irradiation. Copper has found widespread use in electrical applications due to its very favorable electrical conduction properties. However, it is not suitable for many technologically demanding situations because of its low strength. Metallurgical research over the past thirty years has resulted in the development of several copper alloys that have strength levels $\gtrsim$ 400 MPa (60 ksi) while retaining 80% or more of copper's electrical conductivity, but there has been relatively little effort devoted to determining what microstructural parameters are responsible for attainment of these favorable properties. Therefore, part of this thesis research has centered on correlating physical properties with the microstructures of two representative high-strength, high-conductivity copper alloys.

There has recently been an increased interest[2] in the irradiated properties of copper alloys as a result of design studies which call for the incorporation of high-strength, high-conductivity materials in fusion reactors. Requirements of high axial magnet fields have led to a hybrid magnet design where a normal-conducting coil is inserted inside of a shielded superconducting coil. High-strength

copper alloys have been considered for use as high magnetic field insert coils in both tandem mirror and tokamak fusion reactors.[3] Copper alloys are also being considered for use as unshielded magnet coils and as the first wall in compact fusion devices.[4-7] Other proposed areas of use for copper alloys in high irradiation zones include divertors, limiters and radiofrequency antennas.[8-10] Table 1.1 lists some of the various fusion applications for which high strength copper alloys are being considered.

The properties of pure copper following low-dose irradiation have been studied for more than thirty years, and a large data base has been established.[12] However, the behavior of copper following high-dose ($\gtrsim$ 10 dpa) irradiation is not well known. There is also relatively little information available on the response of copper alloys to irradiation at any dose level (see Section IV.B). There are several commercial copper alloys that have unirradiated mechanical and electrical properties which are suitable for fusion reactor applications. When this thesis project was initiated, there was no known irradiation data available for any of these high-strength, high-conductivity copper alloys. There was therefore, a strong need for irradiation data at conditions relevant for fusion reactor applications (1-100 dpa, 50-400°C).

Two candidate high-strength, high-conductivity copper alloys were selected for an investigation of the microstructural alterations that can occur during heavy ion irradiation. AMZIRC and AMAX-MZC are heat-treatable copper alloys manufactured by AMAX Copper, Inc.

Table 1.1. Copper Alloy Applications in Current and Proposed Fusion Devices

Device	Use	Peak Temperature	Maximum Damage Level	Design Yield Stress
RTNS-II[11]	14 MeV Neutron Source Targets	100-200°C	$< 10^{-5}$ dpa	345 MPa
TFCX[4]	Magnet	150°C	< 0.1 dpa	?
CRFPR[5,6]	First Wall	340°C	300 dpa/FPY	75 MPa
	Limiter	370°C	300 dpa/FPY	~ 75 MPa
	Magnet	80°C	1 dpa/FPY	90 MPa
STARFIRE[8]	Limiter	200°C	~ 40 dpa/FPY	330 MPa
MARS[3]	Magnet	150°C	~ 20 dpa/FPY	360 MPa
INTOR[10]	Limiter/Divertor	< 200°C	~ 50 dpa	~ 200 MPa
MINIMARS[7]	Magnet/Shield/ Reflector	590°C	~ 10 dpa/FPY	6 MPa

AMZIRC is a simple binary alloy that contains 0.15% Zr, whereas AMAX-MZC is a quaternary alloy consisting of 0.8% Cr, 0.15% Zr and 0.04% Mg. These alloys have electrical conductivities that are $\gtrsim$ 80% the conductivity of pure copper, and they have yield strengths that exceed 400 MPa (60 ksi). Figure 1.1 shows a plot of the measured yield strength versus electrical conductivity for these two alloys in comparison with pure copper and some other high-strength, high-conduc-

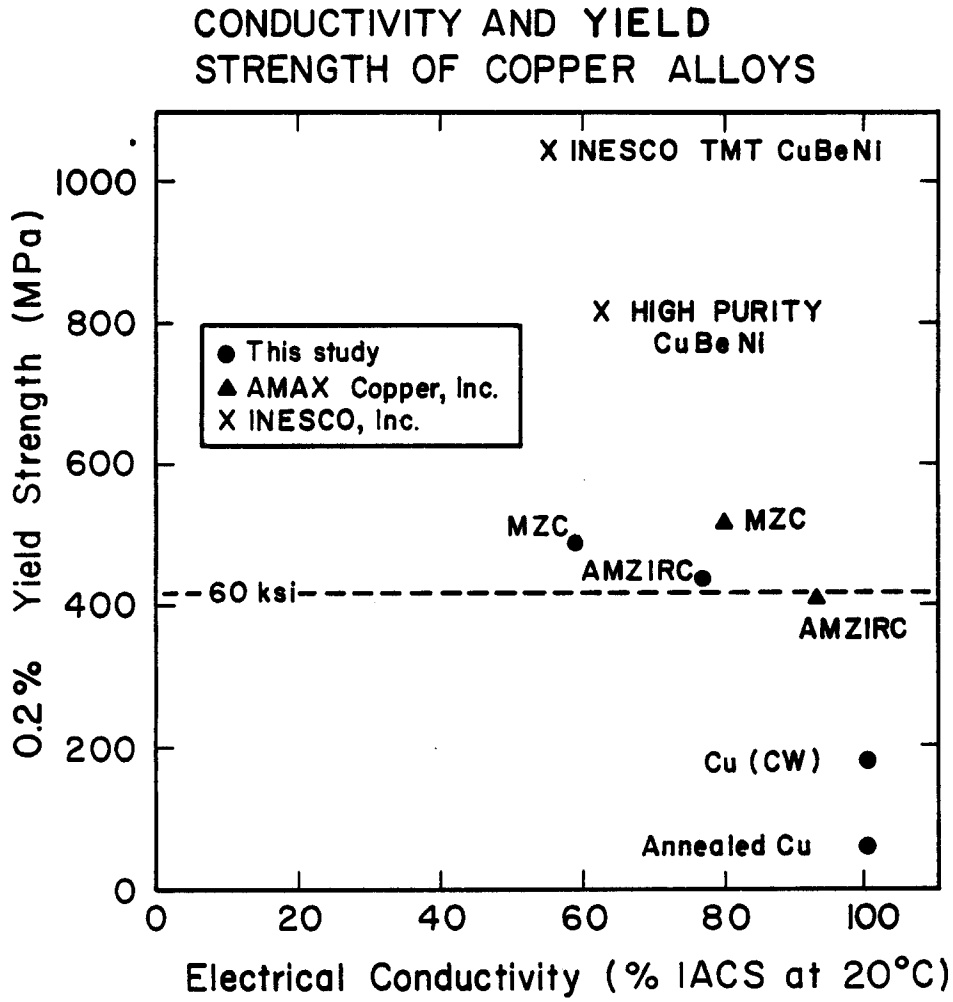

Fig. 1.1. Yield strength and electrical conductivity of selected copper alloys.

tivity copper alloys. The electrical conductivity is given in units of % IACS (International Annealed Copper Standard) at 20°C.[13]

Three distinct research phases were employed in order to fully characterize the potential effects of thermal annealing and radiation damage on the performance of the copper alloys. First, a thorough investigation of the physical properties and microstructures of AMZIRC and AMAX-MZC was performed following a wide range of thermo-mechanical treatments. The effect of 14-MeV Cu ion irradiation on the microstructure of pure copper was then examined over the temperature range of 100-400°C. Finally, the microstructural stability of the two copper alloys was investigated following ion irradiation to peak damage levels of 40 dpa over the temperature range of 100-550°C (0.28-0.61 T_m). Additional irradiations at lower and higher damage levels were also conducted for selected temperatures. All of the irradiated specimens were examined in cross-section using an electron microscope. Comparison of the irradiated microstructure with the microstructure observed following thermal annealing allowed an estimate to be made of the change in physical properties due to irradiation.

Research leading up to this thesis has resulted in twenty-three publications, including seven reviewed papers. A list of these publications is given in Table 1.2.

Table 1.2. List of Previous Publications

1. R.C. Haight, R.M. White and S.J. Zinkle, "A Hybrid Charged-Particle Guide for Studying (n, charged particle) Reactions", Nuclear Data for Science and Technology International Conference, Antwerp, Belgium (Sept. 1982); UCRL-87279 preprint.

2. S.J. Zinkle, R.A. Dodd, G.L. Kulcinski and K. Farrell, "Helium Bubble Formation in Cu, Ni and Cu-Ni Alloys", TMS-AIME Symposium on Radiation Damage Analysis for Fusion Reactors, St. Louis, MO; publ. in J. Nucl. Mater. 117 (1983) 213-217.

3. S.J. Zinkle and G.L. Kulcinski, "14-MeV Neutron Irradiation of Copper Alloys -- Experimental Resistivity Results", DAFS Quarterly Progress Report DOE/ER-0046/8 (Jan. 1982) p. 48.

4. S.J. Zinkle and G.L. Kulcinski, "14-MeV Neutron Irradiation of Copper Alloys -- Review of Resistivity Models and Effect of Defect Clustering", DAFS Quarterly Progress Report DOE/ER-0046/9 (Jan-Feb 1982) p. 93.

5. S.J. Zinkle and G.L. Kulcinski, "14-MeV Neutron Radiation-Induced Microhardness Increase in Copper Alloys", DAFS Quarterly Progress Report DOE/ER-0046/14 (Aug 1983) p. 51.

6. S.J. Zinkle and G.L. Kulcinski, "14-MeV Neutron Radiation-Induced Microhardness Changes in Copper Alloys (Effect of Indenter Load)", UWFDM-558 (Sept. 1983) and DAFS Quarterly Progress Report DOE/ER-0046/15 (Nov. 1983) p. 26.

7. S.J. Zinkle, "Electrical Resistivity of Dislocations in Metals", UWFDM-538 (Sept. 1983).

8. S.J. Zinkle, S.N. Farrens, G.L. Kulcinski and R.A. Dodd, "Irradiated Behavior of High-Strength Copper Alloys", DAFS Quarterly Progress Report DOE/ER-0046/15 (Nov. 1983) p. 127.

9. S.J. Zinkle and G.L. Kulcinski, "14-MeV Neutron Irradiation of Copper Alloys", 3rd Topical Mtg. on Fusion Reactor Materials, Albuquerque, NM (Sept. 1983), J. Nucl. Mater. 122/123 (1984) 449-454.

10. S.J. Zinkle and G.L. Kulcinski, "Low-Load Microhardness Changes in 14-MeV Neutron Irradiated Copper Alloys", Symp. on the Use of Nonstandard Subsized Specimens for Irradiated Testing, Albuquerque, NM (Sept. 1983), to be published as a Special Technical Publication by ASTM.

11. B. Badger, Jr., D.L. Plumton, S.J. Zinkle, R.L. Sindelar, G.L. Kulcinski, R.A. Dodd and W.G. Wolfer, "Experimental Investigation of the Effect of Injected Interstitials on Void Formation", 12th Intern. Symp. on the Effects of Radiation on Materials, June 1984, Williamsburg, VA, to be published in ASTM STP 870, F.A. Garner and J.S. Perrin (Eds.); also UWFDM-582.

12. S.J. Zinkle, G.L.Kulcinski and R.A. Dodd, "Comparison of Thermal and Irradiated Behavior of High-Strength, High-Conductivity Copper Alloys", 12th Intern. Symp. on the Effects of Radiation on Materials, June 1984, Williamsburg, VA, to be published in ASTM STP 870, F.A. Garner and J.S. Perrin (Eds.); also UWFDM-581.

13. S.J. Zinkle, D.H. Plantz, R.A. Dodd and G.L. Kulcinski, "Mechanical Properties and Microstructures of High-Strength Copper Alloys following Thermal Annealing", DAFS Quarterly Progress Report DOE/ER-0046/17 (May 1984) p. 110.

14. S.J. Zinkle and R.L. Sindelar, "Preparation of Ion-Irradiated Foils for Cross-Section Analysis", DAFS Quarterly Progress Report DOE/ER-0046/18 (August 1984) p. 133; also to be presented at the TMS-AIME Symp. on Irradiation Effects Associated with Ion Implantation, Toronto, Oct. 1985.

15. S.J. Zinkle, D.H. Plantz, G.L. Kulcinski and R.A. Dodd, "Microstructures and Physical Properties of Cu-Zr and Cu-Cr-Zr-Mg Alloys", DAFS Quarterly Progress Report DOE/ER-0046/18 (August 1984) p. 143.

16. S.J. Zinkle and R.W. Knoll, "A Literature Review of Radiation Damage Data for Copper and Copper Alloys", UWFDM-578 (June 1984).

17. S.J. Zinkle, D.H. Plantz, A.E. Bair, R.A. Dodd and G.L. Kulcinski, "Correlation of the Yield Strength and Microhardness of High-Strength, High-Conductivity Copper Alloys", 1st Intern. Conf. on Fusion Reactor Materials, Tokyo, Japan, Dec. 3-6, 1984, to be published in the Conference Proceedings in J. Nucl. Mater.; UWFDM-603.

18. S.J. Zinkle, R.A. Dodd and G.L. Kulcinski, "Ion Irradiation of High-Strength, High-Conductivity Copper Alloys at Fusion-Relevant Temperatures", 1st Intern. Conf. on Fusion Reactor Materials, Tokyo, Japan, Dec. 3-6, 1984, to be published in the Conference Proceedings in J. Nucl. Mater.; UWFDM-605.

19. S.J. Zinkle, D.H. Plantz, R.A. Dodd, G.L. Kulcinski and A.E. Bair, "Physical Properties of High-Strength, High-Conductivity Copper Alloys", DAFS Quarterly Progress Report DOE/ER-0046/20 (February 1985) p. 85.

20. S.J. Zinkle and G.L. Kulcinski, "Ion Irradiation of Copper and Copper Alloys to 40 dpa at 100-400°C", DAFS Quarterly Progress Report DOE/ER-0046/20 (February 1985) p. 77.

21. R.L. Sindelar, S.J. Zinkle and G.L. Kulcinski, "Depth-Dependent Swelling in 14 MeV Ion-Irradiated P7 Alloy", DAFS Quarterly Progress Report DOE/ER-0046/20 (February 1985) p. 49.

22. S.J. Zinkle, L.E. Seitzman and W.G. Wolfer, "Stability of Vacancy Clusters in Copper and Other Metals," DAFS Quarterly Progress Report DOE/ER-0046/21 (April 15, 1985).

23. S.J. Zinkle and G.L. Kulcinski, "Radiation Enhanced Recrystallization in Copper Alloys," DAFS Quarterly Progress Report DOE/ER-0046/21 (April 15, 1985).

References for Chapter I

1. G.L. Kulcinski, Contemp. Phys. 20 (1979) 417-447.

2. Copper and Copper Alloys for Fusion Reactor Applications, F.W. Wiffen and R.E. Gold (Eds.), DOE-OFE Workshop Proceedings, (ORNL, CONF-830466), June 1984.

3. L.J. Perkins, J. Nucl. Mater. 122/123 (1984) 1371.

4. D. Cohn, personal communication (1984).

5. R.A. Krakowski, J. Nucl. Mater. 122/123 (1984) 37-50.

6. R.L. Hagenson et al., "Compact Reversed-Field Pinch Reactors: Preliminary Engineering Considerations," LA-10200-MS (Aug. 1984); also see F.W. Clinard, Jr., "Copper Alloy Irradiation Studies in Support of CRFPR First Wall," in Ref. 2.

7. I.N. Sviatoslavsky, "Minimars Blanket Considerations," presented at ORNL Fusion Engineering Design Center, Jan. 1985.

8. "STARFIRE - A Commercial Tokamak Fusion Power Plant Study," (Sept. 1980), Argonne National Laboratory.

9. W.B. Gauster et al., J. Nucl. Mater. 122/123 (1984) 80-90.

10. W.M. Stacey, Jr., et al., Critical Issues, Vol. I, USA FED-INTOR/82-1 Phase 2A report.

11. C. Logan et al., J. Nucl. Mater. 103/104 (1981) 1551-6.

12. S.J. Zinkle and R.W. Knoll, "A Literature Review of Radiation Damage Data for Copper and Copper Alloys," UWFDM-578 (June 1984).

13. ASTM B193-78, "Standard Method of Test for Resistivity of Electrical Conductor Materials," 1983 Annual Book of ASTM Standards, Vol. 2.01, Copper and Copper Alloys; also see P. Gregory et al., Metallurgica 71 (1965) 207. (100% IACS = 1.7241 μΩ-cm.)

CHAPTER II. GENERAL RADIATION DAMAGE THEORY

II.A. Point Defect Production

Irradiation of crystalline solids with energetic neutrons, ions or electrons causes atoms of the bombarded material to be displaced and relocated elsewhere in the crystal. The creation of these Frenkel defects (vacancy-interstitial atom pairs) can give rise to macroscopic alterations in the material properties of the irradiated solid. The density of the Frenkel pairs along the path of the incident particle depends on the type and energy of the particle:[1]

$$N_d(E) = N_o \int \phi(E)\ \sigma(E)\ K(E,T)\ \nu(T)\ dT \qquad (2.1)$$

where N_o is the atomic density of the crystal, $\phi(E)$ is the flux of incident particles with energy E, $\sigma(E)$ is the collision cross-section between the incident particle and the matrix atoms, $K(E,T)$ is the probability that, if an interaction takes place, it will produce a primary knock-on atom (PKA) with kinetic energy T, and $\nu(T)$ is the number of matrix atoms which are subsequently displaced by the PKA.

Fast neutrons have a relatively small collision cross-section, so the PKA's are relatively widely spaced. The energetic PKA's produced while the neutron is slowing down will in turn interact with other lattice atoms. The PKA dissipates its kinetic energy by either displacing other lattice atoms (creating higher-order knock-on atoms) or through electronic interactions (heat). Electronic excitation be-

comes increasingly important with higher PKA energies (high incident neutron energies). The PKA's produced during fast neutron irradiation give rise to dense subcascades of Frenkel defects. A detailed description of the events which occur during the displacement cascade may be found in the literature.[2-4]

Energetic electrons (> 0.5 MeV) are also capable of causing atomic displacements on crystalline materials. The displacement damage is limited to a few Frenkel pairs per nuclear collision due to the small mass of the electron. This produces an isolated point defect damage structure, as opposed to the large displacement cascades produced during fast neutron irradiation.

Ion irradiation results in a displacement cascade which is more dense than that found for neutron irradiation due to the large Rutherford collision cross-section between the incident ion and the lattice atoms. The damage region is limited to a few microns. The displacement damage rate is depth-dependent because the ion-atom collision cross-section increases as the ion velocity decreases. Therefore, the displacement rate near the ion end of range is greater than at the surface by a factor of 5-10.

To provide a means of comparison between the different irradiation environments, a measure of damage level known as the dpa (displacements per atom) has been established. A dose of 1 dpa means that, on the average, each atom in the crystal has been displaced from its lattice site once during an irradiation. It is mathematically given by the time integral of Eq. (2.1) (normalized to the

atomic density). The dpa unit does not account for dose rate effects, Frenkel pair recombination in the cascade region, or spatial rearrangements due to thermally-assisted migration. It also does not consider the effect of transmutation products such as helium or hydrogen. Nevertheless, it is a useful unit for calculating first-order effects that will be expected in various irradiation environments.

The method used to calculate the dpa profile of an ion-irradiated metal may be briefly outlined as follows. More thorough reviews are contained elsewhere.[5,6] The commonly accepted model for determining energy loss of an ion is based on theoretical work of Lindhard and coworkers,[7,8] and is known as LSS theory. LSS theory assumes an amorphous target and also that the nuclear and electronic collisions are independent of each other. The electronic energy loss is assumed to be proportional to the incident ion velocity. The nuclear stopping cross-section is calculated from a screened Thomas-Fermi statistical model of the atom. The theory is applicable to many ion/target combinations over a wide energy range, but it breaks down for moderately low ion energies. There is experimental evidence which indicates that LSS theory overestimates the contribution of electronic stopping for heavy ion irradiations, leading to too short of a calculated ion range -- cross-section studies have shown that the damage peak calculated from LSS theory is 15-20% nearer the surface than the observed peak damage region[9-13] (see Farrell et al.[9] for details.

Once the nuclear and electronic stopping powers have been calculated, the number of displacements caused by an incident particle can be estimated. The commonly accepted procedure is to use the Kinchin-Pease model as modified by Torrens and Robinson.[14]

$$N_d(x)\ (\text{dpa/sec}) = (\phi/N)\ \frac{KS_D(x)}{2\ E_d} \qquad (2.2)$$

where ϕ is the incident particle flux, N is the atomic density of the target, $S_D(x)$ is the energy available for displacements (damage energy), K is the displacement efficiency, and E_d is the spatial-averaged displacement threshold energy. Early computer calculations indicated that the displacement efficiency was independent of the incident particle energy,[14] with a value of K = 0.8. Recent experiments and computer calculations have shown that K varies strongly with energy.[15,16] The value of the displacement efficiency in copper as a function of bombarding particle energy is shown in Fig. 2.1. From this figure it is evident that K ≃ 0.3 should be used to describe the damage state of ion or neutron irradiated copper. However, the value of K = 0.8 will be used in this thesis since it is still the accepted international value.

The displacement energy (E_d) varies with crystallographic direction by a factor of 2-3, so the polycrystal value of E_d must be averaged over all of the crystal orientations. An additional complication is the fact that E_d is temperature-dependent,[17] decreasing by about 70% as the temperature is raised from 4 K to 300 K for elec-

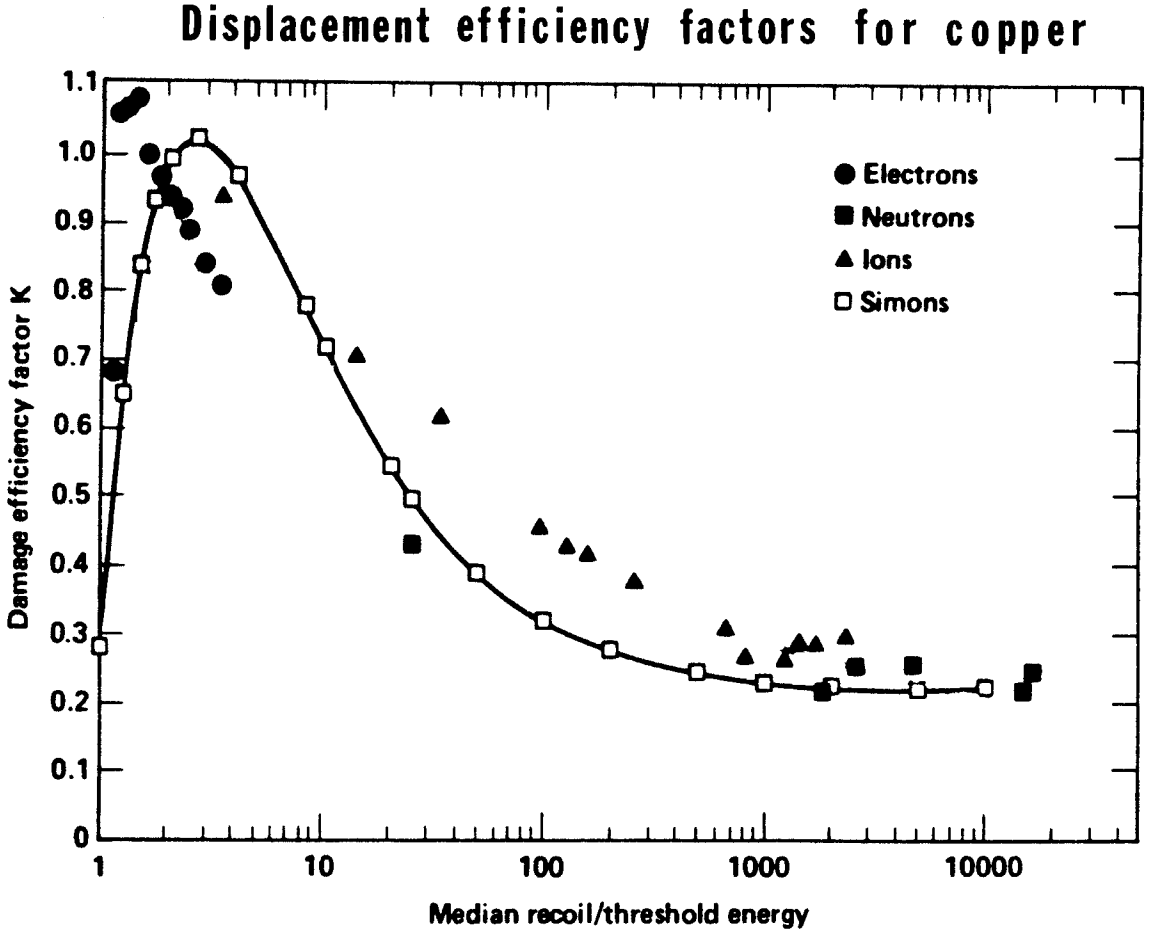

Displacement rate

$$R_D = \frac{\phi K S_D(x)}{2\rho E_D}$$

Fig. 2.1. Displacement efficiency factor for copper (from Ref. 16).

tron irradiation of copper. Indications are that the temperature dependence is much weaker for high energy irradiations,[17] and this effect is neglected in this thesis since no quantitative high-energy irradiation measurements are available. A value of E_d = 29 eV was used in all dpa calculations, in accordance with the value commonly used for copper in the literature.[18]

Manning and Mueller[19] have developed a computer code, EDEP-1, which uses LSS theory to calculate energy deposition and the injected ion distribution as a function of depth for ion irradiation. Brice[20] developed a similar code based on LSS theory which uses a semi-empirical three-parameter formula to calculate the electronic stopping. The Brice Code is more sophisticated than EDEP-1 in that the energy transported by recoil atoms is calculated. Figure 2.2 shows the results of a Brice code calculation of the injected ion distribution and displacement damage profile for 14-MeV Cu ions incident on a copper target (displacement efficiency K = 0.8).

II.A.1 Spatial Distribution of the Damage

Neutron and ion irradiations produce point defects in the form of highly localized displacement cascades. The study of these "cascade effects" through computer simulation[21,22] gives information that is useful in correlating ion and fission neutron irradiations with fusion neutron irradiations. The events which occur during a displacement cascade may be identified as follows:[22] First is the collisional phase (lasting about 10^{-13} sec), during which atomic displacements occur. Simulations indicate that the dis-

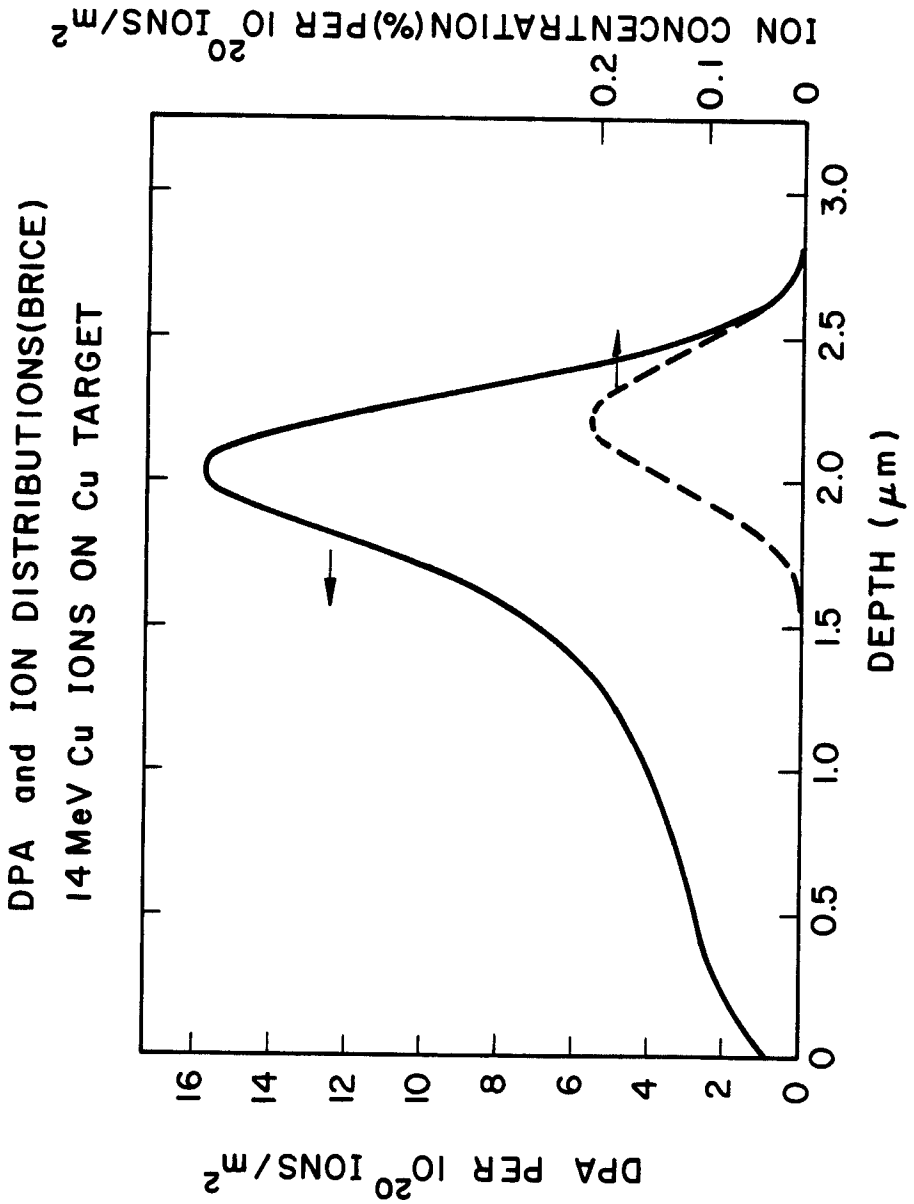

Fig. 2.2. Calculated 14-MeV Cu ion damage profile and injected ion distribution (K = 0.8).

placement cascade exists as a vacancy-rich core surrounded by an interstitial-rich shell. The "cascade cooling" phase begins during the collisional phase and lasts about 10^{-11} sec. During this second phase the displacement cascade approaches thermal equilibrium with its surroundings and defect rearrangement occurs. Short-term annealing then commences, and the cascade defects interact with one another via thermally activated diffusion brought on by the heating from electronic interactions. This process occurs for a time period on the order of 10^{-8} seconds for copper. Simulation studies indicate that the cascade structure following the collisional phase is the dominant factor in determining the final behavior of the created defects[22,23], i.e. the cascade cooling phase is primarily responsible for determining defect production efficiency.

Only a fraction of the defects created during ion or neutron irradiation escape interstitial-vacancy recombination during the cascade cooling and annealing period. The free-defect fraction of a cascade is relatively constant for PKA energies greater than 30 keV.[16,23] The average PKA energy resulting from a 14-MeV neutron irradiation of copper is about 170 keV (Ref. 22). Heinisch[23] has found from computer simulation that about 14% of the interstitials created in a high-energy cascade survive as free defects. Wollenberger[24] experimentally determined from resistivity measurements that about 15% of the interstitials created during a fast-neutron irradiation of copper at 80 K survive correlated recombination events. Using a similar analysis, Zinkle and Kulcinski[25]

estimated that about 16% of the defects created during a 14-MeV neutron irradiation of copper at 25°C escape correlated recombination.

II.B. Void Nucleation Theory

Irradiation produces concentrations of vacancies and interstitials which are much higher than the normal thermal equilibrium concentrations. At sufficiently high temperatures, both vacancies and interstitials are mobile and they may aggregate to form defect clusters. Interstitials generally become mobile in metals at very low temperatures (< 50 K), while vacancies are mobile for temperatures $\gtrsim 0.25\ T_{MP}$.[26] Interstitials rapidly aggregate during irradiation to form dislocation loops, thereby increasing the dislocation density of annealed metals. Dislocations have a long-range interaction with point defects. Interstitial atoms have a stronger attraction to edge-type dislocation sinks than vacancies (dislocation bias) due to their greater relaxation strain.[27-29] As a result there is a higher flux of vacancies arriving at neutral sinks, which may lead to cavity formation and macroscopic swelling.

Void-induced swelling in metals is generally limited to the temperature range of 0.3-0.6 T_{MP}. At lower temperatures, the low vacancy mobility produces a large concentration of single vacancies. The mobile interstitials therefore have an increased probability of recombining with a vacancy instead of migrating to a sink. The lower net vacancy concentration is insufficient to fuel void growth. At

high temperatures, void embryos become unstable due to vacancy re-emission and void nuclei dissolution occurs.

Several theories have been proposed to model the process of irradiation-induced void nucleation. A brief review of some of these theories is presented below. More detailed reviews may be found in the literature.[30,31] The first theories that dealt with the effect of irradiation on void nucleation were developed independently by Katz and Wiedersich[32] and Russell,[33] and are collectively known as WKR theory. These models used classical homogeneous nucleation theory to predict the clustering of vacancies and interstitials in the absence of any impurities.

Voids were originally considered to be neutral sinks. Wolfer and coworkers[34-36] have shown that small, bare voids have a strong bias toward interstitial absorption due to an image force interaction. This would obviously prohibit void nucleation and growth. Therefore, they have suggested that a void surface coating consisting of a shell of impurity atoms may be necessary in order for void nucleation to occur.

Russell[31] has noted that there are several mechanisms by which void nucleation can occur: (a) homogeneous nucleation of vacancy and interstitial clusters, (b) heterogeneous nucleation on single gas atoms or gas atom clusters, (c) co-precipitation of vacancies, interstitials and gas atoms, (d) direct nucleation from the vacancy-rich core of displacement cascades, possibly with stabilization by impurity capture, and (e) nucleation in the presence of surface-active im-

purities (Brownian motion). Using a nodal line/critical point formalism, Russell[31,37] determined that spontaneous void nucleation may occur during neutron irradiation if sufficient helium is present. However, quantitative predictions of the theory did not agree with experimental results.

Solute segregation around a void can act to alter the diffusion coefficients of the point defects, thereby altering void swelling.[38] Nickel enrichment and chromium depletion around voids as compared to the matrix concentration has been observed in irradiated stainless steel.[39-41] Solute segregation around voids has also been observed in copper alloys (see Chapter IV.B). Solute segregation effects on void nucleation have been theoretically investigated by Pillar and Marwick[42] and Si-Ahmed and Wolfer.[43] Si-Ahmed and Wolfer derived void bias factors for interstitials and vacancies that can be used to determine the arrival rates of these point defects at the void.

Another theoretical approach to void nucleation has been developed recently by Wolfer and Wehner.[44,45] The void size is treated as a continuous variable, and a Fokker-Planck equation is used to describe the vacancy cluster distribution. Their results depend rather critically on the value of the sink-averaged interstitial bias factor. Physically reasonable results are obtained when appropriate bias factor parameters are used. They obtained void number densities that are in close agreement with measured values. Previous void nucleation theories based on the WKR formalism (steady-

state nucleation theory) were generally only accurate to within an order of magnitude in their predictions of void number densities. Wehner and Wolfer have shown[45] that void nucleation is an evolutionary process with no steady-state regime. Therefore, it appears that the basic assumption contained in the WKR model (quasi-steady-state conditions) is not valid. However, some of the qualitative predictions of WKR theory are still appropriate. Wolfer has recently reviewed the qualitative features predicted by void nucleation theories.[46]

II.C. Cavity Growth

Once a vacancy cluster becomes larger than a critical size, n^*, it will continue to grow without shrinking upon further irradiation at the same temperature. Most theories on void growth are based on chemical reaction rate theory. This approach was first applied to the swelling problem by Harkness and Li,[47] and was subsequently extended by Wiedersich[48] and Brailsford and Bullough.[49] The basic mathematical model represents the point defect sinks by effective "lossy" sink strengths in a homogeneous continuum. Mansur[50] and others[29,51] have reviewed the subject of cavity growth. The following represents a brief summary of the theory.

Rate equations may be written to describe the point defect production, diffusion and loss to sinks. The various sink strengths are modeled as being uniformly distributed throughout the medium. It is generally assumed that the metal already contains void embryos and interstitial loops. Brailsford et al.[52,53] have analyzed in detail

the strengths of the different sinks, including voids, grain boundaries, dislocations, for surfaces and saturable sinks. Once the point defect concentrations have been obtained from the rate equations, the void growth rate is given by (assuming no divacancy contribution):[54]

$$\frac{dr_v}{dt} = \frac{\Omega}{r_v} \{Z_v^v(r_v)D_v[C_v - C_v^e(r_v)] - Z_i^v(r_v)D_iC_i\} \qquad (2.3)$$

where Ω is the atomic volume, r_v is the void radius, $Z_{i,v}^v$ is the void capture efficiency of interstitials or vacancies and $C_v^e(r_v)$ is the thermal vacancy concentration at the void,

$$C_v^e(r_v) = C_v^e \exp[(\frac{2\gamma}{r_v} - p_g) \frac{\Omega}{kT}] \qquad (2.4)$$

where C_v^e is the bulk thermal vacancy concentration, γ is the surface tension and p_g is the gas pressure in the void. Mansur[54] and Wolfer[55] have investigated the effect of incorporating mobile divacancies into void nucleation and growth equations. Divacancies were shown to have a fairly substantial influence on void swelling, producing increases in swelling at low temperatures and decreases at the peak swelling temperature.

Wolfer[46] recently reviewed void nucleation and growth models and showed that they were in good qualitative agreement with experimental swelling data. Void swelling as a function of dose can be divided into an initial transient regime of low-swelling rate fol-

lowed by a steady-state, higher-swelling rate regime. According to the theory, void nucleation and growth occur during the transition period and the void sink strength approaches the value of the dislocation sink strength. Steady-state swelling commences when the void and dislocation sink strengths become equivalent. The steady-state swelling rate is primarily determined by the net bias of large voids and by the fraction of point defects which survive in-cascade recombination.

II.C.1 Gas Effects

Gases are known to play a major role in the nucleation and growth of voids in irradiated materials.[46,56,57] Helium and hydrogen are continuously produced during neutron irradiation as a result of (n,α) and (n,p) transmutation reactions. Oxygen and other reactive gases are often introduced into metals during fabrication. Reactive gases such as hydrogen and oxygen can become chemisorbed on subcritical-sized void surfaces, thereby reducing the surface energy and the activation barrier for void nucleation[46] (also see Chapter VIII.C).

Farrell[56] has given a recent review of the observed effects of helium on void swelling. Helium is essentially insoluble in metals[58] and it can coalesce along with vacancies to form gas-filled cavities. The cavity gas pressure minimizes the thermal re-emission of vacancies from the cavity and therefore enhances the nucleation process. These small gas cavities may subsequently cause an acceleration or deceleration of swelling as compared to the no-gas

condition, depending on the disposition of the microstructure and experimental conditions. The method by which helium is introduced into the matrix strongly influences cavity swelling.[56] Swelling increases in the following order: cold pre-implantation, hot pre-implantation, and co-implantation. Cavity size scales in the same order, while cavity concentration varies inversely with the above.

II.D. Special Considerations for Ion Irradiation

II.D.1 Effective Temperature Shift

The temperature range of swelling is determined by a balance between point defect recombination, loss to sinks (including voids) and thermal emission of vacancies at voids. The high displacement rates associated with heavy-ion bombardment studies result in increased point defect recombination and a lower ratio of thermally emitted versus in-flowing vacancies. This high displacement rate effect is equivalent to conducting the irradiation at a lower temperature with "normal" displacement rates.

Bullough and Perrin[59] have investigated the effect of displacement damage rate on swelling. From their analysis, the magnitude of the temperature shift of the swelling peak can be derived to be (in its simplest form)

$$\Delta T = (T_i)^2 \frac{k}{E_v} \left[\frac{1}{1 + \frac{kT_i}{E_v} \ln\left(\frac{P_i}{P_n}\right)}\right] \ln\left(\frac{P_i}{P_n}\right) \qquad (2.5)$$

where T_i is the ion irradiation temperature, k is the Boltzmann constant, E_v is the vacancy self-diffusion activation energy and P_i,

P_n are the respective defect displacement rates for ion and neutron irradiation. Equation (2.5) predicts that an ion irradiation of copper at 400°C with a displacement rate of 2×10^{-3} dpa/s will correspond to a neutron irradiation at 280°C with a displacement rate of 10^{-6} dpa/s (assuming a vacancy self-diffusion energy[60] of 2.06 eV). The theory neglects recombination effects,[50] and therefore is not expected to be accurate at the low temperature end of the swelling regime (around 200-250°C for neutron-irradiated copper).

II.D.2 Injected Interstitials

Energetic heavy ions used to create displacement damage in metals come to rest in the form of excess interstitial atoms in the matrix at a depth from the surface on the order of a few microns. Garner[61] has recently reviewed ion irradiation experiments which demonstrate the significant role that the injected ions can play in causing suppression of void swelling. In all cases, a decreased swelling rate was observed in the region where the injected ions come to rest.

Brailsford and Mansur[62] were the first to theoretically investigate the effect of injected interstitials on void growth. At high temperatures (sink-dominated regime) the reduction in void growth was predicted to be small unless voids were much more important than dislocations as point defect sinks. Void growth suppression was predicted to become more pronounced at low temperatures, where recombination is important. (Enhanced recombination lowers the concentration of vacancies and interstitials by an equal amount.

Therefore, the relative contribution of injected interstitials to the total point defect concentration increases when recombination dominates.) The suppression of growth varies linearly with the injected interstitial fraction and also depends strongly on the vacancy migration energy. A subsequent study by Mansur and Yoo[50,63] indicated that large or even total suppression could occur for ion-irradiated metals with a high vacancy migration energy, low bias or low sink strength. Using reasonable parameters, the suppression of void growth is predicted to be $\lesssim$ 50%.

Experimental evidence[61] which indicated that injected interstitials suppressed swelling by a factor of 5 led Plumton and Wolfer[64,65] to investigate the influence of the injected interstitial on void nucleation. They found a dramatic decrease in the void nucleation rate at lower temperatures (recombination regime). Their results are strongly dependent on the vacancy migration energy and the sink strength, with the largest suppression observed for high E_v^M and low sink strength. A recent experimental investigation of the effect of injected interstitials on void formation confirmed that suppression of void nucleation is temperature dependent.[66] Theoretical predictions of the suppression effect were in good qualitative agreement with the experimental observations. It was concluded that cross-section analysis techniques should as a rule be used whenever quantitative void swelling information is desired from ion irradiation studies.

II.D.3 Surface Effects

As mentioned previously, ion irradiation results in a damage zone which is confined to a region extending a few microns in from the surface. Point defect concentrations approach thermal equilibrium values at the free surface if the surface is a good absorber of point defects. Yoo and Mansur[67] have studied the effect of free surfaces on void and loop formation. They found two surface-related phenomena: (1) interstitial loops may preferentially form at an intermediate distance from the surface without the presence of other point defect sinks, whereas they would not be present in a similar bulk (e.g., neutron) experiment. (2) Zones denuded of voids and dislocation loops should exist near the surface. Garner and Thomas[68] experimentally determined a temperature-dependent denuded surface zone width (L_{vf}) from HVEM studies; $L_{vf} \sim (D_v/P)^{1/2}$, where D_v is the vacancy diffusivity and P is the displacement rate. The value of L_{vf} is on the order of 0.5-1.0 μm for displacement rates typical of ion or electron irradiation (10^{-3} dpa/s).

II.D.4 Diffusional Spreading

Ion irradiation results in a depth-dependent profile of point defect concentrations. Point defects may diffuse down these concentration gradients (Ficks law) and cause a broadened point defect profile compared to the calculated initial profile. Evidence of diffusional spreading has been obtained by several researchers.[9,63,66,69] The importance of this effect is that the steady-state point defect concentrations at a given depth do not

coincide with the values obtained from damage calculations such as the BRICE code. In particular, it is predicted that diffusional spreading will decrease void swelling at the damage peak and cause void swelling at depths greater than would otherwise be expected.[63] This may have important consequences when attempts are made to correlate ion irradiation swelling rates with neutron and electron results. Cross-section studies are the best experimental technique to use for assessing the importance of diffusional spreading.

References for Chapter II

1. G.L. Kulcinski, Contemp. Phys. 20 (1979) 417-447.

2. D.R. Olander, Fundamental Aspects of Nuclear Reactor Fuel Elements, ERDA Technical Information Center Document TID-26711-P1, 1976, Chapt. 17.

3. M.W. Thompson, Defects and Radiation Damage in Metals, Cambridge Univ. Press, Cambridge (1969).

4. Radiation-Induced Voids in Metals, J.W. Corbett and L.C. Ianniello (Eds.), U.S.A.E.C. Technical Information Center, CONF-710601, 1972.

5. M.T. Robinson, in Ref. 4, p. 449.

6. G.L. Kulcinski, J.J. Laidler and D.G. Doran, Rad. Effects 7 (1971) 195-202.

7. J. Lindhard, M. Scharff and H.E. Schiott, Mat-Fys. Medd., Kgl. Dan. Vidensk. Selsk. 33 No. 14 (1963).

8. H.E. Schiott, Mat-Fys. Medd., Kgl. Dan. Vidensk. Selsk. 35 No. 9 (1966).

9. K. Farrell, N.H. Packan and J.T. Houston, Rad. Effects 62 (1982) 39-52.

10. O.S. Oen, J. Narayan and T.S. Noggle, in Applications of Ion Beams to Metals, S.T. Picraux, E.P. Eer Nisse, and F.L. Vook (Eds.), (1974) 6339-650.

11. J.B. Roberto and J. Narayan, Fundamental Aspects of Radiation Damage, CONF-751006-P1 (1975) 120-126.

12. J. Narayan, O.S. Oen and T.S. Noggle, J. Nucl. Mater. 71 (1977) 160-170.

13. J.B. Whitley, Ph.D. Thesis, Nuclear Engineering Department, University of Wisconsin-Madison (1978).

14. I.M. Torrens and M.T. Robinson, in Ref. 4, p. 739.

15. R.S. Averback et al., Phys. Rev. B 18 (1978) 4156-4171.

16. J.H. Kinney, M.W. Guinan, Z.A. Munir, J. Nucl. Mater. 122/123 (1984) 1028-1032.

17. K. Urban and N. Yoshida, Phil. Mag. A 44 (1981) 1193-1212.

18. R.R. Coltman, Jr. et al., J. Nucl. Mater. 99 (1981) 284-293.

19. I. Manning and G.P. Mueller, Computer Physics Comm. 7 (1974) 85-94.

20. D.K. Brice, "Ion Implantation Range and Energy Deposition Codes COREL, RASE4 and DAMG2," SAND-7500622, Sandia National Laboratories, Albuquerque, NM, July 1977.

21. M.T. Robinson and I.M. Torrens, Phys. Rev. B9 (June 1974) 5008.

22. H.L. Heinisch, "Computer Simulation of Displacement Cascades in Copper," HEDL-TME 83-17, UC-20, 20c, Hanford Engineering Development Lab. (1983); also M.W. Guinan and J.H. Kinney, J. Nucl. Mat. 103 & 104 (1981) 1319-1324.

23. H.L. Heinisch, J. Nucl. Mater. 117 (1983) 46-54.

24. U. Thesis and H. Wollenberger, J. Nucl. Mater. 88 (1980) 121.

25. S.J. Zinkle and G.L. Kulcinski, J. Nucl. Mater. 122/123 (1984) 449-454.

26. J.W. Corbett, Electron Radiation Damage in Semiconductors and Metals, Solid State Physics Supplement 7, Academic Press (1966).

27. R. Bullough and R.C. Perrin, in Radiation Damage in Reactor Materials, Vol. II, IAEA, Vienna (1969), p. 233.

28. S.D. Harkness and Che-Yu Li, in Radiation Damage in Reactor Materials, Vol. II, (1969), p. 189.

29. J. Gittus, Irradiation Effects in Crystalline Solids, Applied Science Publ. Ltd., Barking, Essex, England (1978).

30. R.M. Mayer and L.M. Brown, J. Nucl. Mater. 95 (1980) 44-107 (seven papers).

31. K.C. Russell, Acta Met. 26 (1978) 1615-1630.

32. J.L. Katz and H. Wiedersich, J. Chem. Phys. 55 (1971) 1414.

33. K.C. Russell, Acta Met. 19 (1971) 753.

34. W.G. Wolfer and M.H. Yoo, ORNL/TM-5398 (May 1976).

35. L.K. Mansur and W.G. Wolfer, J. Nucl. Mater. 69 & 70 (1978) 825-829; also see W.G. Wolfer and L.K. Mansur, J. Nucl. Mater. 91 (1980) 265.

36. W.G. Wolfer, L.K. Mansur and J.A. Sprague, in Radiation Effects in Breeder Reactor Structural Materials, (1977) p. 841.

37. C.A. Parker and K.C. Russell, in Effects of Radiation on Materials, ASTM STP 782, H.R. Brager and J.S. Perrin (Eds.), Scottsdale, AZ, (1982) p. 1042.

38. A.D. Brailsford, J. Nucl. Mater. 56 (1975) 7.

39. P.R. Okamoto and H. Wiedersich, J. Nucl. Mater. 53 (1974) 336.

40. L. Laour et al., ASTM STP 782 (1982) 310.

41. W.G. Wolfer, F.A. Garner and L.E. Thomas, ASTM STP 782 (1982) 1023.

42. R.C. Pillar and A.D. Marwick, J. Nucl. Mater. 83 (1979) 42.

43. A. Si-Ahmed and W.G. Wolfer, ASTM STP 782 (1982) 1008.

44. W.G. Wolfer et al., in Intern. Conf. on Rad. Effects in Breeder Reactor Structural Materials, M.L. Bleiburg and J.W. Bennett (Eds.), (1977) 841.

45. M.F. Wehner and W.G. Wolfer, "Vacancy Cluster Evolution in Metals Under Irradiation," to be published in Phil. Mag. A (1985); also UWFDM-590.

46. W.G. Wolfer, J. Nucl. Mater. 122/123 (1984) 367-378.

47. S.D. Harkness and Che-Yu Li, Met. Trans. 2 (1971) 1457.

48. H. Wiedersich, in 2nd Intern. Conf. on the Strength of Metals and Alloys (ASM, 1970), Vol. 2; also, Rad. Effects 12 (1972) 111.

49. A.D. Brailsford and R. Bullough, J. Nucl. Mater. 44 (1972) 121.

50. L.K. Mansur, Nucl. Tech. 40 (1978) 5.

51. M.H. Wood, R. Bullough and M.R. Hayns, Proc. of the Intern. Conf. on Irradiation Behavior of Metallic Materials for Fast Reactor Core Components, Corsica, France (1979) p. 107.

52. A.D. Brailsford, R. Bullough and M.R. Hayns, J. Nucl. Mater. 60 (1976) 246.

53. A.D. Brailsford, J. Nucl. Mater. 60 (1976) 257.

54. L.K. Mansur and M.H. Yoo, Corsica Conf. Supplement (1979) 9-16.

55. W.G. Wolfer and A. Si-Ahmed, Phil. Mag. A46 (1982) 723.

56. K. Farrell, Rad. Effects 53 (1980) 175-194.

57. A.J.E. Foreman and B.N. Singh, "Role of Inert and Reactive Gases in Void Nucleation," Dimensional Stability and Mechanical Behavior of Irradiated Metals and Alloys (Brighton Conf.), British Nuclear Energy Society, London (1983) 95-99.

58. R. Blackburn, Metallurgical Reviews 11 (1966) 159.

59. R. Bullough and R.C. Perrin, in Irradiation Effects on Structural Alloys in Nuclear Reactor Applications, ASTM STP 484 (1970) 317.

60. R.R. Bourassa and B. Lengeler, J. Phys. F 6 (1976) 1405.

61. F.A. Garner, J. Nucl. Mater. 117 (1983) 177-197.

62. A.D. Brailsford and L.K. Mansur, J. Nucl. Mater. 71 (1977) 110.

63. L.K. Mansur and M.H. Yoo, J. Nucl. Mater. 85/86 (1979) 523.

64. D.L. Plumton and W.G. Wolfer, J. Nucl. Mater. 120 (1984) 245.

65. D.L. Plumton, H. Attaya and W.G. Wolfer, J. Nucl. Mater. 122/123 (1984) 650.

66. B. Badger, Jr., D.L. Plumton, S.J. Zinkle, R.L. Sindelar, G.L. Kulcinski, R.A. Dodd and W.G. Wolfer, 12th Intern. Symp. on the Effects of Radiation on Materials, Williamsburg, VA, June 1984, ASTM STP 870 (1985); also UWFDM-582.

67. M.H. Yoo and L.K. Mansur, J. Nucl. Mater. 62 (1976) 282.

68. F.A. Garner and L.E. Thomas, in Effects of Radiation on Substructure and Mechanical Properties of Metals and Alloys, ASTM STP 529 (1973) 303-325.

69. C.H. Henager, Jr., J.L. Brimhall and E.P. Simonen, Rad. Effects 36 (1978) 49-55.

CHAPTER III. SOLUTE SEGREGATION AND PHASE STABILITY

III.A. Effect of Alloying Elements on Void Swelling

It is well-known from experimental studies of alloys that swelling depends on the solute type and concentration -- solute atoms have been found to either retard or accelerate the nucleation and growth of voids.[1] Experimental data indicates that small changes in the concentrations of matrix alloying elements can lead to very significant changes in swelling.[2] Mansur et al.[3,4] and others[5-7] have recently reviewed the effect of solute segregation and precipitation on swelling.

Various theoretical models have been established to model the effects of solute atoms and precipitates on void swelling. Harkness and Li[8] first hypothesized that point defect trapping by solute atoms could reduce swelling through enhanced defect recombination. They found that a concentration of 0.1% of solute could increase recombination by ten orders of magnitude and reduce swelling by 40%. More sophisticated treatments[9,10] found that the addition of mobile solute atoms to a metal shifted the swelling peak to lower temperatures and decrease the amount of swelling, in agreement with experiment.[5,11] The influence of radiation-induced segregation (RIS) on swelling was found to be dose rate-dependent,[3,5] with the largest segregation effects and least swelling resistance occurring at low damage rates.

Solute segregation to point defect sinks can affect void nucleation and growth by altering the sink capture efficiencies.[12-15] Wolfer and coworkers[12,14] have studied the effect on the void bias of a segregation shell surrounding a void. They found that the void nucleation rate changed by several orders of magnitude when the elastic constants or lattice parameter of the shell differed only slightly from the matrix values. Without segregation effects, void nucleation was only possible if the dislocation bias was greater than 50%. Another effect to consider is that segregation of impurities to the void surface can lower the surface energy, with a resultant increase in the void nucleation rate.

III.B. Solute Segregation

Radiation-induced segregation (RIS) of alloying elements to and away from sinks is a commonly observed phenomenon which is caused by a coupling between defect fluxes and solute fluxes. Most studies have concentrated on relatively simple binary alloy systems, but recent investigations have been carried out on ternary and more complicated alloy systems.[7,16] Okamoto and Rehn[17] have reviewed the information obtained on RIS through surface segregation experiments.

Solute segregation can lead to enrichment or depletion of alloying elements in regions near the surface or internal point defect sinks. This process has several important consequences. Irradiation-enhanced or induced precipitation may occur at locally enriched regions. Alternatively, local changes in composition near precipitate interfaces may cause the dissolution of precipitates, or cause

an alteration in the activation energy for the nucleation of precipitates or voids. The microstructural changes mentioned above can have deleterious effects on the mechanical properties of the irradiated material. Alloys which were prepared with a specific microstructure in order to attain their optimum properties may suffer a radical degradation of these properties. Solute segregation during irradiation may lead to a less-desirable microstructure.

III.B.1 Radiation Enhanced Diffusion

The increased concentration of point defects present in the matrix during irradiation leads to radiation enhanced diffusion.[18,19] In general, the diffusion coefficient is given by $D = \Gamma d^2/Z$, where Γ is the atomic jump frequency, d is the jump distance, and Z is the coordination number of the lattice. The jump frequency depends on the diffusion mechanism (vacancy, interstitial, divacancy, etc). For vacancy diffusion, $\Gamma \sim C_v r_v$ where C_v is the vacancy concentration and r_v is the vacancy jump frequency. The partial diffusion coefficient for vacancy diffusion may then be written as $D_v = r_v d^2/Z$. The general diffusion coefficient depends on the various partial diffusion coefficients in the following manner:[19]

$$D \sim D_v C_v + D_i C_i + D_{2v} C_{2v} + \ldots \qquad (3.1)$$

where D_x (x = v,i,2v,...) is the partial diffusion coefficient and C_x is the concentration of vacancies, interstitials and divacancies. Binding and migration energies of divacancies are not well known, so

one usually only considers vacancy and interstitial diffusion mechanisms. Diffusion via an interstitial-solute mechanism generally only occurs in materials under irradiation, since the thermal equilibrium concentration of interstitials is very small. It is immediately obvious from Eq. (3.1) that an increase in the point defect concentration during irradiation will lead to a direct increase in the diffusion coefficient.

The irradiation-enhanced diffusion coefficient takes on one of three limiting forms depending on the temperature:[18,19] (1) at high temperatures the thermal vacancy concentration dominates over the irradiation-produced point defects and the diffusion coefficient is unaltered by irradiation -- the activation energy is equal to the vacancy self-diffusion energy. (2) At intermediate temperatures, most point defects are lost to fixed sinks. This leads to a diffusion coefficient which is independent of temperature and varies linearly with the atomic displacement rate, P. (3) At low temperatures, point defect recombination becomes the dominant defect loss mechanism. The diffusion coefficient varies as $D \sim \sqrt{r_v P}$ with an activation energy of $E_v^m/2$ (E_v^m is the vacancy migration energy).

Solute segregation may be thought to occur as the result of one of three mechanisms:[20] vacancy (substitutional) site exchange with a neighboring atom; an interstitial atom jumping to a neighboring interstice; or interstitialcy motion, which forces a substitutional atom into an interstice with the interstitial atom taking the vacant substitutional site. Interstitial-type migration occurs in alloys

with significant atomic size differences, while interstitialcy-type migration occurs in alloys with similar solute/solvent sizes.[21] The two interstitial mechanisms are the dominant migration modes at low temperatures, where the vacancy point defects are essentially frozen into the lattice. Vacancy diffusion dominates at all temperatures where the irradiation-produced vacancies are mobile -- above Stage III (300 K for copper).

III.B.2 Theory

The possibility of radiation-induced segregation (RIS) was first postulated by Anthony[22] in 1972. Since that time, there has been an extensive volume of theoretical work done to model the mechanisms of solute segregation.[21,23-38]. RIS requires the occurrence of a defect flux into or out of a region and a preferential coupling of certain alloying elements to these fluxes.[20] Due to the complexity of the problem, no complete physical model exists. Three kinetic models have been developed which are discussed briefly below: (1) size factor, (2) mobile defect-solute complexes, (3) inverse Kirkendall effect.

The size factor model can be used to describe RIS of undersized solute atoms which tend to preferentially exist as interstitials in the lattice.[23] Self-interstitials in BCC and FCC metals are thought to exist in a "dumbbell" configuration, with two atoms sharing a single interstitial site.[24] The strain energy of this configuration can be lowered by incorporating an undersized solute atom into the dumbbell for one of the solvent atoms. This mixed

dumbbell can then migrate by interchanging solvent atoms. The dumbbell will tend to migrate toward point defect sinks during irradiation, which leads to a preferential segregation of the undersized solute atoms around sinks.

The most extensive theoretical modeling of RIS involves the migration to sinks of a defect-solute complex. Anthony[22] first proposed that a solute could be dragged toward a sink along with a point defect if there was a sufficient vacancy-solute binding energy. Johnson and Lam[25] developed a detailed phenomenological model applicable to dilute binary alloys which took into account the effects of both radiation-induced vacancies and interstitials. Large surface enrichments were predicted to occur, with the results most pronounced for temperatures $\lesssim 0.4\ T_M$ depending on the displacement rate.[25,26] They found that the interstitial mechanism was the dominant segregation process. Reduction of the displacement rate increased the amount of solute segregation and shifted the segregation temperature peak downwards. The model predicts solute redistribution for doses as low as 10^{-3} dpa.

Subsequent modifications of the Johnson-Lam model allowed spatially varying defect production rates[27,28] (applicable to ion irradiation) and precipitation at a sink surface.[27-29] These theoretical results predict solute enrichment at the surface and in the region beyond the damage peak, and solute depletion at the peak damage and subsurface regions (unless vacancy-induced inverse Kirkendall effect is the segregation mechanism; see later discussion

in this section). Significant solute segregation can occur at depths of up to twice the range of the incident ions. Okamoto et al.[28] found that the results depend strongly on the range of the incident ion (high-energy versus low-energy ions). They determined that mid-range segregation effects observed with one type of ion may not be observed with another type, which is in agreement with experimental results.[30]

The Johnson-Lam model is restricted to dilute binary alloy systems, and clustering and multiple sinks are not accounted for.[26] In concentrated alloys, a vacancy will be generally surrounded by several solute atoms, so the concept of binding between distinct vacancy-solute pairs becomes meaningless and a different model must be used. Manning,[31,32] Marwick,[33] and Wiedersich et al.[21] have modeled solute segregation in concentrated alloys using the so-called "inverse Kirkendall effect." In the Kirkendall effect, unequal diffusion coefficients in an alloy having a composition gradient causes a net vacancy flux which is proportional to the difference between the two diffusion coefficients. In the inverse Kirkendall effect, a vacancy flux due to irradiation causes segregation of solute atoms (assuming unequal solute and solvent diffusion coefficients) which leads to segregation of the alloy components. Faster diffusing species become depleted at sinks while slow diffusing components become enriched.

The segregation model developed by Marwick[33] for concentrated binary alloys includes only the vacancy contribution to the inverse

Kirkendall effect, and is therefore limited to alloys which do not have a strong solute coupling to interstitial fluxes. This model predicts that the faster diffusing species will diffuse up the vacancy gradient (away from the sink) at a rate proportional to the difference between the two diffusion coefficients. The slower moving species will diffuse down the vacancy gradient and produce an enriched region near the defect sink. The concentration gradient set up by this segregation can induce a Kirkendall flux of vacancies which will oppose the vacancy flux to the sink. This may lead to a reduction in the nucleation rate and growth of voids.

Wiedersich et al.[21,34] developed a simple concentrated solute segregation model which was similar to the treatment by Marwick. This model included the interstitial contribution to the inverse Kirkendall effect. This model is not applicable to dilute alloys in which segregation via vacancy-solute pairs is known to be important. Segregation by interstitial-solute complexes is accounted for by modifying the jump frequencies of A and B interstitials. This approach does not allow interstitialcy-type migration. The solute flux was found to be proportional to the following:[21,35]

$$J_A \propto - \left(\frac{D_A^i}{D_B^i} - \frac{D_A^v}{D_A^v}\right) \nabla C_{i,v} \qquad (3.2)$$

where the D's are the partial diffusion coefficients for solute/solvent migration via interstitial or vacancy-type mechanisms. It is

immediately obvious that during irradiation (since $\nabla C_{i,v} < 0$ near a sink) the element A will become enriched at sinks if $D_A^i/D_B^i > D_A^v/D_B^v$.

Lam[36,37] and Marwick et al.[38] have recently extended the concentrated binary alloy model of Wiedersich et al. to the case of ternary alloys. Comparison of the theory with experimental Fe-Ni-Cr data indicated that vacancy migration is the dominant segregation mechanism in this alloy.

An analysis by Okamoto et al.[28] takes into account mobile defect-solute complexes along with the inverse Kirkendall effect, and is therefore applicable to both dilute and concentrated binary alloys. They found that for a given set of physical parameters there exists a crossover temperature, T_o, below which segregation via mobile complexes will be the dominant redistribution process, and above which the inverse Kirkendall effect is the dominant mechanism. The crossover temperature is caused by the decrease in the defect-solute complex binding energy with increasing temperature and is different for vacancy and interstitial-type segregation.

III.C. Phase Stability During Irradiation

The effect of irradiation on phase stability in alloys has been intensively studied both theoretically and experimentally during the past ten years. Several recent review articles are available which summarize the present theory.[19,39-42] The following mechanisms have been found to occur and have an influence on the irradiation phase stability:[39] radiation-enhanced diffusion, solute segregation, radiation-enhanced precipitation, radiation-induced precipi-

tation (which leads to an apparent phase diagram modification), alteration of the normal sequence of metastable precipitate formation, and precipitate dissolution. Following the terminology put forth by Wilkes,[40] phase transformations may be classified as either radiation-enhanced or radiation-induced. Radiation-enhanced precipitation (REP) refers to transformations in which equilibrium is reached more quickly than in thermally aged specimens. Radiation-induced precipitation (RIP) is used for transformations which revert back to the original phase when the irradiation is removed. In addition to these two transformation schemes, Lee et al.[43] have suggested that radiation-modified precipitation may also occur. These phases develop with compositions that are significantly different from the normal equilibrium phase.

An additional radiation effect in solute segregation which up to now has not received much attention is dose rate. Martin[44] has recently reviewed dose rate effects on RIP and, following a suggestion by Adda et al.[45] has proposed that there is a critical dose rate threshold below which no appreciable phase restructuring occurs. In addition, Sprague et al.[46] have observed that varying the dose rate by a factor of 100 resulted in two entirely different precipitate size distributions in irradiated Ni-Al. The low dose rate samples displayed accelerated thermal coarsening effects, while the pre-irradiation precipitates in the high dose rate samples were replaced by a high density of smaller precipitates (radiation dissolution).

There is no general theory regarding the stability of alloy phases during irradiation. Instead, there are various independent models which can be separately applied to describe a specific situation. These models will now be briefly reviewed. Experimental results regarding solute segregation and phase development of copper alloys under irradiation will be briefly reviewed in Chapter IV.

III.C.1 Thermodynamic Considerations

Solute segregation can cause precipitation at point defect sinks when the solute segregation exceeds its solubility limit. However, as pointed out by Russell,[41] solute segregation cannot produce a phase which would not normally appear at that temperature without irradiation -- solute segregation can only shift the phase diagram laterally. Martin[47] determined that solute segregation can widen but not diminish a two-phase region. This means that solute segregation can cause precipitation in a single phase region but cannot dissolve precipitates to change a two-phase alloy into a single-phase. Therefore, some other mechanism must be responsible for the appearance of phases which are not thermally stable.

Metals under irradiation fall in the regime of irreversible thermodynamics, and may reach a steady state but not equilibrium.[19,41,42] However, by considering the kinetics of the various radiation-induced process, it may be possible to determine the final state of the system. Various authors have attempted to find a thermodynamic-based cause of RIP.[40,48-50] A "constrained phase equilibrium" approach by Yamauchi et al.[49] indicated that excess

vacancies caused a substantial shift in the phase boundaries, consistent with experimental observations. Phase boundaries for coherent precipitation were calculated to shift towards inside the matrix phase (i.e., RIP) when the matrix vacancy concentration was greater than the precipitate vacancy concentration.

An alternative proposal for the thermodynamic effect of point defects on phase stability was made by Martin.[50] For the case of strong defect-defect interaction, it was found that the solute-vacancy distribution could break-up into concentrated and depleted regions, similar to the phenomenon of spinodal decomposition. Phase instability in this model requires high displacement rates and low temperatures, and it appears unlikely that point defect concentrations present in reactors ($< 10^{-4}$) could induce spinodals unless the alloy was already close to a spinodal.[40,41]

Application of radiation-induced order-disorder processes to ordered phases can lead to significant changes in the free energy of the ordered phase. Wilkes and coworkers[51,52] have modeled this radiation mixing effect and obtained radiation-modified phase diagrams for ordered alloys.

III.C.2 Precipitate Nucleation and Growth

Two different basic kinetic approaches have been used to model the effects of excess vacancies and interstitials co-precipitating with solute atoms. Russell and coworkers[53,54] have investigated the nucleation of incoherent precipitates, where point defects are annihilated at the precipitate-matrix interface. Cauvin and

Martin[55,56] have studied coherent precipitate nucleation, where the defects are trapped at the interface as opposed to being absorbed. Experimentally, both heterogeneous and homogeneous radiation-induced precipitation (RIP) have been observed.[44]

Maydet and Russell[53] first studied the effects of point defects on the nucleation of incoherent precipitates. Excess vacancies can relieve the strain energy caused by an oversized precipitate. Using a nodal line analysis, they found that excess vacancies greatly stabilized the precipitate phase if the precipitate volumetric misfit (δ) was positive, and vice versa for $\delta < 0$. The matrix is usually more closely packed than the precipitate phase ($\delta > 0$). This leads to a huge increase in the precipitate nucleation rate. The effect on the precipitate nucleation rate of nucleus destruction by displacement cascades was found to be insignificant in a later analysis.[54]

The Russell model is incomplete in that it only applies to incoherent precipitates and does not consider the effects of solute segregation or disorder resolution. In addition, this theory predicts the homogeneous precipitation of oversized solute atoms during irradiation. This is in contrast to experimental observations which find radiation-induced precipitation in undersaturated solid solutions only for undersized solute atoms.[57] Cauvin and Martin[58] reanalyzed the above model and found that it also predicts radiation-induced incoherent precipitation for undersized solutes. A further extension of the Russell model to include cascade effects was recently presented by Abromeit.[59] Unfortunately, only qualitative trends

may be predicted by this theory due to uncertainty in the values of various parameters.

Cauvin and Martin[55,56] have recently developed a model similar to Russell's[53] which describes the effect of excess vacancies and interstitials on the nucleation of coherent particles. By assuming equilibrium defect trapping at the interface, various critical sizes of the precipitate nucleus can be obtained depending on whether interstitial or vacancy trapping occurs. Irradiation was found to always decrease the solid solubility, i.e. enhance precipitation. The solvus line was predicted to be elevated to temperatures well above the thermal value, with the magnitude of the shift increasing with higher displacement rates and greater atomic misfit of solute. Good agreement was obtained between the calculated solvus and experimental results for the Al-Zn system.

III.C.3 Recoil Resolution

Two basic types of analysis have been made on the effect of collision cascade atoms on the dissolution of a precipitate. The first method, pioneered by Nelson, Hudson and Mazey (NHM),[60] assumes that the precipitates are infinitely spaced and employs the solution to the diffusion field around a spherical particle in an infinite medium. The second method uses a cell model,[40] and the diffusion fields around the precipitates depend on the interparticle spacing.

The NHM model was the first analysis to address the problem of precipitate stability. They considered the solute atom balance between precipitate shrinkage due to recoil resolution and reprecipi-

tation due to irradiation-enhanced diffusion. In this model, a particle loses solute into the matrix from radiation recoil at a rate proportional to its surface area. Precipitate dissolution can occur via two mechanisms; solute "sputtering" from the precipitate surface due to individual high energy atoms from the displacement cascade, or dissolution/disordering of the precipitate due to the collision cascade intersecting the particle and destroying the ordered precipitate structure. According to NHM, the second mechanism would not occur in ordered incoherent precipitates since diffusion across the interface is unlikely. The solute removed from the precipitate is assumed to be uniformly redistributed in the matrix (i.e., no concentration gradients), and can diffuse back to the particle. By considering solute conservation, the precipitate growth rate is given by

$$\frac{dr}{dt} = -yP + \frac{3DC}{4\pi r c_p} - Dr^2 n \qquad (3.3)$$

where P is the displacement rate, D is the enhanced diffusion coefficient, C is the total solute concentration, c_p is the fraction of solute in the precipitate, n is the precipitate number density, and y is a semi-empirical constant which depends on whether atomic sputtering or disorder dissolution is the dominant mechanism for precipitate shrinkage. The solution of this equation indicates that large particles will shrink by resolution while smaller ones grow at their expense via solute diffusion (inverse Ostwald ripening). Brailsford[61] modified the NHM model to allow for a finite resolu-

tion distance while still assuming an infinite interparticle spacing. The NHM model does not consider the effect of increased precipitate solubility at small sizes. This effect was accounted for by Ardell and Schwartz,[62] and was observed to cause the equilibrium particle size to shift to larger values, with a lower limit being set on the particle size.

Chou and Ghoniem[63] have recently investigated the two mechanisms of precipitate dissolution proposed in the NHM model in order to quantify the importance of this parameter (the quantity y in Eq. 3.3). They found that the maximum precipitate size that may be completely destroyed by a 14-MeV neutron cascade is on the order of 1 nm. The dissolution efficiency was seen to vary strongly with neutron energy, with the maximum efficiency observed for neutrons of energy ~ 0.5 MeV.

Wilkes[40] noted that the NHM model allows only shrinkage of equilibrium precipitates during irradiation until a steady-state solute concentration is reached in the matrix. Therefore, no conclusions on the final size distribution can be obtained from this analysis. He proposed a cellular model in which equal-sized precipitates are uniformly distributed throughout the matrix. Solute concentration gradients were allowed to be established with the only restriction being that the gradient was zero at the cell boundary. The precipitate growth/dissolution rate was found to be independent of the diffusion coefficient, unlike the NHM model. Frost and Russell[64,65] expanded on the above model to include transient ef-

fects, i.e. the time required to reach steady-state behavior. Precipitate dissolution was accounted for by a size-dependent dissolution term. Simple analytical expressions were obtained for the matrix solute distribution. The precipitate growth/shrinkage rate was found to vary directly with the irradiation flux and with the cube of the recoil distance, and was essentially independent of the particle spacing. They found that steady-state solute concentrations in the matrix should be approached for irradiation times on the order of 100 seconds.[19] The particle size distribution was found to be determined by the relative importance of thermal coarsening versus recoil resolution, with smaller particle sizes prevalent when recoil resolution dominates. At sufficiently low temperatures all particles were predicted to dissolve if recoil resolution was of sufficient importance. Irradiation was generally found to transform the initial particle distribution into a uniform dispersion of subsized particles.[64,65] The estimated time for complete dispersion varied from 30 years for reactor conditions to 10 days for ion irradiation conditions.[42]

III.C.4 Particle Coarsening

Several different approaches have been used to include the effect of precipitate coarsening during irradiation along with radiation resolution. Bilsby[66] presented the first model which included coarsening effects along with the dissolution effects for the NHM model for precipitates with a distribution of sizes under irradiation. Unfortunately, the model was only valid for small disordering

rates. An independent formulation by Baron et al.[67] used coarsening concepts similar to that of Bilsby. Baron's theory[67,68] also considered the effects of irradiation disordering and enhanced diffusion and, unlike Bilsby, allowed the matrix solute concentration to increase above its thermal value. An expression for the precipitate size distribution was obtained. The maximum stable particle size at steady-state was determined to be inversely related to the disorder dissolution rate as defined by the NHM model. The average particle size was found to be proportional to the maximum particle size, similar to the case of thermal coarsening. The same steady state precipitate size and solute concentration values were found regardless of the starting conditions. Therefore, either precipitate coarsening or dissolution may occur prior to the development of the steady-state particle size distribution. A constant size distribution was predicted for doses on the order of 10 dpa. The model does not include the effects of precipitate renucleation or fragmentation by dislocations.[46]

Urban and Martin[69,70] have recently extended the Cauvin and Martin[55,56] model for point defect recombination-altered phase stability of coherent particles to include coarsening. Irradiation was predicted to greatly enhance the coarsening rate of small particles ($r < 10$ nm). For particles above 15 nm radii, irradiation affected coarsening only through the enhanced diffusion coefficient. However, their analysis neglected precipitate nucleation effects.[69]

References for Chapter III

1. Proc. Intern. Conf. on Radiation Effects in Breeder Structural Materials, M.L. Bleiberg and J.W. Bennet, Eds., Scottsdale, AZ (AIME, 1977).

2. G.R. Gessell and A.F. Rowcliffe, in Ref. 1, p. 431.

3. L.K. Mansur, Nucl. Tech. 40, (1978) 5.

4. L.K. Mansur, M.R. Hayns and E.H. Lee, in Phase Stability During Irradiation, J.R. Holland, L.K. Mansur and D.I. Potter, Eds., Pittsburgh, Oct. 1980, TMS-AIME, p. 359.

5. P.R. Okamoto, N.Q. Lam and H. Wiedersich, Proc. of the Workshop on Correlation of Neutron and Charged Particle Damage, J.O. Stiegler (Ed.), ORNL (June 1976), CONF-760673, p. 111.

6. A. Si-Ahmed, "Vacancy Cluster Nucleation During Irradiation with Preferred Point-Defect Absorption," Ph.D. Thesis, Nuclear Engineering Department, University of Wisconsin-Madison (1981).

7. W.G. Wolfer, F.A. Garner and L.E. Thomas, ASTM STP 782 (1982) 1023.

8. S.D. Harkness and C.Y. Li, in Radiation-Induced Voids in Metals, (1971) p. 798.

9. L.K. Mansur and M.H. Yoo, J. Nucl. Mater. 74 (1978) 228-241.

10. A.D. Brailsford, J. Nucl. Mater. 78 (1978) 354-361.

11. N.Q. Lam, P.R. Okamoto and H. Wiedersich, J. Nucl. Mater. 74 (1978) 101-113.

12. A. Si-Ahmed and W.G. Wolfer, ASTM STP 782 (1982) 1008.

13. F.A. Garner and W.G. Wolfer, J. Nucl. Mater. 102 (1981) 143-150.

14. W.G. Wolfer and L.K. Mansur, J. Nucl. Mater. 91 (1980) 265.

15. A.D. Brailsford, J. Nucl. Mater. 56 (1975) 7.

16. V.K. Sethi and P.R. Okamoto, in Phase Stability During Irradiation, J.R. Holland, L.K. Mansur and D.I. Potter (Eds.), TMS-AIME (Oct. 1980) 109.

17. P.R. Okamoto and L.E. Rehn, J. Nucl. Mater. 83 (1979) 2-23.

18. G.J. Dienes and A.C. Damask, J. Appl. Phys. 29 No. 12 (1958) 1713.

19. K.C. Russell, in Progress in Materials Science, B. Chalmers, J. Christian and T.B. Massaleski, Eds., Pergamon Press, Oxford (1984).

20. H. Wiedersich, in Phase Stability During Irradiation, (1981), p. 23.

21. H. Wiedersich, P.R. Okamoto and N.Q. Lam, J. Nucl. Mater. 83 (1979) 98-108.

22. T.R. Anthony, in Radiation Induced Voids in Metals, (1971) 630.

23. P.R. Okamoto and H. Wiedersich, J. Nucl. Mater. 53 (1974) 336.

24. H.G. Haubold and D. Martinson, J. Nucl. Mater. 69/70 (1978) 644-649.

25. R.A. Johnson and N.Q. Lam, Phys. Rev. B 13 No. 10 (1976) 4364.

26. R.A. Johnson and N.Q. Lam, Phys. Rev. B 15 No. 4 (1977) 1794.

27. N.Q. Lam, P.R. Okamoto and R.A. Johnson, J. Nucl. Mater. 78 (1978) 408-418.

28. P.R. Okamoto, L.E. Rehn and R.S. Auerback, J. Nucl. Mater. 108/109 (1982) 319-330.

29. N.Q. Lam, P.R. Okamoto, H. Wiedersich and A. Taylor, Met. Trans. 9A (1978) 1707-1714.

30. K. Janghorban and A.J. Ardell, Phase Stability During Irradiation, (1981) p. 547.

31. J.R. Manning, Bull. Am. Phys. Soc. 23 (1978) 287.

32. J.R. Manning, Phase Stability During Irradiation, (1981) p. 3.

33. A.D. Marwick, J. Phys. F 8 (1978) 1849.

34. N.Q. Lam, H. Wiedersich and P.R. Okamoto, in Irradiation Behavior of Metallic Materials for Fast Reactor Core Components, Corsica, France, (1979) 45, 51.

35. W. Wagner, V. Naundorf, L.E. Rehn and H. Wiedersich, ASTM STP 782, (1982) 895.

36. N.Q. Lam, A. Kumar and H. Wiedersich, ASTM STP 782, (1982) 985.

37. N.Q. Lam, J. Nucl. Mater. 117 (1983) 106.

38. A.D. Marwick, R.C. Pillar and M.E. Horton, "Radiation Induced Segregation in Fe-Ni-Cr Alloys," Corsica Conf., (1979).

39. A. Wolfenden, J.R. Holland, R.G. Lott and J.A. Spitznagel, in Phase Stability During Irradiation, (1981) 383.

40. P. Wilkes, J. Nucl. Mater. 83 (1979) 166-175.

41. K.C. Russell, J. Nucl. Mater. 83 (1979) 176-185.

42. H.J. Frost and K.C. Russell, "Phase Stability Under Irradiation," in Phase Transformations and Solute Redistribution in Alloys During Irradiation, Res Mechanica Monograph, F.V. Nolfi, Jr. (Ed., Applied Science Publ., England (1983).

43. E.H. Lee, P.J. Maziasz and A.F. Rowcliffe, in Phase Stability During Irradiation, (1981) 191.

44. G. Martin, R. Cauvin, J.L. Bocquet and A. Barbu, in Phase Stability During Irradiation, (1981) 43.

45. Y. Adda, M. Beyeler and G. Brebec, Thin Solid Films 25 (1975) 107-156.

46. J.A. Sprague, J.E. Westmoreland, F.A. Smidt, Jr., and P.R. Malmberg, in Effects of Radiation on Materials: 10th Conf., ASTM STP 725, D. Kramer, H.R. Brager, J.S. Perrin (Eds.), (1981) 528.

47. G. Martin, Phil. Mag. A38 (1978) 131-140.

48. J.L. Bocquet and G. Martin, J. Nucl. Mater. 83 (1979) 186-199.

49. H. Yamauchi and D. de Fontaine, in Phase Stability During Irradiation, (1981) 73.

50. G. Martin, Phil. Mag. 32 (1975) 615.

51. K.Y. Liou and P. Wilkes, J. Nucl. Mater. 87 (1979) 317-330.

52. R.H. Zee and P. Wilkes, J. Nucl. Mater. 97 (1981) 179.

53. S.I. Maydet and K.C. Russell, J. Nucl. Mater. 64 (1977) 101-114.

54. M.R. Mruzik and K.C. Russell, J. Nucl. Mater. 78 (1978) 343-353.

CHAPTER IV. REVIEW OF PREVIOUS EXPERIMENTS

IV.A. Thermal Stability of Cu-Zr and Cu-Cr-Zr Alloys

There have been several investigations[1-18] of the microstructures and physical properties of copper alloys that are similar to the two commercial alloys studied in this thesis work, AMZIRC (Cu-0.15% Zr) and AMAX-MZC (Cu-0.8% Cr-0.15% Zr-0.04% Mg). The Cu-Zr and Cu-Cr alloys are recognized as high-strength, high-electrical conductivity materials, when operated at temperatures below 400°C. Extended use at temperatures above 400°C causes these alloys to lose their high strength due to recrystallization and/or overaging effects.

It is generally observed that precipitation hardening is by itself not an important process in Cu-Zr alloys,[1-6] although there are some claims to the contrary.[7] The high strength of Cu-Zr is attained by cold-working prior to aging. The primary effect of aging is to increase the electrical conductivity of the alloy.[8] In contrast to Cu-Zr, Cu-Cr alloys can develop substantial increases in strength following suitable aging treatments. However, once again the best combination of high strength and conductivity is achieved by cold-working prior to aging. There is no evidence of precipitate overaging effects (as determined from hardness measurements) for Cu-Cr and Cu-Cr-Zr alloys aged up to 200 hours at 400°C.[9,12] However, overaging effects are observed for aging temperatures above 450°C.[9,12,16]

Annealing studies performed on cold-worked and aged Cu-Cr and Cu-Zr type alloys[1,2,6-16] have found that their strength is maintained up to 400-600°C. Recrystallization occurs at higher temperatures and causes a large decrease in the strength of the alloys. The exact value of the recrystallization temperature appears to depend on the prior thermomechanical history of the alloys. The alloy recrystallization temperature of ~ 500°C is significantly higher than that for pure copper (~ 200°C).[7,8,13] The high recrystallization temperature in Cu-Zr has been attributed to the precipitation of Zr-rich particles at grain boundaries.[1,2,9]

The room temperature electrical conductivity of aged Cu-Zr and Cu-Cr type alloys increases steadily with annealing temperature up to about 550°C.[1,6,7,10,12,13,16-18] The increase in conductivity upon annealing is attributed to coarsening of the precipitates. There is no sharp "knee" in the conductivity annealing curve, in contrast to the rapid change observed in the microhardness annealing curve when recrystallization occurs. Cold-working prior to aging has a minimal effect on the electrical conductivity.[8,16] Annealing at temperatures above 550°C causes the conductivity to decrease from its maximum value. This is probably due to solute reentering solution from the precipitates.[1,7,10]

Aging of dilute (< 1% Zr) Cu-Zr alloys from the solution quenched state results in heterogeneous precipitation of Cu_5Zr precipitates along grain boundaries.[1,2,4,9,14,15] Cold-working prior to aging gives rise to precipitation at dislocations. The precipi-

tates then act to pin the dislocations in place, resulting in a high strength alloy. The precipitation process in Cu-Cr and Cu-Cr-Zr alloys is somewhat more complex. Guinier-Preston (G-P) zones on {111} planes are initially observed upon aging. Further aging results in the formation of coherent Cr precipitates. The morphology of the G.P. zones has been reported to be either disk-shaped[16] or spherical.[9] Nai-Yong[9] claimed that the coherent precipitate in Cu-Cr-Zr and Cu-Cr-Zr-Mg was a Heusler type, given by Cu_2Cr (Zr/Mg). Aging above 550°C was said to cause dissolution of the Heusler precipitate and cause formation of Cr and Cu_5Zr precipitates. There does not appear to be justification at this time for such a complex precipitation sequence (see phase diagram discussion in Chapter VI).

Cu-Zr-Cr alloys have superior strength and comparable electrical conductivity when compared to Cu-Zr and Cu-Cr alloys.[1,2,7,12,13] Addition of Zr to Cu-Cr results in the formation of grain boundary precipitates, thereby leading to an alloy with improved high temperature strength. Trace additions of Mg and Zr to Cu-Cr were found to reduce the width of the grain boundary precipitate free zone.[9] This improves the strength of the grain boundaries. It has been observed that addition of small amounts of deoxidizers such as Mg or Zr greatly suppresses grain boundary porosity and improves the ductility of commercial copper and its alloys.[9,19] Embrittlement of copper is believed to be caused by segregation of oxygen to grain boundaries.[20]

The role of the alloying elements contained in AMZIRC (Cu-Zr) and AMAX-MZC (Cu-Cr-Zr-Mg) may be summarized as follows: Zr improves grain boundary strength and raises the recrystallization temperature. It also acts as a deoxidizer, thereby improving ductility. Cr increases the matrix strength by precipitating out as a homogeneous coherent precipitate (precipitation hardening). Mg improves ductility by acting as a deoxidizer. It may also slow down the kinetics of Cu-Zr precipitation.[13]

IV.B. Radiation Effects in Copper and Copper Alloys

A thorough review of previous radiation damage studies on copper and copper alloys has recently been published by this author.[21] A brief updated summary of this review is given below.

IV.B.1 Solute Segregation and Phase Stability Experiments

The effects of irradiation on the phase stability and solute segregation characteristics of at least sixteen different binary copper alloys has been examined.[21] Effects such as short range ordering, radiation-induced segregation (RIS), and radiation-induced precipitation (RIP) have commonly been observed. Unfortunately, there are no known studies of any significance concerning the alloys investigated in this thesis, namely Cu-Cr and Cu-Zr. The most extensive studies to date on copper alloys have been conducted on Cu-Be, Cu-Co and Cu-Fe. Evidence of precipitate dissolution following neutron or ion irradiation has been obtained for precipitate sizes smaller than 2.5 nm in all three of these alloys.[22-28] There is little effect of irradiation on precipitates larger than 5 nm. Ir-

radiation has generally been found to accelerate the precipitation kinetics, and in some cases RIP has been observed[22,23,29,30] (Cu-Be, Cu-Ni, Cu-Si). Evidence of solute segregation to grain boundaries, dislocations and void surfaces has been obtained for irradiated Cu-Ag,[31] Cu-Be,[22] Cu-Ni,[31-33] and Cu-Ge and Cu-Si.[34]

IV.B.2 Void and Dislocation Loop Experiments

Copper has been found to be susceptible to void formation when irradiated to doses on the order of a fraction of a dpa at temperatures between 200 and 550°C (0.35-0.61 T_m).[21] Figure 4.1 shows the irradiation doses and temperatures that have been investigated to date. It is obvious from Fig. 4.1 that there is a lack of high-fluence neutron irradiation data on copper and copper alloys.

IV.B.2.1 Pure Copper

There have been many[21] observations of void formation in pure copper following neutron,[35-47,85] electron[49-61] or ion[37,62-68] irradiation. Most of the neutron studies were limited to damage levels of less than 1 dpa. Figure 4.2[48] shows the swelling versus temperature response for pure copper as determined from these investigations. The average void diameter at damage levels of $\lesssim$ 0.5 dpa increases from ~ 5 nm to greater than 150 nm as the neutron irradiation temperature is increased from 220 to 500°C.[36,37] The void density decreases rapidly from a maximum of 4 x $10^{20}/m^3$ over this same temperature range, showing that high temperatures favor growth and inhibit nucleation. The void density increases linearly with fluence up to doses of 3 x 10^{23} n/m^2 (~ 0.02 dpa) for neutron

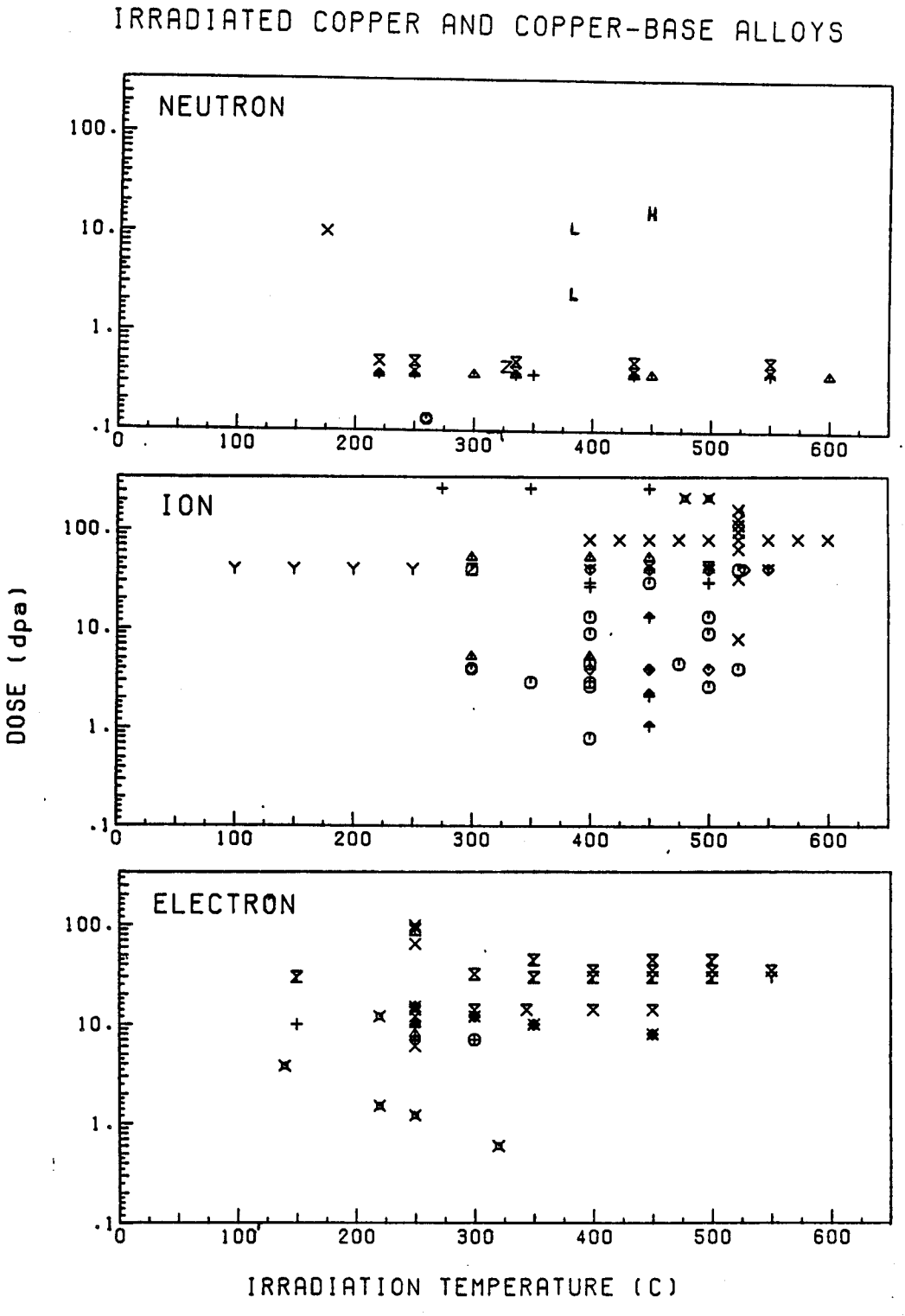

Fig. 4.1. Summary of previous radiation studies of copper alloys (see text).

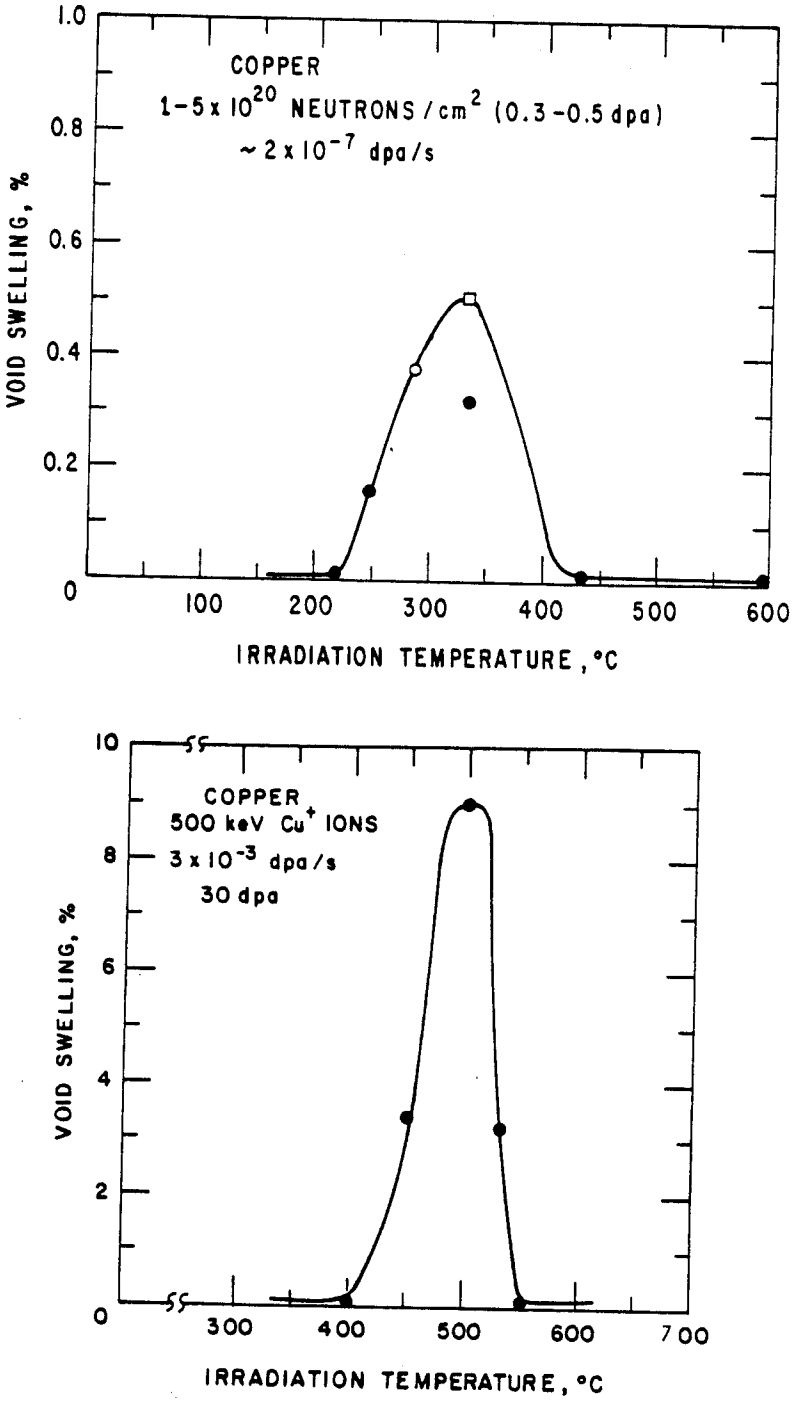

Fig. 4.2. Temperature dependence of void swelling in irradiated copper (from Ref. 48).

irradiation at 285°C,[40] and then increases at a rate less than linear for fluences up to at least 1.2 x 10^{24} n/m^2 (0.1 dpa). The threshold fluence for void swelling has been found[44] to be less than 10^{21} n/m^2 (10^{-4} dpa). Brager et al.[47] have recently reported that a high-fluence (16 dpa) neutron irradiation of copper at 450°C resulted in a swelling level of 6.5%. Livak and Clinard[85] have recently measured swelling levels of 7% for copper irradiated to 10 dpa with neutrons (EBR-II) at 385°C. These measurements represent the highest known swelling amounts for neutron-irradiated copper.

Swelling levels as high as 17% have been observed in HVEM-irradiated copper.[50,51] There is apparently no appreciable incubation dose prior to steady state swelling for high purity copper[49] (however, also see Ref. 55). The steady state swelling rate for electron irradiation ranges from 0.5-0.8%/dpa.[49,51,55] The amount of void swelling depends critically on the dislocation density,[50,51,53,54,59] and it appears that maximum swelling occurs for a cold-work level of ~ 50%. A minimum dislocation density is necessary before void formation can occur, in agreement with theory.[69] There have been several studies of the effect of gas on void formation in electron irradiated copper. Preinjected helium enhances void formation for concentration levels up to 50 appm.[55] Too much helium (2000 appm) apparently overstimulates void nucleation and suppresses observable void swelling.[50] Glowinski[54] found that ordinary high-purity copper swelled easily, while copper that had been degassed in a high vacuum prior to irradiation showed reduced swelling

and a shift in the swelling peak to lower temperatures by about 150°C (from 500 to 350°C). No voids were observed in degassed copper specimens irradiated at temperatures above 440°C. A model has been developed in this thesis to explain this observation in terms of the effect of oxygen on void stability (see Section VIII.D).

Most of the ion irradiation studies on copper have been conducted at relatively low ion energies ($\lesssim$ 500 keV), and are therefore susceptible to surface effects. Nevertheless, some interesting observations have been made. Figure 4.2 shows the temperature-dependent swelling profile for ion-irradiated copper.[48] An increase in the ion damage rate from 1 x 10^{-4} dpa/s to 1 x 10^{-3} dpa/s caused the swelling curve to shift upward in temperature by 50°C.[65] The peak swelling temperature shift between neutron (2 x 10^{-7} dpa/s)[41] and ion (1 x 10^{-3} dpa/s) irradiation was 165°C. The high dose rate caused a lower density of larger voids at the swelling peak compared to the low dose rate. Measured swelling rates for ion irradiation are generally much lower than those observed for neutron and electron irradiations.[21] This is probably due to surface effects. Swelling rates ranged from 0.05%/dpa for 200 keV Cu ions (peak damage depth ~ 50 nm)[63] to 0.3%/dpa for 500 keV Cu ions (peak damage depth ~ 150 nm).[65] A minimum dislocation density is apparently necessary for void formation, and there is a direct correlation between void number density and dislocation density.[66] Void formation tended to occur near interstitial loops or dislocation lines.

Glowinski et al.[65-67] conducted an extensive investigation of the effect of gas on void formation in ion-irradiated copper. Outgassing of copper specimens prior to irradiation eliminated void swelling at what previously had been the peak swelling temperature. Partial outgassing resulted in a bimodal void size distribution, with reduced swelling. Preimplantation of outgassed specimens with helium or oxygen resulted in void formation during irradiation. However, preimplantation of hydrogen suppressed observable void formation even in specimens that had not been outgassed. Helium was observed to be somewhat more efficient than oxygen in nucleating voids and interstitial loops for implanted concentrations of less than 30 appm. These gas effect observations will be discussed in more detail in Section VIII.D.

There have been many observations of dislocation loops in irradiated copper (see Refs. 21, 70-72, for reviews). Both perfect[55,73] and faulted[55,74,75] loops have been observed, with the majority being of the faulted type.[72] There is some evidence that faulted loops are stable at lower temperatures, while only perfect loops and stacking fault tetrahedra (SFT) are stable at higher temperatures.[76] Small loops tend to be vacancy-type and large loops are predominantly interstitial.[70-72] Several recent studies have found that SFT are the most common configuration for vacancy clusters in irradiated copper.[77-81] There is also evidence that faulted loops may dissociate to form SFT.[72]

IV.B.2.2 Copper Alloys

With few exceptions (Cu-Ag), the addition of alloying elements to copper results in a reduction of void swelling. No void formation has been observed in irradiated (up to 100 dpa) Cu-Be containing greater than 0.1 at.% Be.[22,23,47,50,63,82] Cu-Ag and Cu-Cd generally show enhanced swelling compared to pure copper,[30,47,50,55] although swelling suppression was observed in one experiment.[63] Reduced swelling compared to pure copper has been reported for the following solutes: Au, Fe, Ge, In, Mg, Pt, Sb and Si.[30,37,41,44,49,63,68] Various reasons have been proposed to explain the reduction in swelling, including: (1) the lower stacking fault energy of the alloy makes other vacancy cluster morphologies favorable compared to void formation,[37,41,44] and (2) fast diffusing solutes may occupy interstitial positions, thereby increasing the probability of vacancy-interstitial recombination.[68] However, these proposals do not appear to be generally applicable. Cu-Ni has been found to be very resistant to void swelling.[41,55,56,62,63] The swelling resistance is due to a suppression of void growth.[55,56] It has been proposed that submicroscopic radiation-induced Ni atom clusters are formed which act as interstitial traps, thereby increasing point defect recombination.[62,83] Cu-Co[22] and Cu-Al_2O_3[47,85] are also resistant to void swelling. It appears likely that point defect trapping at the precipitate/matrix interface may play a role in their swelling suppression. Preimplantation of

carbon into pure copper also results in a reduction of void swelling.[67]

There have been three very recent irradiation studies involving the alloys investigated in this thesis, AMZIRC and AMAX-MZC. Brager et al.[47] found that MZC exhibited 1% swelling following neutron irradiation to 16 dpa at 450°C. This swelling level was substantially less than that observed for pure copper, but was higher than the swelling observed for Cu-Al_2O_3 or Cu-Be. Spitznagel and Davis[84] investigated the microstructure of cold-worked plus aged AMZIRC following dual ion beam (Si + He) irradiation to 5 dpa at 425 and 500°C. Evidence of radiation-enhanced recovery and recrystallization was observed. Void formation was heterogeneous and often concentrated at the boundaries of the recovered regions. The localized swelling rate was ~ 1 to 5%/dpa, with the overall swelling rate much lower. There also appeared to be an orientation dependence of the void swelling. Livak and Clinard[85] observed that MZC did not swell at all, while AMZIRC exhibited ~ 3.5% swelling following a 10 dpa neutron irradiation at 385°C. Pure copper swelled 7% for the same irradiation conditions. Both alloys lost a considerable portion of their strength following irradiation. The decrease in strength was more severe for AMZIRC ($\Delta\sigma_y \simeq 200$ MPa), and its final yield strength was similar to that of pure copper ($\sigma_y \simeq 70$ MPa). It appears that these alloys may have recrystallized during irradiation (see Section VIII.B).

Copper alloy loop studies have centered on the effect of stacking fault energy on loop formation. Copper alloyed with Al, Be, Ge,

Si, Ni or Zn (low stacking fault energy alloys compared to copper) had a greater visible cluster concentration and an increased concentration of SFT as compared to pure copper.[79,80,86] No SFT were observed in irradiated pure copper in Ref. 79.

References for Chapter IV

1. T. Nagai et al., Trans. Jap. Inst. Metals 14 (1973) 462-469.
2. H. Suzuki, M. Kanno and I. Kawakatsu, J. Jap. Inst. Metals (NKG) 33 (1969) 628-633.
3. M.J. Saarivirta, Metal Ind. 103 (1963) 685-688.
4. B.I. Bozic, D.V. Mihailovic and M.L. Kostic, Glas Hem Drus, Beograd 35, No. 7-8 (1970) 405-414.
5. Source Book on Copper and Copper Alloys, ASM (1979), Metals Park, OH, pp. 156, 163, 166.
6. M. Sugiyama, H. Suzuki, H. Kitano and T. Sato, J. Jap. Inst. Metals. 30 (No. 1) (1966) 32-37.
7. T. Maruta, J. Japan Copper and Brass Res. Assn. 2 (No. 1) (1963) 89-96.
8. M. Reverchon in Le Traitement Themique du Cuivre et de ses Alliages (Heat Treatment of Copper and its Alloys) Chapt. 3, Trait. Therm., March 1979 (133) pp. 61-66.
9. T. Nai-Yong, "High Temperature Deformation and Fracture of Cu-Cr Type Alloys," Ph.D. Thesis, University of Waterloo (1983).
10. Z. Henmi and T. Nagai, Trans. Jap. Inst. Metals 10 (1969) 305-313.
11. C. Logan et al., J. Nucl. Mater. 103/104 (1981) 1551-6.
12. H. Suzuki, I. Kawakatsu and H. Kitano, J. Jap. Inst. Metals. 31 (1967) 342-6.
13. W.R. Opie, Y.T. Hsu and R.J. Smith, in Copper and Its Alloys, Inst. of Metals Monograph No. 34 (1970), London, pp. 264-7.

14. E.N.C. Dalder, W. Ludemann and B. Schumacher, "Thermal Stability of Four High-Strength, High-Conductivity Copper Alloys," in Copper and Copper Alloys for Fusion Reactor Applications, DOE-OFE Workshop Proc., F.W. Wiffen and R.E. Gold (Eds.), CONF-830466, June 1984, p. 252.

15. C.E. Sohl and R.J. DeAngelis, "Avoidance of Softening in Dilute Alloys of Copper Containing Hexagonal Solute Additions," INCRA Project Report No. 127 (1970).

16. D.V. Assadi, "Microstructure and Properties of Dilute Copper Age Hardening Alloys," Ph.D. Thesis, New York University, (1974); INCRA Contractor Report No. 207.

17. M. Kanno and H. Suzuki, J. Japan Copper and Brass Res. Assn. 11 (No. 1) (1972) 88-94.

18. P.W. Taubenblat, W.R. Opie and Y.T. Hsu, Met. Eng. Quart. 12 (1972) 41-45.

19. W.R. Opie et al., J. Inst. Metals 98 (1970) 204.

20. T.G. Nieh and D. Nix, Met. Trans. 12A (1981) 893-901.

21. S.J. Zinkle and R.W. Knoll, "A Literature Review of Radiation Damage Data for Copper and Copper Alloys," UWFDM-578 (June 1984).

22. R.W. Knoll, "Effects of Heavy Ion Irradiation on the Phase Stability of Several Copper-Base Alloys," Ph.D. Thesis, Nuclear Engineering Dept., University of Wisconsin-Madison (1981).

23. M.-P. Macht et al., J. Nucl. Mater. 122/123 (1984) 698-702.

24. G.R. Piercy, J. Phys. Chem. Solids 23 (1962) 463-477.

25. A. Blaise, J. de Physique 26 (1965) 361-5.

26. A. Boltax, Nucl. Appl. 1 (1965) 337-347.

27. T.H. Gould and D.H. Vincent, J. de Physique 35, Suppl. C6, (No. 12) (1974) 315-9.

28. J.M. Denney, Phys. Rev. 94 (No. 5) (1954) 1417-8.

29. W. Wagner et al., J. Phys. F 12 (1982) 405-424.

30. T. Takeyama, in New Trends in Electron Microscopy in Atom Resolution, Materials Science and Biology (Conf. Proc.), H. Hashimoto et al. (Eds.), Dalien, China, July 1981, (Science Press, Beijing, China, 1982) pp. 78-86.

31. H. Takahashi et al., J. Nucl. Mater. 103/104 (1981) 1415-1420.

32. T. Takeyama, Bull. Jap. Inst. Metals 22 (No. 2) (1983) 135-7.

33. L.E. Rehn et al., Scripta Met. 15 (1981) 683-7.

34. H. Saka, Phil. Mag. A48 (1983) 239-250.

35. J.L. Brimhall and B. Mastell, J. Nucl. Mater. 29 (1969) 123-5.

36. V. Levy et al., in Voids Formed by Irradiation of Reactor Materials, S.F. Pugh et al. (Eds.), BNES (1971) pp. 64-68.

37. Y. Adda, in Radiation-Induced Voids in Metals, J.W. Corbett and L.C. Ianniello (Eds.), AEC Symp. Series No. 26, CONF-710601 (1972), pp. 31-81.

38. A. Wolfenden, Rad. Effects 15 (1972) 255-8.

39. J.L. Brimhall et al., in Radiation-Induced Voids in Metals, J.W. Corbett and L.C. Ianniello (Eds.), AEC Symp. Series No. 26, CONF-710601 (1972), p. 338.

40. J.L. Brimhall and H.E. Kissinger, Rad. Effects 15 (1972) 259-272.

41. M. Labbe and J.P. Pourrier, J. Nucl. Mater. 46 (1973) 86-98.

42. M. Labbe et al., J. Nucl. Mater. 49 (1973/74) 232-4.

43. R.B. Adamson et al., J. Nucl. Mater. 92 (1980) 149-154.

44. C.A. English, J. Nucl. Mater. 108/109 (1982) 104-123.

45. M. Eldrup et al., Rad. Effects 54 (1981) 65-80.

46. N. Yoshida et al., J. Nucl. Mater. 122/123 (1984) 664-8.

47. H.R. Brager, H.L. Heinisch and F.A. Garner, "Effects of Neutron Irradiation at 450°C and 16 dpa on the Properties of Various Commercial Copper Alloys," 1st Intern. Conf. on Fusion Reactor Materials, Tokyo, Dec. 1984 (to be published in J. Nucl. Mater.).

48. W.M. Stacey, Jr., et al., Critical Issues, Vol. I, USA Fed INTOR/82-1, Appendix VII.A Materials Data Base Assessment, Section A.2.2, Properties of Copper Alloys, (1982), pp. 395-415.

49. T. Takeyama et al., J. Nucl. Mater. 89 (1980) 253-262.

50. M.J. Makin, in Voids Formed by Irradiation of Reactor Materials, S.F. Pugh et al. (Eds.), BNES (1971) 269-274.

51. T. Leffers et al., J. Nucl. Mater. 118 (1983) 60-67.

52. S.B. Fisher, Rad. Effects 7 (1971) 173-7.

53. E. Kenik and T.E. Mitchell, Rad. Effects 24 (1975) 155-160.

54. L.D. Glowinski, J. Nucl. Mater. 61 (1976) 8-21.

55. P. Barlow, "Radiation Damage in Pure FCC Metals and Alloys in HVEM," Ph.D. Thesis, University of Sussex, England (1977).

56. T. Leffers, B.N. Singh and P. Barlow, Riso-M-1937, Research Establishment Riso, Roskilde, Denmark (May 1977); also see Singh et al., 5th Intern. Conf. on HVEM, Kyoto, Japan (Aug. 1977), pp. 581-4.

57. K. Hinode et al., Rad. Effects 32 (1977) 73-77.

58. S.B. Fisher et al., Phil Mag. A40 (1979) 239-255.

59. T. Leffers et al., Irradiation Behavior of Metallic Materials for Fast Breeder Core Components, (Intern. Conf.) Corse, France (1979), pp. 235-240.

60. S.N. Buckley et al., Rad. Effects 59 (1982) 203-9.

61. B.N. Singh and T. Leffers, Proc. Sixth Intern. Conf. on HVEM, Antwerp, 1980, Electron Microscopy 4 (1980) 262-5.

62. D.J. Mazey and F. Menzinger, J. Nucl. Mater. 48 (1973) 15-20.

63. K-H. Leister, "Influence of Solutes on Heavy Ion Induced Void Swelling in Binary Copper Alloys," Ph.D. Thesis, Kernforschungszentrum Karlsruhe, (May 1983), KfK Report 3499.

64. J.M. Lanore et al., Fund. Aspects of Radiation Damage in Metals, Vol. 2, M.T. Robinson and F.W. Young (Eds.), Gatlinburg, TN (1975), CONF-751006-P2, pp. 1169-1179.

65. L.D. Glowinski et al., J. Nucl. Mater. 47 (1973) 295-310.

66. L.D. Glowinski and C. Fiche, J. Nucl. Mater. 61 (1976) 22-28.

67. L.D. Glowinski and C. Fiche, J. Nucl. Mater. 61 (1976) 29-40.

68. H. Venker et al., in Radiation Effects in Breeder Reactor Structural Materials, (Intern. Conf.), M.L. Bleiberg and J.W. Bennett (Eds.), Scottsdale, AZ (June 1977), AIME, pp. 415-420.

69. W.G. Wolfer, J. Nucl. Mater. 122/123 (1984) 367-378.

70. M. RÜhle, in Proc. Symp. on Radiation Damage in Reactor Materials, Vol. 1, (Vienna, 1969), pp. 113-158.

71. M. Wilkens, in Vacancies and Interstitials in Metals, A. Seeger et al. (Eds.), (North-Holland, 1970), p. 485.

72. B.L. Eyre, J. Phys. F 3 (1973) 422.

73. J. Narayan and S.M. Ohr, J. Nucl. Mater. 85/86 (1979) 515-9.

74. M.M. Wilson, Phil. Mag. 24 (1971) 1023-77.

75. A.Y. Stathopoulos et al., Phil. Mag. A44 (1981) 285-308.

76. C.A. English et al., Phil. Mag. 34 (1976) 603-614.

77. M. Ipohorski and M.S. Spring, Phil. Mag. 20 (1969) 937-941.

78. H. Fujita et al., Jap. J. Appl. Phys. 21 (1981) L235-6.

79. A.Y. Stathopoulos et al., Phil. Mag. A44 (1981) 309-322.

80. C.A. English, J. Nucl. Mater. 108/109 (1982) 104-123.

81. N. Yoshida et al., J. Nucl. Mater. 122/123 (1984) 664-8.

82. C. Kinoshita and T.E. Mitchell, Electron Microscopy 4 (1980) 263-9.

83. P. Barlow, T. Leffers and B.N. Singh, Riso-M-2129, Research Establishment Riso, Roskilde, Denmark (August 1978).

84. J.A. Spitznagel and J.W. Davis, "Response of Selected High Strength, High Conductivity Copper Alloys to Simulated Fusion Irradiation and Temperature Conditions," ADIP Progress Report, Fall 1984.

85. R.J. Livak and F.W. Clinard, Jr., "High-Dose Neutron Radiation Damage Study of Copper Alloys for the CRFPR First Wall," presented at the EPRI Review Meeting of the Westinghouse Ion Irradiation Program on Copper Alloys, Feb. 20, 1985, Palo Alto, CA.

86. L.M. Howe and M. Rainville, Rad. Effects 16 (1972) 203-9.

CHAPTER V. SUMMARY OF RELATED WORK ON COPPER ALLOYS

Prior to the selection of a thesis topic, this author was involved in a variety of research projects involving copper and copper alloys. The results of these studies were not directly applicable to the main thesis research and are therefore separately summarized here.

V.A. Helium Bubble Formation in Cu, Ni and Cu-Ni Alloys

Cu-Ni alloys have been found to be resistant to void swelling (see review in Chapter IV). However, the cause of the void swelling suppression has not been determined with certainty. A study of helium bubble formation in Cu-Ni alloys was initiated in order to investigate this phenomenon.[1] The purpose of the investigation was to determine if helium bubble formation was possible in the void-resistant Cu-Ni alloys. A significant difference in the alloy bubble parameters as compared to pure Cu and Ni would indicate that there is some fundamental difference in the way that cavities are formed in Cu-Ni alloys.

Cu, Ni and Cu-Ni alloys (20%, 50%, 80% Ni) were irradiated with 200-400 keV ^{3}He ions at a constant homologous temperature of 0.65 T_m to obtain a helium concentration of 200 appm. The specimens were annealed at 0.65 T_m for one hour following the irradiation, and were then thinned and examined in an electron microscope. Helium bubbles were observed in all samples in the near vicinity of dislocations and grain boundaries. The helium bubble concentration and size was simi-

lar for copper and the alloys ($10^{20}/m^3$, d = 20 nm). The helium bubbles in pure nickel were significantly smaller and of higher density compared to the rest of the specimens ($10^{21}/m^3$, d = 7 nm). Calculations indicated that most of the implanted helium could be accounted for in visible bubbles. Nothing was found concerning helium bubble growth in the Cu-Ni system that would explain the suppression of void swelling in the alloys. The cause of the anomalous behavior at helium bubbles in pure nickel compared to the other specimens was not addressed. However, the nickel results are in good agreement with theoretical predictions.[2]

V.B. 14-MeV Neutron Irradiation of Copper Alloys

Electrical resistivity and Vickers microhardness measurements were made on copper and copper alloyed with 5 at.% of either aluminum, manganese or nickel following a room temperature 14-MeV neutron irradiation[3] up to a maximum fluence of 3×10^{21} n/m^2. A previous investigation[4] of these materials had found that they all exhibited similar radiation hardening effects, but the Cu-Al alloy contained twice as many visible defect clusters. This indicated that a substantial fraction of the defects responsible for the observed radiation hardening were below the resolution limit of electron microscopy (~ 1 nm). Our investigation used resistivity methods, which is sensitive to submicroscopic defect clusters, along with microhardness measurements in an attempt to characterize the nature of the cluster size distribution. The irradiation consisted of four incremental

fluences up to a maximum level of about 3 x 10^{21} n/m^2. The electrical resistivity measurements were made at liquid helium temperature.

Analysis of the resistivity measurements on pure copper provided an estimate of the fraction of vacancies and interstitials that escape recombination. This quantity is important for radiation damage modeling.[5] It was determined that at least 11% (and most likely 16%) of the defects created in copper during 14-MeV neutron irradiation at 25°C escape correlated recombination events. This value is in very good agreement with a previous estimate of 15% obtained from a resistivity study of copper irradiated with fission neutrons.[6]

The electrical resistivity of the copper alloys decreased following low-fluence irradiation (Fig. 5.1), indicating that perhaps short range ordering was occurring. Irradiation to 2 x 10^{21} n/m^2 resulted in a net increase in resistivity of Cu-Al and Cu-Ni compared to their nonirradiated value. The resistivity of Cu-Mn was still less than its nonirradiated value at the maximum fluence investigated in this study.

The resistivity increase of pure copper (see Fig. 5.1) was proportional to the square root of neutron fluence (ϕt) which indicates that the defect cluster density $N_{cl} \propto (\phi t)^{1/2}$. The Vickers microhardness of copper and the copper alloys (see Fig. 5.2) was proportional to $(\phi t)^{1/4}$. Noting that defect cluster hardening[7] is theoretically proportional to $(N_{cl})^{1/2}$, this also implies that $N_{cl} \propto (\phi t)^{1/2}$. The resistivity and microhardness predictions of the fluence dependence of defect clusters are in disagreement with some

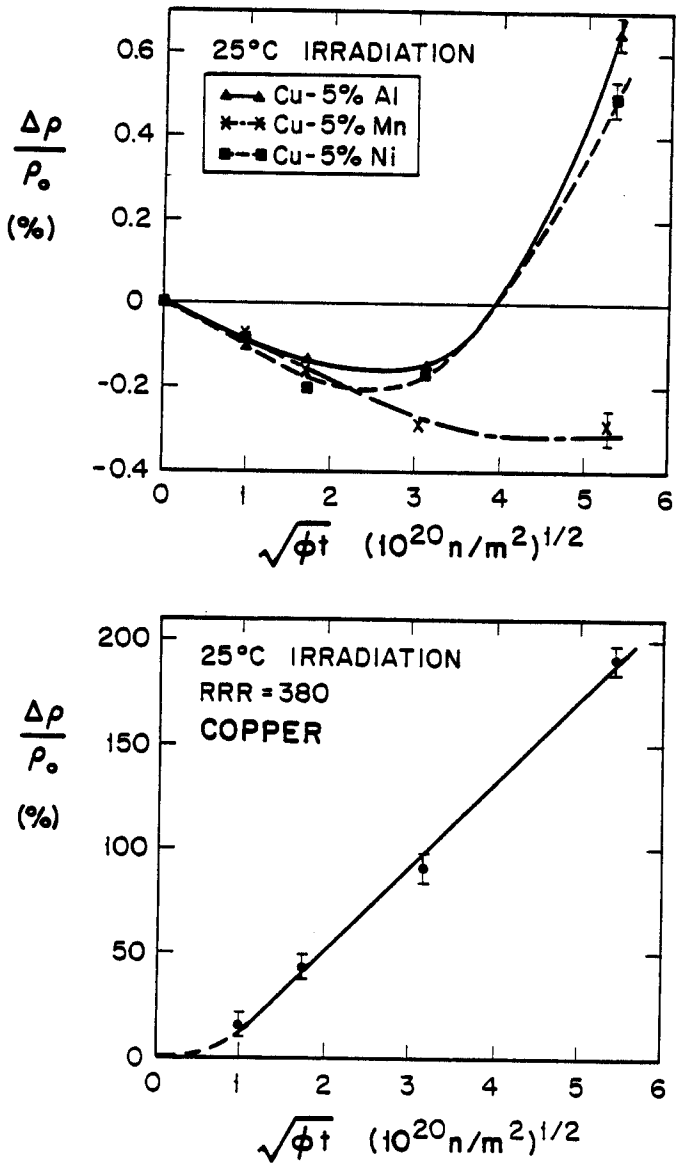

Fig. 5.1. Resistivity change at 4.2 K in 14-MeV neutron irradiated copper and copper alloys.

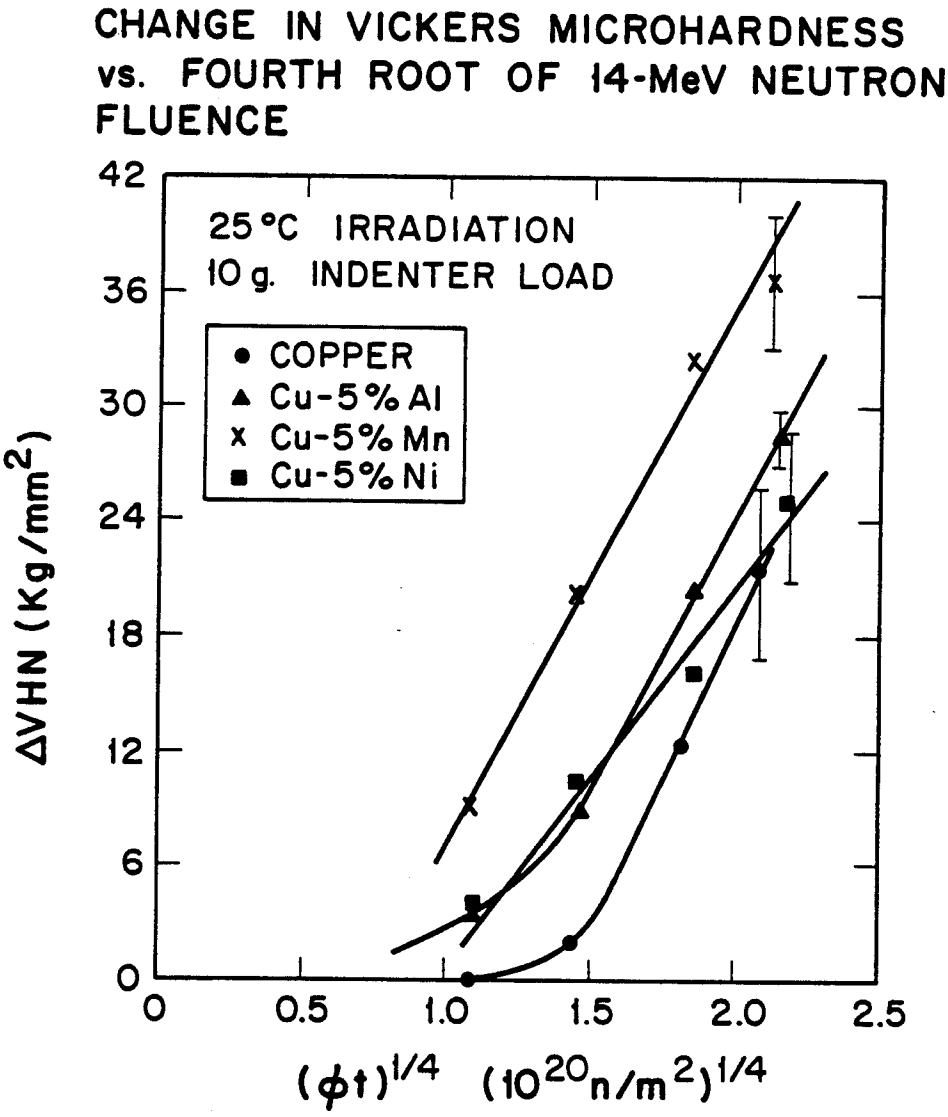

Fig. 5.2. Change in Vickers microhardness of 14-MeV neutron irradiated copper and copper alloys.

limited TEM observations of Brager et al.,[4] who found that the visible cluster density was roughly linear with fluence. Unfortunately, TEM analysis of our specimens has not yet been performed, so we cannot conclusively identify the source of this discrepancy. It is possible that the visible cluster density may be proportional to the fluence, while the total cluster density varies as $(\phi t)^{1/2}$. However, an analysis of the resistivity and microhardness predictions of cluster densities in copper at a given fluence gives values that are in good agreement with the visible cluster densities reported by Brager et al.[4] It was therefore concluded that all of the defect clusters that are responsible for resistivity changes and radiation hardening may be observed using TEM. A recent microscopy study of neutron irradiated copper[8] reported that the defect cluster density was not proportional to ϕt at low fluences, and it appears that the density may be $\sim (\phi t)^{1/2}$ for irradiations near room temperature.

It has been common practice[9,10] to use the empirical relation $N(d) = N_0 \exp(-d/d_0)$ to describe the defect cluster size distribution in irradiated metals. There is no theoretical justification for using such a size distribution. The log-normal (skewed gaussian) is a more physically reasonable distribution function, since it describes the probability distribution for clustering events that are restricted to be greater than a minimum size but are unbounded for large sizes.[11] This is a good mathematical description of the nucleation process. A survey of reported defect cluster size distributions indicated that most of them could be described by a log-

normal distribution. It was therefore proposed for the first time in Ref. 3 that log-normal distributions should be used for describing defect cluster size distributions. A recent theoretical model describing defect clustering during irradiation predicts a dislocation loop size distribution that is similar to a log-normal distribution (although somewhat more complex).[12]

In the course of evaluating the electrical resistivity data from the copper and copper alloy specimens, this author surveyed a large fraction of the published papers that have dealt with resistivity contributions of defects in metals. Of particular interest was the contribution of dislocations to the electrical resistivity, since defect clusters are generally in the form of dislocation loops for metals irradiated at low temperatures (< 200°C for copper). A report was written that summarized the literature to date.[13] It has been found[14] that the dislocation core provides the dominant contribution to the resistivity of a dislocation. Therefore, the resistivity of a perfect dislocation loop of diameter d is approximately equal to the resistivity of a dislocation line of length πd. For a faulted loop, one also has to include the resistivity due to the stacking fault. The net effect is that clustering of point defects into dislocation loops can cause a reduction in the effective Frenkel pair resistivity. Figure 5.3 compares the resistivity per defect as a function of dislocation loop size for perfect and faulted loops. The effective resistivity per defect for a 50-50 concentration of vacancies and interstitials in copper is 1 $\mu\Omega$-m/at. fraction defects.

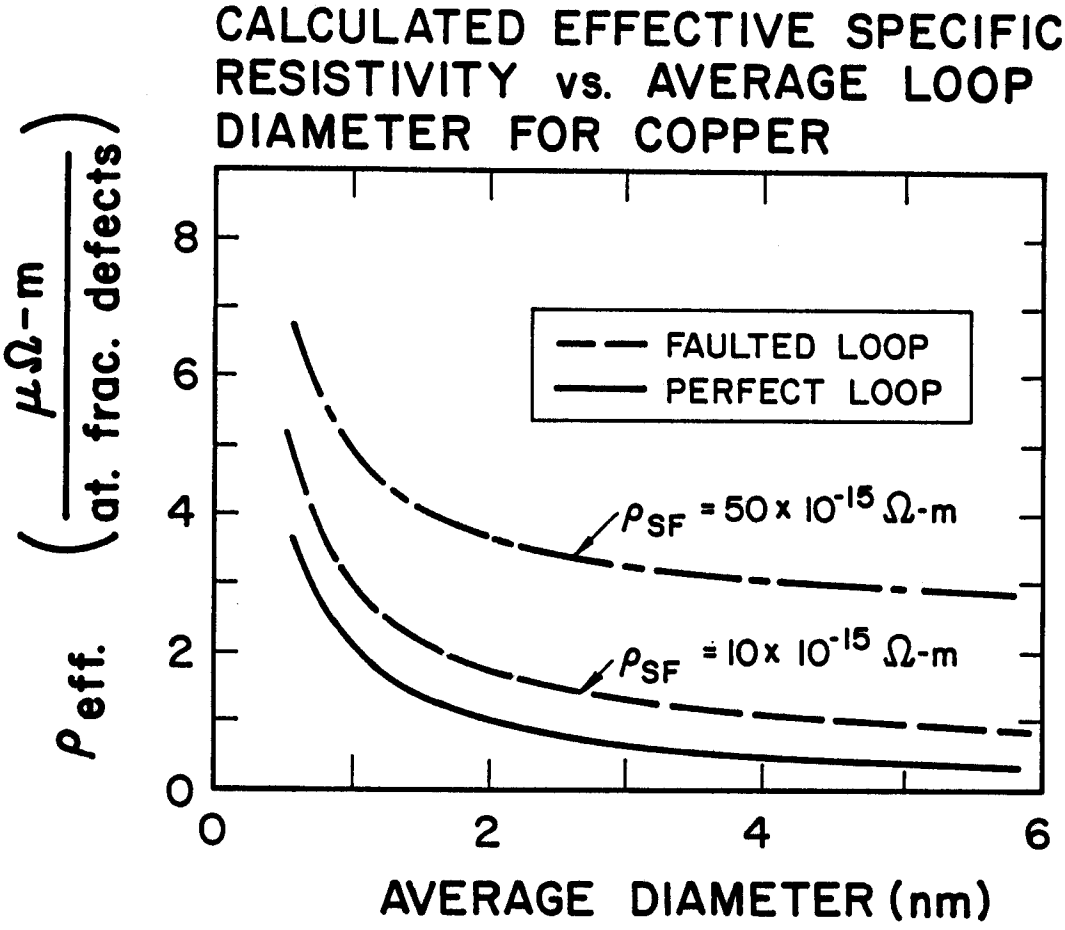

Fig. 5.3. Calculated effective specific resistivity of point defect clusters vs. average loop diameter for copper, assuming a log-normal distribution of dislocation loops.

Therefore, there will be a substantial reduction in the observed resistivity for perfect loops with diameters larger than 2 nm.

An extensive investigation[15] was conducted on the radiation-induced microhardness changes observed in the copper alloys irradiated with 14-MeV neutrons (also see Ref. 3). The indenter load was restricted to values of 10 g or less due to the small specimen thickness. More than 2400 indentations were measured for 40 different experimental conditions (4 metals, 5 fluence levels including unirradiated condition, 2 indenter load values: 5 g and 10 g). As shown in Fig. 5.4, there was a large effect of indenter load on the microhardness results. The lower load had a longer incubation fluence before radiation hardening was observed. This resulted in a lower measured hardness change (i.e., less radiation hardening) as compared to high-load measurements at any given fluence. It is well known that the microhardness at low loads is very sensitive to the microstructure, as shown in Fig. 5.5 (also see Ref. 16). However, it was anticipated that the change in microhardness following irradiation should be independent of indenter load since neutron irradiation results in a relatively uniform, fine scale damage compared to the sampling volume of typical low-load microhardness tests. The observations mentioned above show that this assumption is not valid and that low-load microhardness measurements generally cannot be used for quantitative purposes.

Examination of the fluence dependence of radiation hardening in the four metals revealed that it was proportional to $(\phi t)^{1/4}$ for both

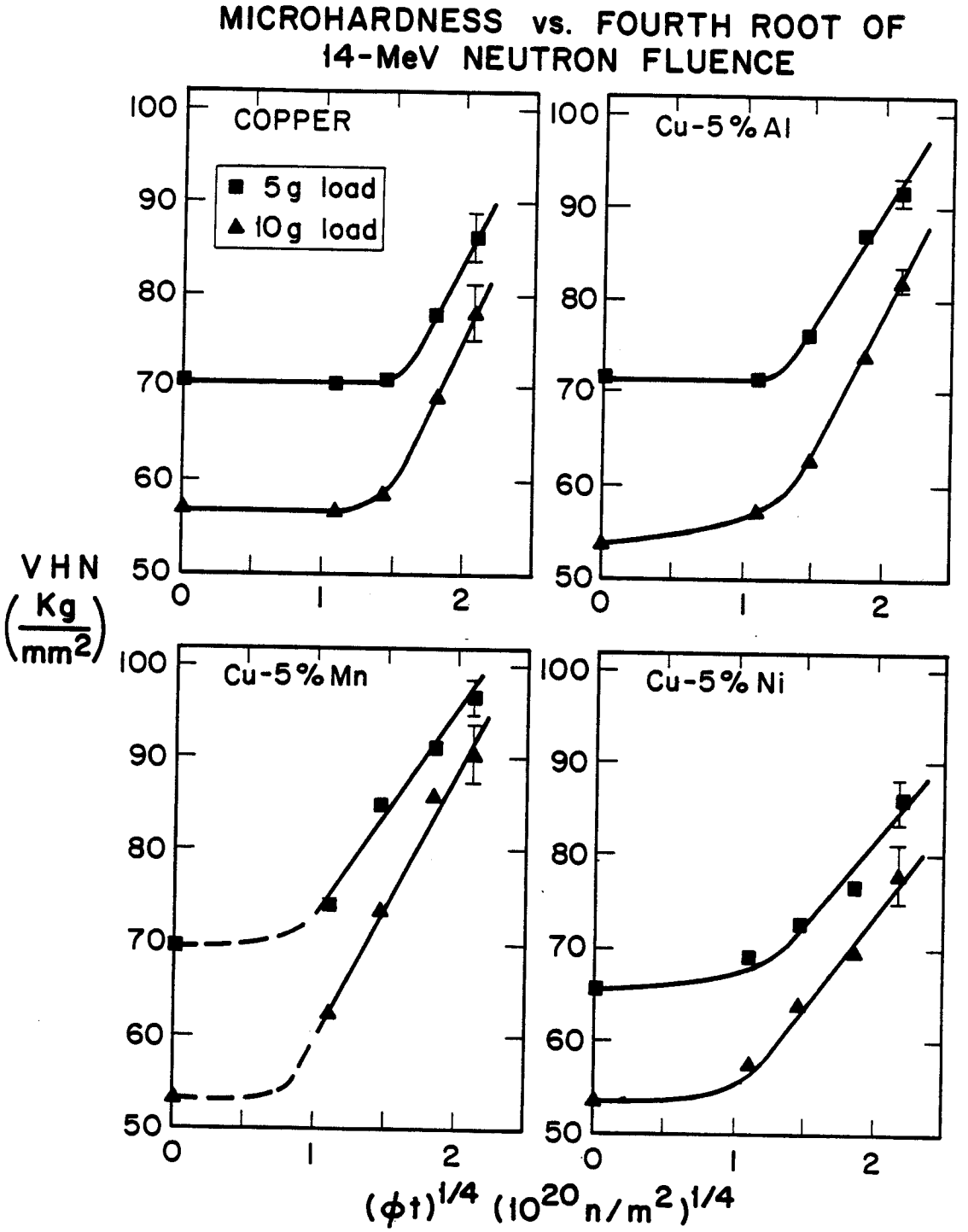

Fig. 5.4. Vickers microhardness of 14-MeV neutron irradiated copper alloys at 5 g and 10 g.

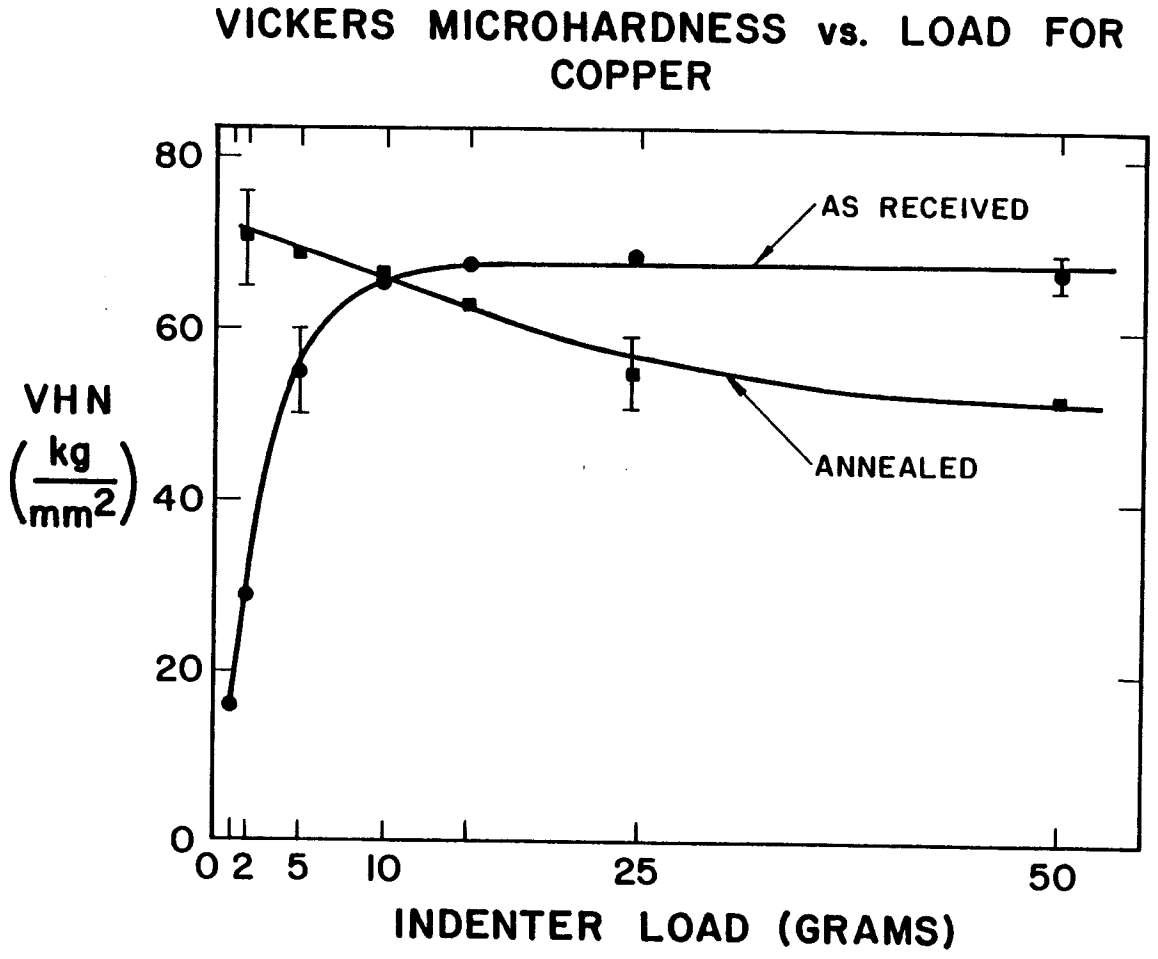

Fig. 5.5. Load dependence of Vickers microhardness for annealed and cold-worked copper.

values of indenter load. Also, the copper alloys exhibited measurable radiation hardening at lower fluences than pure copper for both indenter load values. Therefore, it appears that low-load microhardness measurements are useful for qualitative analysis of radiation hardening.

References for Chapter V

1. S.J. Zinkle, R.A. Dodd, G.L. Kulcinski and K. Farrell, J. Nucl. Mater. 117 (1983) 213-217.

2. D.S. Whitmell and R.S. Nelson, AERE R6863 (1972).

3. S.J. Zinkle and G.L. Kulcinski, J. Nucl. Mater. 122/123 (1984) 449-454.

4. H.R. Brager, F.A. Garner and N.F. Panayotou, J. Nucl. Mater. 103/104 (1981) 995.

5. W.G. Wolfer, J. Nucl. Mater. 122/123 (1984) 367-378.

6. U. Theis and H. Wollenberger, J. Nucl. Mater. 88 (1980) 121.

7. N.M. Ghoneim et al., in Proc. 11th Intern. Symp. on Effects of Radiation on Materials, ASTM STP 782, Scottsdale, AZ (1982), 1054.

8. Y. Shimomura, H. Yoshida, M. Kiritani, K. Kitagawa and K. Yamakawa, "Electron Microscopic Studies of Damage Evolution in Fission Neutron Irradiated Metals," 1st Intern. Conf. on Fusion Reactor Materials, Tokyo (Dec. 1984).

9. M. Rühle and J.C. Crump, III, Phys. Stat. Sol. A2 (1970) 257.

10. B.L. Eyre, J. Phys. F 3 (1973) 422.

11. F. Schückher, in Quantitative Microscopy, R.T. DeHoff and F.N. Rhines, Eds. (McGraw-Hill, 1968) p. 205.

12. M.N. Pletnev and Yu.M. Platov, Phys. Met. Metallogr. 40, No. 2, (1975) 64-69.

13. S.J. Zinkle, "Electrical Resistivity of Dislocations in Metals," University of Wisconsin Fusion Technology Institute Report UWFDM-538 (1983).

14. R.A. Brown, J. Phys. F 7 (1977) 1283.

15. S.J. Zinkle and G.L. Kulcinski, "Low-Load Microhardness Changes in 14-MeV Neutron Irradiated Copper Alloys," Symp. on the Use of Nonstandard Subsized Specimens for Irradiated Testing, Albuquerque, NM (Sept. 1983); to be published by ASTM.

16. B.W. Mott, Micro-indentation Hardness Testing, Butterworths Scientific Publications, London (1956).

CHAPTER VI. EXPERIMENTAL PROCEDURE

VI.A. Metallurgy of Cu-Zr and Cu-Cr-Zr

Two commercial copper alloys were investigated in this thesis, namely AMZIRC (Cu-0.15% Zr) and AMAX-MZC (Cu-0.8% Cr-0.15% Zr-0.04% Mg), manufactured by AMAX Copper Inc.[1] Various levels of strength and electrical conductivity may be obtained in these alloys depending on the heat treatment. The AMZIRC alloy confirms to the requirements of copper No. C15000 and the MZC alloy corresponds with copper No. C18100 (ASTM-SAE Unified Numbering System).[2] Cr and Mg are both oversized solutes in copper, with volumetric size factors of 19.7% and 50.8%, respectively.[3] The size factor for Zr apparently has not been measured, although it is known that Zr is a fast diffuser in copper.[2] Both AMZIRC and AMAX-MZC are prepared using oxygen-free, high conductivity (OFHC) copper.

There have been many investigations of the Cu-Zr phase diagram.[4-15] Six intermediate phases have been identified. The composition of the most Cu-rich phase, which is of interest in our case, is still somewhat uncertain. However, it appears likely that the stoichiometry is Cu_5Zr,[11] or possibly Cu_9Zr_2.[8] The structure of this phase is also uncertain. Various researchers have claimed crystal symmetries of orthorhombic,[13] hexagonal,[16,17] cubic,[14] and tetragonal or possibly fcc.[10,12] Figure 6.1 shows the most current version of the Cu-Zr phase diagram.[11] The solubility of Zr in Cu is very limited (0.17 wt.% Zr; 0.12 at.% Zr).

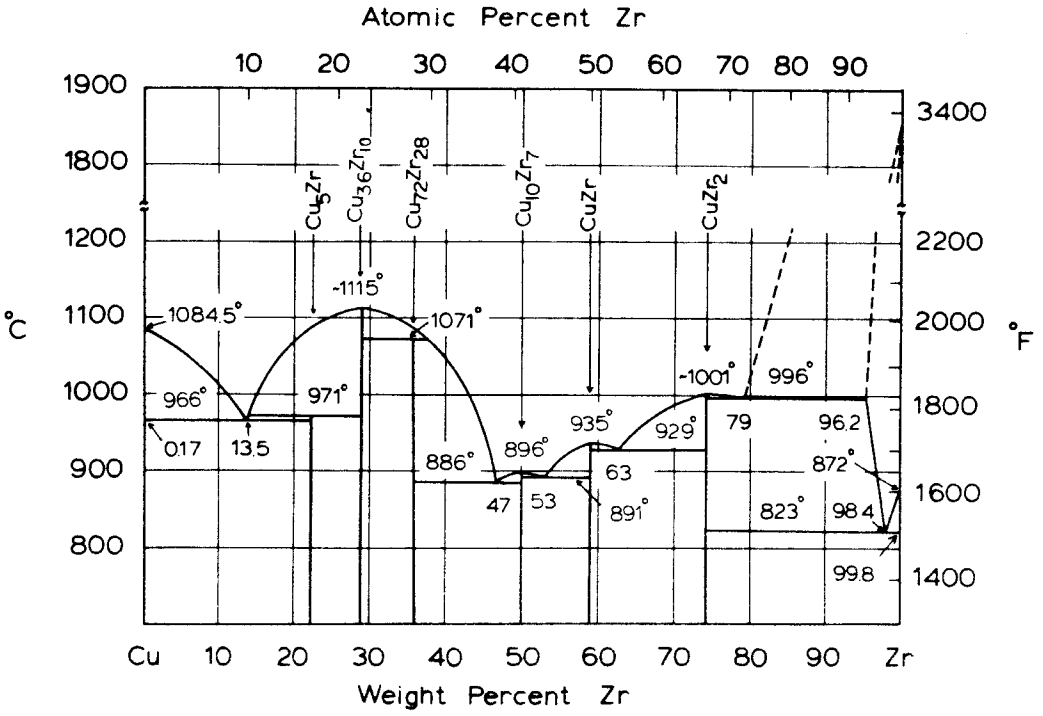

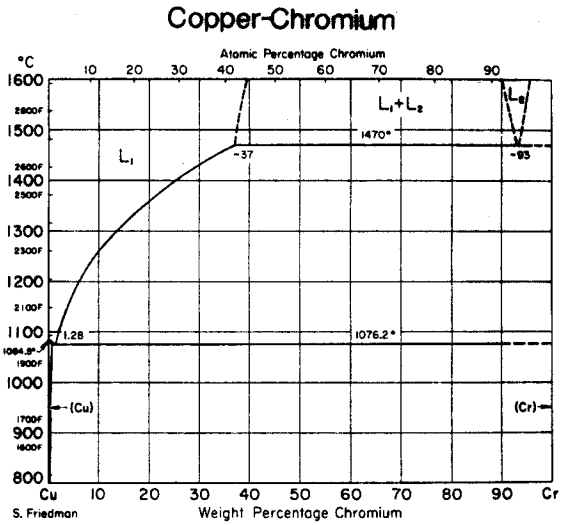

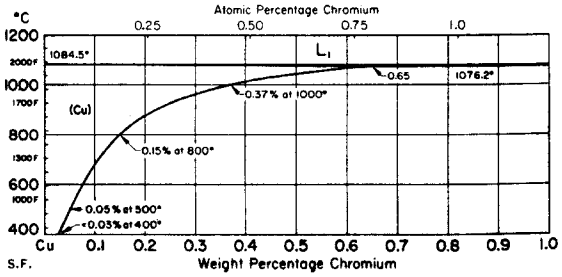

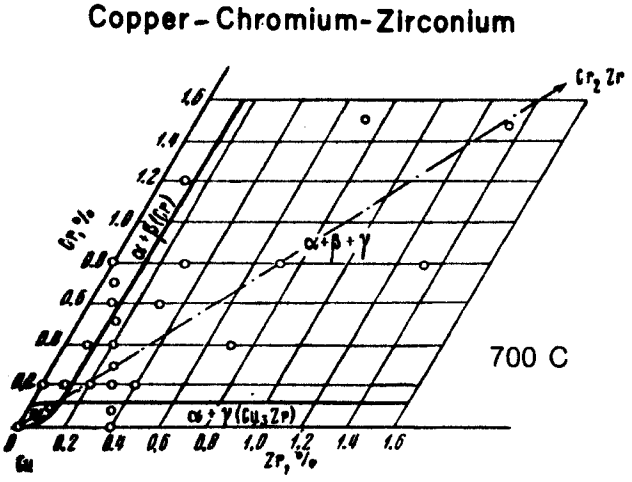

Fig. 6.1. Phase diagrams for Cu-Zr, Cu-Cr and Cu-Cr-Zr.

The phase diagram[2] for Cu-Cr is also given in Fig. 6.1. No Cu-Cr precipitates are known to exist. The solubility of Cr in Cu is small (0.8 at.% at the alloy eutectic temperature). There are a limited number of published investigations that have studied the Cu-Cr-Zr ternary phase diagram.[13,15,18-23] Zakharov et al.[20] initially reported the existence of Cr_2Zr in the Cu-rich corner of the diagram, but subsequent studies did not observe this phase (at least for Cr and Zr concentrations of less than 1.5% each). Figure 6.1 shows the latest version of the Cu-Cr-Zr phase diagram (700°C isothermal section).[21]

VI.B. Irradiation Facility

The copper and copper alloy irradiations were conducted at the University of Wisconsin Heavy-Ion Irradiation Facility.[23] A recent modification of the target chamber[24] provides thermal isolation between the specimens, so that an individual sample will only be heated during its irradiation. A schematic of the irradiation facility is shown in Fig. 6.2.

A SNICS (Source of Negative Ions by Cesium Sputtering) type negative ion source developed by Billen and Richards[27,28] is used to produce Cu^- (or other negative ions). This source is capable of producing beam currents in excess of 50 μA for several different species of ions. The negative ions exit the source with an energy equal to the sputter cathode potential (2-4 kV). The beam is identified and stripped of impurity elements by passing through an analyzing magnet and a 90° electrostatic mirror.

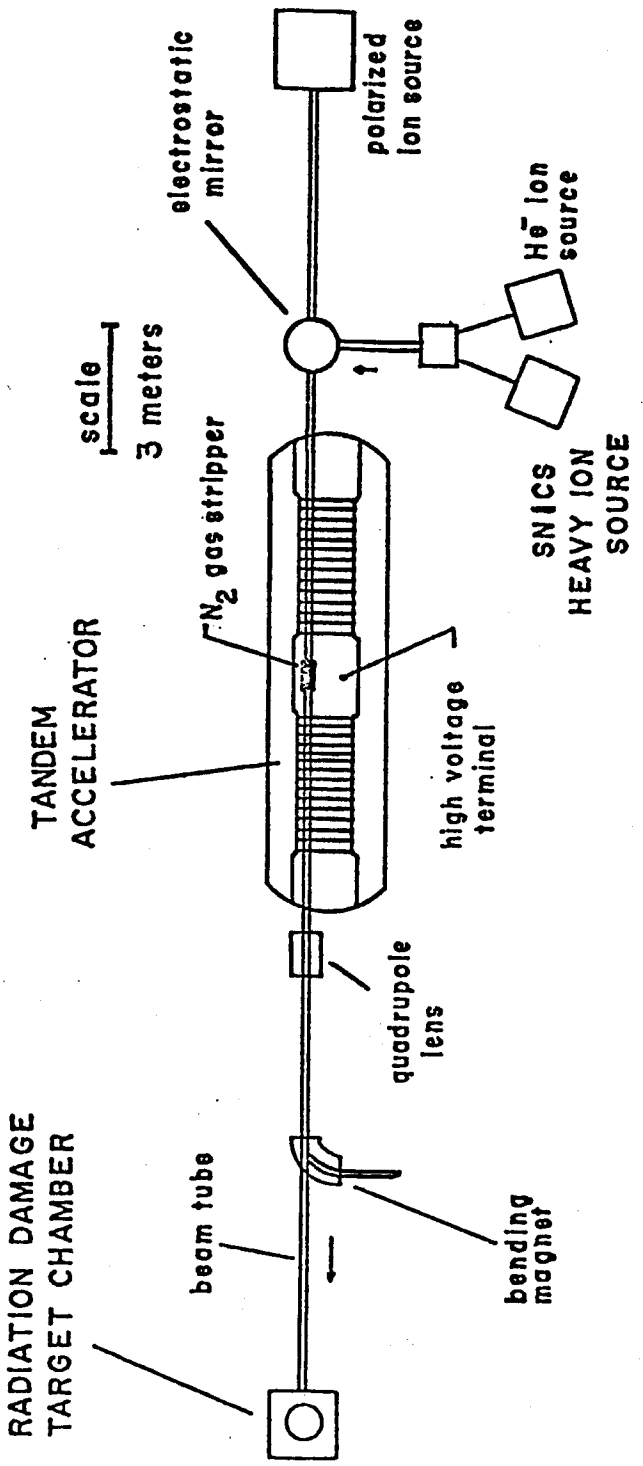

Fig. 6.2. Schematic of University of Wisconsin heavy ion irradiation facility.

The negative ions are injected into the tandem Van de Graaf accelerator (High Voltage Engineering Corporation, model EN) at ground potential and are accelerated into the high-voltage terminal, which operates with a positive potential V. A N_2 gas stripper located in the high voltage terminal converts the negative ions into positive ions via atomic collisions. A distribution of positive charge states are created due to the random nature of the stripping process. These positive ions are then accelerated towards the ground potential at the far end of the tandem accelerator. The energy of the positive ions leaving the accelerator therefore depends on the charge state of the exiting ions. For a Cu ion beam at a dome voltage of 3.5 MV, most of the ions exit as Cu^{3+}. This means that most of the Cu^{3+} ions exit at 14 MeV (E_{ion} = eV(1 + n), where n is the charge state). The particular charge state of the ions reaching the target is controlled by a quadrupole lens located just outside of the high energy end of the accelerator, and the charge state distribution can be monitored at the target stand. Use of appropriate lens and magnet settings leads to over 99% of the beam consisting of Cu^{3+}.

The Heavy Ion Target Chamber and its associated vacuum system is shown schematically in Fig. 6.3. The target section lies ~ 1/2° off the tandem axis in order to prevent low Z ions and neutral atoms from striking the target. The target section consists of three differentially pumped sections so as to provide a very low vacuum at the sample chamber stage. The first stage uses a 200 ℓ/sec diffusion pump, the intermediate stage has a 400 ℓ/sec titanium sublimator

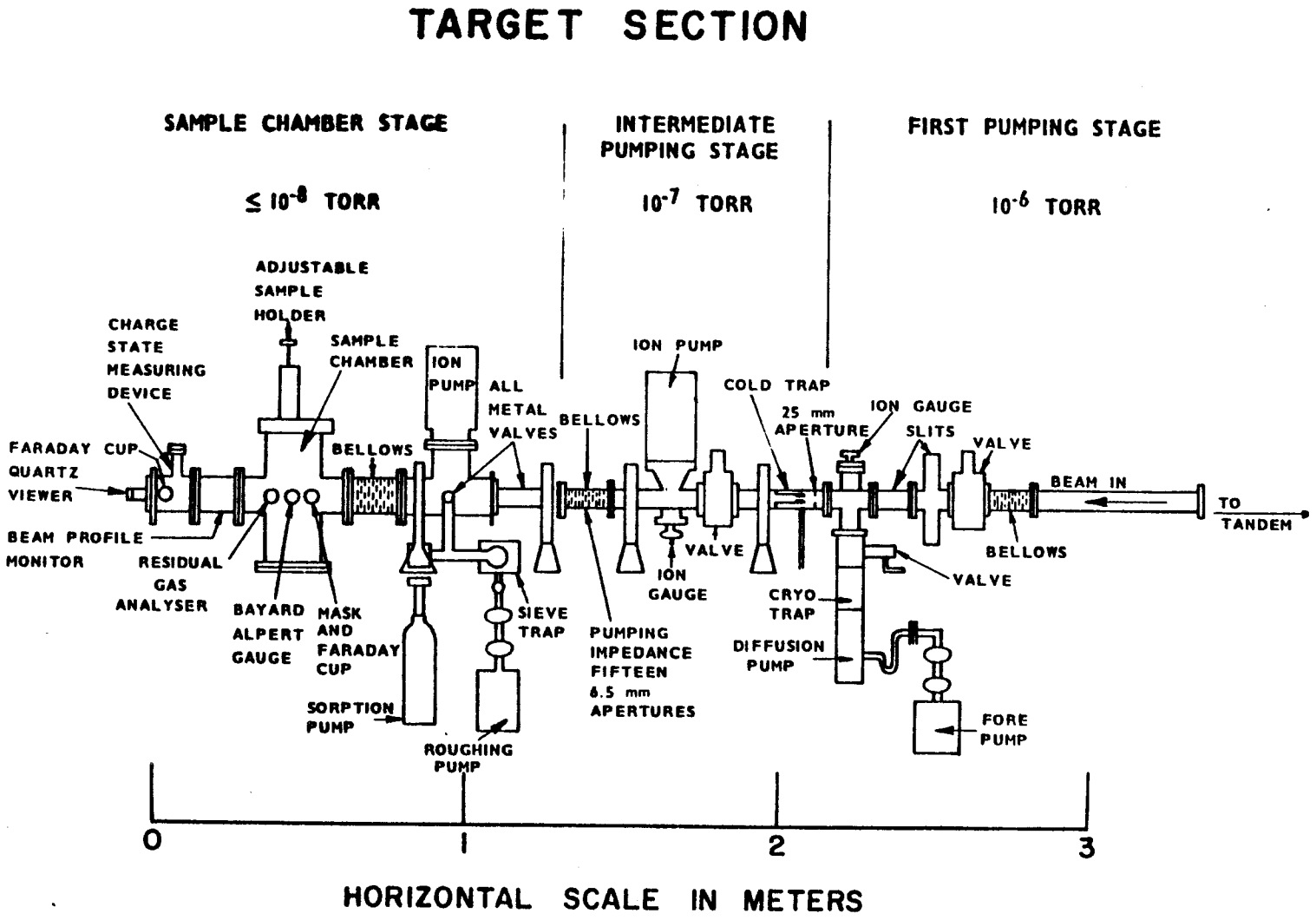

Fig. 6.3. Schematic of heavy ion irradiation target chamber and associated vacuum system.

pump, and the sample chamber is equipped with a large orbitron pump. A series of low-conductance Ta apertures separate the target chamber from the intermediate stage. The composition of gases in the sample chamber can be determined with a residual gas analyzer which is mounted on the target chamber. Faraday cups located in front and behind the sample chamber are used to measure the beam current at regular time intervals during an irradiation. A 3 mm mask aperture located immediately in front of the sample chamber is used to explicitly define the incident beam. The beam intensity profile is essentially constant over the 3 mm beam spot diameter.

The specimen holder assembly[24] consists of a carousel with eight individual sample holders. Samples are individually heated during irradiation by thermal radiation from ohmic-heated tantalum sheets. Individual thermocouple leads allow continuous monitoring of all eight specimens during an irradiation run. Specimens adjacent to the sample being irradiated are thermally shielded from the heater to prevent post-irradiation annealing effects. The range of operating temperatures for the heater is roughly 100-700°C. The temperature of specimens immediately adjacent to the heater is about 50°C for low temperature irradiations and is $\lesssim$ 450°C for a 700°C irradiation.

VI.C. Specimen Preparation and Analysis

Foil strips of the AMZIRC and AMAX-MZC copper alloys of thickness 10 mils (250 μm) were obtained from AMAX Copper, Inc., in both the cold-worked plus aged (CWA) condition and the solution annealed plus aged (SAA) condition. The CWA heat treatment consisted of a

solution anneal at 950°C for 45 minutes in an inert environment (water quench) followed by 90% cold rolling and then aging for 30 minutes at 375°C for the AMZIRC alloy and 400°C for the MZC alloy. The SAA heat treatment consisted of a solution anneal at 930°C for 45 minutes (water quench) followed by aging for one hour at 450°C for AMZIRC and 500°C for MZC. Some of the CWA foils were subsequently annealed at 950°C for 100 hours in evacuated quartz tubes at the University of Wisconsin and quenched in water (SA condition). One-half of these foils were then aged in evacuated quartz tubes for 1 hour at 470°C for both alloys (UW SAA condition).

The high purity (Marz grade) copper used in this investigation was obtained from Materials Research Corporation in the form of 10 mil foil strip. The foils were annealed at 800°C for 1.5 hours and cooled to room temperature in a hydrogen atmosphere prior to their preparation for irradiation.[25] Table 6.1 lists the impurity levels contained in the pure copper and in the OFHC copper used to make the alloys[28] as determined by the manufacturers.

VI.C.1 Thermal Anneal Study

A substantial portion of this thesis study was devoted to an investigation of the physical properties and microstructures of AMZIRC and MZC following thermal annealing.* Specimens of dimensions 0.5 by 5 cm were cut from the CWA foils of both alloys, mechanically polished (0.3 μm alumina powder), and then annealed for times ranging

*The author wishes to acknowledge the experimental assistance of D.H. Plantz during this portion of the research.

Table 6.1. Impurity Analysis of the Specimen Stock Material in Weight Parts Per Million (ppm)

Element	High Purity Copper	Copper Alloys
C	6	---
H	< 1.0	0.5-2
O	< 5.0	< 3
N	< 1.0	---
Ag	0.5	8-25
Al	1.0	---
As	---	< 3
Ca	0.4	---
Cd	*	< 1
Co	*	---
Cr	0.3	---
Fe	0.8	3-10
Mn	*	< 0.4
Ni	*	3-13
P	---	< 3
Pb	0.7	3-8
S	0.5	6-20
Sb	---	3-8
Si	0.3	---
Sn	*	< 3
Te	---	< 2
Zn	1.5	< 1

*< 0.1 ppm

from 0.25 to 100 hours in a high-vacuum furnace. Post-anneal cooling used a combination of furnace and air cooling. The specimen temperature (as monitored by calibrated chromel-alumel thermocouples attached to the specimen container) decreased by at least 100°C within one minute following the anneal. Temperature control was maintained to within ±5°C. The annealing temperatures that were investigated ranged from 300 to 600°C in 50°C increments. The pressure in the vacuum chamber ranged from 1×10^{-6} to 1×10^{-9} torr during the anneal, with the higher pressures pertaining to the beginning of the anneal. Different specimens of each alloy were used for each of the different annealing conditions. All specimens were electropolished for about 5 seconds in a solution of 33% HNO_3/67% CH_3OH at 5 volts and -20°C upon removal from the furnace in order to remove the oxide layer present from the anneal.

Room temperature Vickers microhardness measurements were made on the as-received (CWA, SA, SAA, UW SAA) and annealed specimens of both alloys at an indenter load of 200 grams using a vibration-isolated Buehler Micromet microhardness tester. A minimum of nine different indentations in three widely separated areas were measured for each specimen. The microstructures of selected specimens were examined in a JEOL TEMSCAN-200CX electron microscope operated at 200 kV. TEM disks were punched from the annealed foils and jet-electropolished in a commercial (Fishione) polisher using a solution of 33% HNO_3/67% CH_3OH cooled to -30°C at an applied potential of 15-20 V (90 mA). Some specimens were also examined in an optical microscope. The

specimens were electropolished following their mechanical polishing, and then were etched by immersing into a solution of 225 ml CH_3OH, 12 g $FeCl_3$ and 7 ml HCl for 5 to 10 seconds.

Electrical resistivity specimens were prepared from the as-received and annealed alloys by first attaching the metal foils to a plexiglass base with an adhesive lacquer. A diamond saw was used to cut strips of nominal width 200 μm (2 inch length). These resistivity "wires" were then floated off from the plexiglass base by immersing the assembly in acetone, which dissolved the adhesive lacquer. This procedure produced uniform specimens of small cross-sectional area without introducing deformation to the "wire." Severe deformation would have occurred if conventional shearing methods had been used. The average cross-sectional area of each specimen was determined by measuring the mass and length of the specimen, and then dividing by the mass density (8.96 g/cm^3).

Resistivity measurements were performed at room temperature (23°C) on all specimens, and additional measurements were made at 77 K and 4.2 K on the as-received (CWA and SAA) copper alloys. Standard 4-point probe resistivity methods were followed,[29] using a Keithley nanovolt detector and a 4-digit multimeter for the voltage readings. The gauge length over which the voltage drop was measured was about 1.5 inches (4 cm). The current density was maintained at about 200 A/cm^2. Readings were taken with the current going both ways through the sample and the results averaged in order to cancel the effect of thermal emfs. One to two resistivity "wires" were

measured for each thermal annealing condition. Approximately four specimens of each alloy were tested to determine the as-received (CWA and SAA) resistivity. The main sources of experimental error were due to uncertainties in the cross-sectional area (nonuniformities in the wire cross-section) and in the gauge length.

Miniature tensile specimens were punched from the as-received (CWA, SAA, SA) and annealed foils and deburred at Hanford Engineering Development Laboratory (HEDL) using standard[30] techniques. The nominal dimensions of the gauge section were 5.1 by 1.0 by 0.25 mm. The actual cross-sectional area for each tensile specimen was determined by measuring the width and thickness of the gauge section at five different locations and averaging the results.[31] A minimum of two tensile specimens were tested in the longitudinal direction for each of the annealing conditions in this study using a precision horizontal test frame with a free-running crosshead speed of 2.5 μm/s (measurements made at HEDL). Several CWA and SAA specimens were also tested in the transverse direction. Data for each tensile test were collected at room temperature in both a digital and analog (load-elongation plot) manner. The 0.2 percent offset yield strength and ultimate tensile strength were calculated using a computer-based digital data acquisition program.[32] The strength parameters of selected specimens were also calculated by standard graphical techniques at the University of Wisconsin using the analog data. The results were in good agreement with the computer-generated values.

VI.C.2 Ion Irradiation Study

All of the irradiated specimens were examined using the cross-section technique.[33] The following summarizes the experimental procedure.

Foils of dimension 0.5 by 1.0 cm are cut from the 250 μm (0.010 inch) thick copper or copper alloy stock material with a diamond saw. These foils are mounted on a standard polishing block and are mechanically polished using successively finer grades of sandpaper, finishing with 600 grit. The assembly is then placed in a Syntron® vibratory metallographic polisher using a distilled water slurry of 0.3 μm alumina powder. Polishing for a period of 6-12 hours results in a very smooth, pit-free surface. The foils are then removed from the polishing block with acetone and turned over, and the entire polishing sequence is repeated on the other foil surface. Immediately prior to irradiation the foils are electropolished for about 10 seconds in a solution of 33% HNO_3/67% CH_3OH cooled to -50°C at an applied potential of 5-10 volts. This electropolish removes the work-hardened surface layer present after mechanical polishing and gives an optically smooth, oxide-free surface. The specimens are transported to the irradiation facility in vials filled with methanol. The foils are exposed to air for a period of about 1/2 hour while they are being mounted onto the carousel sample holder assembly. The sample chamber vacuum prior to and during the irradiation is typically on the order of 1×10^{-5} Pa (1×10^{-7} torr).

Upon completion of the irradiation the samples are removed, given an identification mark, and then stored in a vacuum dessicator backfilled with high-purity argon until they are scheduled to be electroplated with copper. Figure 6.4 schematically outlines the basic steps required to obtain a cross-sectioned TEM specimen. The critical points in the procedure are steps 2 and 4, where the irradiated foil is electroplated and thinned, respectively. Special care prior to and during the electroplating step is required in order to obtain a uniform, thick deposit layer with good adhesion to the foil surface. Improper surface preparation can cause cracking at the interface and may prevent electron microscopy results from being obtained.

The electroplating technique used in this thesis research parallels that developed by Knoll[25] for copper alloys. The irradiated foils were thoroughly degreased using acetone prior to their preparation for electroplating. The sample is then electropolished for 2 seconds in a solution of 33% HNO_3/67% CH_3OH cooled to -50°C at an applied potential of 5 V. This process is intended to remove the oxide layer and any carbon contaminants that may be present on the foil surface. The foil is then transferred to the plating solution (180 g $CuSO_4$, 30 ml H_2SO_4, 950 ml H_2O), where it is made anodic for 1 second using a current density of 100 mA/cm^2. Interferometer measurements indicate that the total depth removed during the electropolish and strike treatment is less than 0.1 μm. Following the strike treatment, the polarity of the plating cell is reversed

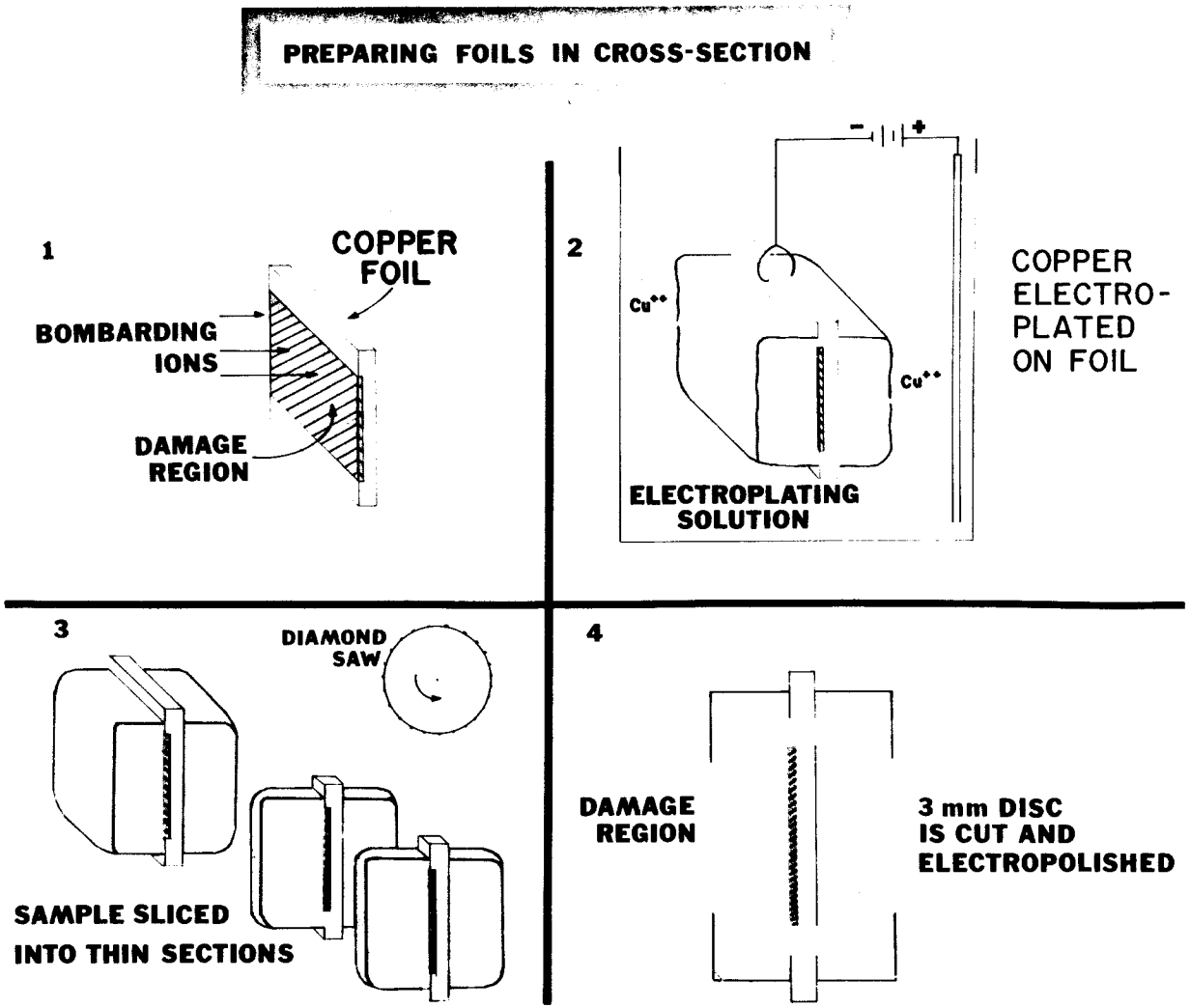

Fig. 6.4. Outline of procedure followed to prepare a TEM specimen in cross-section.

and the foil is electroplated at a current density of 100-150 mA/cm^2. The sacrificial copper anodes are thoroughly cleaned in a solution of 50% HNO_3/50% H_2O prior to the start of electroplating. The anodes are placed in cotton bags during the plating process to prevent sludge from electrodepositing on the foil. The electroplating process proceeds until the total plated thickness exceeds 3 mm; this normally takes about 24 hours.

The cross-section technique has been employed by several previous workers at the University of Wisconsin.[25,34,35] Several modifications to the basic procedure have been introduced by this author and R.L. Sindelar during the course of this thesis research.[36] The electroplating sample holder has been redesigned so as to optimize the plating rate and to provide fairly uniform electrodeposited layers (Fig. 6.5). The small 0.5 by 0.5 cm "window" in the holder serves to minimize foil edge effects on the plate layer, thereby enhancing uniform deposition. A common aquarium air stone is used to create a fine stream of gas bubbles (nitrogen or argon). The gas bubbles are directed through the channel in the bottom of the sample holder and flow over the foil surface. This fine gas stream sweeps away the hydrogen bubbles that form on the foil surface due to electrolysis. Failure to remove these H_2 bubbles while electroplating would result in a porous plating.

Upon completion of the plating, the sample is mounted in epoxy and sliced normal to the irradiated surface using a diamond saw of 6 mil thickness. Typically, 6 to 8 slices of thickness 200 μm each

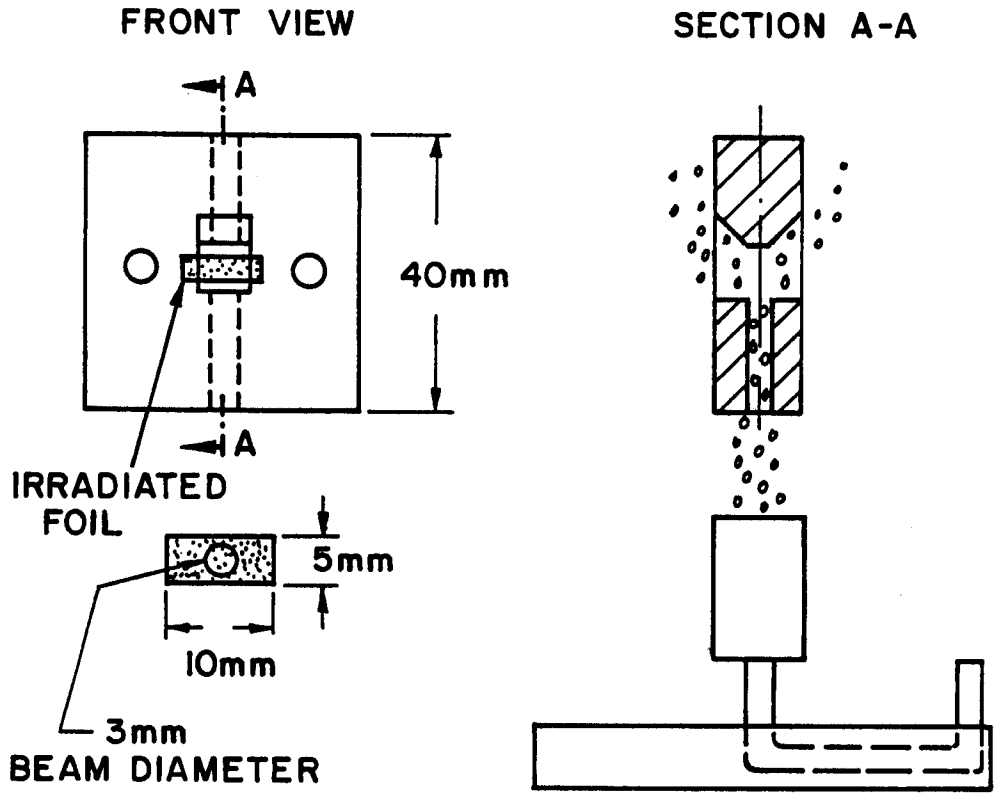

Fig. 6.5. Schematic of sample holder and gas bubbler used for electroplating ion-irradiated foils.

are obtained from the irradiated region. A 3 mm disk is punched from the center of these wafers. The disk is thoroughly cleaned in acetone to remove cutting oil contaminants from the foil surface prior to electropolishing. This cleaning is necessary in order to prevent contamination of the electropolishing solution, which could cause misleading signals during microchemical analysis.

The 3 mm disk is thinned using a commercial (Fishione) twin jet electropolisher in preparation for examination in an electron microscope. The foil is thinned until perforation occurs using a solution of 33% HNO_3/67% CH_3OH cooled to -30°C with an applied potential of 15-20 V (90 mA current). A simple technique was developed in order to ensure that perforation first occurs in the near vicinity of the irradiated boundary. Both sides of the TEM disk are covered with a protective lacquer with the exception of a ~ 50 μm wide strip centered along the irradiated boundary. The specimen is then electropolished for a period of time ranging from 20 seconds to $\gtrsim$ 2 minutes depending on the foil thickness and the particular metal being investigated. The lacquer is then removed and the specimen is polished until perforation occurs. Adequate thin area in the damage region has been obtained in about 80% of the cross-sectioned specimens that were prepared using this technique. Since six to eight specimens were generally available from each plated sample, this high success rate allowed multiple specimens to be analyzed when desired.

Figure 6.6 is an optical micrograph that shows a typical result for an irradiated copper alloy cross-section specimen. The parallel,

dark bands running horizontally across the micrograph outline the residual step height change from the prepolish treatment. Electron-transparent regions that extend along the irradiated boundary for distances of $\gtrsim$ 100 μm have been obtained under favorable conditions. Figure 6.7 shows a portion of the TEM thin area found along the irradiated boundary of an annealed AMZIRC specimen.

Porosity problems were encountered in several plated samples in the present study. The problem was finally resolved by carefully controlling the gas flow rate at a value around 40 ml/minute. Use of either too high or too low of a bubbling rate resulted in porosity problems. Porosity in the plated material makes it very difficult to prepare a TEM specimen because the jet-polishing unit cannot distinguish between holes in the plating and in the foil (the electropolishing process is terminated before a hole forms on the foil interface). The specimens containing porous plating were salvaged by using a 1 mil tantalum foil with a small hole in its center as a selected-area mask. This procedure covered up the holes in the plating and allowed electropolishing to continue until a hole perforated in the foil. However, the quality of the TEM specimen was generally poor compared to specimens prepared by conventional methods (i.e., limited thin area).

VI.C.3 Irradiation Parameters and Analysis

Table 6.2 shows the damage levels and temperatures investigated for the 14-MeV Cu ion-irradiated copper and copper alloys. AMZIRC and MZC specimens in the cold-worked plus aged (CWA) condition con-

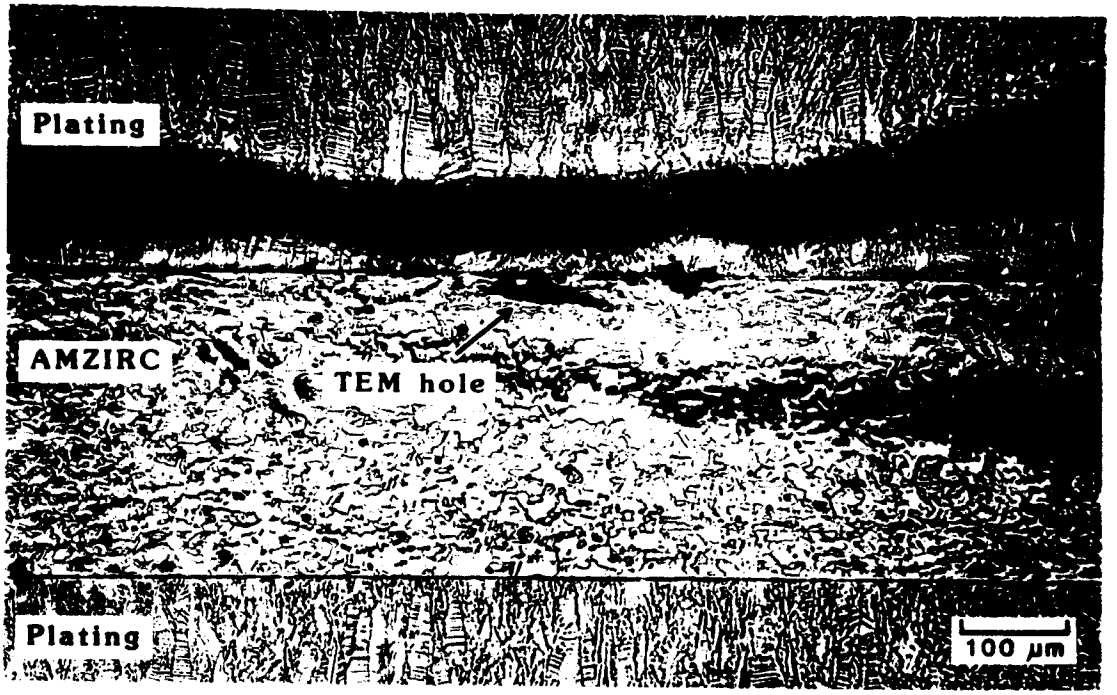

Fig. 6.6 Optical micrograph of a thinned cross-section specimen. The arrow points to the perforation in the foil next to the irradiated boundary.

Fig. 6.7. Representative thin area in a cross-sectioned AMZIRC specimen.

stitute the bulk of the irradiation conditions. A limited investigation was also made on pure copper and on the alloys in the solution annealed plus aged condition. The damage levels given in Table 6.2 correspond to the calculated peak damage (2 μm depth); the damage level at the 1 μm depth is roughly 25% of this value (see Fig. 2.2). The depth dependent damage was calculated from the Brice code (see Section II.A); a 14-MeV Cu ion fluence of $3 \times 10^{20}/m^2$ corresponds to a peak damage level of 40 dpa. The ion flux was relatively constant for all irradiated specimens at 5×10^{16} ions/m^2-s (actual values ranged from 4×10^{16} to $6 \times 10^{16}/m^2$-s). This corresponds to a calculated damage rate of 1.7×10^{-3} dpa/s at the 1 μm depth and 7×10^{-3} dpa/s at the 2 μm depth. The resultant irradiation times for the 40 dpa peak damage level specimens were ~ 1.5 hours.

Conventional transmission electron microscopy was performed on the thermal annealed and irradiated specimens using a JEOL TEMSCAN-200CX electron microscope operated at 200 kV. Specimen thicknesses were determined from either stereomicroscopy or else extinction fringes.[37] Qualitative microchemical analysis of the precipitates contained in the two copper alloys was made using energy dispersive x-ray spectroscopy (EDS) techniques while operating the microscope in the STEM mode.

Table 6.2. Temperature and Dose Matrix for Ion Irradiation Study

Dose (dpa)* \ Temperature (°C)	100	150	200	250	300	400	500	550
120					A			
40	A, M Z, C	A, M	A, M R, Z, C	A, M	A(a), Z C, H, E	A, M R, Z, C	A, M(b)	A
10					M(c)	A, M	A(c)	A

*calculated peak damage level (2 μm depth)

A: cold-worked plus aged AMZIRC
M: cold-worked plus aged MZC
R: solution anneal plus aged AMZIRC
Z: solution annealed plus aged MZC
C: pure copper
H: copper injected with 45 appm H
E: copper injected with 45 appm He

(a) annealed prior to irradiation
(b) irradiated with 14-MeV Ni ions
(c) 4 dpa at peak

References for Chapter VI

1. Interim Publications on AMZIRC and AMAX-MZC Copper Alloys, distributed by AMAX Base Metals Research & Development, Inc., 400 Middlesex Ave., Carteret, NJ 07008 (received 1982).

2. Metals Handbook, Vol. 2, "Properties and Section: Nonferrous Alloys and Pure Metals," and Vol. 8, "Metallography, Structures and Phase Diagrams," 8th Ed., American Soc. Metals, Metals Park, OH.

3. H.W. King, J. Mater. Sci. 1 (1966) 79-90.

4. M.J. Donachie, J. Inst. Metals 92 (1964) 180.

5. G. Hillmann and W. Hoffmann, Z. Metallkunde 56 (1965) 279.

6. L. Meny et al., J. Microscop. 6 (1967) 111.

7. A.J. Perry and W. Hugi, J. Inst. Metals 100 (1972) 378.

8. J.M. Vitek, Z. Metallkunde 67 (1976) 559.

9. G.M. Kuznetsov et al., Sov. Non-Ferrous Met. Res. 6 (No. 6) (1978) 267-8.

10. V.A. Phillips, Metallogr. 7 (1974) 137.

11. M.Y-W. Lou and N.J. Grant, Met. Trans. 15A (1984) 1491.

12. G.M. Fedorov et al., Met. Sci. and Heat Treatment 20 (1978) 1025-6.

13. T. Nai-Yong, "High Temperature Deformation and Fracture of Cu-Cr Type Alloys," Ph.D. Thesis, University of Waterloo (1983).

14. P. Forey et al., C.R. Acad. Sci. Paris, Series C 291 (1980) 177.

15. I. Kawakatsu et al., J. Jap. Inst. Metals 31 (1967) 1253-7.

16. L. Bsenko, J. Less-Common Metals 40 (1975) 365.

17. J-P. Gabathuler et al., Acta Cryst. 31 (1975) 608.

18. T. Maruta, J. Jap. Copper and Brass Res. Assn. 2 (No 1) (1963) 89-96.

19. M. Kanno and H. Suzuki, J. Jap. Copper and Brass Res. Assn. 11 (No. 1) (1972) 88-94.

20. M.V. Zakharov et al., Metallov. i. Obrab. Metallov. (Metallography and Processing of Metals) 3 (1956) 23-27.

21. V.N. Fedorov et al., Russ. J. Phys. Chem. 46 (No. 1) (1972) 103-4.

22. G.M. Kuznetsov et al., Sov. Non-Ferrous Met. Res. 8 (No. 4) (1980) 391-3.

23. G.M. Kuznetsov et al., Sov. Non-Ferrous Met. Res. 10 (No. 6) (1982) 465-8.

24. H.V. Smith and R.G. Lott, Nucl. Instr. Methods 143 (1977) 125.

25. R.W. Knoll, Ph.D. Thesis, Nuclear Engineering Dept., University of Wisconsin-Madison (1981).

26. J.H. Billen and H.T. Richards, Proc. Symp. Northeastern Accel. Personnel, CONF-781051, Oak Ridge, TN (Oct. 1978), p. 137.

27. J.H. Billen, IEEE Trans. Nucl. Science NS-28 (1981) 1535-9.

28. A.R. Graviano, AMAX Base Metals Research & Development Co., Carteret, NJ (private communication, 1983).

29. ASTM B193-78, "Standard Method of Test for Resistivity of Electrical Conductor Materials," 1983 Annual Book of ASTM Standards, Vol. 2.01, Copper and Copper Alloys.

30. N.F. Panayotou, "Design and Use of Nonstandard Tensile Specimens for Irradiated Materials Testing," Symp. on Use of Nonstandard Subsized Specimens for Irradiated Testing, Albuquerque, NM, Sept. 1983, to be published by ASTM.

31. N.F. Panayotou, HEDL, private communication (Sept. 1983). Dimensional measurements were made by A.E. Bair (summer student at HEDL).

32. Computer code written by H.L. Heinisch (HEDL).

33. R.A. Spurling and C.G. Rhodes, J. Nucl. Mater. 44 (1972) 341-4.

34. J.B. Whitley, Ph.D. Thesis, Nuclear Engr. Dept., University of Wisconsin-Madison (Aug. 1978).

35. D.B. Bullen, Ph.D. Thesis, Nuclear Engineering Dept., University of Wisconsin-Madison (May 1984).

36. S.J. Zinkle and R.L. Sindelar, "Preparation of Ion-Irradiated Foils for Cross-Section Analysis," DAFS Quarterly Progress Report DOE/ER-0046/18 (Aug. 1984), pp. 133-141.

37. P.B. Hirsch et al., Electron Microscopy of Thin Crystals, (Krieger Publ. Co., 1977).

CHAPTER VII. EXPERIMENTAL RESULTS

VII.A. Microstructures and Properties of As-Received Copper Alloys

VII.A.1 As-Received Microstructure

Figure 7.1 shows optical micrographs of AMZIRC and AMAX-MZC in the cold-worked plus aged (CWA) and solution annealed plus aged (SAA) conditions. The CWA microstructures are typical of a heavily cold-worked material; the rolling direction is easily discernible. A coarse ($\lesssim$ 5 μm), randomly distributed precipitate is visible in the matrix of both alloys. Microchemical analysis using energy dispersive x-ray spectroscopy (EDS) on a scanning electron microscope indicates that these particles are Zr-rich. The microstructure of the SAA alloys consisted of large grains, and a lower density of the large precipitates compared to the CWA case. The SAA alloy grain sizes were 80 μm and 26 μm for AMZIRC and MZC, respectively.

Part of the CWA alloy stock was annealed in evacuated quartz tubes for 100 hours at a temperature of 950 ± 20°C. At the end of the solution anneal, evidence of partial melting was observed in the bottom of the MZC capsule. No evidence of melting was evident in the AMZIRC capsule that was simultaneously annealed with the MZC specimens. The eutectic melting temperature of AMZIRC (Cu-0.15% Zr) is 966°C.[1] This indicates the melting temperature of the quaternary MZC alloy (Cu-Cr-Zr-Mg) is below that of the binary AMZIRC alloy by $\lesssim$ 15°C.

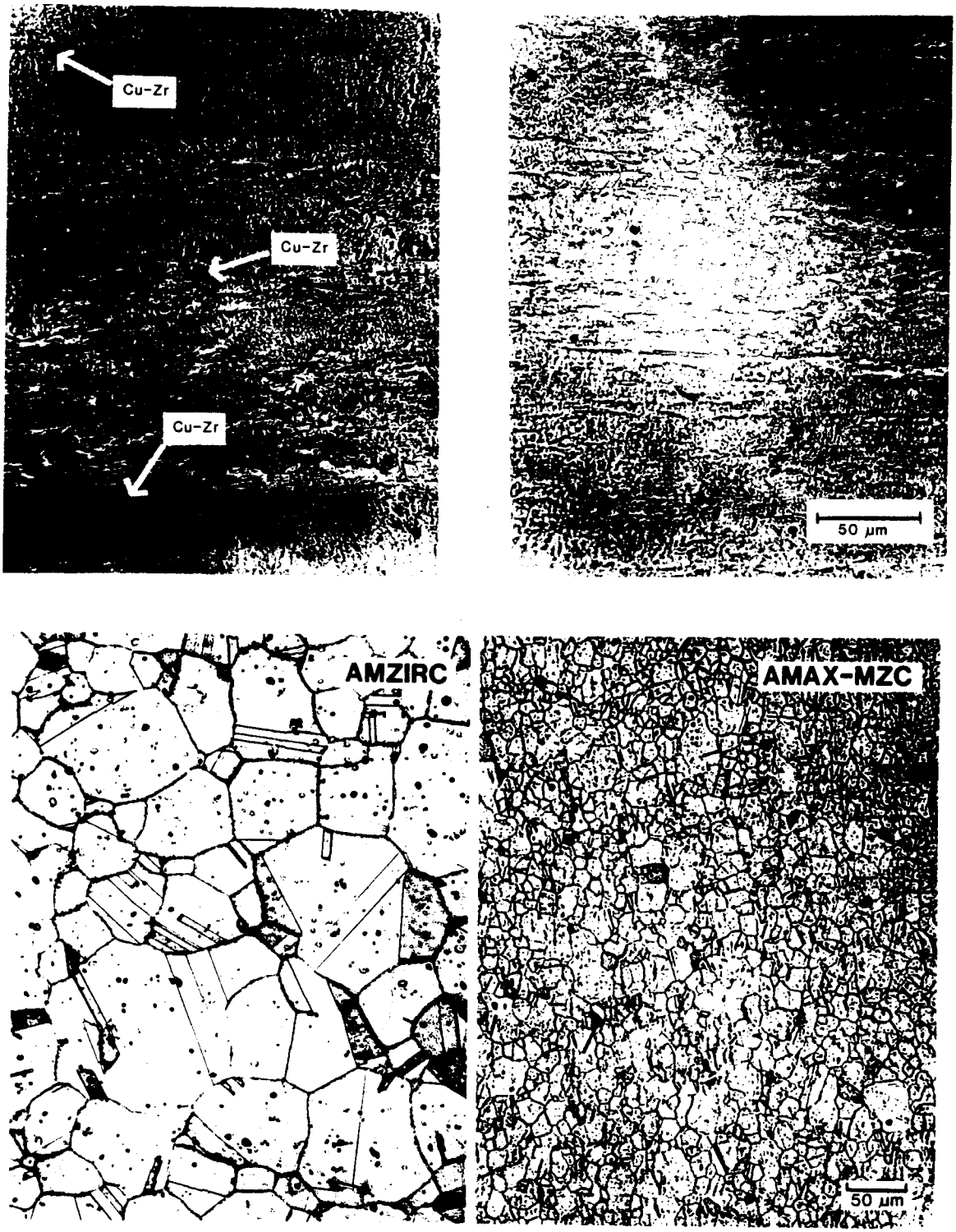

Fig. 7.1. Optical microstructure of cold-worked plus aged (top) and solution annealed plus aged (bottom) copper alloys.

Optical and SEM examination of the solution annealed MZC specimens revealed an interesting microstructure (see Fig. 7.2). Large faceted Cr-rich particles were observed on the surface of the annealed specimens. Mechanically polishing of the surface removed these particles, and none were observed in the interior depths of the foils. It seems likely that these particles may be chromium oxide precipitates. One possible sequence describing their formation is as follows: Chromium is surface-active and readily goes to the surface, creating a precipitate-free zone in the near-surface region. Chromium from the matrix interior migrates to the near-surface region in order to maintain a uniform concentration profile. These solute atoms are also attracted to the surface, creating a "syphon" effect. The chromium at the surface can react with the residual oxygen in the quartz tube to form chromium oxide. The occurrence of these Cr-rich particles indicates that chromium levels in excess of the solute solubility limit at the alloy melting point (0.65% Cr) are present in MZC. Therefore, the alloy could be manufactured with a lower Cr content and still maintain the same precipitation-hardening characteristics.

Figure 7.3 displays optical micrographs of the cold-worked plus aged (CWA) alloys as viewed in cross-section. Once again the rolling direction is evident. Coarse precipitates are visible in both alloys, with AMZIRC having the higher density of the two. Representative TEM micrographs of AMZIRC and AMAX-MZC are presented in Fig. 7.4 at two different magnifications. The microstructure is similar for

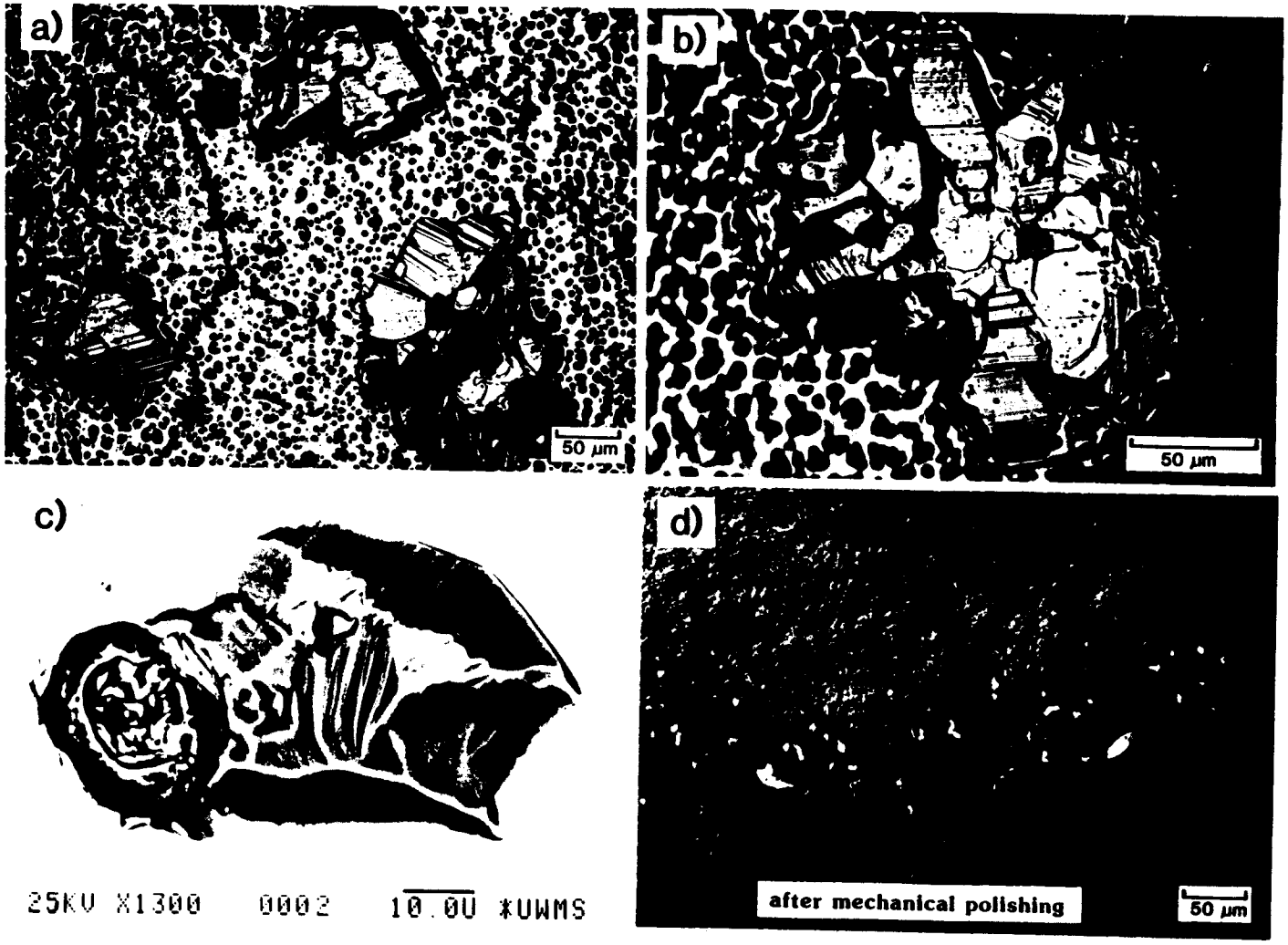

Fig. 7.2. Chromium rich particles on the surface of annealed MZC: Optical (a,b) and SEM (c) micrographs showing large size and faceted surface. Photo (d) shows the annealed foil after a short mechanical polish has removed some of the surface.

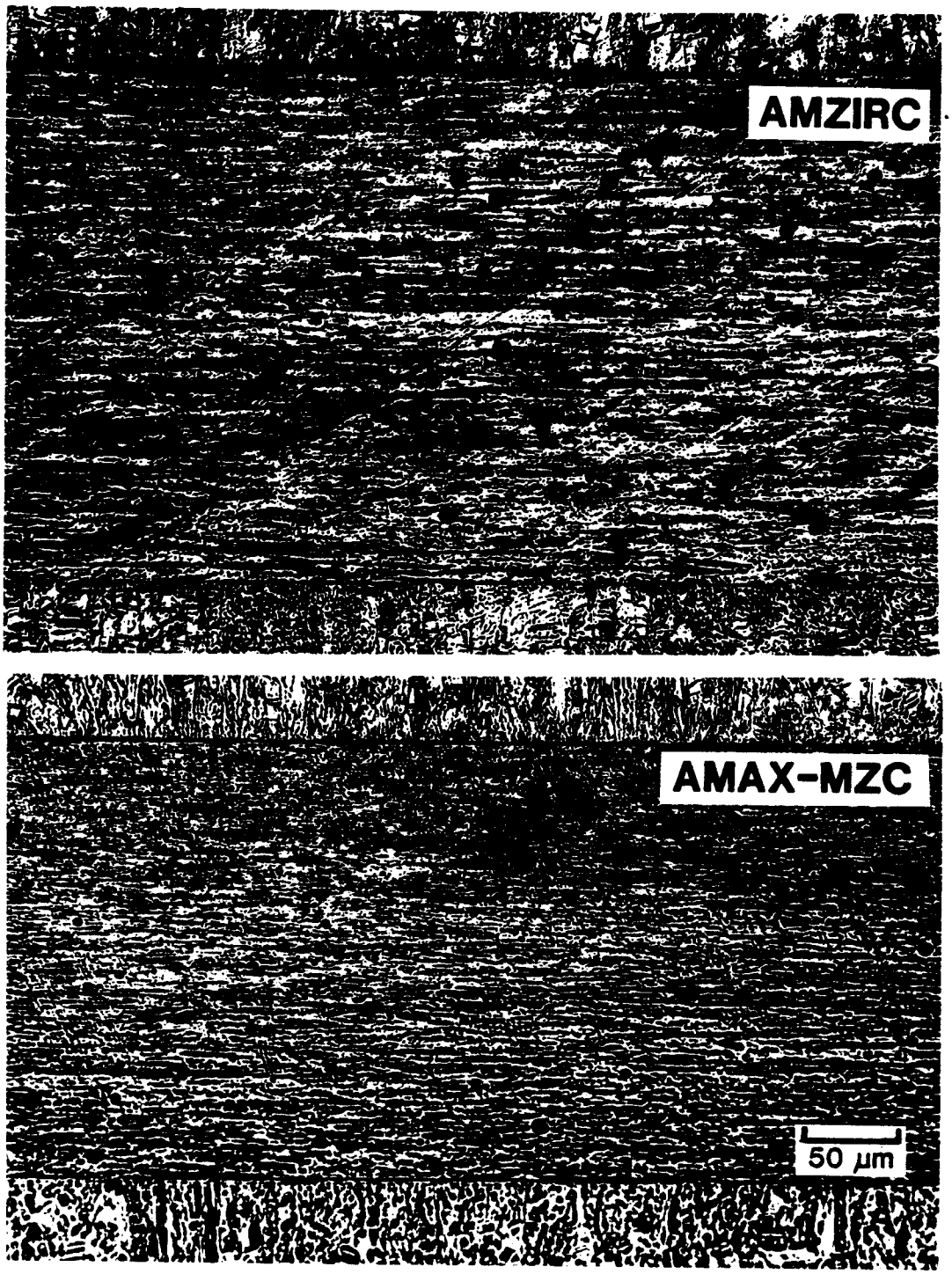

Fig. 7.3. Optical microstructure of cross-sectioned alloys.

GENERAL MICROSTRUCTURE OF AS-RECEIVED COPPER ALLOYS

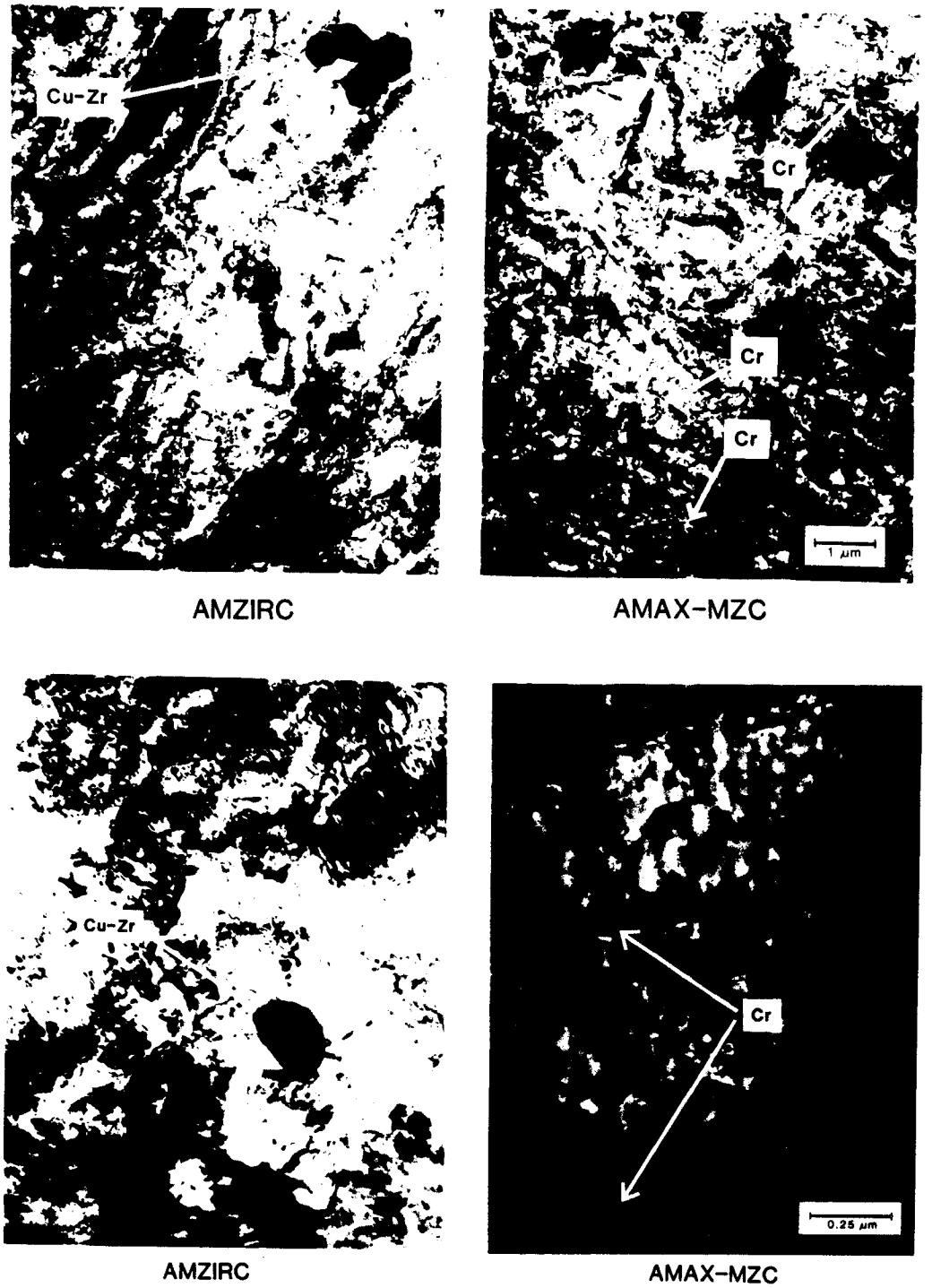

Fig. 7.4 TEM microstructure of cold-worked plus aged copper alloys at low (top) and medium (bottom) magnifications.

both alloys -- a high degree of work hardening is evident from the high dislocation density. The AMZIRC alloy contains a relatively coarse precipitate of diameter 0.1 to 5 μm and density $\lesssim 10^{18}/m^3$. These particles have been identified as pure zirconium by using a combination of EDS and microdiffraction techniques. The AMAX-MZC alloy contains a somewhat lower density of these Zr particles and has in addition a low density ($\gtrsim 10^{18}/m^3$) of large pure chromium precipitates. These Cr precipitates range in size from 0.1 to 1 μm. Examples of the Zr and Cr precipitates are visible in Fig. 7.4.

Chromium is readily electropolished in the HNO_3/CH_3OH solution used to thin the copper alloys for examination in the electron microscope. Therefore, the chromium particles are relatively transparent compared to the matrix unless they are oriented in a strongly diffracting condition. Zirconium is not easily electropolished in the copper polishing solution and generally appears as a black precipitate in the microscope due to its large thickness. The top micrograph in Fig. 7.5 shows a typical example of this behavior in solution annealed plus aged AMAX-MZC. The bottom left micrograph gives an example of a very large zirconium particle observed in CWA AMZIRC following thermal annealing. The bottom right micrograph shows a string of large Zr precipitates that are elongated in the rolling direction of the foil. The large size of the Cr and Zr precipitates (> 0.1 μm) observed in the AMZIRC and MZC alloys precludes the possibility that they were formed during the short aging treatment. It appears that these alloys were not completely homogenized during

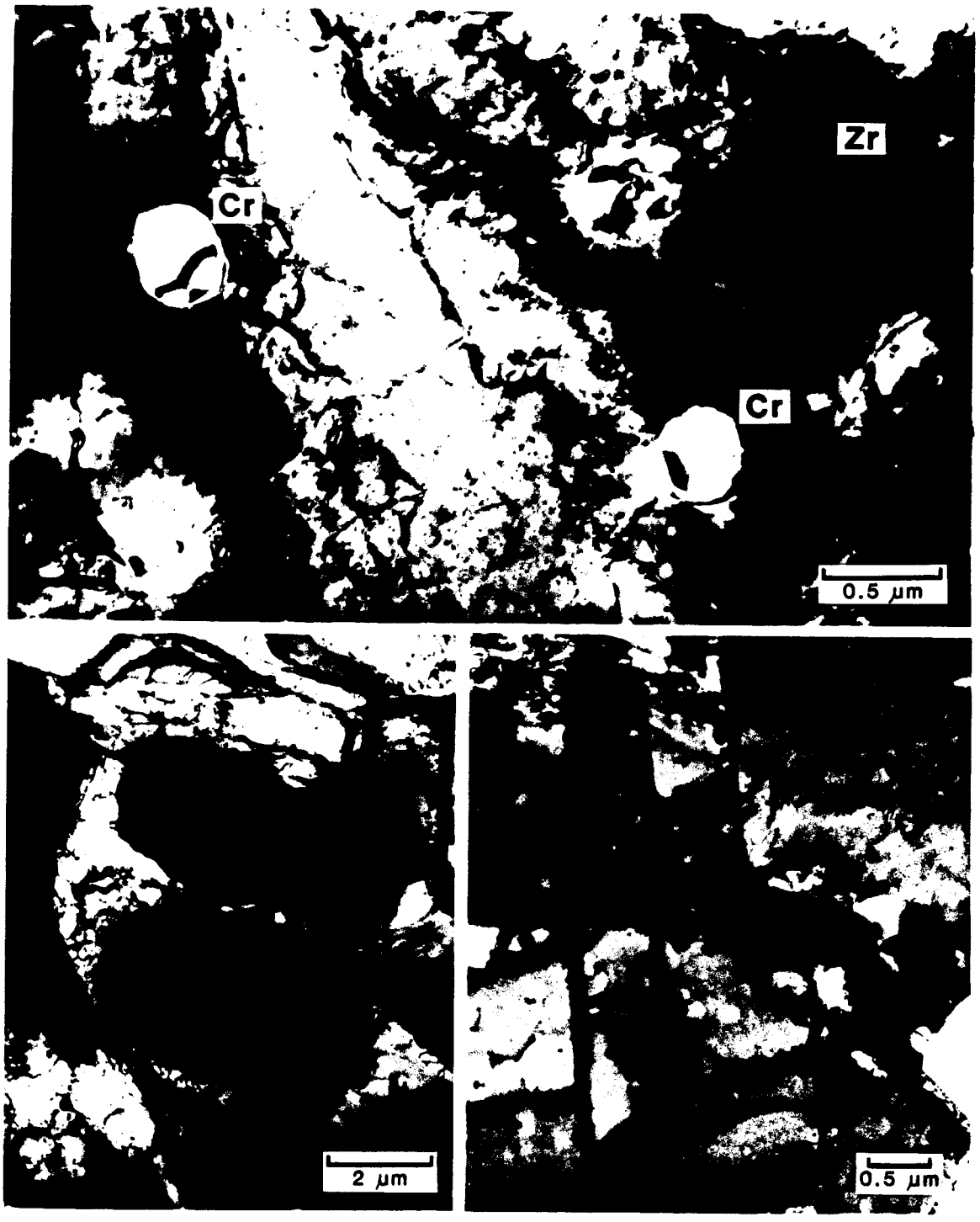

Fig. 7.5. Zr and Cr particles in solution annealed plus aged copper alloys

their fabrication. Since these large precipitates are not related to the precipitates formed during the aging treatment and they do not have any substantial effect on the physical properties, they were generally avoided when "representative" micrographs of the alloys were taken.

Figure 7.6 shows the TEM microstructures of CWA AMZIRC and AMAX-MZC as seen in cross-section before and after thermal annealing. The as-received microstructure has a pronounced texture in the rolling direction consisting of elongated subgrains. Microdiffraction analysis indicated that the boundaries between subgrains are large angle boundaries in the direction perpendicular to the rolling direction. On the other hand, small angle grain boundaries ($\lesssim 5°$ tilt angle) were commonly observed in the longitudinal direction. The large angle grain boundaries provided preferential sites for heterogeneous nucleation of precipitates during the aging treatment which followed the cold-working. This phenomenon was best observed by annealing the CWA foils and then examining the microstructure in cross-section, as shown in the right-hand side of Fig. 7.6. Precipitate "stringers" are visible with a distribution geometry that matches the cold-worked subgrain structure. The MZC alloy also has a homogeneous distribution of small precipitates. The heterogeneous precipitation on subgrain boundaries tends to stabilize the subgrain structure and raise the alloy recrystallization temperature.[2] Cold-working of the copper alloys appeared to give rise to a preferred texture -- the subgrains were generally oriented so that their (110) normal was

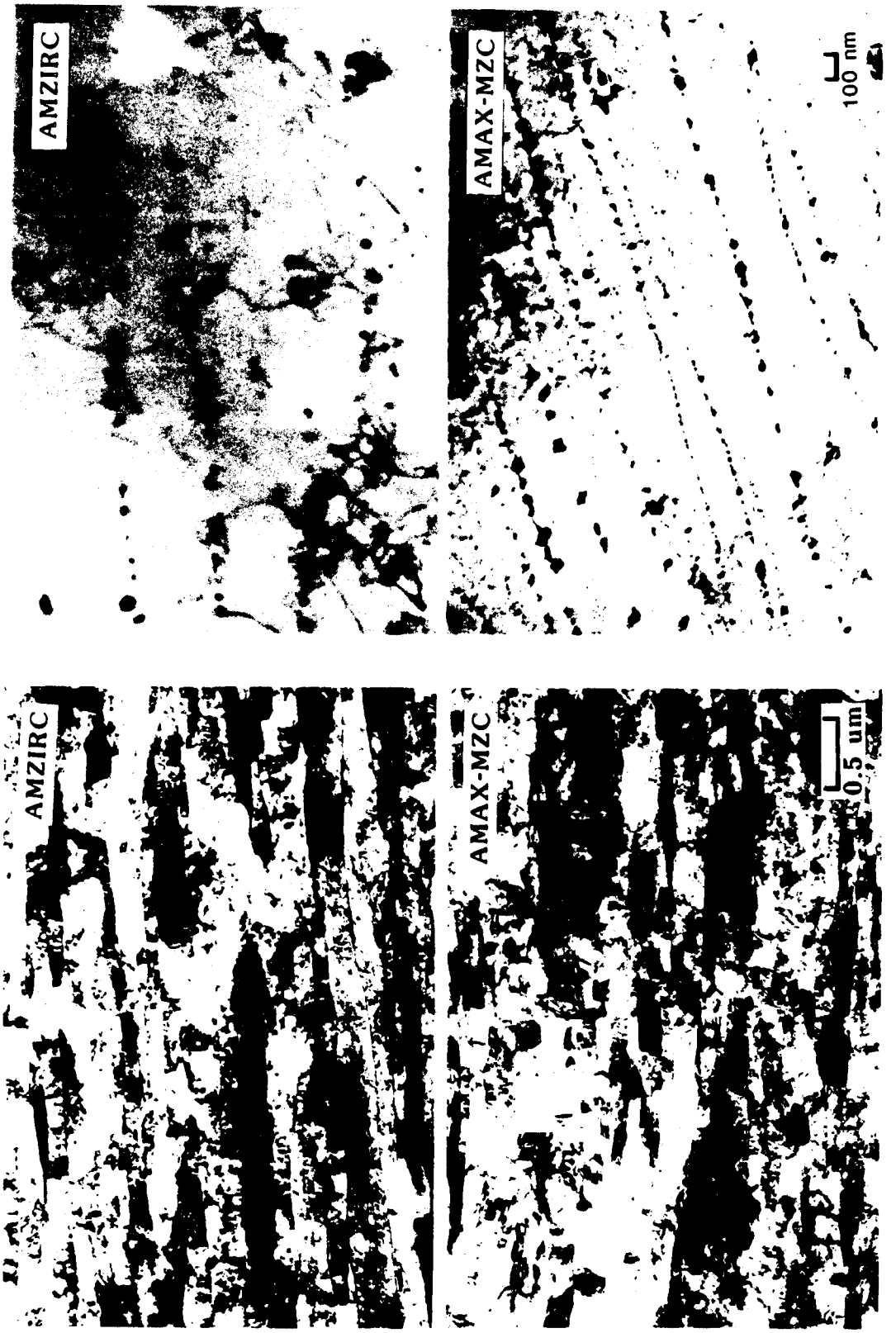

Fig. 7.6. TEM cross-section microstructure of cold-worked plus aged alloys before (left) and after (right) annealing.

close to perpendicular to the cold-rolled foil surface. This type of texture has been commonly observed in cold-rolled copper alloys.[3,4]

Figure 7.7 shows the microstructures of AMZIRC and AMAX-MZC in the solution annealed plus aged (SAA) condition. The precipitates in AMZIRC are incoherent and tend to be heterogeneously distributed along grain boundaries, as shown in Fig. 7.7. Previous researchers have reported similar observations (see Section IV.A). The grain boundary precipitate size ranges from 10 to 50 nm. The dominant microstructural feature in aged AMAX-MZC is a high density of Cr precipitates that are uniformly distributed throughout the matrix. These precipitates have an average diameter of 6 nm and a density of $\sim 4 \times 10^{21}/m^3$. The resultant visible Cr precipitate volume fraction is $\sim 5 \times 10^{-4}$, which is much less than the chromium solute concentration of 8×10^{-3}. Therefore, most of the chromium is apparently contained in solution or in submicroscopic clusters following a 1 hour aging of AMAX-MZC at 500°C. As discussed later (Section VII.A.2), electrical resistivity measurements indicate a similar conclusion.

Although the precipitate in aged AMZIRC tends to preferentially form at heterogeneous sites, there is also an appreciable density of these incoherent precipitates in the matrix (see Fig. 7.8). The distribution appears to be bimodal; there is a large-sized population with a 10 nm average diameter and $1 \times 10^{21}/m^3$ density that is superimposed on a small-sized precipitate distribution of average diameter $d = 4$ nm and density $n \gtrsim 4 \times 10^{22}/m^3$. AMAX-MZC contains a similar

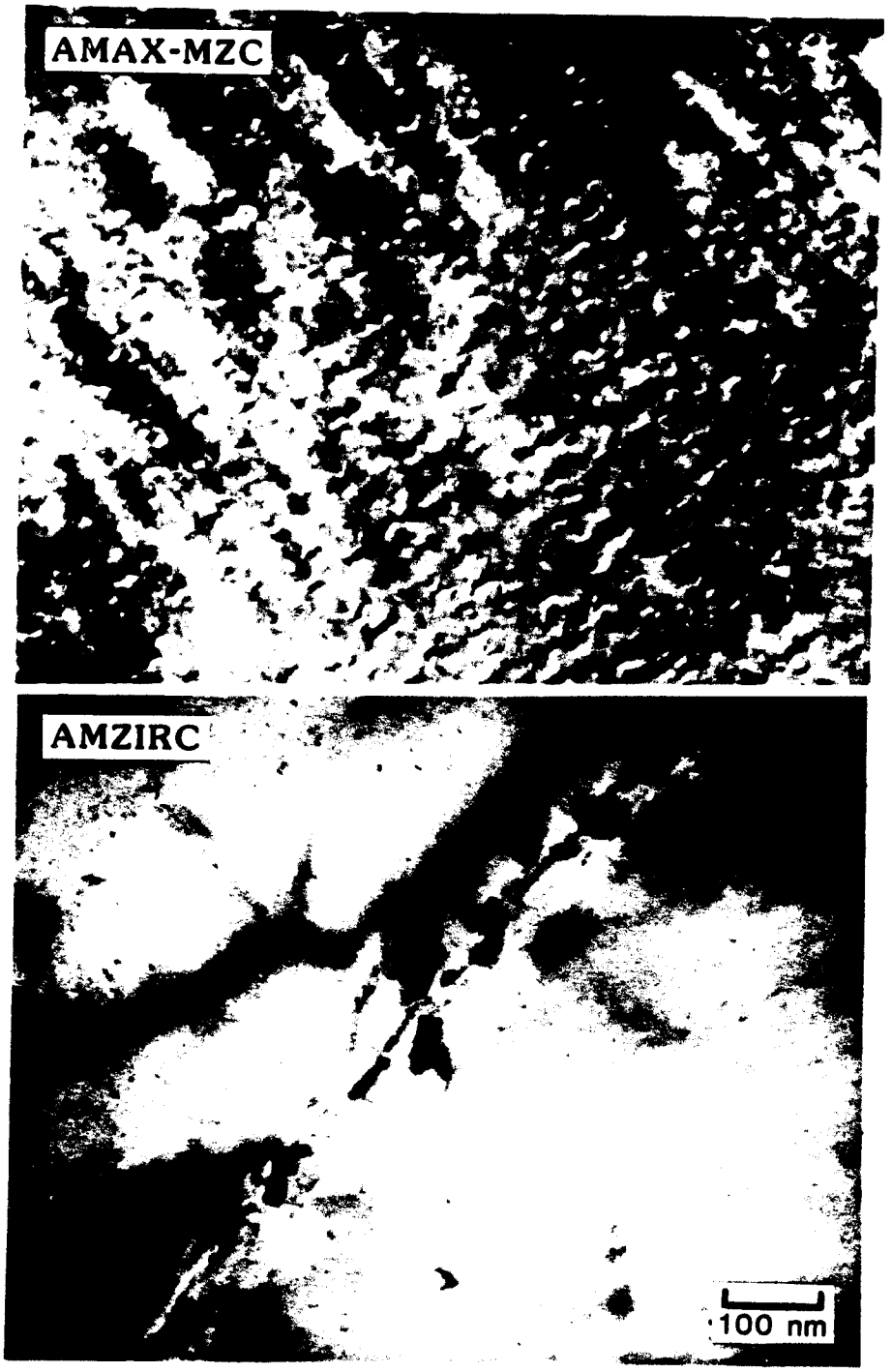

Fig. 7.7. Precipitates in solution annealed plus aged copper alloys. Top: Coherent Cr precipitates; Bottom: Cu_5Zr precipitates on a grain boundary.

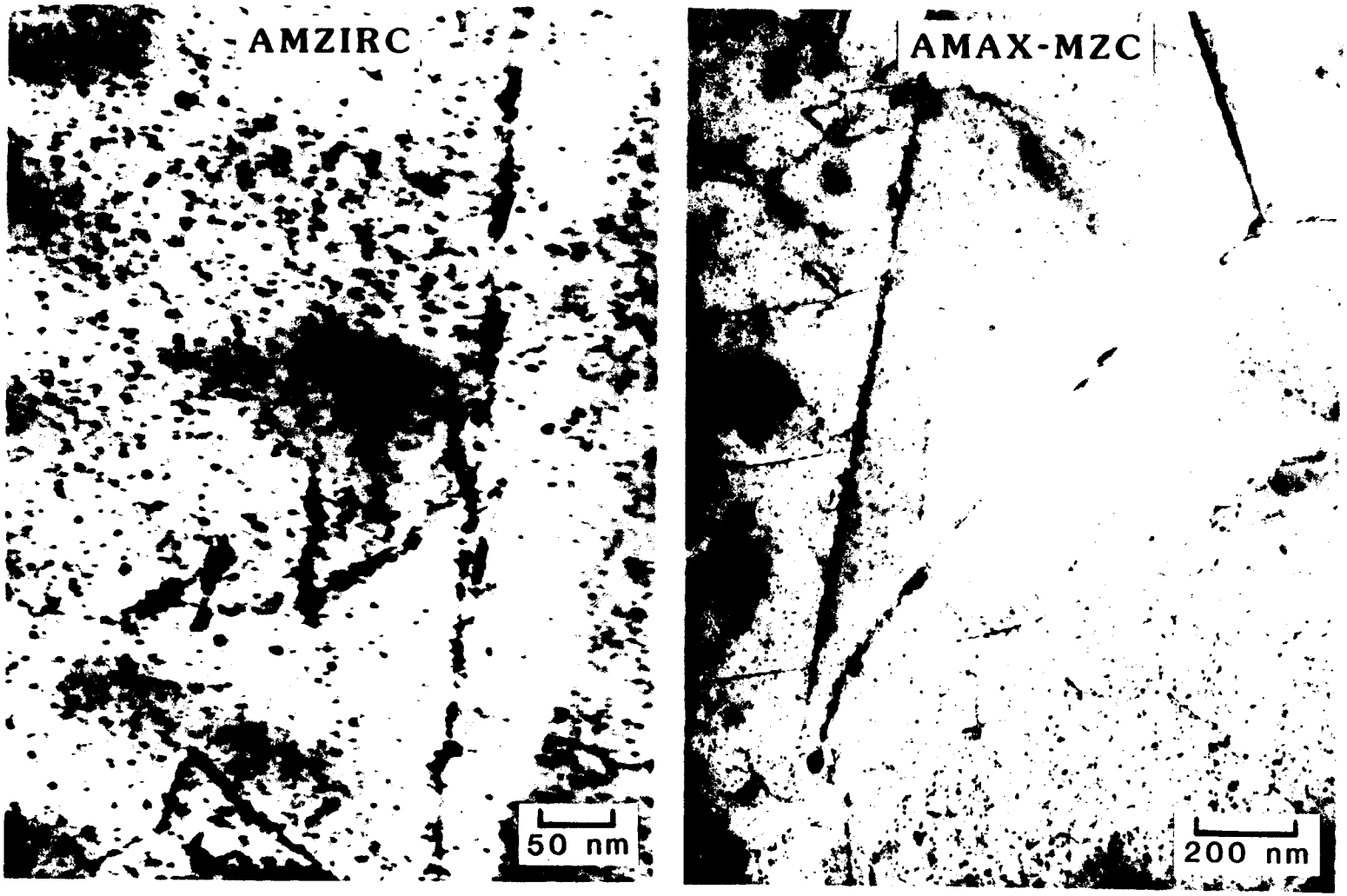

Fig. 7.8. Grain boundary and matrix precipitates in aged copper alloys.

distribution of incoherent precipitates along its grain boundaries and in the matrix. These incoherent Cu-Zr precipitates are apparently Cu_5Zr (see Section VI.A).

TEM tilting experiments indicate that the morphology of the Cu_5Zr matrix precipitate is disk-shaped. The habit plane of this precipitate was determined using methods outlined by Edington.[5] As shown in Fig. 7.9, the Cu_5Zr platelet habit plane appears to coincide with the {111} matrix plane. This is in agreement with a previous study of Cu_5Zr precipitates by Phillips.[41] The visible Cr precipitates in aged AMAX-MZC have a semi-coherent precipitate-matrix interface (see Fig. 7.9). This is evident from the characteristic black-white coherency strain contrast that is parallel to the diffraction vector, g.[6]

VII.A.2 Physical Properties of As-Received Alloys

Table 7.1 summarizes the measured physical properties of AMZIRC and AMAX-MZC in the solution annealed (SA), solution annealed plus aged (SAA) and cold-worked plus aged (CWA) conditions. AMZIRC has the higher electrical conductivity of the two for all thermomechanical treatments while AMAX-MZC has the higher strength. There was no difference in the tensile properties as measured in the transverse and longitudinal directions for the AMZIRC alloy. The AMAX-MZC alloy exhibited a 10% larger yield strength in the transverse direction compared to the longitudinal direction for both the CWA and the SAA conditions. This finding is in agreement with studies on other cold-rolled copper alloys that have a similar texture.[3] The values in

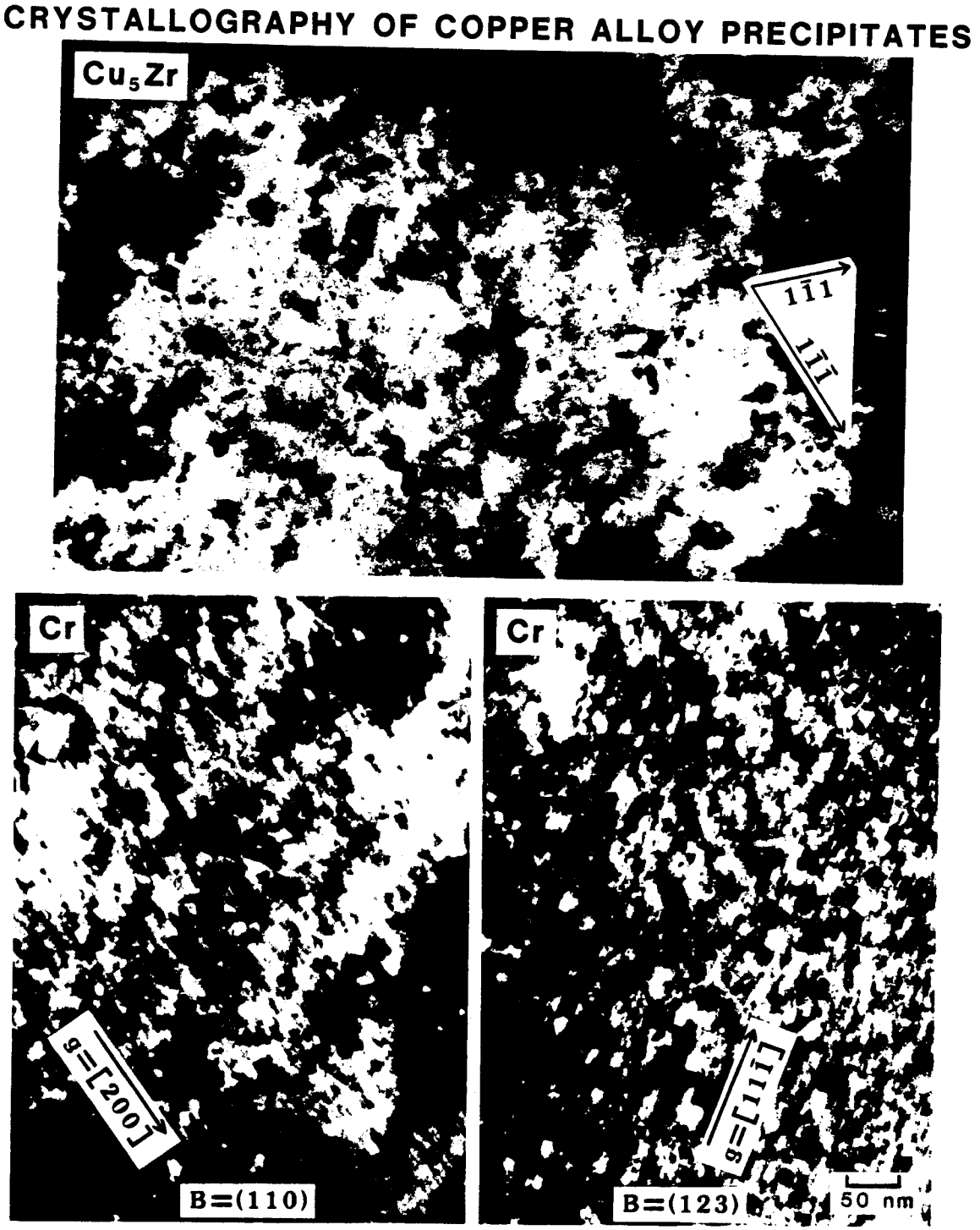

Fig. 7.9. Crystallography of copper alloy precipitates (see text).

Table 7.1. Measured Physical Properties at 20°C

Alloy	Heat Treatment	Grain Size	Microhardness	Yield Strength (0.2% Offset)	Tensile Strength	Elongation in 5.1 mm	Electrical Conductivity
AMZIRC	SA	300 μm	50 HV	110 MPa	150 MPa	21%	---
	SAA	80 μm	51 HV	140 MPa	200 MPa	27%	75% IACS
	CWA	0.4 μm	150 HV	440 MPa	500 MPa	9%	76% IACS
	SAA*	300 μm	48 HV	---	---	---	---
MZC	SA	270 μm	46 HV	92 MPa	120 MPa	14%	---
	SAA	26 μm	78 HV	220 MPa	260 MPa	23%	53% IACS
	CWA	0.4 μm	170 HV	490 MPa	540 MPa	9%	59% IACS
	SAA*	270 μm	84 HV	---	---	---	---

SA: solution annealed (water quench)

SAA: solution annealed, then aged 1 hour at 450°C for AMZIRC and 500°C for MZC

CWA: 90% cold-worked, then aged 0.5 hours at 375°C for AMZIRC and 400°C for MZC

SAA*: UW Treatment; solution annealed then aged 1 hour at 470°C

Table 7.1 represent the average of the two measured orientations. The miniature tensile test results for the CWA alloys are slightly lower than values measured by the manufacturer on the same lot of materials -- tensile tests performed by AMAX Copper Inc. indicated that both alloys had yield strengths in excess of 500 MPa.[7] Electrical conductivity tests were not performed by the manufacturer.

The AMZIRC alloy develops its high strength only after cold-work plus aging, and it shows minimal precipitation hardening (compare SA, SAA microhardness and yield strengths in Table 7.1). AMAX-MZC exhibits an appreciable amount of precipitation hardening, but once again most of its strength in the CWA condition can be attributed to cold-work effects. These findings are in good agreement with previous observations on Cu-Zr, Cu-Cr and Cu-Cr-Zr type alloys (see literature review in Section IV.A). The elongation to fracture is on the order of 20-30% for the SA and SAA alloys. The fracture elongation drops to 9% for both AMZIRC and AMAX-MZC in the CWA condition due to their high cold-work level (90%) prior to aging.

The measured ductility of the SA alloys was less than that of the SAA alloys. This behavior is contrary to the expected trend since ductility generally decreases when strength increases.[8] The relatively low ductility of the SA alloys is probably due to grain size effects -- ductility is known to decrease with increasing grain size,[8] and the SAA alloys have a much smaller grain size than the SA alloys due to the different solution annealing treatments (Table 7.1). The anomalous behavior may also be caused by the use of mini-

ature tensile specimens. A common rule-of-thumb is that at least 10 grains across the smallest cross-sectional dimension of a tensile specimen are required to obtain bulk behavior.[9] Researchers have found that there is no grain size effect on the measured yield or tensile strength for miniature tensile specimens of austenitic or ferritic steel as long as the minimum specimen thickness to grain size ratio (t/d) is greater than ~ 4.[9,10] Therefore, the minimum tensile specimen results should be valid except for SA alloy condition (t/d ~ 1) and possibly AMZIRC in the SAA condition (t/d ~ 3).

Figure 7.10 shows representative load-elongation curves for the two copper alloys in the CWA and SAA condition. There is little or no work-hardening mechanisms present in the CWA alloys. On the other hand, substantial work-hardening occurs in the SAA alloys during plastic deformation. The yield strength of the CWA alloys is more than twice as high as for the SAA alloys. However, it is interesting to note that the toughness (defined as the area contained under the stress-strain curve) is greater for the SAA alloys than for the CWA alloys.

Examination of Table 7.1 reveals that cold-working prior to aging has no effect on the electrical conductivity, but it leads to a two-fold increase in the yield strength of AMZIRC and AMAX-MZC. This finding is in good agreement with previous studies on Cu-Zr and Cu-Cr-Zr alloys[11,12] (also see references in Section IV.A). This is an indication that the electrical resistivity is not affected by the dislocations and subgrains present in these alloys from their cold-

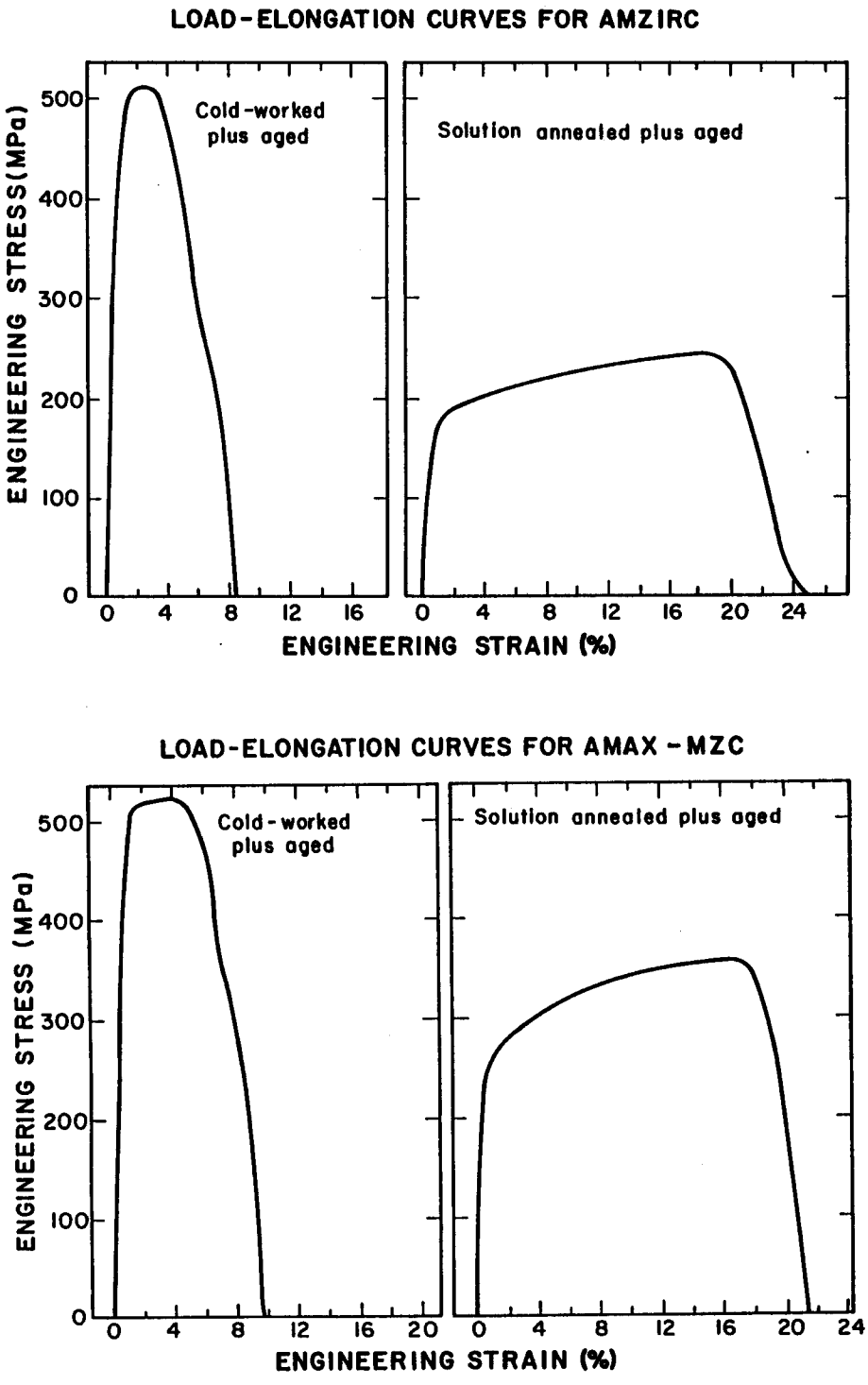

Fig. 7.10. Load-elongation curves for the copper alloys.

working prior to aging. Therefore, the electrical conductivity is primarily limited by the solute resistivity contributions in solution or in the form of precipitates. Table 7.2 lists the measured electrical properties of AMZIRC and AMAX-MZC in the SAA and CWA conditions. The measured residual resistivity ratio (RRR) is larger for the CWA condition as compared to the SAA condition. This once again indicates that the dislocations present in the CWA alloys have a negligible effect on the electrical resistivity. The room temperature conductivity at AMZIRC is about 40% larger than that of AMAX-MZC for both heat treatment conditions.

The measured electrical resistivity may be compared with the theoretical value for dilute alloys by invoking appropriate assumptions. This allows a determination to be made as to which microstructural feature has the dominant effect on the measured resistivity. Four components of the alloy resistivity may be identified: grain boundaries, dislocations, solute atoms and precipitates. Reasonably accurate theoretical estimates can be made for the resistivity contributions of the first three components. The effect of small precipitates on the electrical resistivity is difficult to determine due to parametric uncertainties.[13]

The specific resistivity of grain boundaries in copper has been reported to range from 1×10^{-16} Ω-m^2 to 3.1×10^{-16} Ω-m^2.[15] Fickett[16] reported that a value of about 1.6×10^{-16} Ω-m^2 gave the best results for his data. Analysis of the resistivity data from the control samples of a 14-MeV neutron irradiation experiment by this

Table 7.2. Measured Electrical Properties of AMZIRC and AMAX-MZC

Alloy	Heat Treatment	Resistivity (nΩ-m) 296 K	77 K	4.2 K	RRR = ρ 296/ρ 4.2	Conductivity (20°C)
AMZIRC	SAA	23.4 ± 0.2	8.3 ± 0.2	5.9 ± 0.1	4.0	75% IACS*
	CWA	22.9 ± 0.8	6.8 ± 0.6	4.0 ± 0.3	5.7	76% IACS
MZC	SAA	33.0 ± 0.6	18.7 ± 0.9	18.3 ± 0.9	1.8	53% IACS
	CWA	29.4 ± 0.6	14.4 ± 0.8	13.5 ± 0.8	2.2	59% IACS

SAA = solution annealed plus aged, CWA = cold-worked plus aged

*IACS = International Annealed Copper Standard, 100% IACS = 17.241 nΩ-m[29]

Table 7.3. Calculated Resistivity Contributions at 4.2 K from Various Defects in Copper Alloys

Alloy	Calculated Resistivity Contribution (nΩ-m) Grain Bound.	Disln.	Cr	Zr	Mg	Cr ppt.	Cu_5Zr	Total
SAA AMZIRC	0.01	0	---	1.6	---	---	1.2	2.8
CWA AMZIRC	< 1.4	0.26	---	1.3	---	---	1.2	< 4.2
SAA MZC	0.02	0	< 30	1.75	1.0	$\gtrsim$ 0.07	1.2	< 32.5
CWA MZC	< 1.4	0.26	< 30	1.4	1.0	0.1	1.2	< 35

author[17] yields a grain boundary specific resistivity of 2.1 x 10^{-16} Ω-m^2. A value of 2 x 10^{-16} Ω-m^2 was used for the calculations that follow. The specific resistivity of dislocations in copper[18] is equal to 1.3 x 10^{-25} Ω-m^3. The measured dislocation density ranged from ~ $10^{12}/m^2$ for the SAA alloys to ~ 2 x $10^{15}/m^2$ for the CWA alloys.

The specific resistivities of the solute atoms contained in AMZIRC and AMAX-MZC have been measured to be ρ_{Cr} = 40 nΩ-m/at.% (Refs. 19-21), ρ_{Mg} = 10 nΩ-m/at.% (Refs. 19,20) and ρ_{Zr} = 100 nΩ-m/at.% (Refs. 20,22). The equilibrium solute concentrations of Cr, Mg and Zr in copper were determined from solubility data given in Refs. 23-25, respectively. The solubility of Mg in copper is fairly high, so that all of the Mg present in MZC (0.1 at.%) should remain in solution. Analysis of the TEM data given in Section VII.A.1 indicates that most of the Cr in aged AMAX-MZC is contained in submicroscopic clusters. Simple diffusion calculations indicate that the Cr solute mobility[26] is not sufficient at the aging temperatures of 375-500°C for equilibrium to be reached during the aging time of 0.5 to 1 hour. For example, the Cr diffusion distance during the aging treatment for SAA AMAX-MZC is calculated to be $\sqrt{Dt}$ = 28 nm. This may be compared with the observed average chromium interparticle spacing of 63 nm. The aging treatment for CWA AMAX-MZC is even less ($\sqrt{Dt}$ = 1.3 nm). Therefore it appears that most of the Cr in AMAX-MZC may still be in solution or in small solute clusters following the aging treatment, especially when one takes into account the incubation time

required for precipitate nucleation. Zirconium, on the other hand, is a fast diffuser in copper ($\sqrt{Dt} \gtrsim 1$ μm in the present case) and its matrix concentration should correspond to the equilibrium value.

The contribution of the precipitates to the measured electrical resistivity of the copper alloys is difficult to estimate. The electrical resistivity of Cu_5Zr has apparently never been determined, but analysis of data contained in Refs. 22 and 27 indicates that it is on the order of 10 nΩ-m/at.% Zr (1.7 nΩ-m/at.% Cu_5Zr). The electrical resistivity of pure chromium[28] is 129 nΩ-m. Application of the multiphase resistivity rule[28] gives an estimate of the resistivity contribution of the precipitates. This approximation breaks down if the average distance between precipitates, $\bar{\ell}$, is less than or on the order of the electron mean free path,[13] λ. Unfortunately, this is the case for both the Cr and the Cu_5Zr precipitates that are being investigated here; $\bar{\ell}/\lambda \simeq 0.01$ and 0.2 for the Cr and Cu_5Zr precipitates, respectively (values determined from TEM measurements and equations given in Ref. 13). The multiphase resistivity calculation is nevertheless useful for obtaining a lower bound estimate of the precipitate resistivities.

Table 7.3 shows the calculated resistivity contributions from the various sources present in the copper alloys. Comparison with the measured resistivity values at 4.2 K (Table 7.2) indicates that there is fair agreement. The calculated resistivities of AMZIRC are close to the measured values for the two heat treatment conditions. The calculated residual resistivities of MZC are high by a factor of

two. This is apparently due to an overestimation of the resistivity contribution of the Cr solute -- some submicroscopic clustering of Cr atoms has probably occurred. From Table 7.3 it is evident that dislocations have a negligible effect on the total resistivity of the alloys. The effect of grain boundaries in the CWA alloys is predicted to be significant. For this calculation, the specific resistivity of subgrain boundaries was assumed to be the same as that for grain boundaries. Other researchers have claimed that low angle boundaries have a specific resistivity of $\lesssim$ 10% of the large angle grain boundaries.[15] This would result in an insignificant subgrain resistivity contribution in the CWA alloys. In summary, it appears that the electrical conductivity of AMZIRC and AMAX-MZC is primarily limited by the resistivity contributions of its precipitates and solute atoms.

The precipitates in AMZIRC in the SAA condition do not result in a large increase in strength as compared to the SA condition (see Table 7.1). The shear stress increase due to precipitates is given by[30,31]

$$\Delta\tau = \frac{Gb}{\beta}\sqrt{nd} \qquad (7.1)$$

where G is the shear modulus, b is the Burgers vector, and n and d are the precipitate density and average diameter. Beta (β) is a constant that ranges from 1.2 for a random array of incoherent precipitates to $\gtrsim$ 1.8 for small coherent precipitates.[31] An estimate of

the yield stress may be obtained by applying the Von Mises criterion, $\Delta\sigma_y = \sqrt{3}\ \Delta\tau$. Application to the measured heterogeneous precipitate parameters of SAA AMZIRC results in a predicted yield strength increase of 30 MPa for the aged alloy compared to the solution annealed alloy, in good agreement with the observed yield stress increase (30 MPa). The AMAX-MZC alloy contains both semi-coherent Cr precipitates and incoherent Cu_5Zr precipitates. The strengthening contributions of the different precipitates are combined in quadrature,[32] $\Delta\tau \sim \{(\Delta\tau_1)^2 + (\Delta\tau_2)^2\}^{1/2}$. The calculated strength increase for AMAX-MZC in the SAA condition is 80 MPa, which is less than the measured yield stress increase of 130 MPa (Table 7.1). The discrepancy may be due to hardening by submicroscopic Cr atom clusters which were not considered in the calculation.

VII.B. Effects of Thermal Annealing on Physical Properties

A thermal annealing study was initiated in order to investigate the microstructural stability of AMZIRC and AMAX-MZC in the cold-worked plus aged (CWA) condition. Vickers microhardness, electrical resistivity and miniature tensile tests were performed at room temperature on the CWA alloys following thermal annealing at temperatures of 150 to 600°C for anneal times ranging from 0.25 to 100 hours. Table 7.4 lists the data that was obtained from this study.

The Vickers microhardness and electrical conductivity of AMZIRC and AMAX-MZC are shown in Fig. 7.11 as a function of annealing temperature for a 1 hour anneal. The Vickers microhardness number (VHN) is constant for annealing temperatures $\leq$ 300°C. At higher

Table 7.4. Physical Properties of Cold-Worked Plus Aged Copper Alloys Versus Thermal Annealing Conditions

		20°C Properties Following Anneal for Indicated Time (hr)									
	Anneal	Vickers Microhardness (HV)				Yield Strength (MPa)			Electrical Conductivity (% IACS)		
Alloy	Temp.	0.25	1	10	100	0.25	1	10	0.25	1	10
AMZIRC	300	---	147	---	142	---	440	---	---	83	---
	350	---	148	142	131	---	409	387	---	90	85
	400	140	134	133	76	436	386	362	78	90	95
	450	132	122	82	57	394	337	232	77	95	97
	475	---	114	---	---	---	307	---	---	97	---
	500	121	61	55	---	369	184	151	81	100	106
	550	61	56	---	---	148	159	---	101	100	---
	600	---	49	---	---	---	138	---	---	88	---
MZC	300	---	168	---	165	---	460	---	---	58	---
	350	---	168	165	154	---	453	485	---	75	88
	400	161	158	146	99	445	424	414	73	80	86
	450	154	139	122	69	406	410	313	81	89	90
	475	---	144	---	---	---	360	---	---	86	---
	500	144	86	76	---	418	238	186	79	99	94
	550	81	77	---	---	209	190	---	87	90	---
	600	---	66	---	---	---	156	---	---	84	---

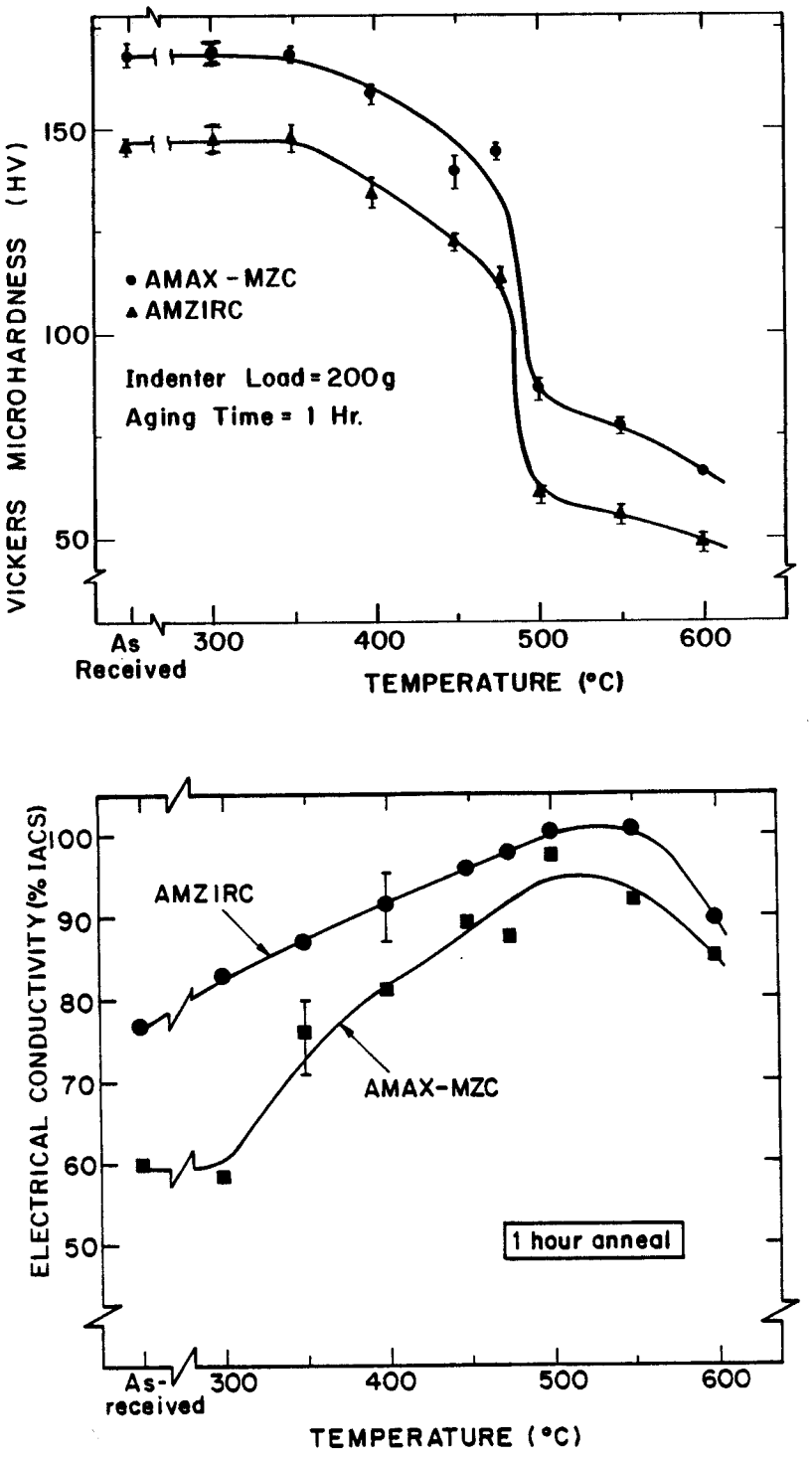

Fig. 7.11. Vickers microhardness and electrical conductivity at 20°C of the cold-worked plus aged copper alloys vs. anneal temperature.

temperatures, it first slowly decreases and then decreases rapidly at a temperature of 475°C. Thermal annealing at temperatures above 500°C causes a gradual decrease in VHN with increasing temperature. AMAX-MZC has a higher microhardness number than AMZIRC for all of the thermal annealing conditions. This is an indication that precipitation hardening effects are more pronounced in AMAX-MZC as compared to AMZIRC.

The general shape of the microhardness annealing curve is typical of that for cold-worked metals.[33] The sharp drop in VHN over a narrow temperature range is generally associated with recrystallization processes, whereas the gradual decrease in VHN at lower annealing temperatures corresponds to recovery processes. Figure 7.12 shows the TEM microstructure of the two alloys in the as-received and in two annealed conditions. Dislocation rearrangement and a general reduction in dislocation density is evident in the microstructures of both alloys following a 1 hour anneal at 450°C. This confirms that the 350 to 450°C annealing stage corresponds to recovery processes. Annealing for 1 hour at 500°C results in the formation of dislocation-free grains with high angle grain boundaries. This shows that recrystallization does indeed coincide with the rapid drop in VHN at 475°C. The important conclusion from this thermal anneal study is that both AMZIRC and AMAX-MZC lose their high strength upon recrystallization. Their strength after recrystallization approaches values typically found for annealed copper.

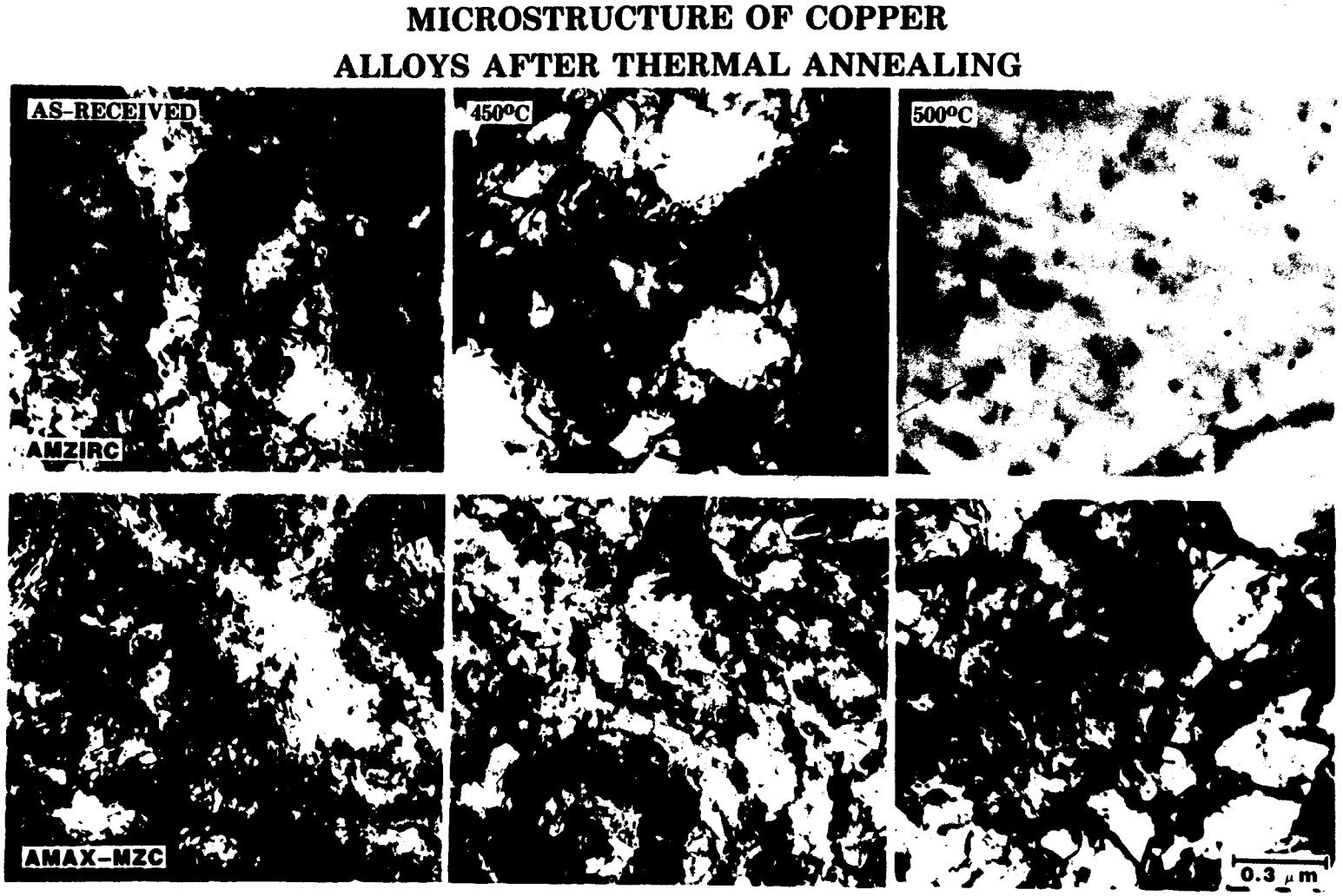

Fig. 7.12. Microstructure of the cold-worked plus aged copper alloys vs. anneal temperature (1 hour anneal).

The general form of the microhardness annealing curve is in good agreement with published results in the literature for Cu-Zr and Cu-Cr-Zr alloys (see Section IV.A for a review). It is well established that these alloys exhibit a large decrease in strength upon recrystallization from the cold-worked plus aged condition. The exact value of the recrystallization temperature for AMZIRC and AMAX-MZC appears to depend strongly on the prior thermomechanical history of the alloy. Various researchers have observed 1 hour recrystallization temperatures that are significantly lower[34] or higher[35,36] than the value of 475°C which was obtained in the present investigation.

The room temperature electrical conductivities of both AMZIRC and AMAX-MZC increase steadily following a 1 hour anneal at temperatures $\lesssim$ 550°C (Fig. 7.11). The maximum observed electrical conductivities were about 100% IACS and 95% IACS for AMZIRC and AMAX-MZC, respectively. Thermal annealing at temperatures above 550°C caused the conductivity to decrease from the maximum value. This effect has been previously observed in Cu-Zr and Cu-Cr-Zr alloys[35,37] and is probably due to solute reentering solution from the precipitates. The thermal annealing response of the electrical conductivity of AMZIRC and AMAX-MZC observed in this study is in fairly good agreement with results found in the literature (see Section IV.A). The curve of conductivity versus annealing temperature does not exhibit a well-defined "knee" such as was found in the microhardness measurements (Fig. 7.11). This variance in behavior occurs because micro-

hardness and resistivity measurements are sensitive to different microstructural features.[33]

In order to get a better estimation of the kinetics involved in the recovery and recrystallization processes in AMZIRC and AMAX-MZC, supplemental annealing studies were performed in conjunction with the 1 hour study (Table 7.4). Figure 7.13 displays the data obtained from microhardness, tensile and resistivity measurements of specimens annealed for times ranging from 0.25 to 100 hours. From the microhardness data, it is evident that the recrystallization temperature shifts to lower values for longer annealing times. The arrows in the microhardness annealing curves correspond to the VHN of the solution annealed alloys. Cold-worked plus aged AMZIRC that has recrystallized has a hardness that is similar to the solution annealed value. This indicates that no precipitation hardening mechanism exists in AMZIRC specimens following recrystallization. Conversely, the microhardness numbers of the recrystallized MZC specimens are substantially higher than that of solution annealed MZC. It therefore appears that precipitation hardening mechanism is still operating in AMAX-MZC following recrystallization.

The yield stress of the annealed copper alloys follows a trend that is very similar to the microhardness results. The significance of this observation will be discussed in Section VIII.A. The electrical conductivity curves at different annealing times follow the same general form as the 1 hour data with the exception of the 0.25 hour AMZIRC curve. In this case, the measured conductivity was

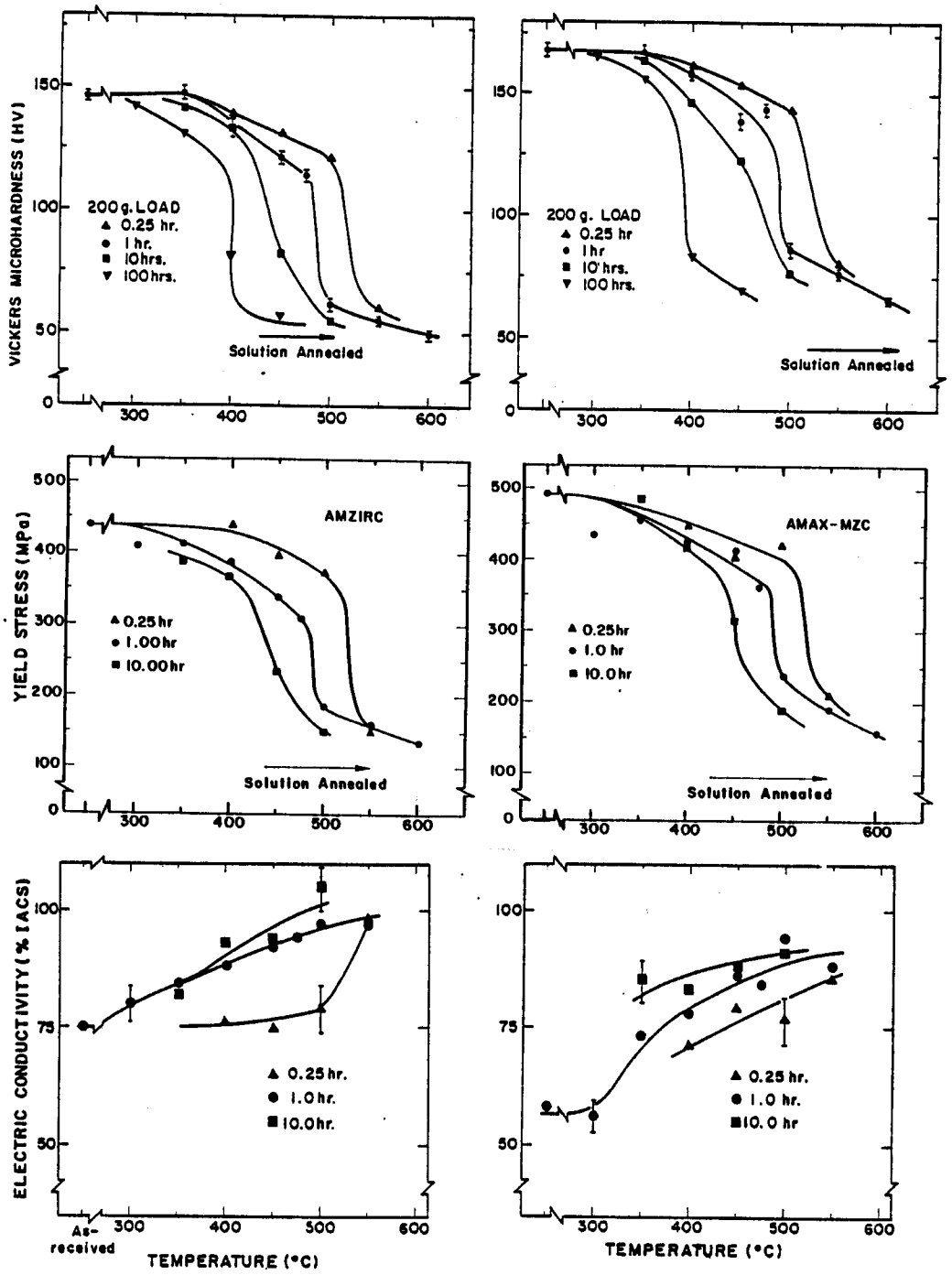

Fig. 7.13. Physical properties of the cold-worked plus aged copper alloys vs. anneal conditions.

constant at about 75% IACS until the annealing temperature exceeded 500°C. A large increase in conductivity was observed between 500 and 550°C. This may be an indication of a characteristic recovery temperature of AMZIRC for short term annealing at high temperatures.

The general physical property trends following annealing of the cold-worked plus aged alloys may be summarized as follows: Electrical conductivity, ductility and the work hardening coefficient all increase following the anneal. Conversely, microhardness, yield stress and ultimate tensile stress (i.e., all strength parameters) decrease upon annealing.

The recrystallization process was observed to be rather heterogeneous when investigated on a microscopic scale. Figure 7.14 shows some typical examples of this heterogeneity in an AMZIRC specimen annealed for 1 hour at 450°C. In the top micrograph, a region containing small recrystallized grains ($d \gtrsim 0.5$ μm) with well-defined large angle grain boundaries is visible whereas the adjacent region is still in the process of forming cell wall boundaries (recovery). The dislocation density in this micrograph changes from $\sim 10^{12}/m^2$ to $\sim 10^{14}$-$10^{15}/m^2$ over a distance of less than 1 μm. The bottom micrograph shows a large recrystallized region surrounded by matrix that is still undergoing recrystallization. It is believed that the acceleration of the recrystallization process may be associated with the large zirconium particle that is present in this region (see arrow). It was generally observed that recrystallization was at a more advanced stage in regions that were adjacent to large zirconium

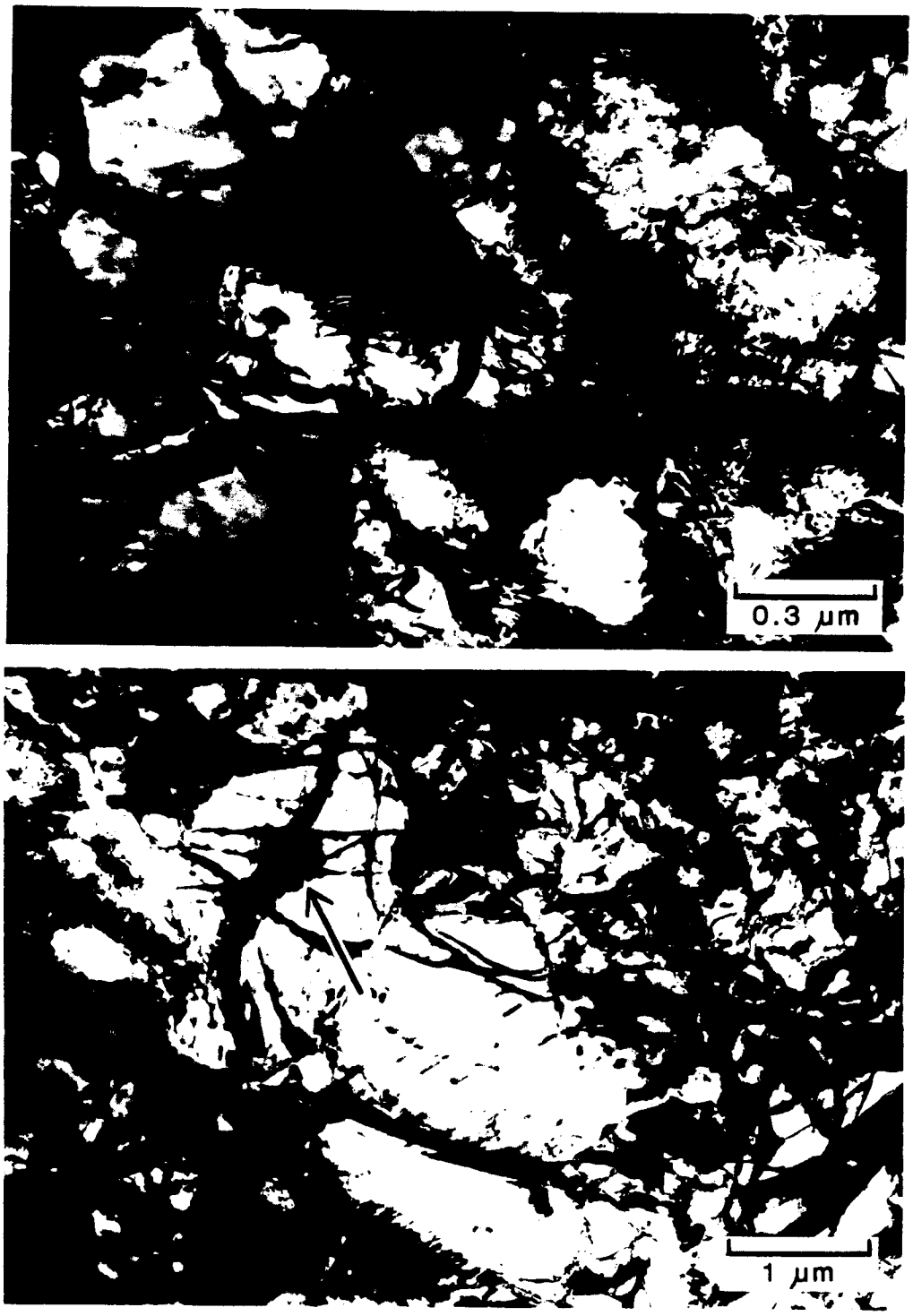

Fig. 7.14. Heterogeneous recrystallization in annealed AMZIRC. The arrow in the bottom micrograph points to a Zr particle.

precipitates. This effect has been observed by other researchers, and the effect of second phase particles on recrystallization may be summarized as follows:[38] Small particles (d < 1 μm) inhibit recrystallization by pinning subboundaries whereas large particles (d > 1 μm) stimulate the nucleation of grains in their vicinity. The solute atoms and small precipitates present in AMZIRC and AMAX-MZC result in a high recrystallization temperature for these alloys (T_R ~ 475°C) compared to pure copper (T_R ~ 200°C). However, the existence of the large zirconium particles in the alloys (present as a result of incomplete homogenization during fabrication, see Section VII.A.1) tends to lower the recrystallization temperature. Efforts should be made to keep the concentration of these large second phase particles at a minimum level.

Evaluation of the data presented in Table 7.4 and Figs. 7.11 and 7.13 reveals that a variety of combinations of strength and electrical conductivity are possible for AMZIRC and AMAX-MZC. It is evident that AMZIRC is generally superior to AMAX-MZC in terms of maximum achievable conductivity. On the other hand, AMAX-MZC is capable of a larger yield strength value than AMZIRC at a given operating temperature. The best combination of high strength and conductivity is obtained by aging the alloys at conditions slightly below that required for recrystallization. The resultant optimum yield strength and electrical conductivity values are (400 MPa, 90% IACS) for AMZIRC and (425 MPa, 85% IACS) for AMAX-MZC.

VII.C. Microstructure of Copper Alloys Following Ion Irradiation

VII.C.1 Irradiated Cold-Worked Plus Aged Alloys

Foils of AMZIRC and AMAX-MZC in the cold-worked plus aged (CWA) condition were irradiated with 14-MeV Cu ions to a peak damage level of 40 dpa at temperatures of 100-550°C (0.28-0.61 T_M). No void formation was observed in any of the irradiated specimens for these conditions.

Figure 7.15 shows the cross-section microstructure of CWA AMZIRC following irradiation to a peak damage level of 40 dpa at temperatures of 400, 500 and 550°C. This type of presentation allows both the damage region and nonirradiated regions of the foil to be simultaneously examined. At 400°C there is evidence of recovery of the dislocation structure and also an enlarged grain size in the irradiated part of the foil. The microstructure of the nonirradiated region showed no obvious signs of recovery at 400°C. Both the control and damage regions of AMZIRC were completely recrystallized following irradiation at 500 and 550°C (Fig. 7.15). Recrystallization in the damage and control regions also occurred in AMZIRC irradiated at these temperatures to peak fluences of 10 dpa (0.5 hour irradiation time). Cu_5Zr precipitates of average size d ~ 50 nm are visible in the recrystallized regions of Fig. 7.15. No difference was observed in the precipitate size or density between the irradiated and nonirradiated regions.

The effect of irradiation temperature on the damage microstructure of CWA AMAX-MZC at 400 and 500°C is shown in the cross-

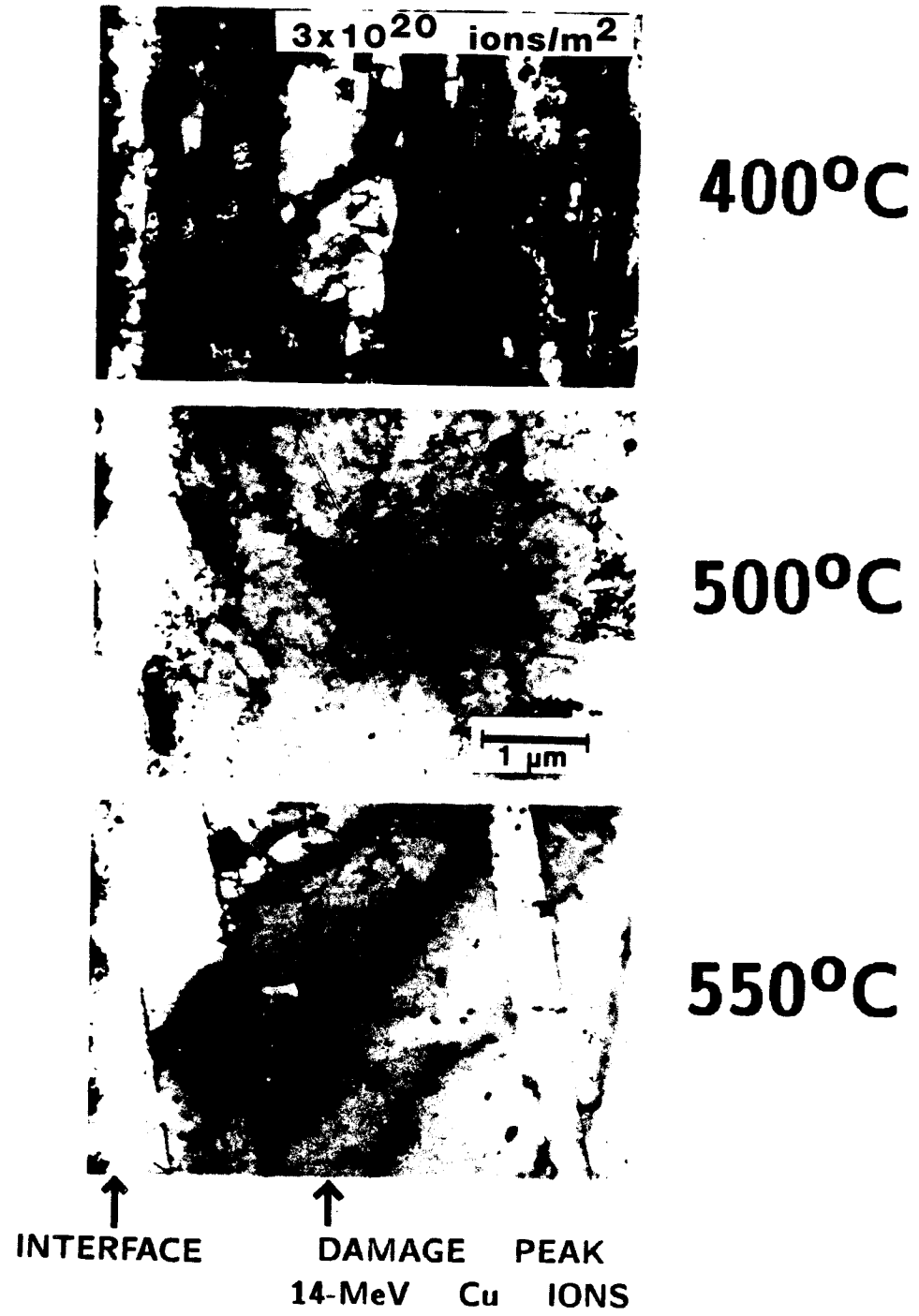

Fig. 7.15. Cross-section microstructure of cold-worked plus aged AMZIRC following ion irradiation to a calculated peak damage level of 40 dpa at 400-550°C.

section micrographs of Fig. 7.16. Ion irradiation at 400°C to a peak damage level of 40 dpa caused partial recrystallization to occur, while the nonirradiated microstructure remained essentially unchanged from the as-received condition. This irradiation response was similar to that observed in AMZIRC at 400°C (see Fig. 7.15). Irradiation at 500°C resulted in a fine-grained (grain diameter = 1.0 μm) microstructure in the damage region, while the control region recrystallized completely and had an average grain size of $\ell \gtrsim 5$ μm. Microdiffraction analysis of the damage region of the 500°C specimen revealed that the subgrains were separated by predominantly high angle boundaries, along with some low angle ($\lesssim 5°$ tilt) boundaries. It appears that some type of solute segregation or precipitation mechanism may be pinning the subgrain boundaries of MZC in the damage region during the recrystallization process (solute atoms are known to reduce the grain boundary mobility in metals;[39] also see Section VIII.B). No differences in the matrix precipitate size or density in the damage region versus the nonirradiated region were discernible.

A limited investigation was made on the effects of damage level on the observed microstructure of AMZIRC and AMAX-MZC at elevated temperatures (400-550°C, see Table 6.2). Figure 7.17 compares the cross-section microstructures of AMZIRC and AMAX-MZC following a 400°C irradiation to a peak damage level of 12 dpa. The irradiated microstructures of this and other low fluence studies (1-10 dpa) were similar to those conducted at the same temperatures but at a damage level of 40 dpa. On the basis of this investigation, it is concluded

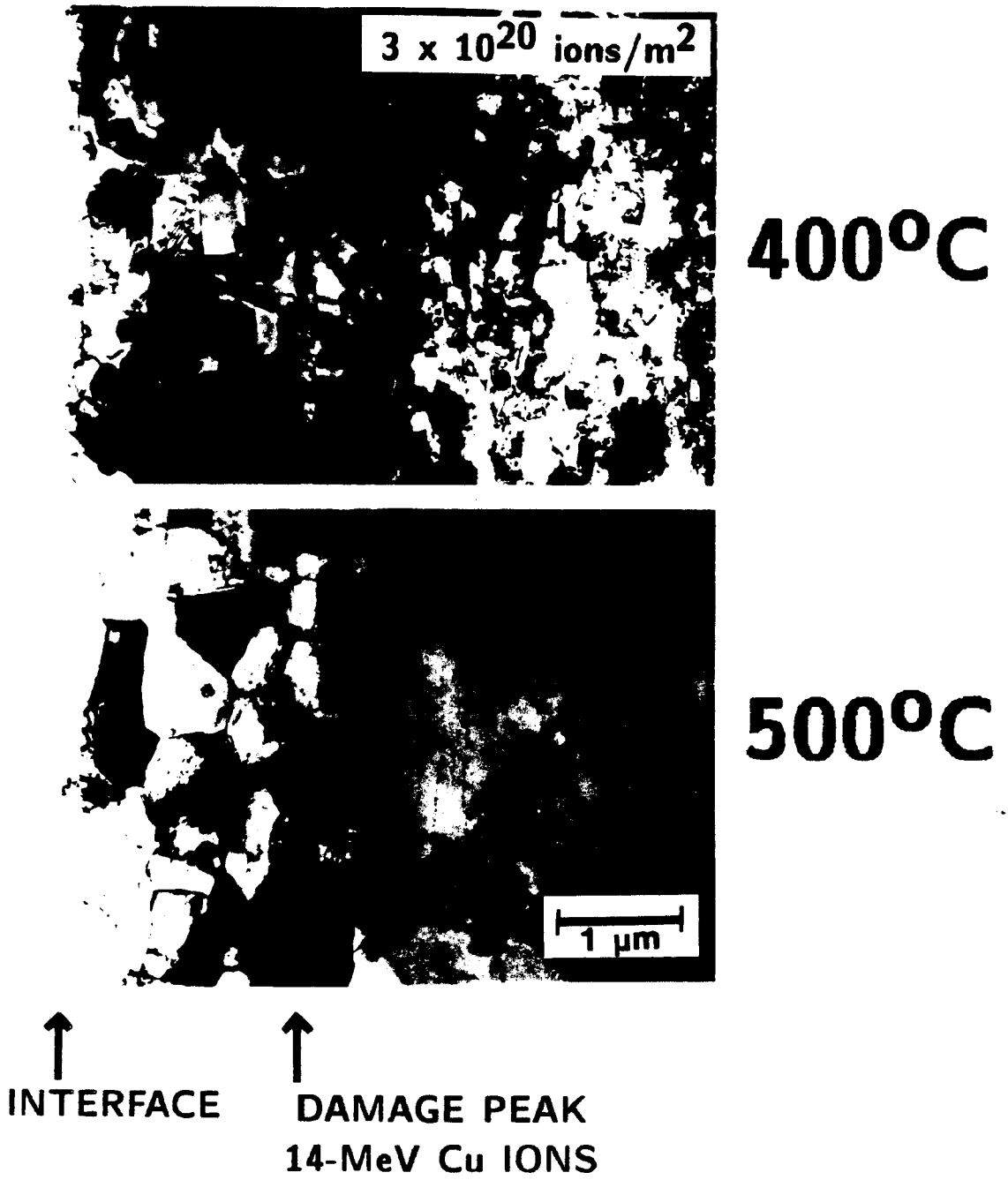

Fig. 7.16. Cross-section microstructure of cold-worked plus aged AMAX-MZC following ion irradiation to a calculated peak damage level of 40 dpa at 400 and 500°C.

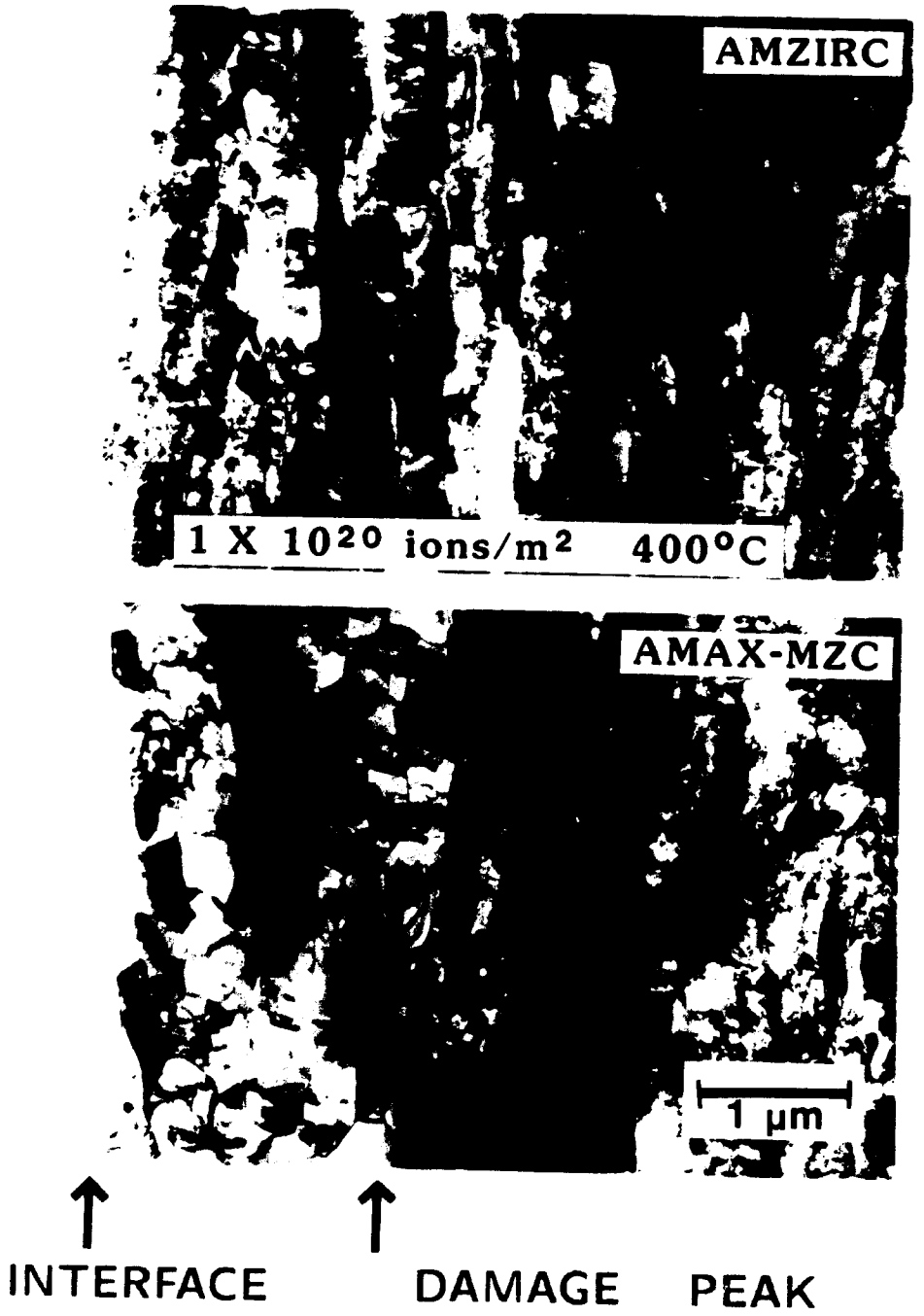

Fig. 7.17. Comparison of the cross-section microstructures of AMZIRC and AMAX-MZC following ion irradiation to a peak damage level of 12 dpa at 400°C.

that the damage microstructure evolution with regard to recovery and recrystallization processes is essentially complete following damage levels as low as 1 dpa.

Subsequent irradiations investigated the microstructural stability of cold-worked plus aged AMZIRC and AMAX-MZC at lower irradiation temperatures. Figure 7.18 shows the cross-section microstructure of AMZIRC following irradiation at 300°C to a peak damage level of 120 dpa. The dislocation density is lower in the damage region compared to the nonirradiated region, indicating that radiation-enhanced recovery has occurred.

Radiation-enhanced recovery, but not recrystallization, was observed in both AMZIRC and AMAX-MZC following irradiation to a peak damage level of 40 dpa over the temperature range of 100-250°C. Figure 7.19 shows the effect of 250°C irradiation on the microstructure of AMAX-MZC. The cross-section microstructure is shown in the top micrograph, while the bottom two micrographs show representative irradiated and nonirradiated portions of the foil at higher magnification. Partial recovery of the cold-worked dislocation structure has occurred in the irradiated region of the foil whereas the unirradiated microstructure remains similar to that of the as-received alloy. Subgrain development is observed to be more advanced in the damage region compared to the control. A third feature is the appearance of small "black spots" in the irradiated regions of the foil. Similar results were obtained for the AMZIRC alloy irradiated under the same conditions.

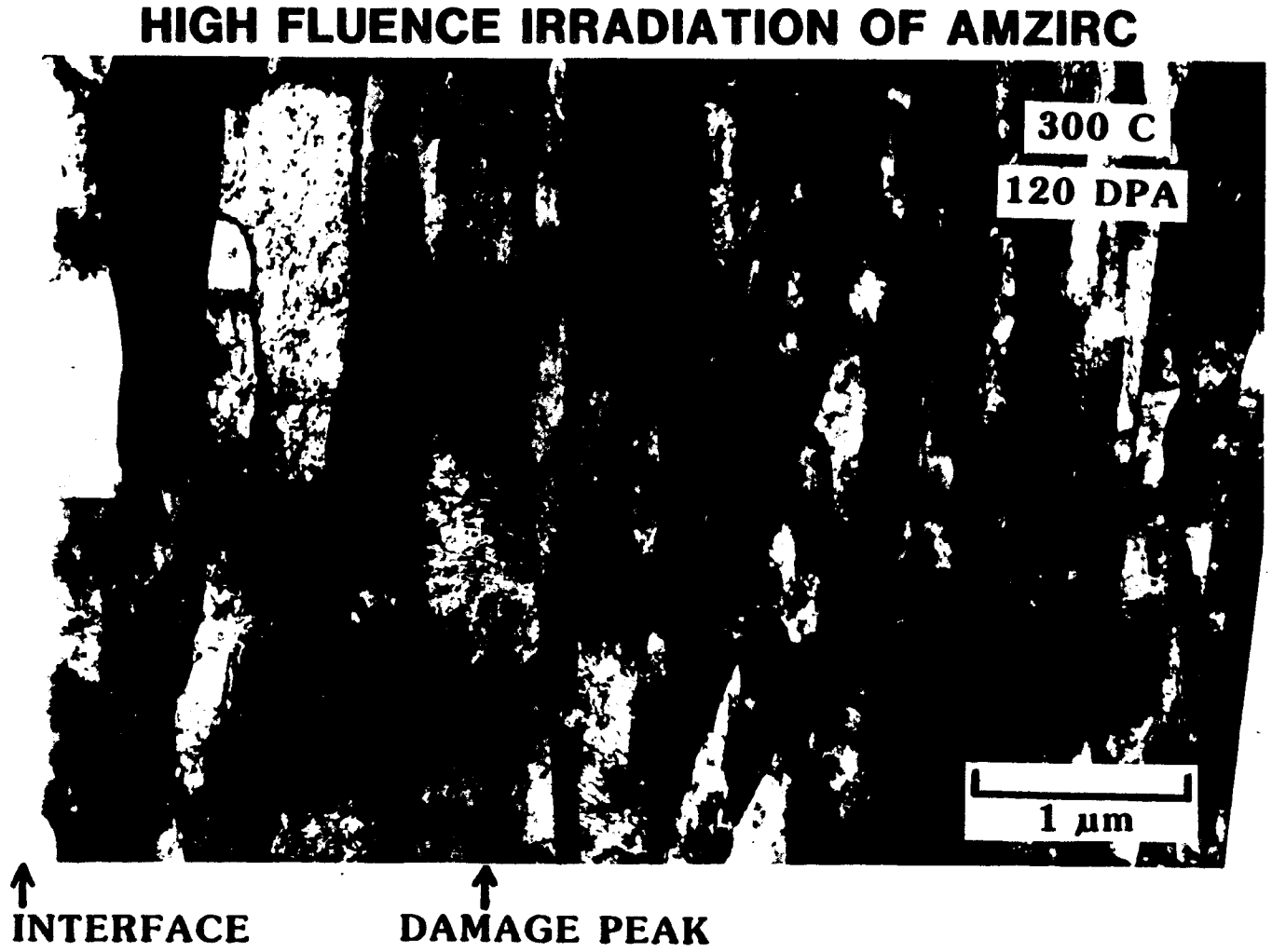

Fig. 7.18. Cross-section microstructure of AMZIRC following ion irradiation to a peak damage level of 120 dpa at 300°C.

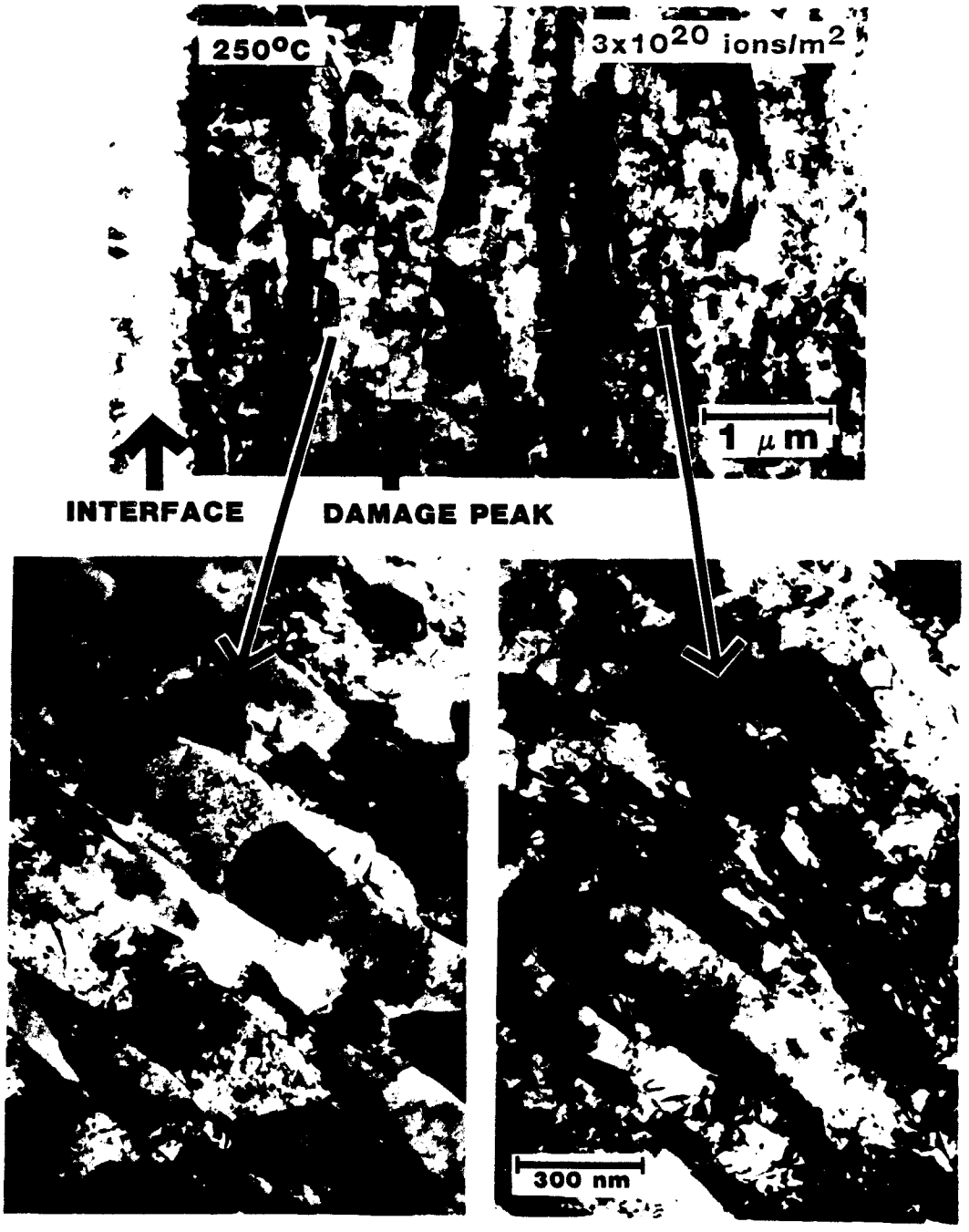

Fig. 7.19. Microstructure of cold-worked plus aged AMAX-MZC following ion irradiation to a peak damage level of 40 dpa at 250°C.

The irradiated microstructures of both alloys showed very little temperature dependence over the temperature interval of 100-250°C. Figure 7.20 shows the microstructures of AMZIRC and AMAX-MZC following irradiation at 100°C. Once again, some of the cold-worked dislocation structure has recovered during irradiation. Indications of subgrain nucleation are visible in both micrographs. Both alloys contain a high density of small black spots.

A variety of interesting microstructural features were observed following irradiation of AMZIRC and AMAX-MZC. Figure 7.21 shows examples of moiré fringes and aligned dislocations. The moiré fringes are associated with the interference contrast from overlapping subgrains.[40] The observed features are apparently due to recovery and recrystallization processes that are associated with the ion irradiation.

Both of the cold-worked plus aged copper alloys contained a large number of small subgrains following irradiation. This is evident by viewing Fig. 7.22, which shows a sequence of micrographs at different tilt angles taken from the same region in AMAX-MZC following irradiation to 10 dpa at 150°C. Tilting the specimen causes the subgrains to come into and out of contrast in the electron microscope. A series of different subgrains are visible in Fig. 7.22 as the tilt angle is varied from -12 to +2.5°.

Figure 7.23 shows the irradiated microstructure of AMZIRC as a function of irradiation temperature from 100 to 500°C. The damage levels in this figure are all about 10 dpa with the exception of the

MICROSTRUCTURE OF COPPER ALLOYS IRRADIATED AT 100°C

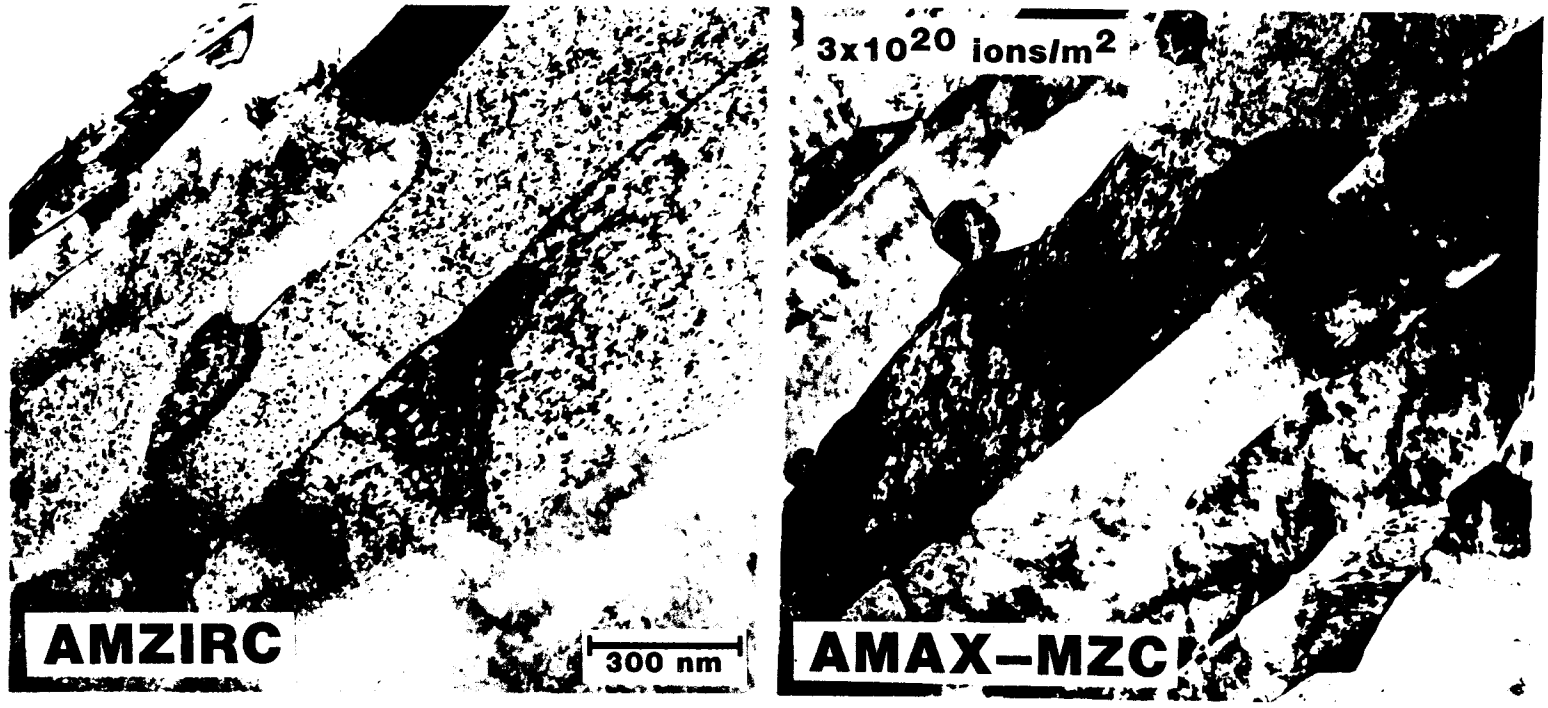

Fig. 7.20. Microstructures of cold-worked plus aged AMZIRC and AMAX-MZC following a 10 dpa ion irradiation at 100 C.

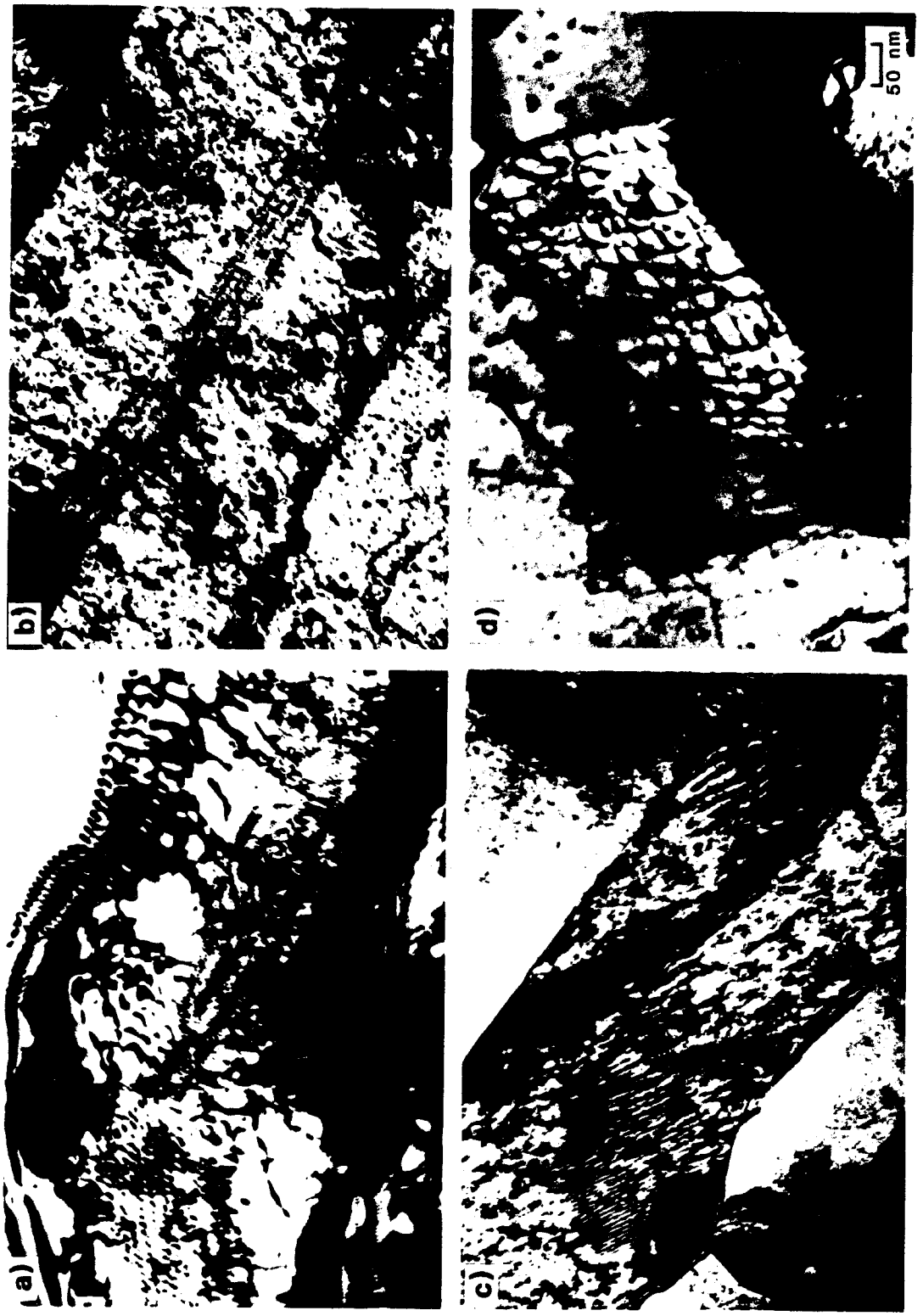

Fig. 7.21. Moiré fringes (a,c) and aligned dislocations (b,d) in irradiated copper alloys.

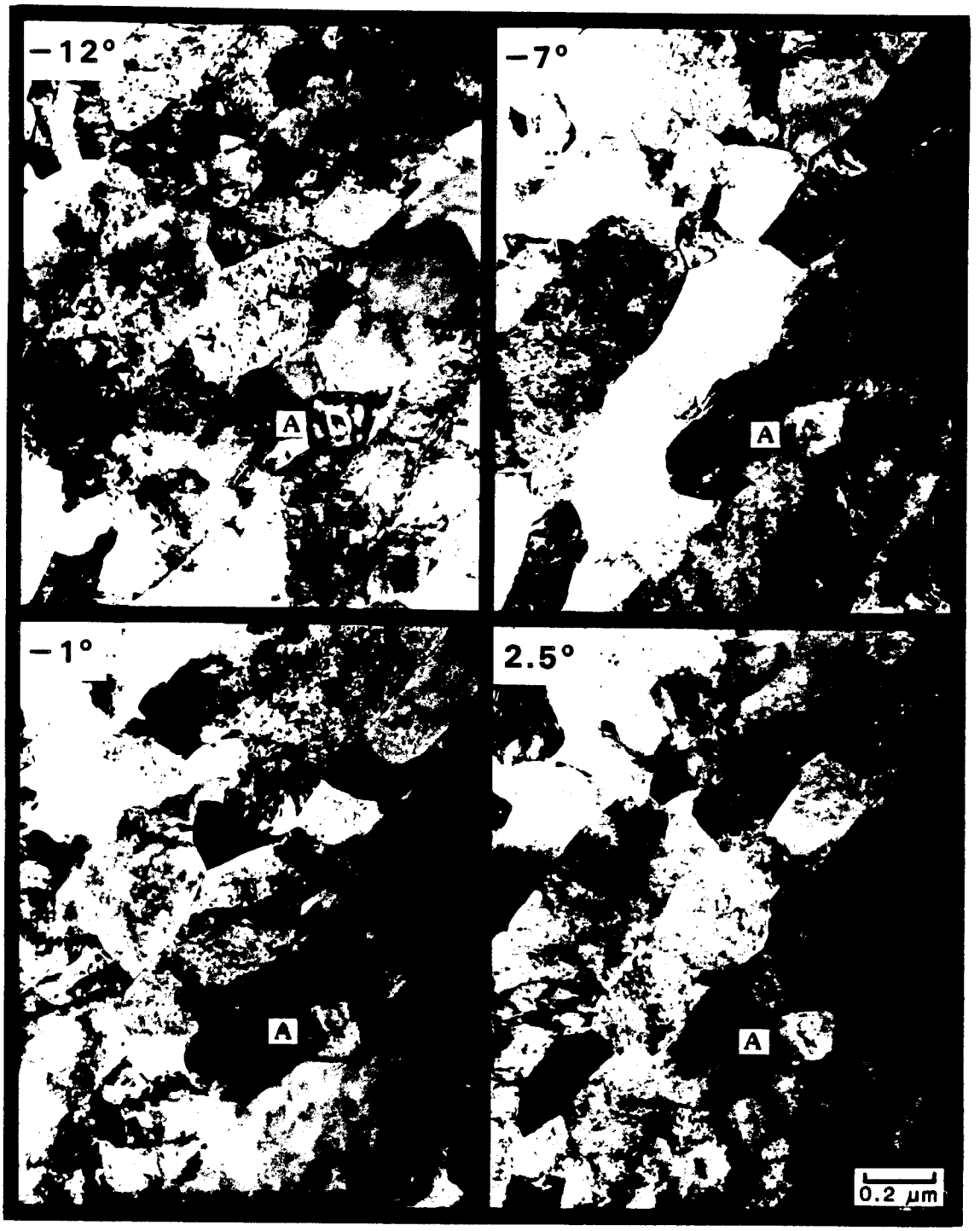

Fig. 7.22. Low-angle tilt series showing subgrains coming in and out of contrast in AMAX-MZC irradiated to 10 dpa at 100 C.

300°C microstructure, which corresponds to about 30 dpa. The irradiated microstructure was observed to be similar over the temperature range of 100 to 250°C -- recovery of the cold-worked dislocation structure occurred, a high density of black spot damage was evident, and the subgrain size remained stable. Irradiation temperatures of 300°C and above resulted in a different microstructure. The black spot density decreased rapidly with increasing temperature above 250°C, and essentially no black spots were visible at 400°C. The subgrain size increased with increasing irradiation temperature over the range of 300 to 500°C. Complete recrystallization occurred following irradiation at 500°C.

Figure 7.24 shows the temperature-dependent damage microstructure of AMAX-MZC over the temperature range of 100 to 500°C. The damage levels in this figure are also nominally 10 dpa with the exception of the 300°C microstructure, which is about 3 dpa. The low-temperature (100-250°C) microstructure of irradiated AMAX-MZC was observed to be very similar to that of AMZIRC (compare Figs. 7.23 and 7.24). Black spot formation and a stable subgrain size were observed in this temperature range. The microstructure began to change at 300°C and above; the black spot density decreased and the subgrain size increased with increasing temperature. The enlarged subgrain size is an indication that recrystallization is occurring during ion irradiation at temperatures $\gtrsim$ 300°C.

It was mentioned in the beginning of this section that no void formation was observed in either of the cold-worked plus aged alloys

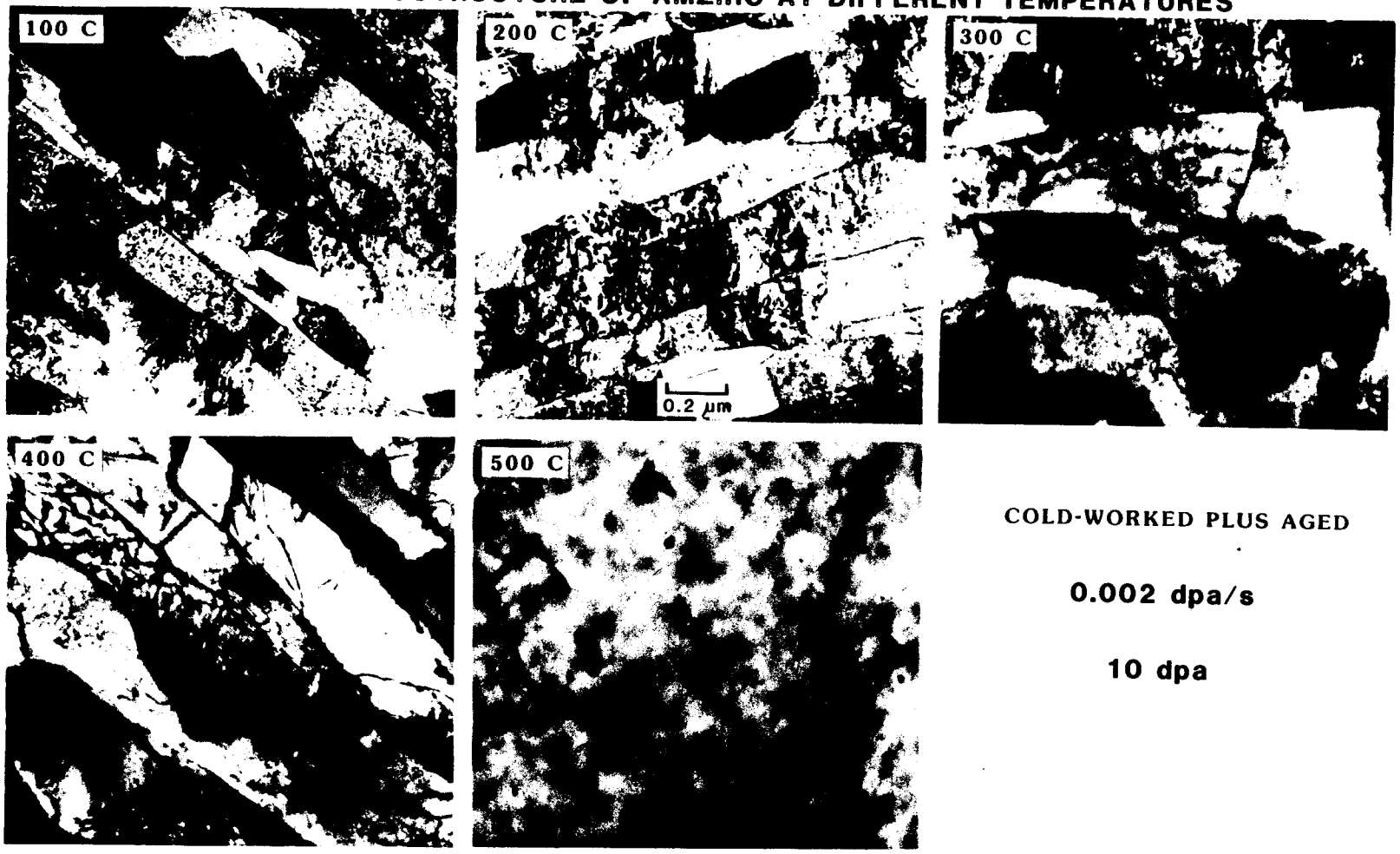

Fig. 7.23. Microstructure of cold-worked plus aged AMZIRC following ion irradiation to 10 dpa at 100-500°C.

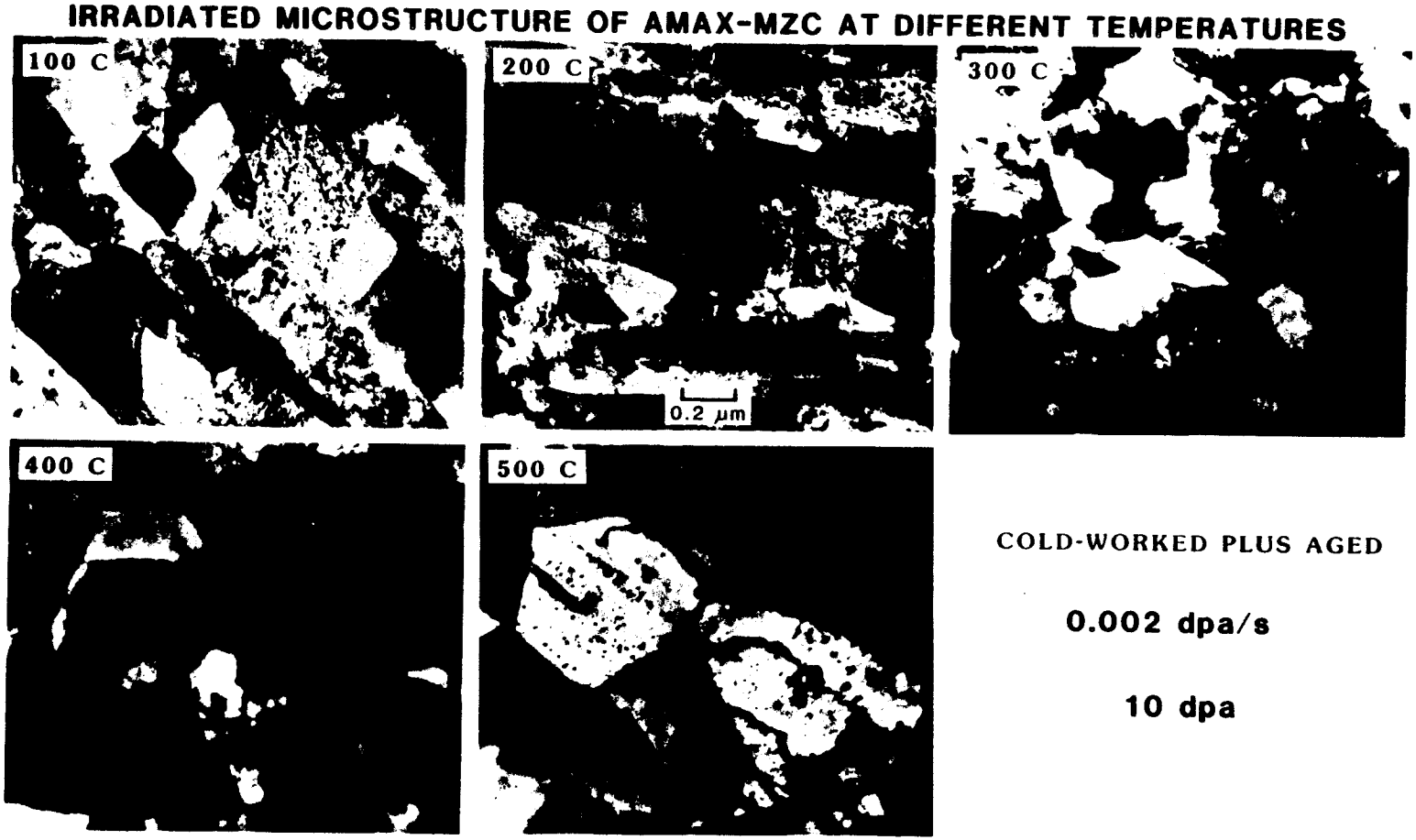

Fig. 7.24. Microstructure of cold-worked plus aged AMAX-MZC following ion irradiation to 10 dpa at 100-500°C.

following irradiation to 40 dpa over the temperature range of 100-550°C (0.28-0.61 T_M). However, a 40 dpa, 300°C irradiation of a cold-worked plus aged AMZIRC sample that was inadvertently annealed prior to its irradiation resulted in a very low density of large voids. Figure 7.25 shows a cross-section micrograph of 4 voids that were observed following ion irradiation of this sample. The average void size was $\gtrsim$ 300 nm and the void density was estimated to be $\lesssim 10^{17}/m^3$. The voids were faceted, and it was determined that the surfaces were bound by {111} planes.

The presence of voids in the annealed AMZIRC specimen suggested that the high dislocation density that is initially present in the cold-worked plus aged copper alloys may be delaying the onset of void formation (recall that ion irradiation of cold-worked plus aged AMZIRC at 300°C to a peak damage level of 120 dpa did not result in any observable void formation, see Fig. 7.18). A limited irradiation study was subsequently carried out on AMZIRC and AMAX-MZC in the solution annealed plus aged condition. The precipitate evolution was also studied in these irradiated alloys in order to determine whether precipitate coarsening or dissolution processes were occurring.

VII.C.2 Irradiated Solution Annealed Plus Aged Alloys

No significant amount of void formation was observed in the solution annealed plus aged copper alloys following ion irradiation to 40 dpa over the temperature range of 100-400°C (0.28-0.50 T_M). Figure 7.26 shows cross-section micrographs of SAA AMZIRC following irradiation at 200 and 400°C. The top two micrographs show the

Fig. 7.25. Isolated voids observed in annealed AMZIRC following ion irradiation at 300°C to a peak damage level of 40 dpa.

cross-section microstructure of AMZIRC irradiated at 400°C in low (multibeam) and high contrast (two beam) conditions. The cross-section microstructure of AMZIRC irradiated at 200°C is shown in the bottom micrograph. Precipitate "stringers" were commonly observed in the irradiated region of the foil for the 400°C irradiation condition, and they were also occasionally found in nonirradiated regions. Irradiation of AMZIRC at 200°C resulted in a high density of "black spot" damage. There was no definitive indication of radiation damage for the 400°C specimen, with the exception of a low density of small voids ($n_v \simeq 5 \times 10^{19}/m^3$, $d_v \simeq 8$ nm; $\Delta V/V \simeq 1 \times 10^{-5}$). Stereomicroscopy on selected cavities indicated that they were contained within the foil and were not simply due to precipitates falling out of the foil during electropolishing.

Figure 7.27 shows the cross-section microstructure of solution annealed plus aged AMAX-MZC following ion irradiation to 40 dpa at temperatures of 100-300°C. There was no evidence of void formation in irradiated AMAX-MZC over the temperature range of 100-400°C. Black spot damage was evident for irradiation temperatures of $\leq$ 300°C. The semi-coherent Cr precipitates that were initially present in SAA AMAX-MZC apparently became incoherent following ion irradiation at 100-400°C -- no coherency strain contrast (black-white streaking) was observable for precipitates in the irradiated region. This is in agreement with previous irradiation studies on coherent precipitates in copper alloys.[42,43]

CROSS-SECTION MICROSTRUCTURE OF ION-IRRADIATED AMZIRC

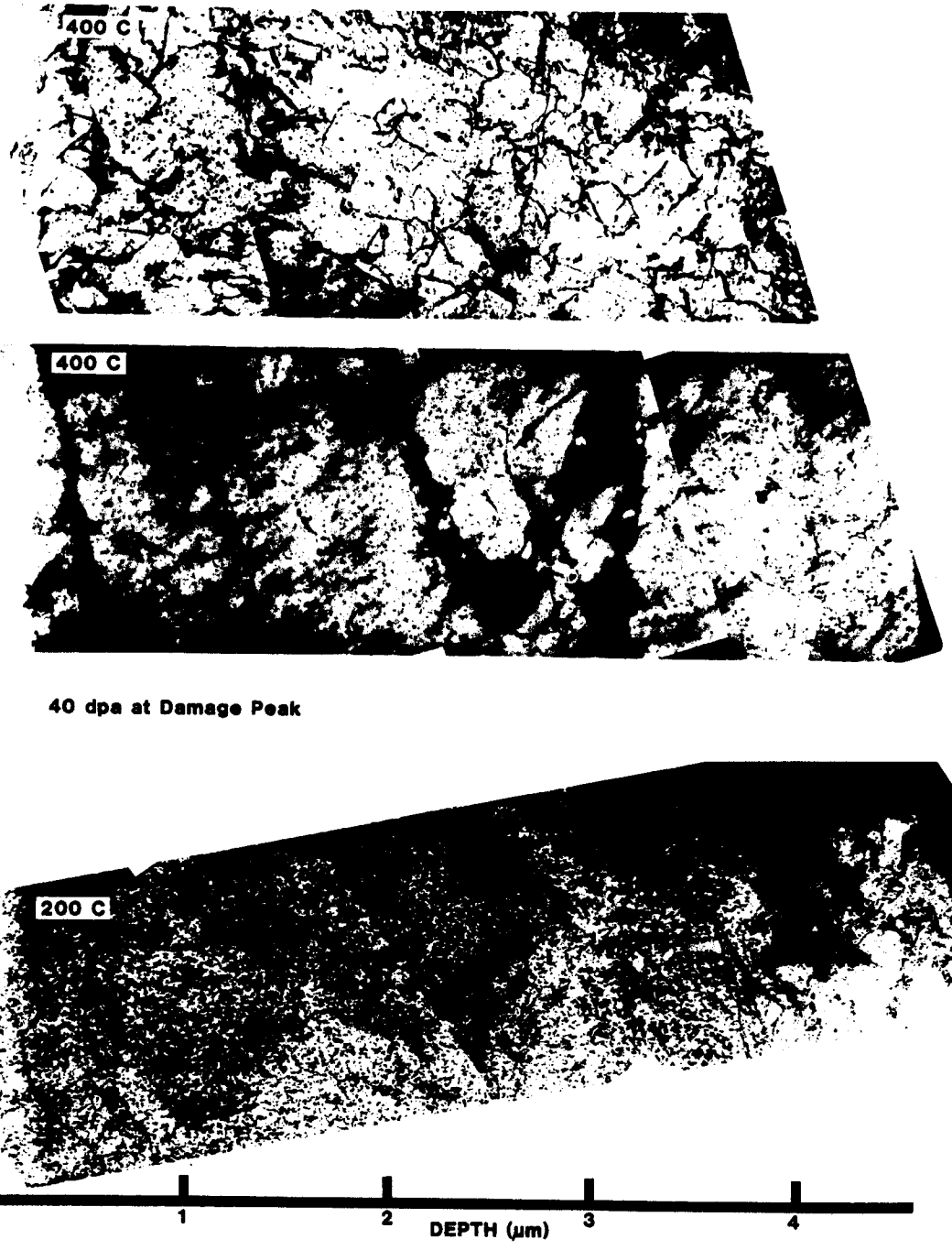

Fig. 7.26. Cross-section microstructure of solution annealed plus aged AMZIRC following ion irradiation to a peak damage level of 40 dpa at 200 and 400°C.

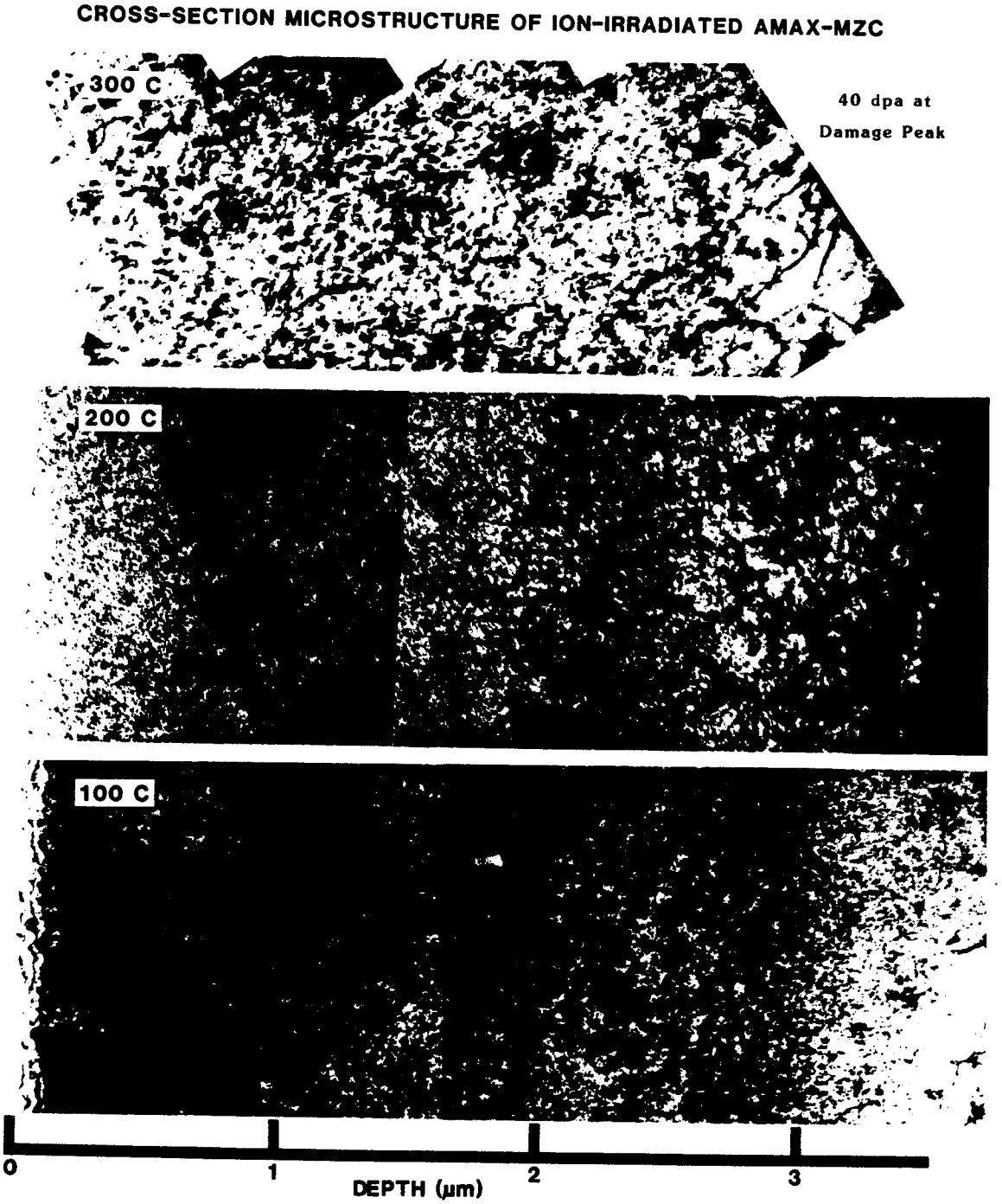

Fig. 7.27. Cross-section microstructure of solution annealed plus aged AMAX-MZC following ion irradiation to a peak damage level of 40 dpa at 100-300°C.

Figure 7.28 shows the precipitate microstructure of AMZIRC and AMAX-MZC following irradiation to 10 dpa at 400°C. The top micrograph shows grain boundary and matrix Cu_5Zr precipitates in SAA AMZIRC. There was no discernible change in the morphology or size distribution of these precipitates in the irradiated versus nonirradiated regions of the foil. The bottom two micrographs show matrix precipitates from irradiated (10 dpa) and nonirradiated regions of SAA AMAX-MZC following ion irradiation at 400°C. There is no evidence of radiation-induced coarsening or dissolution of the matrix precipitates for these irradiation conditions.

Figure 7.29 shows the typical irradiated microstructure of AMAX-MZC following ion irradiation to 10 dpa at 100 and 300°C. The low temperature (100°C) microstructure is characterized by a bimodal distribution, consisting of precipitates and/or large defect clusters (d = 5-10 nm) superimposed on a fine-scale distribution of stacking fault tetrahedra (SFT) and unresolved defect clusters/precipitates. The SFT had an average size of 2.4 nm and a density of about 3 x $10^{22}/m^3$. The total defect cluster density in MZC irradiated at 100°C was 8 x $10^{22}/m^3$, with an average size of 2.9 nm. Ion irradiation of MZC at 300°C resulted in a larger average defect cluster size compared to irradiation at 100°C (Fig. 7.29). The contrast of many of these larger clusters is similar to that expected for dislocation loops.[6,40] The loop density at 300°C was about 5 x $10^{20}/m^3$ and the average diameter was 20 nm.

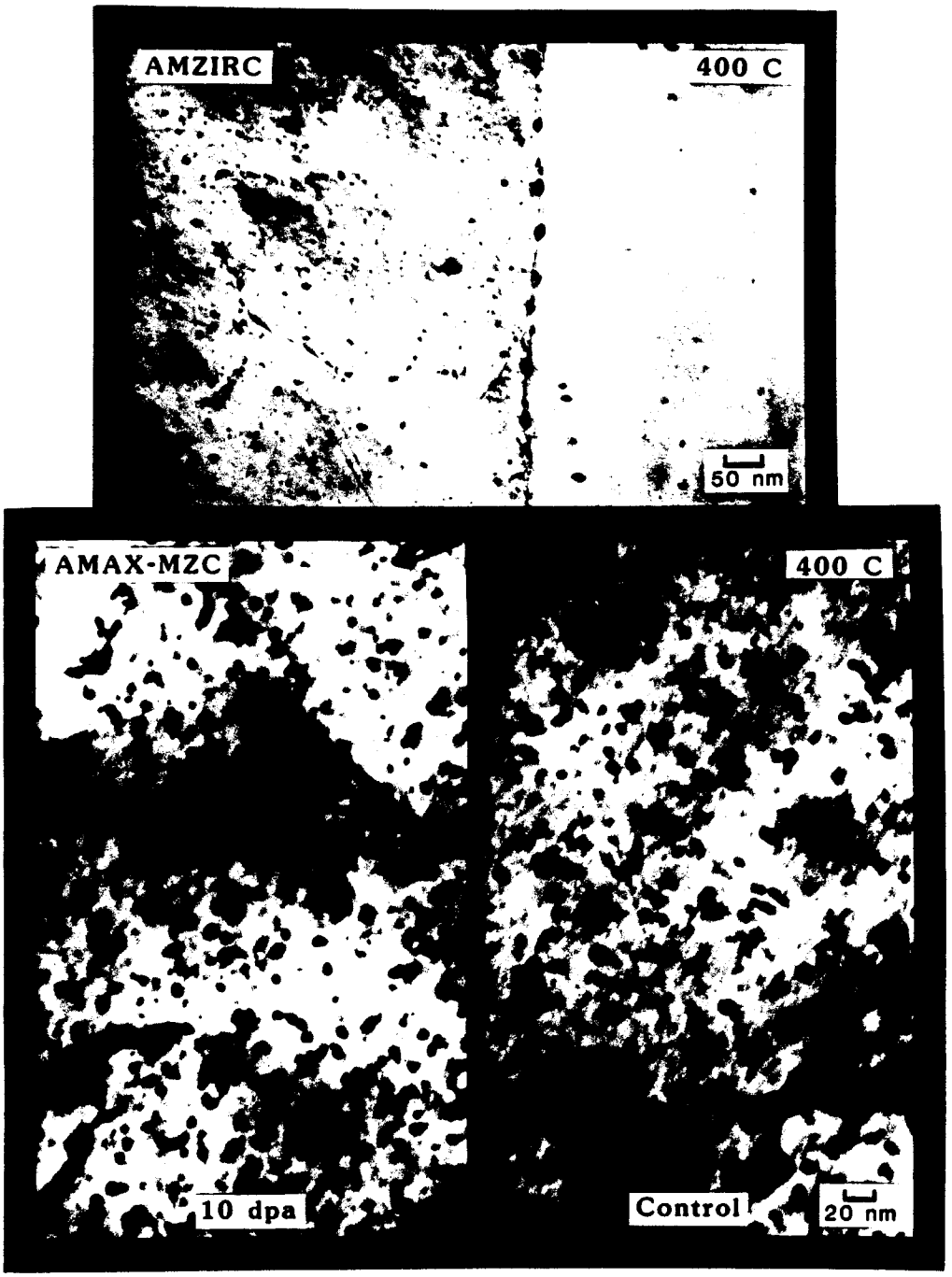

Fig. 7.28. Precipitate stability in irradiated alloys at 400 C. The top micrograph shows grain boundary and matrix precipitates in AMZIRC. The bottom micrographs compare the matrix precipitates in AMAX-MZC from irradiated and nonirradiated regions of the foil.

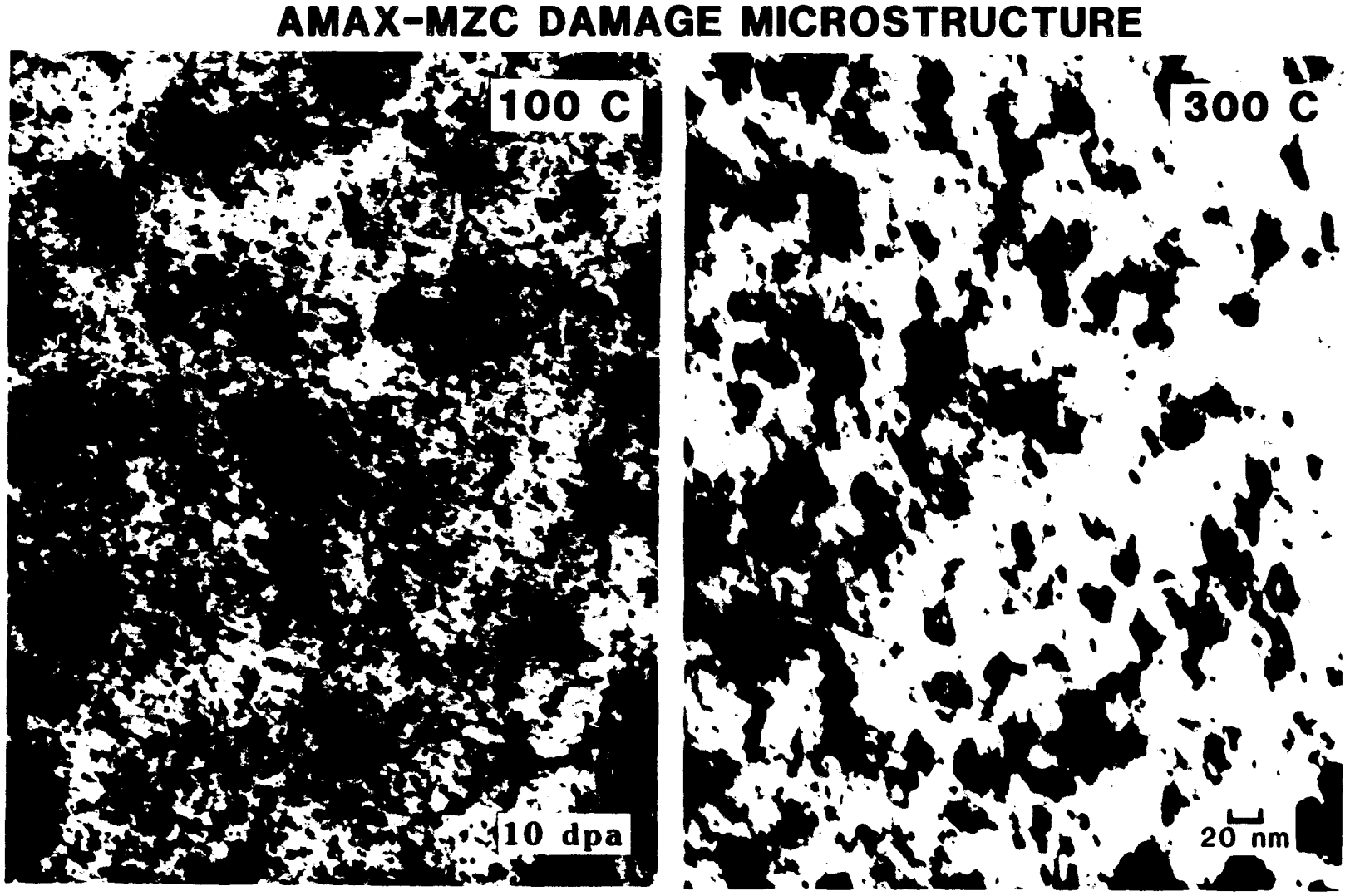

Fig. 7.29. Microstructure of AMAX-MZC following ion irradiation to 10 dpa at 100 and 300°C.

The damage microstructure of SAA AMAX-MZC was observed to be somewhat more coarse in the peak damage region compared to the mid-range damage regions following ion irradiation at 100°C (see, e.g., the cross-section micrograph in Fig. 7.27). Figure 7.30 shows the end of range microstructure in more detail. The peak damage microstructure consists of relatively large defect clusters that are superimposed on a background of fine-scale damage. These large clusters appear to be dislocation loops, with an average size of 8 nm and a density of 1 x $10^{21}/m^3$. The clusters may be interstitial-type loops, since there is an excess of interstitial defects in this region due to the coincidence of the peak damage region and the mean range of the bombarding Cu ions.

A closer analysis of the precipitates in irradiated AMZIRC and AMAX-MZC revealed the presence of moiré fringe contrast on some of the small precipitates. Figure 7.31 shows an example of this behavior in an MZC specimen irradiated to 10 dpa at 100°C along with the corresponding diffraction pattern. The moiré fringe contrast is due to a slight mismatch in the lattice plane spacings of the precipitate and the copper matrix.[6,40] Since this precipitate was observed in both irradiated AMZIRC (Cu-Zr) and AMAX-MZC (Cu-Cr-Zr-Mg), it is probably a Cu-Zr precipitate. This fringed precipitate was also occasionally observed in nonirradiated regions of the alloys, which indicates that the precipitate may be radiation-enhanced. The precipitate apparently has a cube-on-cube orientation relationship with the copper matrix. The precipitate lattice plane spacing for

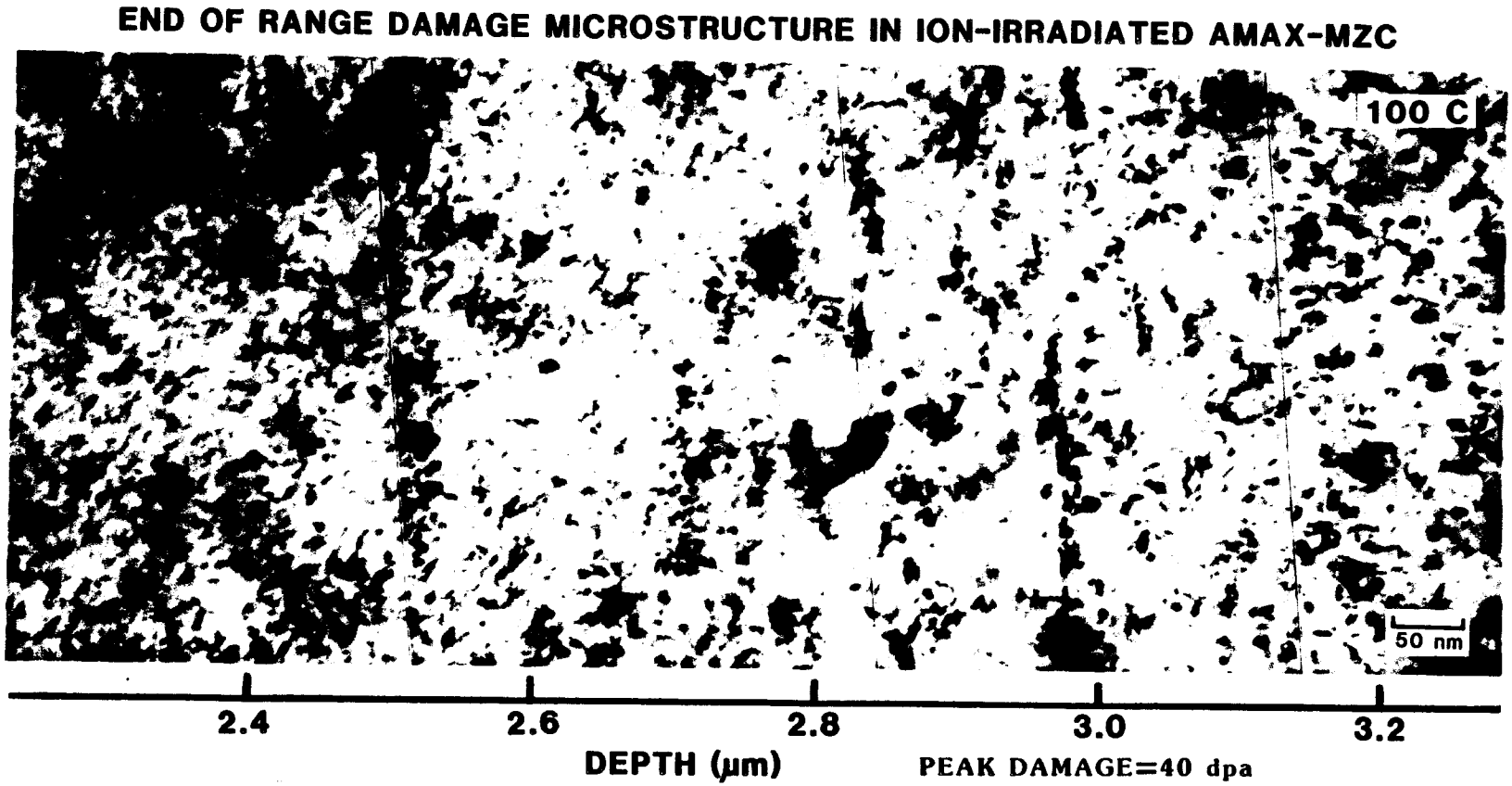

Fig. 7.30. End of range damage microstructure in solution annealed plus aged AMAX-MZC following ion irradiation to a peak damage level of 40 dpa at 100 C.

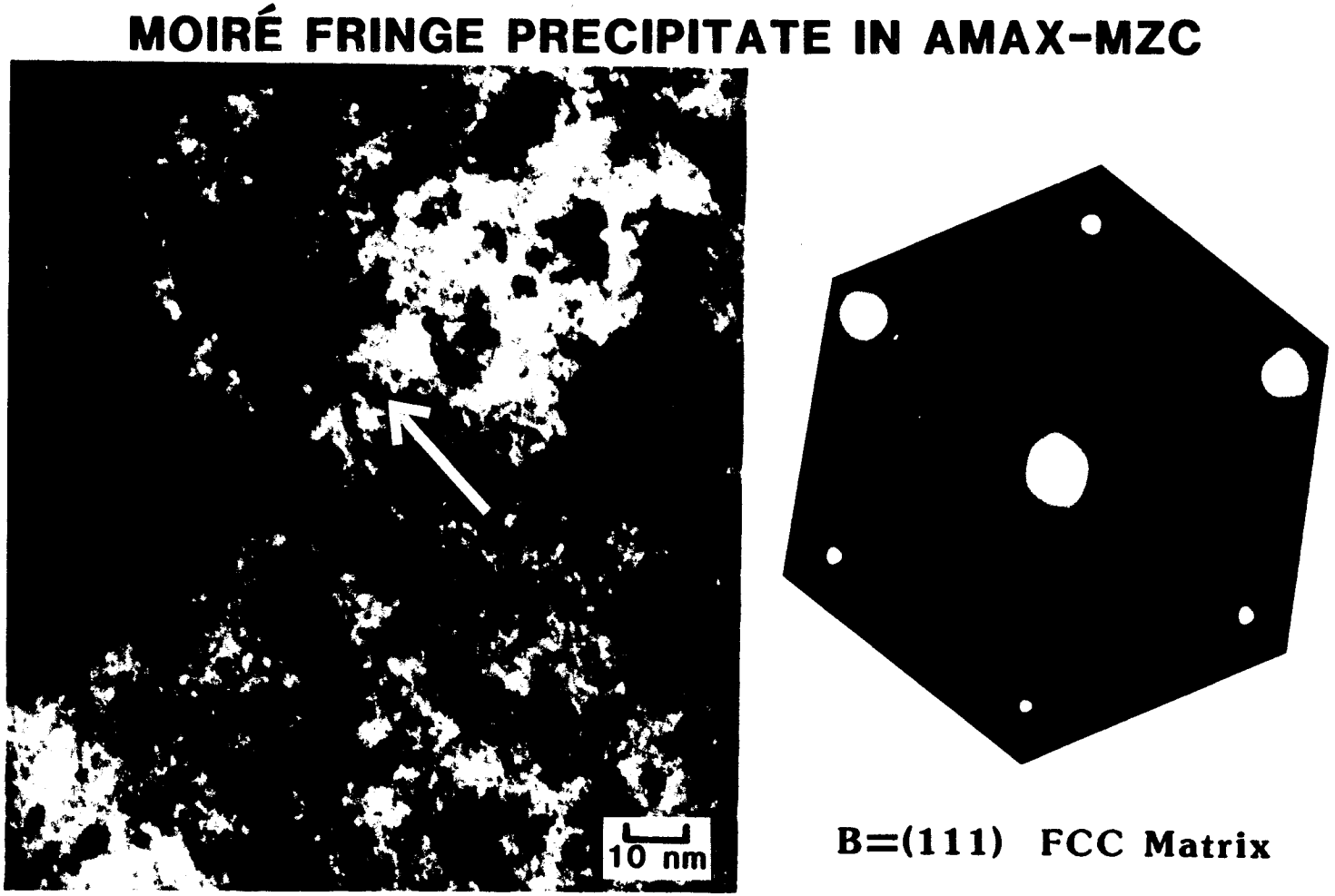

Fig. 7.31. Moiré fringe precipitate in AMAX-MZC following ion irradiation to 10 dpa at 100°C and associated matrix plus precipitate diffraction pattern.

the low-index planes in fig. 7.31 is 0.295 nm. This corresponds to a lattice parameter of 0.84 nm if the precipitate crystal structure is fcc. The precipitate size and density were 5 nm and ~ 5 x $10^{20}/m^3$ for both AMZIRC and AMAX-MZC following ion irradiation at 100-300°C. The average precipitate size increased to 10 nm and the density decreased to 1 x $10^{20}/m^3$ following ion irradiation at 400°C.

VII.D. Microstructure of Copper Following Ion Irradiation

Ion irradiation of pure copper to peak damage levels of 40 dpa over the temperature range of 100-400°C (0.28-0.50 T_M) resulted in "black spot" damage, but no significant void formation. A sparce distribution of voids was observed in pure copper irradiated at 400°C. The average void diameter for this condition was $\lesssim$ 100 nm, with an estimated density of only $10^{17}/m^3$ ($\Delta V/V \lesssim 5 \times 10^{-5}$). No voids were observed in pure copper for any of the other irradiation conditions. A room temperature preimplantation of 45 appm He into copper followed by a 40 dpa peak damage ion irradiation at 300°C resulted in the formation of small cavities in the He implanted region (0.5-1.5 μm depth). The damage level in the He implanted region was roughly constant at 10 dpa (see Fig. 2.2). The visible cavities were of small size, d = 2.6 nm, and high density, n $\gtrsim$ 6 x $10^{21}/m^3$ ($\Delta V/V \simeq 5 \times 10^{-5}$). Conversely, preimplantation of 45 appm H in pure copper did not produce any observable cavity formation following a 300°C, 40 dpa peak damage irradiation.

Figure 7.32 shows the cross-section microstructures of ion-irradiated copper for irradiation temperatures of 100-400°C. Evidence

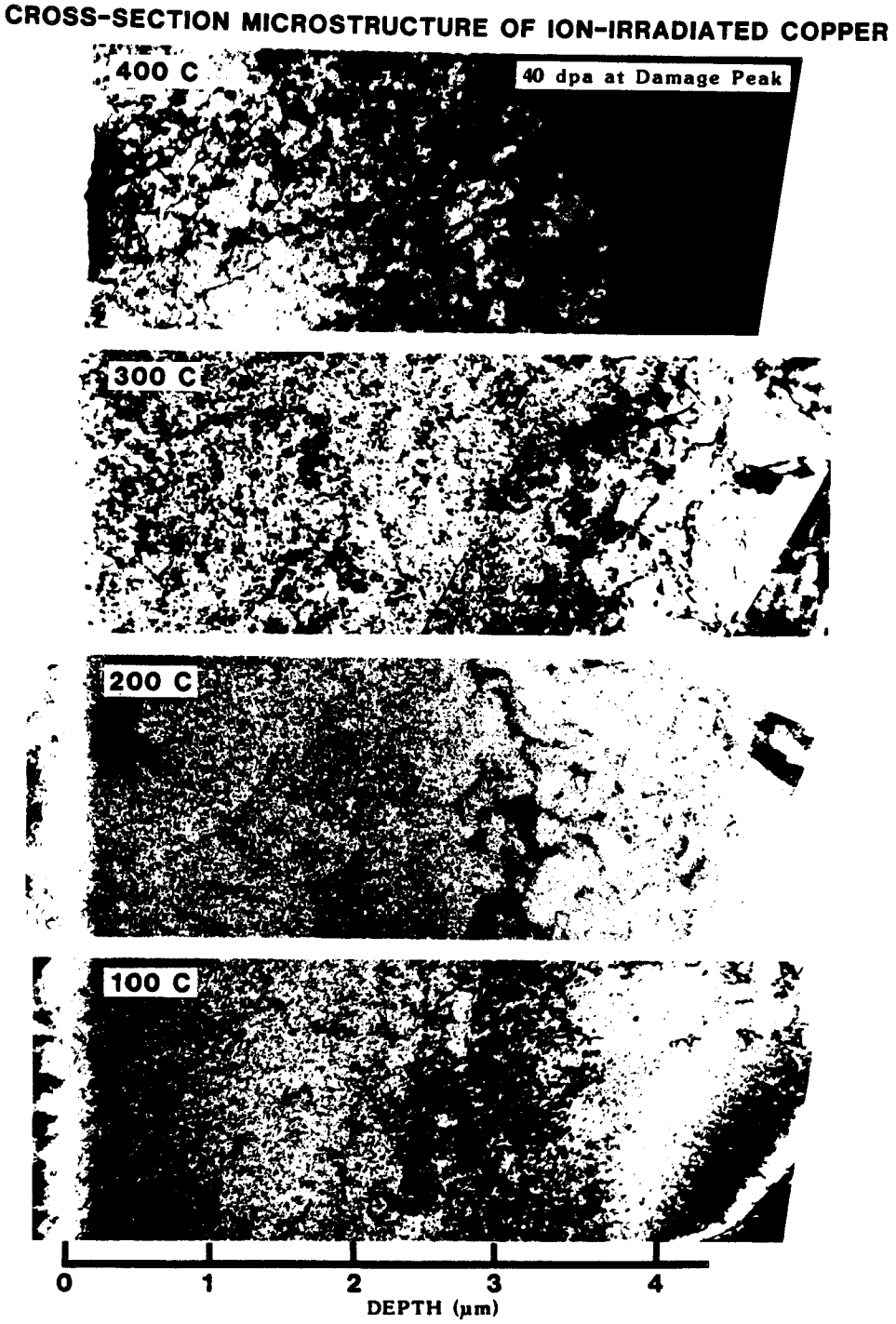

Fig. 7.32. Cross-section microstructure of copper following ion irradiation to a peak damage level of 40 dpa at 100-400 C.

of radiation damage exists to depths in excess of 3.5 μm, which is significantly deeper than the predicted damage range obtained from a Brice calculation for 14-MeV Cu ions incident on a copper target (Fig. 2.2). The significance of this observation will be discussed in Section VIII.E. The defect cluster density was roughly constant for irradiation temperatures of 100 and 200°C. Irradiation at temperatures above 300°C resulted in a very low defect cluster density. This temperature effect is more easily seen in Fig. 7.33, which shows representative weak beam dark field micrographs of copper irradiated to 10 dpa at temperatures of 100-400°C. The low temperature (100-300°C) damage microstructure consists of localized regions of large defect clusters which are superimposed on a background of small defect clusters. It is possible that these enlarged clusters are due to subcascades.

A more detailed analysis of the black spot damage revealed several significant features. Figure 7.34 shows enlarged black spot defects in irradiated copper that are located in the near vicinity of dislocation lines. Since dislocation lines are known to be a preferential sink for interstitials, it appears likely that the large defect clusters in Fig. 7.34 may be small interstitial loops which have grown as a result of a favorable incident point defect flux. The observation of enhanced cluster sizes on dislocations in ion irradiated copper agrees very well with experimental results by Yoshida et al.[44] on 14-MeV neutron irradiated copper. They found that about

temperatures, it first slowly decreases and then decreases rapidly at a temperature of 475°C. Thermal annealing at temperatures above 500°C causes a gradual decrease in VHN with increasing temperature. AMAX-MZC has a higher microhardness number than AMZIRC for all of the thermal annealing conditions. This is an indication that precipitation hardening effects are more pronounced in AMAX-MZC as compared to AMZIRC.

The general shape of the microhardness annealing curve is typical of that for cold-worked metals.[33] The sharp drop in VHN over a narrow temperature range is generally associated with recrystallization processes, whereas the gradual decrease in VHN at lower annealing temperatures corresponds to recovery processes. Figure 7.12 shows the TEM microstructure of the two alloys in the as-received and in two annealed conditions. Dislocation rearrangement and a general reduction in dislocation density is evident in the microstructures of both alloys following a 1 hour anneal at 450°C. This confirms that the 350 to 450°C annealing stage corresponds to recovery processes. Annealing for 1 hour at 500°C results in the formation of dislocation-free grains with high angle grain boundaries. This shows that recrystallization does indeed coincide with the rapid drop in VHN at 475°C. The important conclusion from this thermal anneal study is that both AMZIRC and AMAX-MZC lose their high strength upon recrystallization. Their strength after recrystallization approaches values typically found for annealed copper.

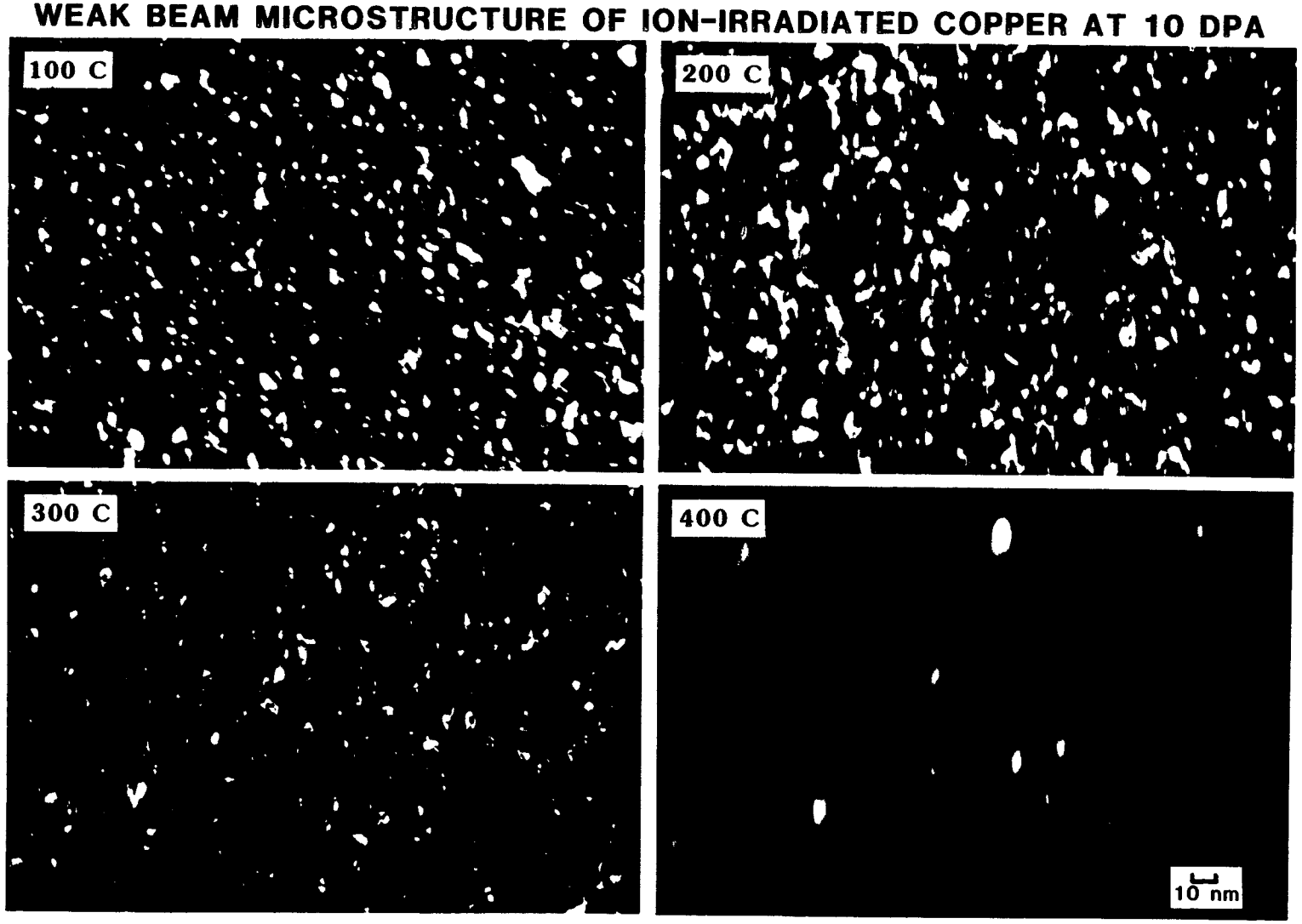

Fig. 7.33. Weak beam dark field microstructure of defect clusters in copper following ion irradiation to 10 dpa.

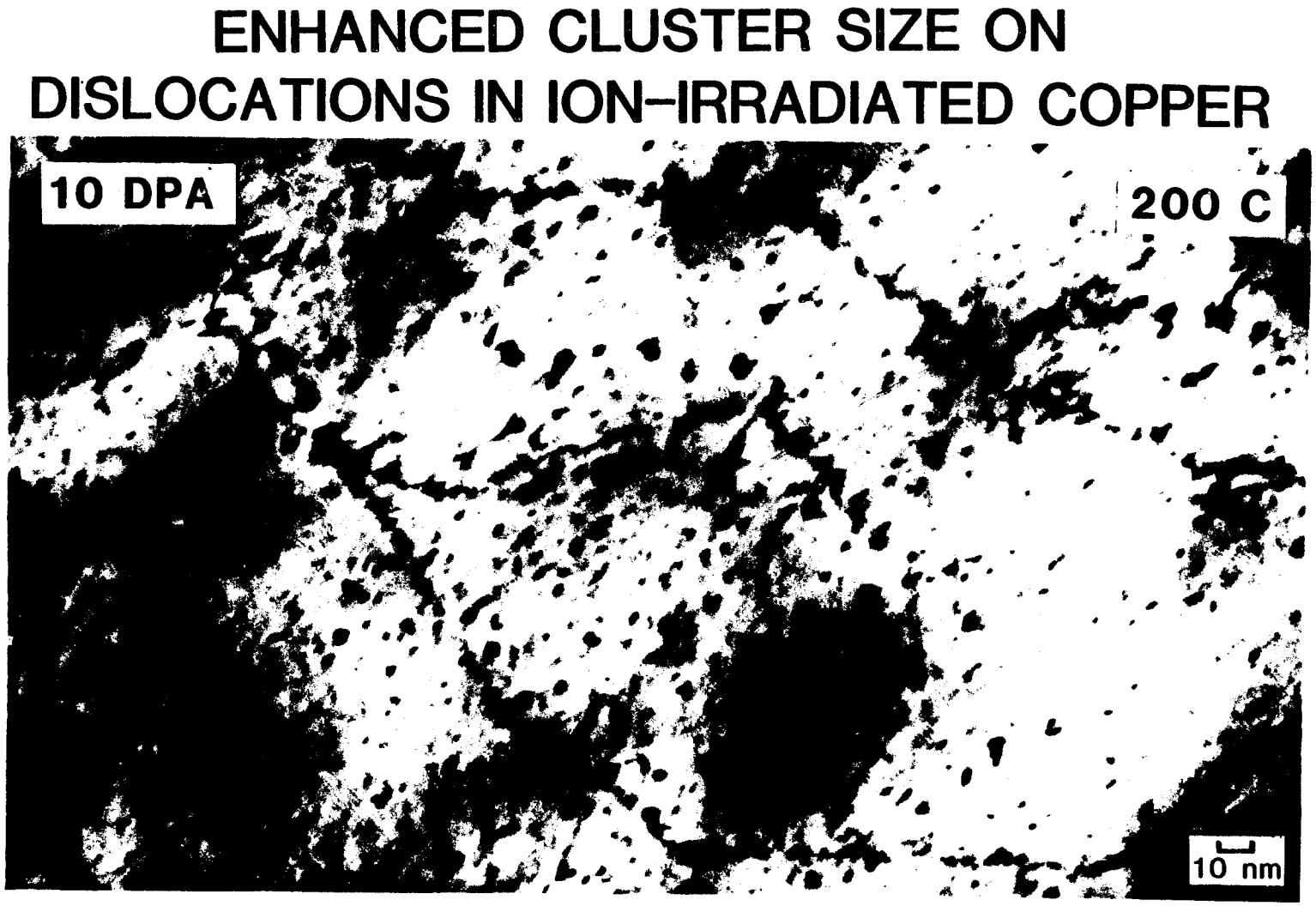

Fig. 7.34. Enlarged defect clusters on dislocations in copper following ion irradiation to 10 dpa at 200°C.

80% of the large clusters located near dislocations were interstitial-type loops.

Figure 7.35 gives the high-magnification bright field microstructure of pure copper irradiated with Cu ions to 10 dpa at 200°C. Triangle-shaped stacking fault tetrahedra (SFT) are visible along with other black spot defects that have no definite shape. Figure 7.36 shows the high-resolution weak beam dark field microstructure of irradiated copper at 200°C. Once again, a high density of SFT are visible.

There does not appear to be any substantial zone that is denuded of SFT in the vicinity of grain boundaries. Figure 7.37 illustrates the weak beam dark field microstructure of irradiated copper at a grain boundary. Formation of SFT occurs right up to the boundary, although there is possibly a lower SFT density within the first 10 nm of the grain boundary. Previous studies[45] have found that there is no denuded zone at grain boundaries for small defect clusters (< 5 nm) observed in copper following neutron irradiation. A denuded zone of ~ 100 nm width was observed for defects with sizes greater than 5 nm (predominantly interstitial-type clusters).

The measured defect cluster density and size distribution in ion-irradiated copper is shown in Fig. 7.38. The top graph is a plot of the SFT and total defect cluster density as a function of irradiation temperature. Representative error bars are indicated on the data points. The main source of error was due to uncertainties in the foil thickness. The foil thickness was determined from thickness

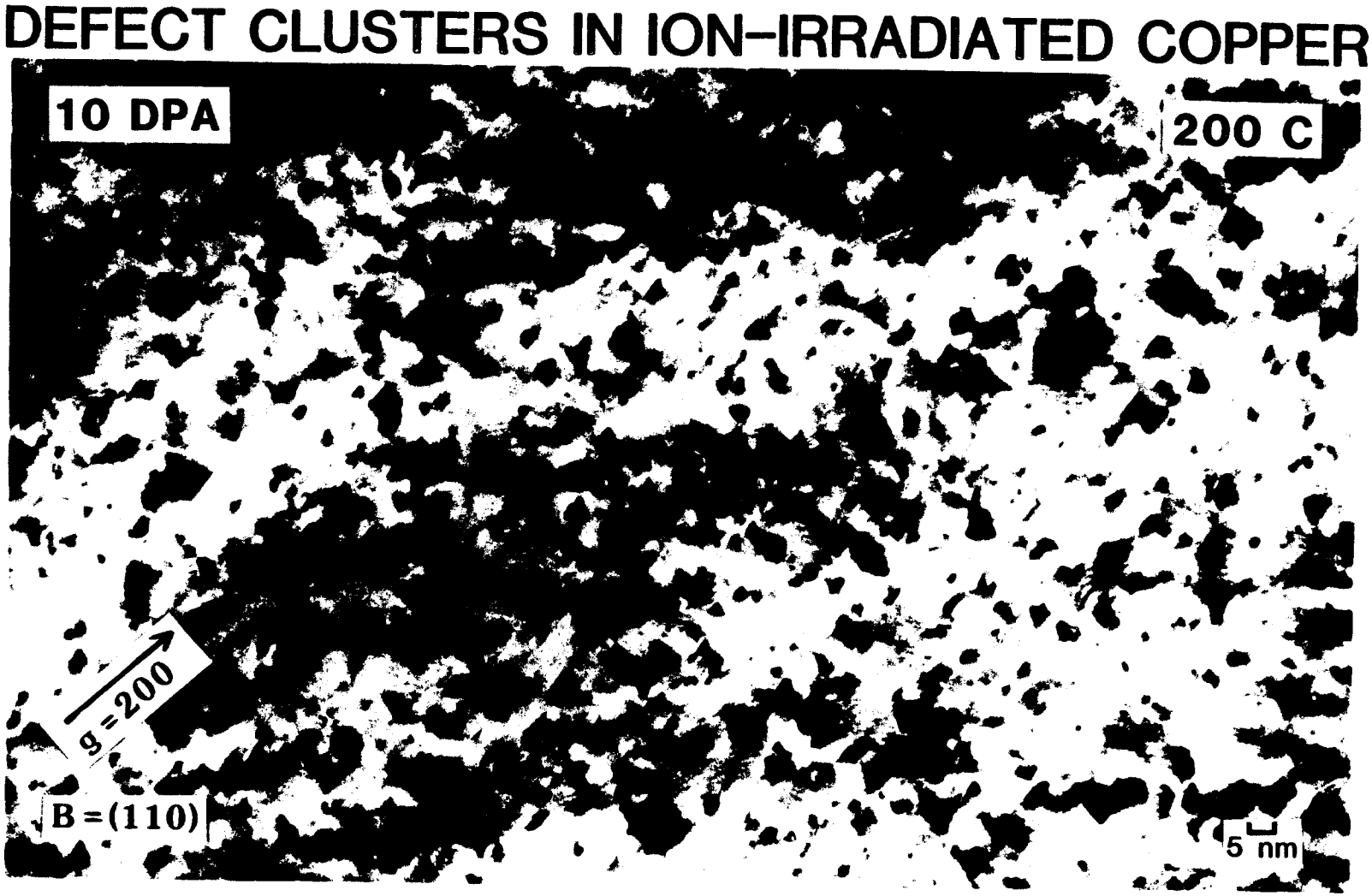

Fig. 7.35. Bright field microstructure of copper irradiated to 10 dpa at 200°C showing triangle-shaped stacking fault tetrahedra.

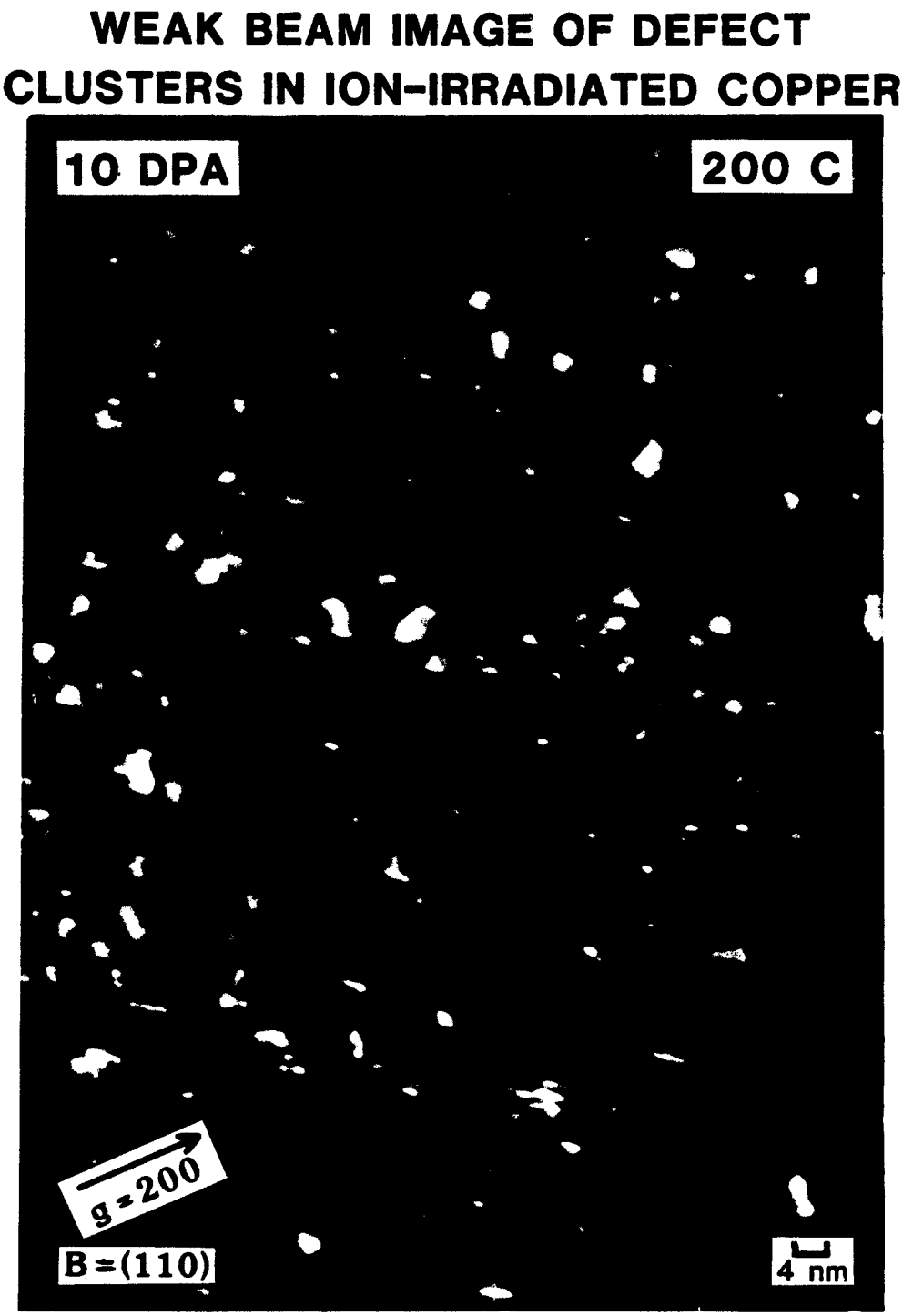

Fig. 7.36. Weak beam dark field microstructure of copper following ion irradiation to 10 dpa at 200°C.

DAMAGE MICROSTRUCTURE IN COPPER ADJACENT TO A GRAIN BOUNDARY

Fig. 7.37. Defect clusters adjacent to a grain boundary in copper irradiated to 10 dpa showing no significant denuded zone.

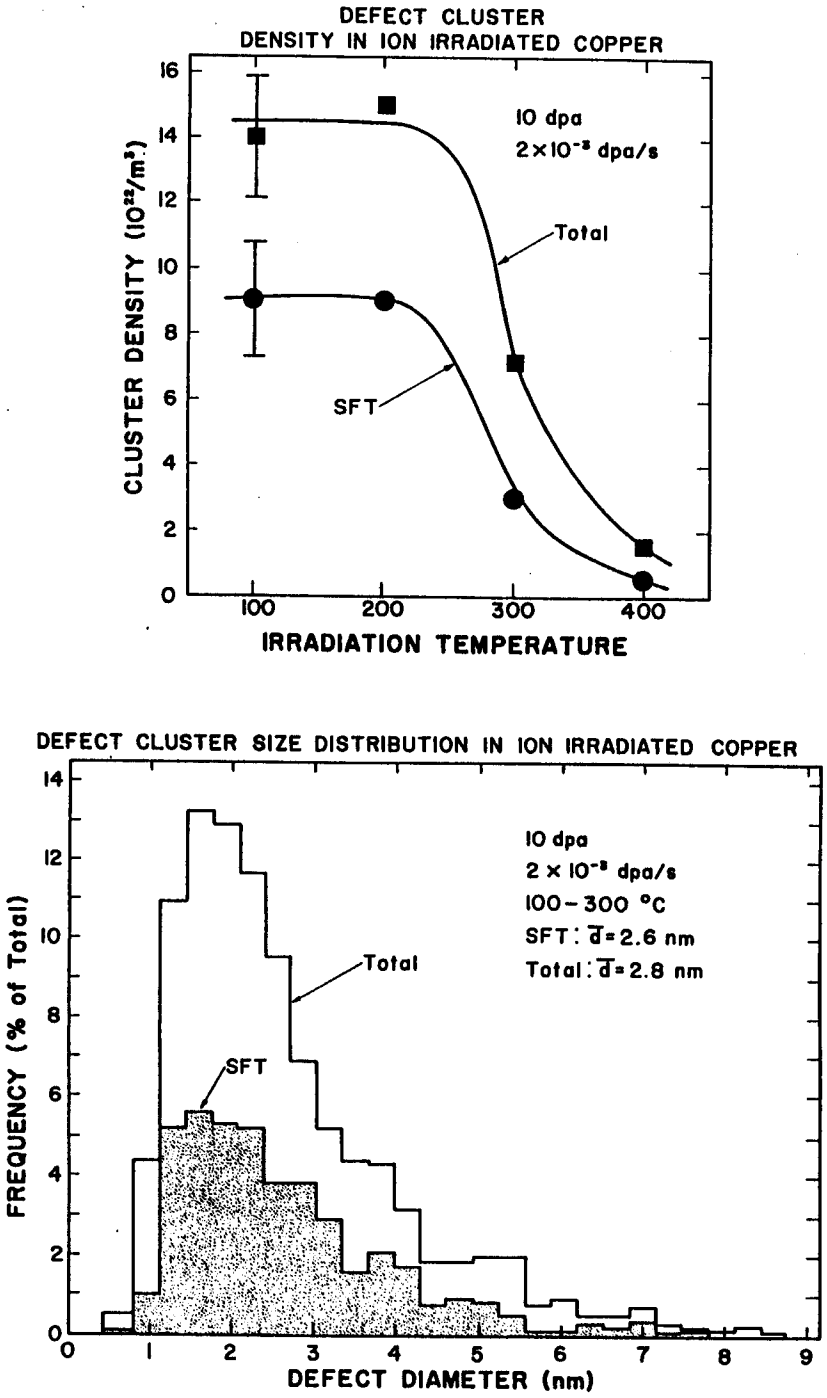

Fig. 7.38. Density and size distribution of stacking fault tetrahedra and total defect clusters in ion-irradiated copper.

fringes with an estimated ±20% accuracy. Both the SFT and total cluster density are constant for irradiation temperatures $\leq$ 200°C with values of 9 x $10^{22}/m^3$ and 1.4 x $10^{23}/m^3$, respectively. Irradiation at $\geq$ 300°C results in a sharp decrease in the cluster densities. The general trend of the cluster density versus irradiation temperature curve is in good agreement with previous investigations of ion irradiated copper,[46] i.e. the defect cluster density is constant for irradiation temperatures below 250°C and the density decreases rapidly for irradiation temperatures above 300°C. The fraction of defect clusters that are SFT is $\gtrsim$ 60% for irradiation temperatures of 100-200°C (Fig. 7.38). This fraction decreases at higher irradiation temperatures, becoming about 30% for irradiation at 400°C.

The bottom graph in Fig. 7.38 is a histogram showing the size and frequency of defect clusters observed. The measurements were made from bright field and weak beam dark field micrographs with a total print magnification of about 1 x 10^6. A total of 500 to 1500 defect clusters were counted using a Zeiss particle analyzer for each of the irradiation temperatures from 100-300°C. Only 150 clusters were counted for the 400°C irradiation condition due to the low cluster density. The SFT and total cluster size distributions were very similar for irradiation temperatures of 100-300°C. The size distributions appear to be close to log-normal, with a peak at about 2 nm. The mean SFT and total cluster diameters were determined to be

2.6 and 2.8 nm, respectively, over this temperature range. The mean defect size was $\gtrsim$ 4 nm following irradiation at 400°C.

Irradiation of copper at 100°C resulted in a coarsened damage microstructure in the peak damage region compared to the midrange damage microstructure (see Fig. 7.32). This difference in the peak and midrange damage microstructures was not evident at the other (higher) irradiation temperatures that were investigated, i.e. 200-400°C. A similar coarse peak damage microstructure was observed in SAA AMAX-MZC irradiated at 100°C (see Fig. 7.30). Figure 7.39 compares the peak and midrange damage microstructures of copper irradiated at 100°C. The larger defect clusters in the peak damage region appear to be dislocation loops, with an average diameter of 12 nm and a density of $\gtrsim$ 1 x $10^{21}/m^3$. These parameters are close to the measured values for the large loops in the peak damage region of MZC irradiated at 100°C (8 nm, 1 x $10^{21}/m^3$).

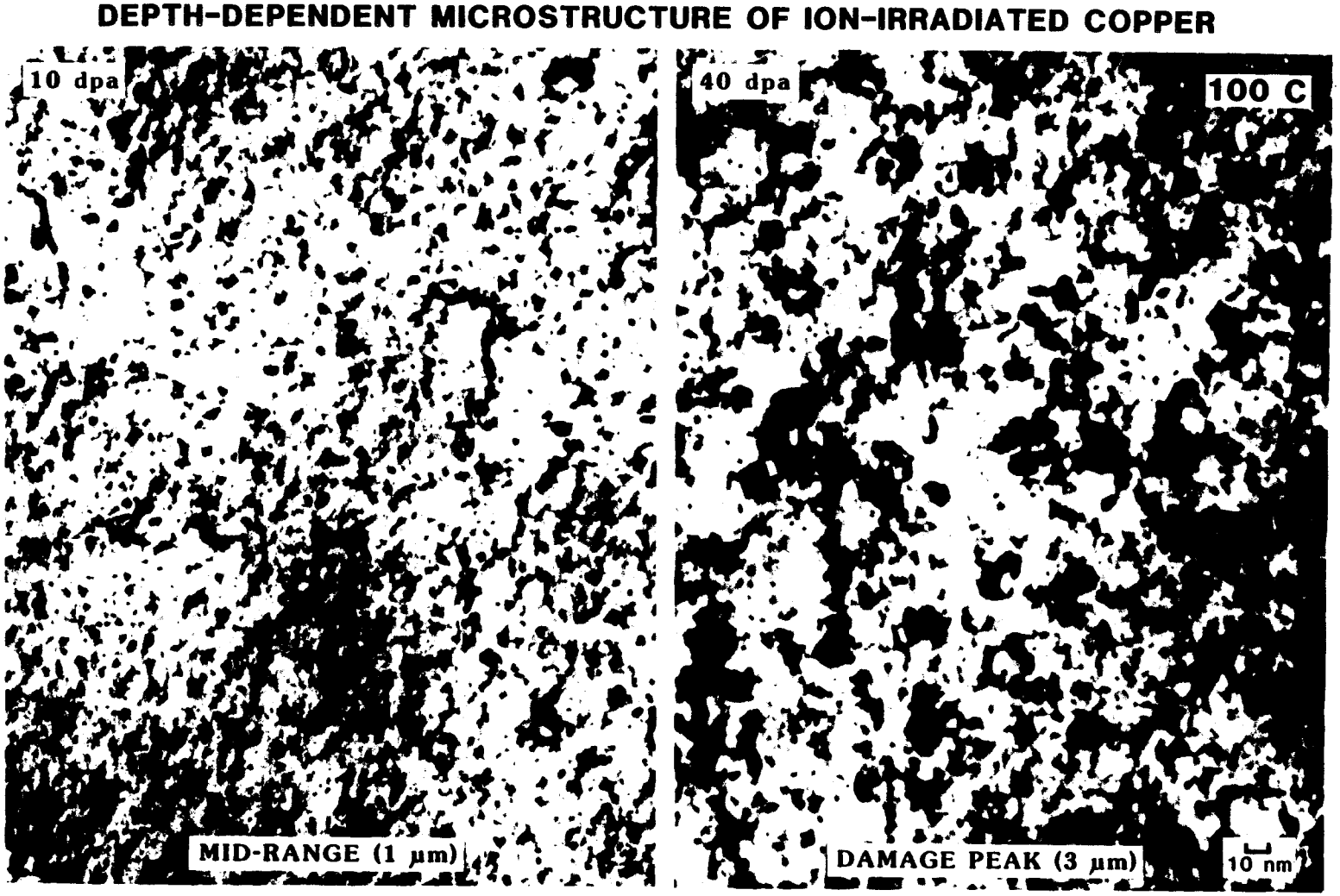

Fig. 7.39. Midrange and peak damage microstructure in copper irradiated with 14-MeV Cu ions to a peak damage level of 40 dpa at 100 C.

References for Chapter VII

1. M.Y-W. Lou and N.J. Grant, Met. Trans. A 15 (1984) 1491.

2. T. Nagai et al., Trans. Jap. Inst. Metals 14 (1973) 462. Also see Section IV.A.

3. R.R. Hart et al., Met. Trans. 1 (1970) 3163.

4. I.L. Dillamore and W.T. Roberts, Met. Rev. 10 (1965) 271-380.

5. J.W. Edington, Electron Diffraction in the Electron Microscope, Practical Electron Microscopy in Materials Science Monograph 2 (Phillips Technical Library, 1974); also see P.B. Hirsch et al., Electron Microscopy of Thin Crystals (Krieger Publ. Co., 1977).

6. J.W. Edington, Interpretation of Transmission Electron Micrographs, Practical Electron Microscopy in Materials Science Monograph 2 (Phillips Technical Library, 1974).

7. A.R. Graviano, AMAX Base Metals Research & Development, Inc., Carteret, NJ (private communication, Fall 1983).

8. G.E. Dieter, in Ductility, H.W. Paxton (Ed.), ASM Seminar, Oct. 1967, pp. 19-24.

9. N.F. Panayotou, "Design and Use of Nonstandard Tensile Specimens for Irradiated Materials Testing," in Symp. on Use of Nonstandard Subsized Specimens for Irradiated Testing, Albuquerque, NM, Sept. 1983, ASTM STP 888 (1985).

10. N. Igata et al. and D.G. Rickerby, in Symp. on Use of Nonstandard Subsized Specimens for Irradiated Testing, Albuquerque, NM, Sept. 1983, ASTM STP 888 (1985).

11. M. Reverchon, Heat Treatment of Copper and Its Alloys III: Structural Hardening, Traitement Thermique 133 (Mar. 1979) 61-66.

12. D.V. Assadi, "Microstructure and Properties of Dilute Copper Age Hardening Alloys," Ph.D. Thesis, New York Univ. (Feb. 1974); INCRA Report No. 207.

13. A.J. Hillel and P.L. Rossiter, Phil. Mag. B 44 (1981) 383-8.

14. P. Gregory et al., Metallurgia 74 (1966) 71-5.

15. P.V. Andrews et al., Phil. Mag. 19 (1969) 887.

16. F.R. Fickett, "Investigation of the Behavior of High Purity Copper in High Magnetic Fields," INCRA Report No. 186A (Aug. 1973).

17. S.J. Zinkle and G.L. Kulcinski, J. Nucl. Mater. 122/123 (1984) 449.

18. R.A. Brown, J. Phys. F 7 (1977) 1283.

19. F.J. Blatt, Physics of Electronic Conduction in Solids, (McGraw-Hill, 1968) 196-202.

20. CRC Handbook of Electrical Resistivities of Binary Metallic Alloys, K Schröder (Ed.) (CRC Press, 1983).

21. P. Gregory et al., Metallurgia 71 (1965) 207.

22. A.M. Korol'kov and E.V. Lysova, in Structure and Properties of Light Alloys, ERDA, National Science Foundation, ERDA-TR-75 (1980) 21-27 (translated from Russian).

23. R.O. Williams, Trans. ASM 52 (1960) 530 (referenced in Elliott, Constitution of Binary Alloys, McGraw-Hill).

24. M. Hansen and K. Anderko, Constitution of Binary Alloys, (McGraw-Hill, 1958).

25. V. Zwicker, Metall. 16 (1962) 409.

26. D.B. Butrymowicz, J.R. Manning and M.E. Mead, Diffusion Rate Data and Mass Transport Phenomena for Copper Systems, Monograph V in the INCRA Series on the Metallurgy of Copper (1977); also contained in a 5-part series in J. Physical and Chem. Ref. Data, 2-6 (1973-1977).

27. A.F. Clark et al., Cryogenics 10 (1970) 295. The authors mistakenly reported this value as the specific resistivity of pure zirconium in copper. The resistivity was measured on an aged Cu-Zr alloy and therefore the excess resistivity is due to the Cu_5Zr precipitate.

28. C. Kittel, Introduction to Solid State Physics, 5th Ed. (Wiley, 1976).

29. ASTM B193-78, Standard Method of Test for Resistivity of Electrical Conductor Materials, 1983 Annual Book of ASTM Standards Vol. 2.01, Copper and Copper Alloys. (The measured resistivity was corrected to 20°C for the conductivity calculation using ASTM standard methods.)

30. A.L. Bement, in 2nd Intern. Conf. on The Strength of Metals and Alloys, Vol. 1, Pacific Grove, CA (ASM, 1970) 693.

31. L.M. Brown in Proc. 5th Intern. Conf. on The Strength of Metals and Alloys, Vol. 3, P. Haasen et al. (Eds.), (Pergamon Press, 1979).

32. N.M. Ghoniem et al., in Effects of Radiation on Materials, H.R. Brager and J.S. Perrin (Eds.), ASTM STP 782 (1982) 1054.

33. R.E. Reed-Hill, Physical Metallurgy Principles, 2nd Ed. (Brooks/Cole, 1973) 267-325.

34. C. Logan et al., J. Nucl. Mater. 103/104 (1981) 1551.

35. T. Maruta, J. Japan Copper and Brass Res. Assn. 2 (1963) 89.

36. H. Suzuki et al., J. Japan Inst. Metals 33 (1969) 628.

37. T. Nagai et al., Trans. Jap. Inst. Metals 14 (1973) 462.

38. S. Dermarkar et al., Acta Met. 31 (1983) 1315.

39. H. Gleiter and B. Chalmers, High Angle Grain Boundaries, Progress in Materials Science Vol. 16 (Pergamon, 1972) 127-178.

40. P.B. Hirsch et al., Electron Microscopy of Thin Crystals, (Krieger, 1977).

41. V.A. Phillips, Metallography 7 (1974) 137-155.

42. R.W. Knoll, Ph.D. Thesis, Nuclear Engineering Dept., University of Wisconsin-Madison (1981).

43. S.J. Zinkle and R.W. Knoll, "A Literature Review of Radiation Damage Data for Copper and Copper Alloys," UWFDM-578 (June 1984).

44. N. Yoshida et al., J. Nucl. Mater. 122/123 (1984) 664.

45. M.J. Makin, A.D. Whapham and F.J. Minter, Phil. Mag. 7 (1962) 285.

46. C.A. English et al., Phil. Mag. 34 (1976) 603.

CHAPTER VIII. DISCUSSION

VIII.A. Effect of Thermal Annealing on Physical Properties

AMAX-MZC has a higher strength than AMZIRC for all annealing conditions investigated in this study (Fig. 7.13). Conversely, AMZIRC has a higher electrical conductivity compared to AMAX-MZC at all conditions. The higher strength of AMAX-MZC compared to AMZIRC is apparently due to precipitation hardening effects (see Section VII.A.2). The aging studies performed in this thesis indicate that AMZIRC (Cu-Zr) develops only a slight precipitation hardening response. This is in agreement with the majority of studies to date on Cu-Zr alloys, as reviewed in Section IV.A. On the other hand, AMAX-MZC (Cu-Cr-Zr-Mg) exhibits appreciable precipitation hardening.

The measured electrical conductivities of the cold-worked plus aged alloys were significantly below the manufacturer's quoted values (see Fig. 1.1). Analysis of the thermal annealing data in Table 7.4 reveals that the electrical conductivity was greatly enhanced by short term annealing at temperatures $< 400°C$ whereas the alloy strength was only slightly reduced. It therefore appears that the alloys were given an insufficient aging treatment by the manufacturer -- improved electrical properties and similar mechanical properties could have been achieved by aging an additional 1 hour at 350-400°C (the aging treatment of the as-received alloys consisted of a 0.5 hour anneal at 375 and 400°C for AMZIRC and AMAX-MZC, respectively). The resultant optimum yield strength and electrical conductivity

values are (400 MPa, 90% IACS) for AMZIRC and (425 MPa, 85% IACS) for AMAX-MZC (see Table 7.4).

Both AMZIRC and AMAX-MZC develop their optimum properties through a combination of cold-work plus aging. This leads to very attractive strength and electrical conductivity values for low temperature applications. However, the high strength of these alloys is lost when recrystallization occurs (Section VII.B). The recrystallization temperature depends on the annealing time and is about 475°C for both AMZIRC and AMAX-MZC for a 1 hour anneal. It has been empirically established that the recrystallization rate of metals follows an Arrhenius relationship.[1] The microhardness annealing data may therefore be plotted as a single curve by making use of the Larson-Miller parameter,[2] as shown in Fig. 8.1 for the two alloys. The two curves contain all of the short term annealing data presented in Table 7.4. The sharp decrease in Vickers microhardness number in the two plots corresponds to recrystallization, and occurs at a critical Larson-Miller parameter value of P_{crit} = 15.0 for both alloys.

Analysis of the Larson-Miller equation at its critical recrystallization value allows an estimation to be made of the recrystallization temperature for long-term annealing. Table 8.1 summarizes the extrapolated time dependent recrystallization temperatures obtained from this analysis. The curves in Fig. 8.1 predict a recrystallization temperature of 320°C for both AMZIRC and AMAX-MZC for a 20 year anneal, which is the maximum design lifetime of a

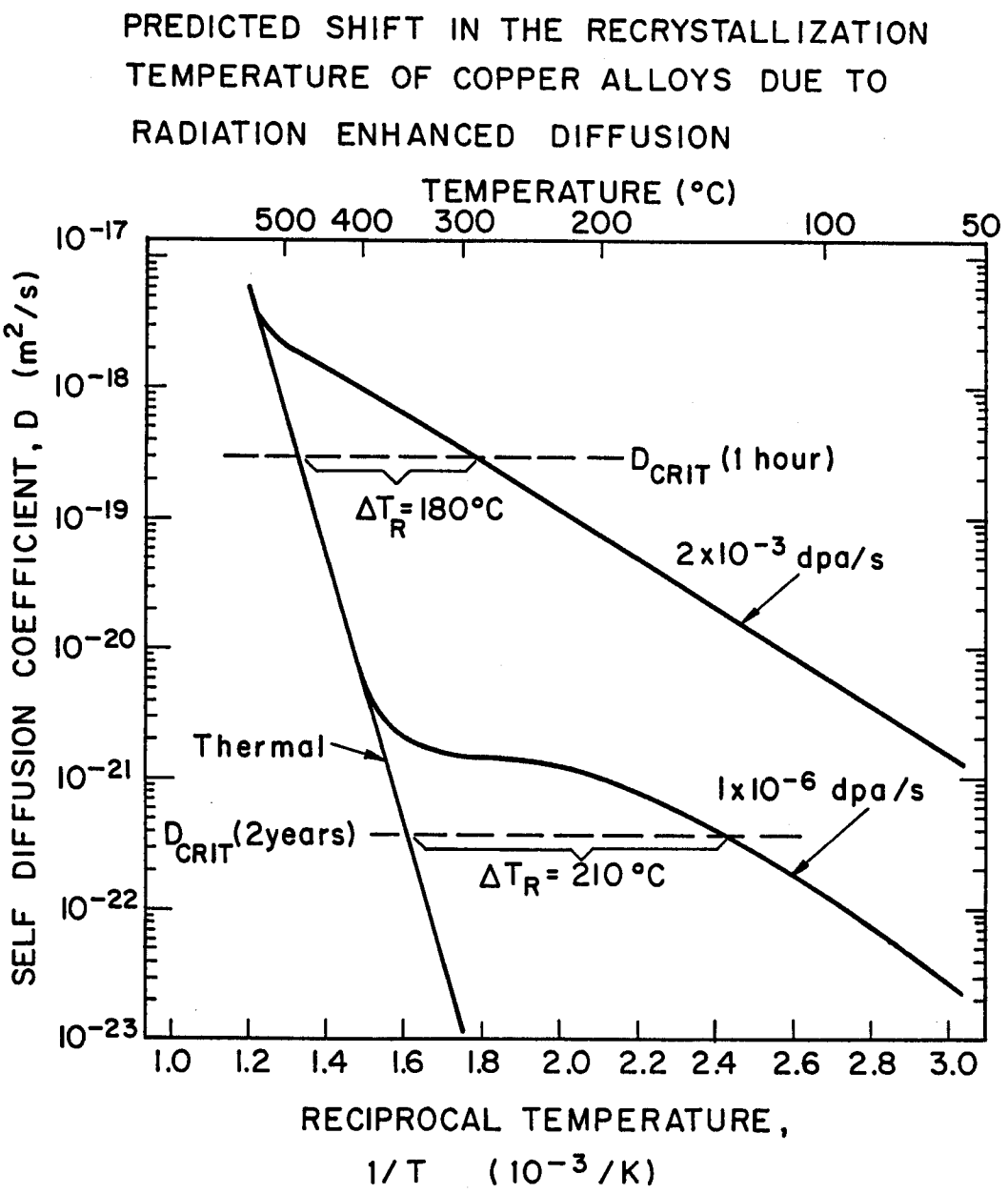

Fig. 8.5. Predicted shift in recrystallization temperature for the irradiated cold-worked plus aged copper alloys.

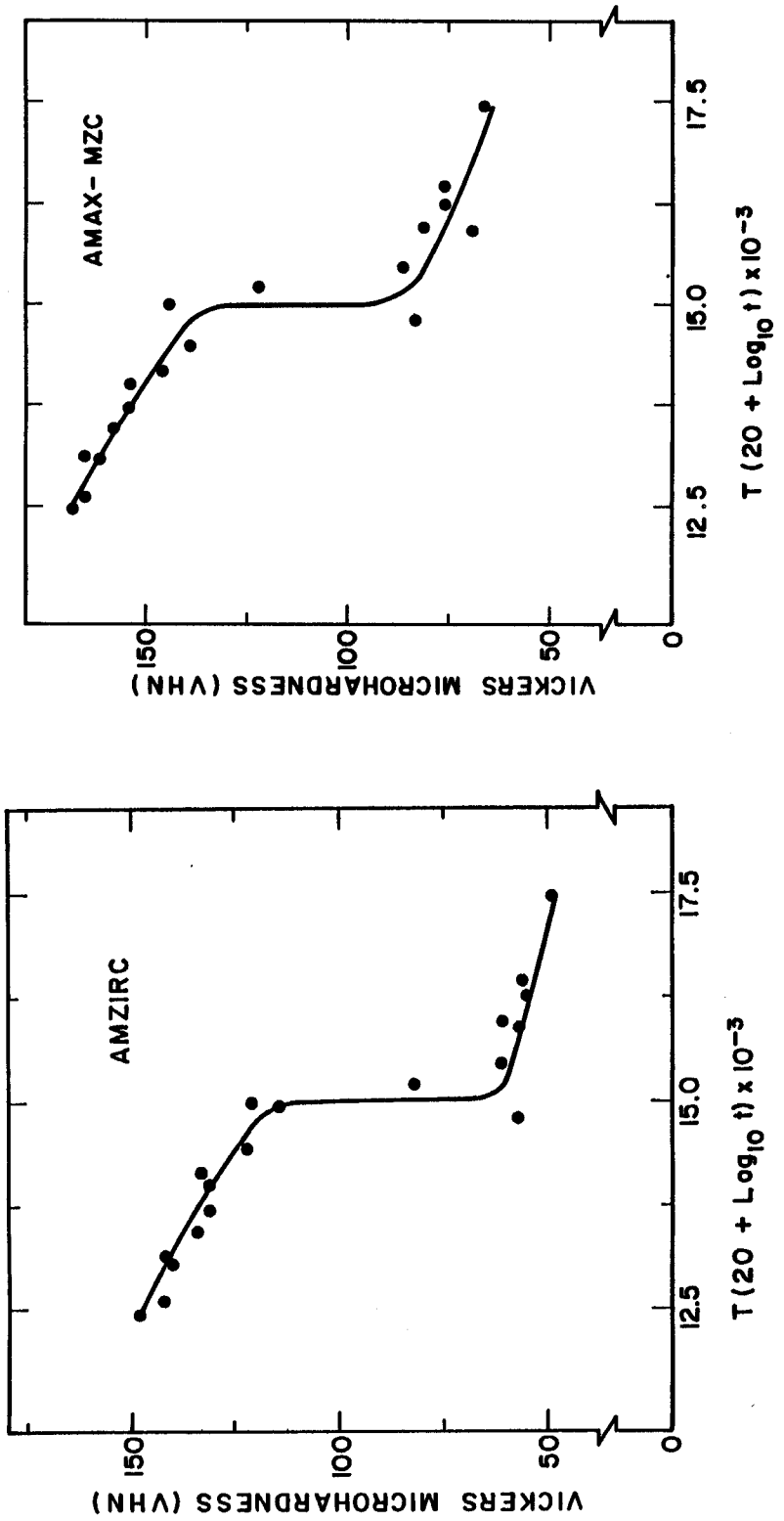

Fig. 8.1. Vickers microhardness vs. Larson-Miller parameter for cold-worked plus aged alloys in the as-received and annealed conditions.

Table 8.1. Predicted Recrystallization Temperature (T_R) of AMZIRC and AMAX-MZC

Anneal Time:	1 Month	1 Year	10 Years
T_R	380°C	350°C	330°C

copper alloy device in a fusion reactor.[3] Therefore, from a pure thermal annealing viewpoint, these alloys should not be designed for long-term high-strength operation in any environment where the ambient temperature will exceed 300°C -- otherwise recrystallization may occur with an accompanying loss in strength and possible failure of the device. Stress[4] and irradiation effects may limit the safe operation of these devices to even lower temperatures due to enhanced recrystallization effects (see Section VIII.B). It was noted in Section VII.B that the large particles present in AMZIRC and MZC (due to incomplete homogenization of the alloys during fabrication) generally act to accelerate the recrystallization process. Because of this, steps should be taken to minimize their concentration in these alloys. Problems with failure of 14-MeV neutron source targets at Lawrence Livermore National Laboratory[5] during operation may possibly be due to large Zr particles in AMZIRC accelerating the recrystallization (softening) process.

It is simple to derive that the critical Larson-Miller parameter at recrystallization, P_{crit}, is related to an Arrhenius-type activation energy (Q) by the following:

$$P_{crit} \times 10^3 = \frac{Q}{2.303\ R} \qquad (8.1)$$

where R is the gas constant. Analysis of Fig. 8.1 (P_{crit} = 15.0) indicates that the activation energy for recrystallization of AMZIRC and AMAX-MZC is Q = 3.0 eV. This may be compared with the activation energy for self-diffusion in copper,[6] Q_{SD} = 2.07 eV.

Comparison of the measured Vickers microhardness number (VHN) and yield strength (σ_y) of cold-worked plus aged AMZIRC and AMAX-MZC in their as-received and annealed states leads to a linear relationship (see Fig. 7.13, Table 7.4). The yield strength-microhardness correlation plots for AMZIRC and AMAX-MZC are given in Fig. 8.2. Data for the alloys in the solution annealed and solution annealed plus aged conditions are also included in these plots. A linear correlation between VHN and yield strength (σ_y) exists over the entire range of conditions investigated. The correlation equations that describe the least squares fit to the data are, for AMZIRC

$$\sigma_y(\text{ MPa}) = 3.03\ \text{VNH} - 38 \qquad (8.2)$$

and for AMAX-MZC,

$$\sigma_y\ (\text{MPa}) = 3.00\ \text{VHN} - 17\ . \qquad (8.3)$$

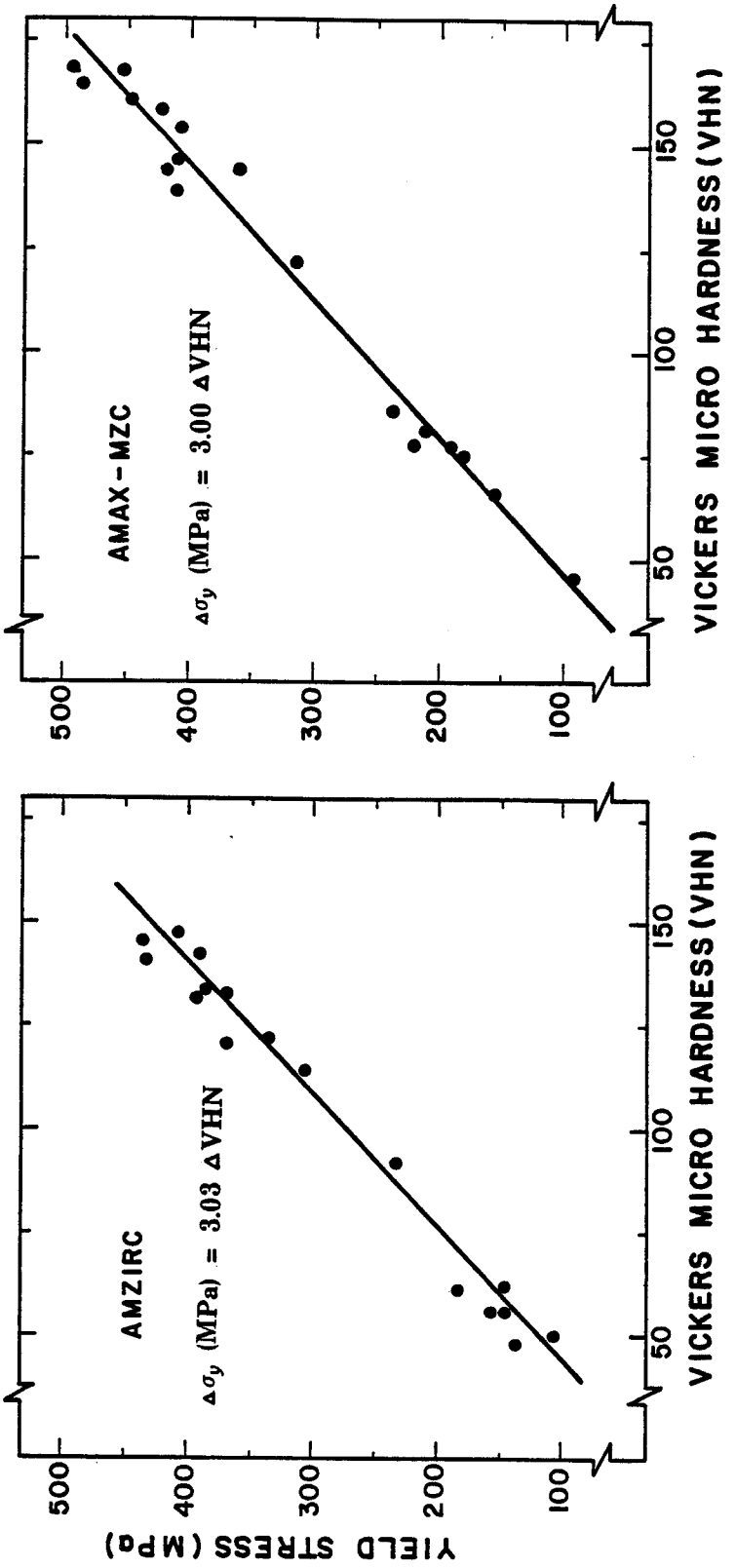

Fig. 8.2. Correlation of the yield strength and Vickers microhardness number for the cold-worked plus aged and annealed copper alloys.

The fact that the correlation plots have a nonzero intercept is believed to indicate that the correlations are not applicable for very low strength alloys (< 100 MPa yield strength). However, it should be noted that this strength level is less than the solution annealed yield strengths of the alloys.

One valid criticism of the experimental procedure followed in this investigation is that all tensile specimens were punched from foils after they had been annealed. It is uncertain whether edge deformation due to punching had a significant effect on the measured mechanical properties of the annealed miniature tensile specimens.

It is surprising that the correlation plot of yield strength and VHN is linear over the entire range of possible thermomechanical conditions for AMZIRC and AMAX-MZC. As evidence in Fig. 7.12, the microstructures of the two alloys changed dramatically as a result of annealing. Theoretically, the shape of the correlation plot should depend on the work hardening coefficient,[7,8] which increased from n = 0.04 to n = 0.5 following annealing of the cold-worked plus aged alloys. The slope of the correlation plot was the same for both the precipitation-hardenable alloy (AMAX-MZC) and the alloy which does not exhibit appreciable precipitation hardening effects (AMZIRC). The derived correlation for these high-strength, high-conductivity copper alloys, $\sigma_y \sim 3.0$ VHN, is identical to the relation found for the strength increase in copper and solid solution copper alloys due to radiation hardening.[9] Similar correlation results have also been reported for nonirradiated copper and other metals.[7,10]

VIII.B. Radiation Enhanced Recrystallization in Copper Alloys

It was determined in Section VII.C.1 that ion irradiation of AMZIRC and AMAX-MZC at temperatures $\gtrsim$ 300°C resulted in an enhancement of recrystallization. Another recent study of AMZIRC has similarly found that ion irradiation causes an acceleration of recovery and recrystallization processes.[11] There have been several previous observations of radiation-enhanced recrystallization effects in metals following neutron and electron irradiation (see, e.g., Refs. 12-18). The acceleration of the recrystallization process during irradiation has been proposed to be caused by an increase in the grain boundary mobility due to a supersaturation of vacancies (radiation-enhanced diffusion) or by an increase in the grain nucleation rate.[13,15,16,18] However, there has been relatively little effort devoted to making quantitative predictions of the magnitude of these effects. It is important to quantitatively establish the effect of irradiation on lowering the recrystallization temperature of high-strength alloys such as AMZIRC and AMAX-MZC since a large portion of their strength is lost when recrystallization occurs (Section VII.B).

The degree of radiation-enhanced recrystallization as a function of irradiation temperature may be quantified by making appropriate measurements of the subgrain size in irradiated and nonirradiated regions of the foils. The most common procedure is to measure the grain size using the intercept method. In the present analysis, no distinction is made between the nucleation of subgrains (polygoniza-

tion) and grains (primary recrystallization). Instead, the approach of Vaidya and Ehrlich[17] has been adopted where recrystallization is taken to start with the formation of subgrains and it proceeds until grain growth processes become important.

Figure 8.3 shows the change in grain size in the longitudinal (rolling) direction as a function of irradiation temperature for AMZIRC and AMAX-MZC, as determined from TEM measurements. Figure 8.4 shows the dependence of subgrain area (as viewed in cross-section) on irradiation temperature. Both large angle and small angle boundaries have been included in the measurements presented in Figs. 8.3 and 8.4. It has been proposed that the subgrain area is a better parameter for determining the degree of recrystallization.[17] Measurements on samples irradiated at the same temperature but at different damage levels ranging from 1 to 40 dpa indicated that there was no dose dependence on subgrain size for this range of damage levels. This is in agreement with another study[14] which found that recrystallization effects in cold-worked copper were independent of neutron fluence for damage levels $\gtrsim$ 0.01 dpa. Figures 8.3 and 8.4 show that the subgrain size and area are independent of the ion irradiation temperature over the interval 100-300°C for both AMZIRC and AMAX-MZC. The subgrain size in this temperature range is equal to the measured as-received (nonirradiated) value (0.4 μm, 0.34 μm for AMZIRC and AMAX-MZC, respectively).

The subgrain size and area increased above the as-received values following ion irradiation at temperatures greater than 300°C,

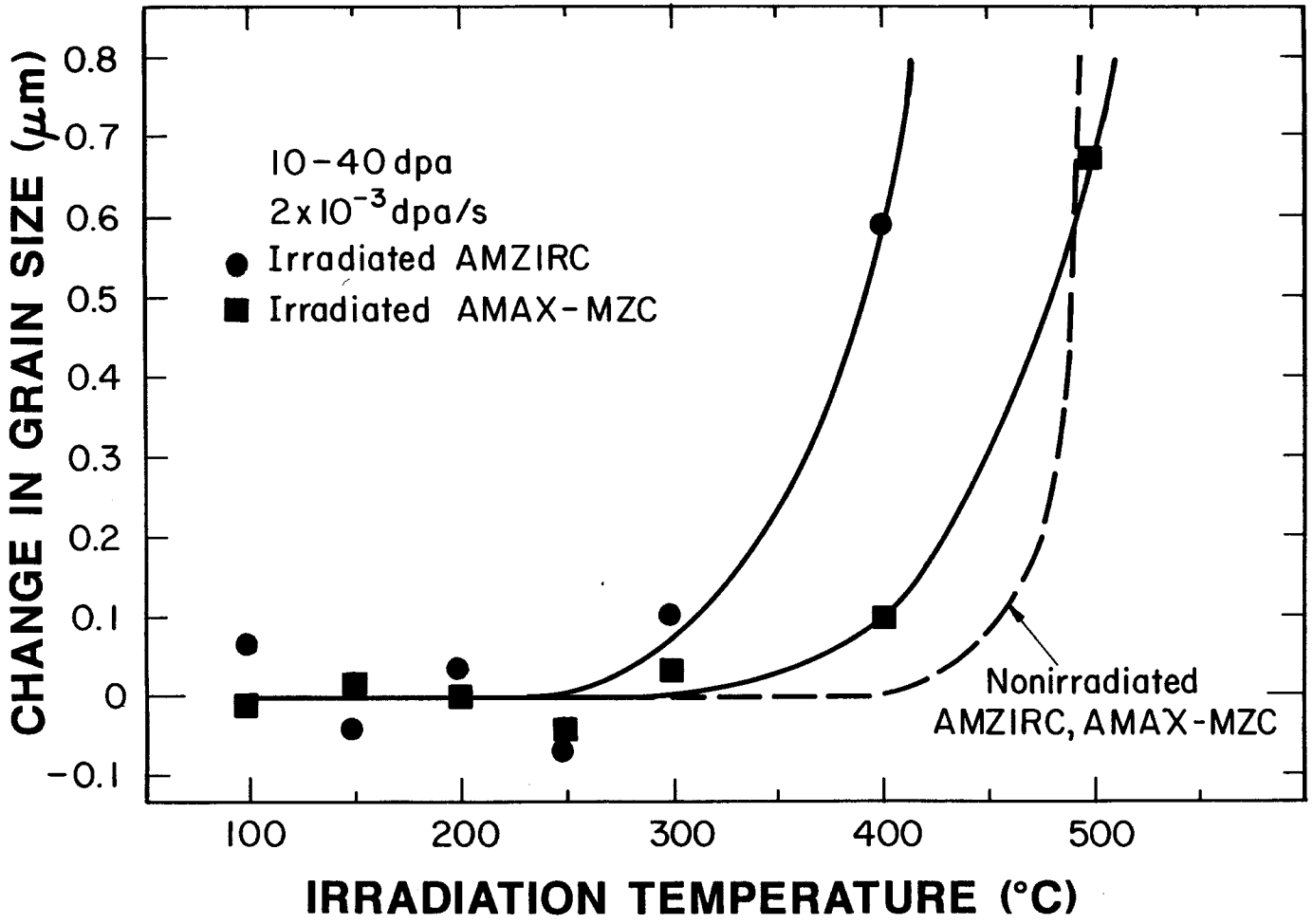

Fig. 8.3. Grain size of cold-worked plus aged copper alloys vs. irradiation temperature. The initial grain sizes were 0.4 and 0.34 μm for AMZIRC and MZC, respectively.

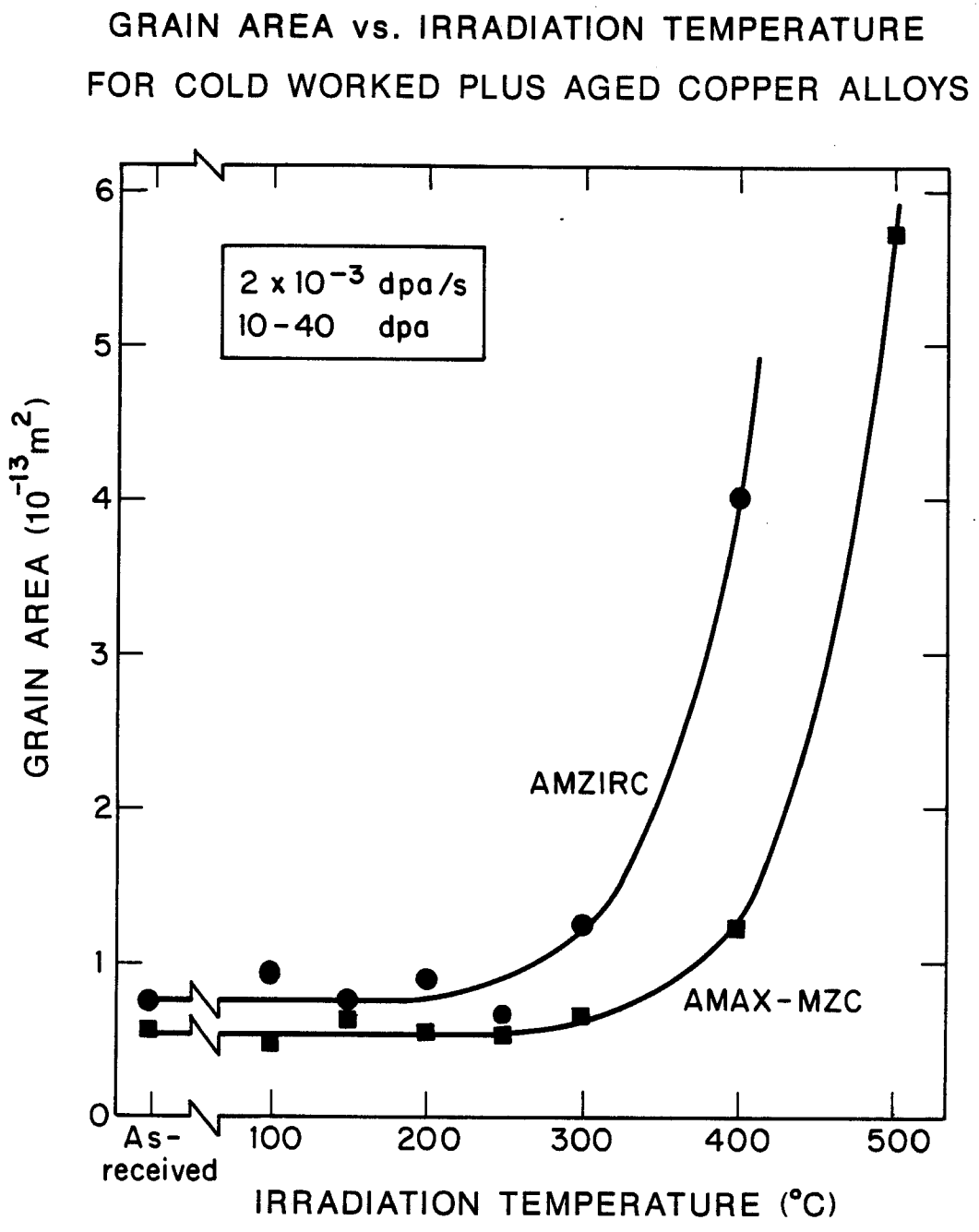

Fig. 8.4. Grain area (including subgrains) of cold-worked plus aged copper alloys vs. irradiation temperature. Note that the grain/subgrain area is constant for irradiation temperatures below 300°C, with a value equal to that of the as-received material.

indicating that recrystallization was occurring. Subgrain nucleation was visible in irradiated regions of the foils (Section VII.B). The subgrains were generally found along preexisting high angle grain boundaries. In the absence of irradiation, the subgrain size of both alloys was determined to be constant up to 475C for a 1 hour anneal, with a rapid increase at higher temperatures. Figure 8.3 (subgrain size) suggests that AMZIRC begins to recrystallize at ~ 350°C during ion irradiation, while AMAX-MZC does not start to recrystallize until irradiation temperatures of ~ 450°C are reached. Figure 8.4 (subgrain area) indicates that recrystallization has started to occur following ion irradiation at 300°C in AMZIRC and 400°C in AMAX-MZC. This represents an effective shift in the recrystallization temperature of these two alloys due to ion irradiation of ~ 75°C for AMAX-MZC and ~ 150°C for AMZIRC.

A quantitative prediction of the shift in the recrystallization temperature (ΔT_R) during irradiation may be made by assuming that the acceleration of recrystallization kinetics is solely due to radiation-enhanced diffusion. The radiation-enhanced diffusion coefficient was determined from a calculation of the vacancy concentration during irradiation based on steady state nucleation theory. Only monovacancy diffusion was considered to contribute to the radiation-enhanced diffusion. Figure 8.5 shows the calculated temperature-dependent self-diffusion coefficient of copper for conditions appropriate to ion irradiation (2×10^{-3} dpa/s), neutron irradiation (1×10^{-6} dpa/s) and thermal annealing. The predicted shift in recrystal-

lization temperature during irradiation may be obtained as follows: The recrystallization temperature of AMZIRC and AMAX-MZC for a 1 hour thermal anneal is about 475°C. This corresponds to a self-diffusion coefficient of 3×10^{-19} m^2/s. During ion irradiation at 2×10^{-3} dpa/s, the radiation-enhanced self-diffusion coefficient equals 3×10^{-19} m^2/s for an irradiation temperature of about 300°C (Table 8.1). The shift in the recrystallization temperature due to ion irradiation is therefore predicted to be $\Delta T_R \simeq 180°C$.

Neutron irradiation at 1×10^{-6} dpa/s has no effect on the self-diffusion coefficient for irradiation temperatures above 375°C due to a low vacancy supersaturation at high temperatures (Fig. 8.5). The extrapolated recrystallization temperature of AMZIRC and AMAX-MZC for a 2 year anneal is $\lesssim$ 350°C (Table 8.1), which corresponds to a self-diffusion coefficient of about 4×10^{-22} m^2/s. The predicted recrystallization temperature for a 10^{-6} dpa/s neutron irradiation is about 140°C ($\Delta T_R \simeq 210°C$). Many of the proposed applications for high strength copper alloys in fusion devices require operation at irradiation temperatures of 100-350°C for several years[3] (also see Table 1.1). The preceding calculations indicate that AMZIRC and AMAX-MZC will recrystallize in this type of an irradiation environment (probably with an accompanying loss of strength).

It is well established that recrystallization requires a sufficiently large driving force in combination with adequate atomic mobility in order to proceed.[15,16,18] Irradiation tends to increase the driving force for recrystallization by creating defect

clusters in the lattice. The atomic mobility is also increased during irradiation due to a supersaturation of point defects (radiation-enhanced diffusion). Previous studies have shown that grain boundary mobility is directly related to the vacancy concentration in the matrix.[13,15,18] In this regard, it is believed that radiation-enhanced recrystallization differs from irradiation creep in the sense that thermal creep has been shown to be independent of radiation-enhanced diffusion.[19,20] This may be due to the fact that irradiation creep involves a "directional flux" of defects whereas recrystallization simply requires adequate mobility in any direction. However, it certainly has not been proven in this thesis that radiation-enhanced diffusion is responsible for the observed accelerated recrystallization kinetics.

The predicted shift in the recrystallization temperature of AMZIRC due to ion irradiation (Fig. 8.5) is in reasonable agreement with the actual observations (Fig. 8.4). In particular, the predicted and observed recrystallization temperatures for AMZIRC during ion irradiation are both about the same, 300°C. The results for AMAX-MZC are not in as close of agreement; the predicted and observed recrystallization temperatures are 300°C and 400°C, respectively.

The difference between the predicted and observed radiation-enhanced recrystallization temperature of AMAX-MZC is probably due to the neglect of solute/precipitate effects in the recrystallization calculations. Vaidya and Ehrlich[17] found that slight variations in the composition of irradiated stainless steel resulted in a spectrum

of recrystallization stages that ranged from unrecrystallized to completely recrystallized. In the present case, AMZIRC is a simple binary alloy containing 0.15% Zr whereas AMAX-MZC is a quaternary alloy containing 0.65% Cr, 0.15% Zr and 0.04% Mg.

Examination of the damage microstructure of the two alloys following irradiation at different temperatures indicated that recrystallization is initiated in both AMZIRC and AMAX-MZC at temperatures of ~ 300°C, i.e. subgrain nucleation occurs (Figs. 7.23, 7.24). However, the coalescence and growth of these subgrains during irradiation is suppressed in AMAX-MZC relative to AMZIRC (Fig. 8.4). This results in a sluggish recrystallization response of AMAX-MZC that is maintained up to irradiation temperatures of 500°C. Chromium and magnesium are both oversized solutes in copper[21] and are expected to migrate away from vacancy sinks such as grain boundaries during irradiation (vacancy inverse Kirkendall effect). It has also been observed that solutes which are repelled from grain boundaries act to strongly retard grain growth.[18,22] Therefore, it appears that irradiation enhances the initiation of recrystallization in AMAX-MZC (subgrain formation), but retards subgrain coalescence and subsequent grain growth. Irradiation enhances all phases of recrystallization in AMZIRC.

The grains formed during radiation-enhanced recrystallization of AMZIRC and AMAX-MZC were generally not equiaxed, but instead were elongated in the rolling direction. Measurements of the grain size in cross-section provided results on the longitudinal (ℓ) and z com-

ponents of the grain size (the z direction is perpendicular to the rolling plane, i.e. at right angles to the longitudinal and transverse directions). The cross-section grain size ratio (ℓ/z) decreased slightly with increasing irradiation temperature. The AMAX-MZC subgrains were closer to being equiaxed ($\ell/z = 1$) than the AMZIRC subgrains. The values of ℓ/z for the as-received, 100°C irradiated, and 400°C irradiated cold-worked plus aged alloys were (2.6, 2.6, 2.3) for AMZIRC and (2, 2, 1.5) for AMAX-MZC. Previous recrystallization studies have also found a preferential orientation of recrystallized grains with respect to the original cold-worked texture.[18] Some of the anisotropy in grain size in the present case may also be due to the experimental conditions -- the irradiated zone in which radiation-enhanced recrystallization occurred was essentially unlimited in the longitudinal and transverse directions, but it extended only 2 to 3 μm in the z direction.

Recent neutron irradiation studies of AMZIRC and AMAX-MZC have found that their yield strengths decreased following irradiation to 10-15 dpa at temperatures of 450°C[23] and 385°C.[24] Since these irradiation temperatures are too high for radiation-enhanced diffusion processes to be important (Fig. 8.5), the observed softening is probably due to thermal annealing effects alone. It should be noted that these irradiation temperatures are above the predicted thermal anneal recrystallization temperature of AMZIRC and MZC for the > 1000 hr irradiation times that were incurred (see Table 8.1).

VIII.C. Microstructural Changes in Irradiated Copper Alloys

Under suitable conditions, theory predicts that irradiation can lead to either precipitate coarsening or dissolution[25] (also see Section III.C). TEM examination of the irradiated solution annealed plus aged AMZIRC and AMAX-MZC copper alloys did not produce any evidence of precipitate coarsening or dissolution. Quantitative measurements of the precipitate parameters at ion irradiation temperatures below 400°C were complicated by the presence of "black spot" defects formed during the irradiation. It was difficult to distinguish between the small ($d < 4$ nm) precipitates and point defect clusters, with the exception of the defect clusters in the form of SFT. However, there does not appear to be any well developed indications of precipitate dissolution or coarsening at ion irradiation temperatures of 100-300°C. At higher irradiation temperatures, the black spot density decreases to an insignificant level and direct measurement of the irradiated precipitate size and density is possible. There was no difference between the irradiated and nonirradiated precipitate parameters at 400°C (see Fig. 7.28). Piercy[26] indirectly observed that neutron irradiation dissolved precipitates with a diameter $\lesssim$ 2.5 nm in Cu-2% Co. Chou and Ghoniem[27] have predicted that complete dissolution can occur for precipitates smaller than 1 nm. The average precipitate size in the present study ranged from 4 nm (Cu_5Zr) to 6 nm (Cr). This size may be large enough to prevent any significant dissolution from occurring.

A high density of small stacking fault tetrahedra (SFT) were observed in the solution annealed plus aged copper alloys and pure copper irradiated at temperatures of 100-300°C. The mean SFT size in all cases was about 2.5 nm, and was independent of temperature over the range 100-300°C. The measured SFT density was significantly higher for irradiated pure copper (9 x $10^{22}/m^3$) than for the copper alloys (~ 3 x $10^{22}/m^3$). This indicates that solute and/or precipitate trapping of point defects may be occurring at a significant level during irradiation of the copper alloys. The difference in SFT densities between irradiated copper and the copper alloys also implies that SFT formation occurs via a homogeneous nucleation mechanism -- one would expect to find similar SFT densities for copper and the copper alloys if the SFT were formed directly in the vacancy-rich cores of the displacement cascades.

The formation of SFT and other defect clusters following low temperature irradiation provides an increase in the strength of metals (radiation hardening). This strengthening effect will tend to offset the strength decrease that may occur in irradiated cold-worked plus aged alloys due to radiation-enhanced recrystallization (Section VIII.B). The yield strength increase ($\Delta\sigma_y$) due to small defect clusters such as loops (and also probably SFT) is given by[28]

$$\Delta\sigma_y \simeq \frac{Gb}{2}\sqrt{nd} \qquad (8.4)$$

where G is the shear modulus, b is the Burgers vector, and n and d

are the defect cluster density and mean diameter. Using the defect cluster parameters given in the preceding paragraph the calculated strength increase for copper and copper alloys irradiated at 100-300°C is predicted to be 50 to 100 MPa. Yield strength increases as large as 300 MPa have been observed in neutron irradiated copper.[29,30]

A qualitative assessment of the strength increase or decrease due to ion irradiation can be obtained by performing a scratch hardness test[8,31,32] on an irradiated cross-section specimen. Scratch hardness tests were performed on several irradiated copper and copper alloy cross-section specimens using a standard phonograph turntable. Specimen preparation consisted of a mechanical polish followed by an electropolish in a HNO_3/CH_3OH solution. Figure 8.6 shows the results of qualitative scratch hardness tests that were made on copper and cold-worked plus aged AMZIRC following ion irradiation to a peak damage level of 40 dpa at 100°C. The indenter load was about 0.5 g in both cases. There is a strong indication of radiation hardening in the copper specimen as indicated by the narrow scratch width in the ion-irradiated region compared to the nonirradiated region scratch width. There is either no strength change or perhaps a slight amount of radiation hardening in the AMZIRC specimen.

One mechanical property aspect which remains uncertain concerns the loss of ductility in copper following irradiation. This problem becomes especially severe with increasing amounts of prior cold work. Makin[33] found that the ductility of 20% cold-worked copper fell to

SCRATCH HARDNESS OF ION-IRRADIATED METALS

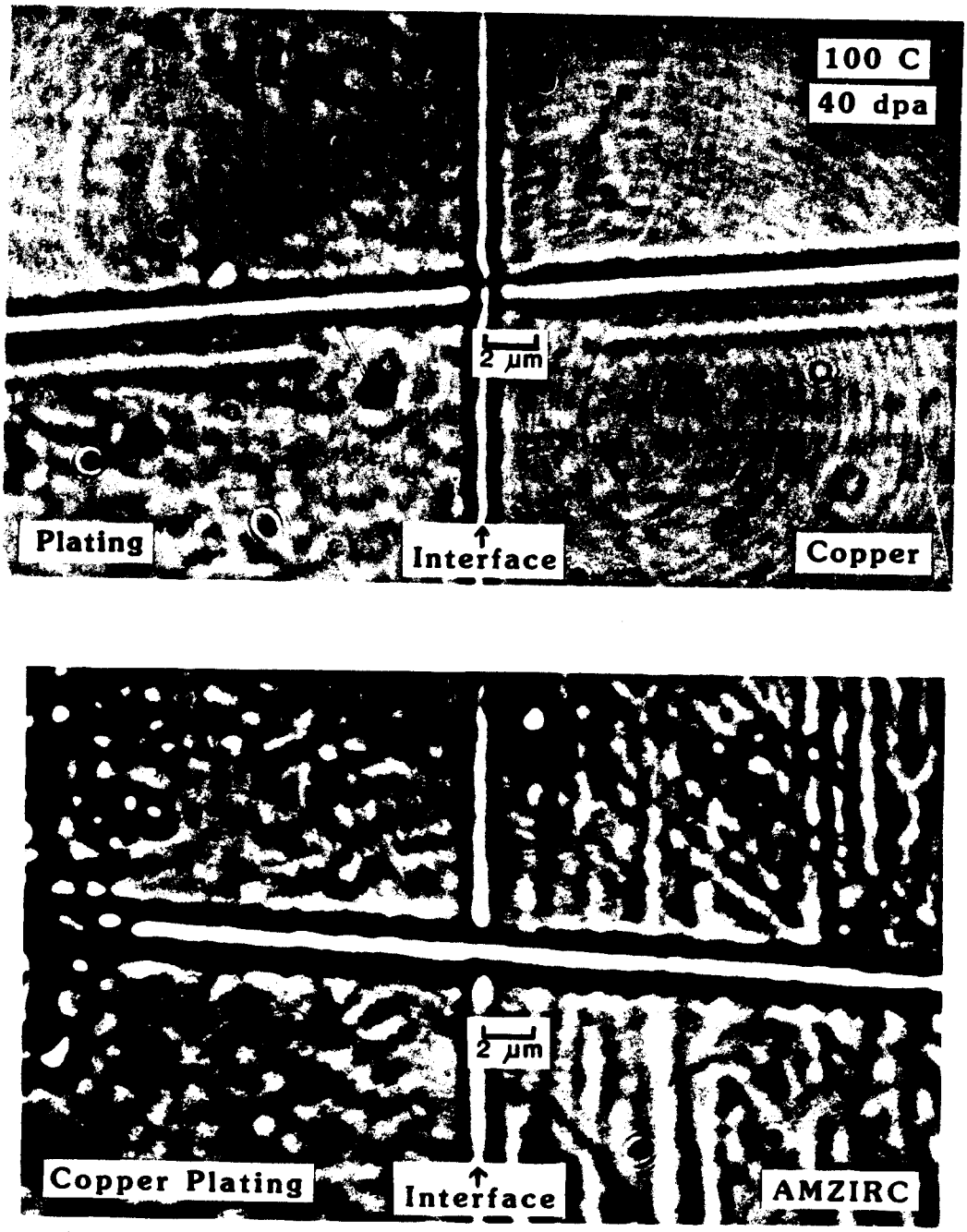

Fig. 8.6. Scratch hardness of copper (top) and cold-worked plus aged AMZIRC following ion irradiation to a peak damage level of 40 dpa at 100°C

zero after a dose of only 6 x 10^{23} n/m^2 ($\lesssim$ 0.1 dpa). Most high-strength copper alloys, including AMZIRC and AMAX-MZC, rely on high cold-work levels to maintain their high strength. This may lead to embrittlement problems during irradiation.

Irradiation of solution annealed plus aged AMZIRC and AMAX-MZC resulted in the formation of a small precipitate that was also occasionally observed in the nonirradiated alloys (Fig. 7.31). An attempt was made to determine the crystal system of the Cu_5Zr phase that appears in solution annealed plus aged AMZIRC (and AMAX-MZC). As mentioned in Section VI.A, various researchers have claimed the crystal structure of Cu_5Zr to be orthorhombic,[34] tetragonal[35] face-centered cubic,[35,36] or hexagonal.[37,38] Approximately 15 Cu_5Zr diffraction patterns were compared against the possible patterns[39] that could be obtained from these systems. It is concluded that Cu_5Zr cannot be either fcc or tetragonal.

VIII.D. Stability of Vacancy Clusters in Copper

High dose electron and ion irradiation studies have generally found[30] that void formation occurs easily in copper and copper alloys for irradiation temperatures of 300-550°C. In addition, low dose neutron irradiation studies[30] have also found that copper readily forms voids at doses as low as 10^{-4} dpa. These findings are in conflict with the ion irradiation results presented in this thesis (Sections VII.C, VII.D) for copper and copper alloys, where no substantial void formation was observed following irradiation to 40 dpa over a wide temperature range. A previous thesis study at the Uni-

versity of Wisconsin[40] likewise determined that void formation did not occur in pure copper following ion irradiation at temperatures of 400 to 500°C.

A vacancy cluster stability model is presented in this section that serves to clarify the physical basis for the difference in irradiated copper microstructures. It has been recognized for some time that gases such as helium,[41] oxygen[42] and hydrogen[43] in general promote void swelling. Recent experimental work at the University of Wisconsin[40,44] and elsewhere has found that gas may be required for void formation. The model presented in this section examines the relative energy of the void compared with other vacancy cluster configurations both in the absence and in the presence of gas. It is concluded that the SFT is more stable than the void in pure copper. However, the presence of small amounts of oxygen and/or helium cause the void to be the most stable vacancy cluster morphology.

VIII.D.1 Energetics of Vacancy Cluster Formation

The relative stabilities of vacancy clusters may be determined using procedures given by previous workers.[45,46] Four types of vacancy cluster morphologies were considered, namely the void, the perfect circular dislocation loop, the faulted (Frank) loop, and the stacking fault tetrahedron. Various equations are available that describe the energy of a dislocation loop. We have chosen the expressions derived by Kroupa,[47] since they are valid for small sizes. The energy of a perfect dislocation loop is given by[47]

$$E_p = \frac{Gb^2}{2(1-\nu)} \{2R + (2R - \varepsilon) [(1 - 0.5\ K^2)\ F(K) - E(K)]\} \qquad (8.5)$$

where $$K^2 = \frac{4R(R-\varepsilon)}{(2R-\varepsilon)^2}$$

$$F(K) = \frac{2}{\pi} \int_0^{\pi/2} \frac{d\phi}{\sqrt{1-K^2\sin^2\phi}}$$

$$E(K) = \frac{2}{\pi} \int_0^{\pi/2} d\phi\ \sqrt{1-K^2\sin^2\phi}$$

and G = shear modulus, $b = a_o/\sqrt{2}$ = Burgers vector of a perfect loop, υ = Poisson's ratio, R = loop radius and ε = core radius, $\varepsilon \simeq b$. F(K) and E(K) are elliptical integrals of the first and second kind, respectively. They may be solved numerically using polynomial approximations.[48]

A faulted vacancy loop may be described by a similar equation:[47]

$$E_F = \frac{b_F^2}{b^2} E_p + A\gamma \qquad (8.6)$$

where $b_F = a_o/\sqrt{3}$ = Burger's vector of a faulted loop, A = loop area and γ = stacking fault energy.

The energy of a stacking fault tetrahedron (SFT) is given by[49]

$$E_T = \frac{Gb^2L}{6\pi(1-\nu)} \{\ln \frac{4L}{b} + 1.017 + 0.97\ \nu\} + \sqrt{3}\ L^2\gamma \qquad (8.7)$$

where L = tetrahedron edge length. The energy of a void may be expressed as[50]

$$E_V = 4\pi R_V^2 \Gamma \left(1 - \frac{0.8}{N+2}\right) \tag{8.8}$$

where R_V = void radius, Γ = surface energy of a flat surface, and N = number of vacancies in the void. The term in parenthesis is an empirical correction to the surface energy due to curvature effects.

Values for the materials parameters[51-53] required in the energy calculations are given in Table 8.2. Calculations were performed at homologous temperatures near the peak void swelling temperature, 0.45 T_M. The effect of temperature on the vacancy cluster energies is rather small, and the calculated results are reasonably valid over the entire void swelling temperature regime.

Figure 8.7 shows the calculated energy per vacancy of the different cluster morphologies as a function of the number of vacancies in the cluster for pure copper. Similar calculations have been performed on other common metals.[91] The stacking fault tetrahedron (SFT) is predicted to be the most stable configuration for small ($\lesssim$ 1000 vacancies) clusters in copper. Void formation is predicted to never be energetically favorable. The perfect loop is the most stable configuration at very large vacancy cluster sizes. Since vacancy cluster nucleation necessarily occurs at small sizes, the stability of the small clusters ($\lesssim$ 1000 vacancies) is expected to exert the dominant effect on the final observed morphology. (As dis-

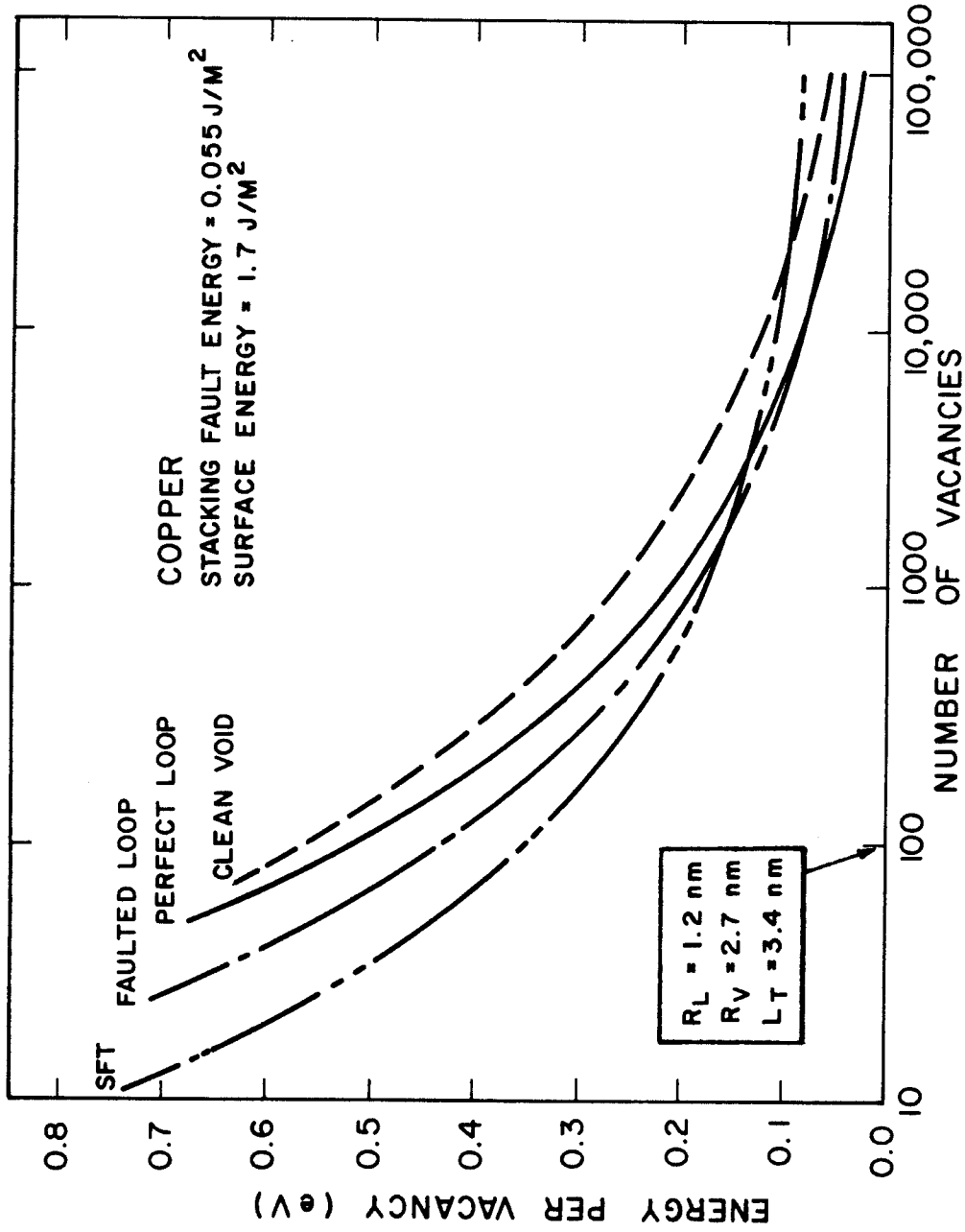

Fig. 8.7. Vacancy cluster energies in pure copper.

Table 8.2. Materials Parameters for Copper

G(51)	ν(51)	a_o(51)	γ(52)	r(53)
48.3 GPa	0.343	0.361 nm	0.055 J/m^2	1.7 J/m^2 @ 400°C

cussed later, there is an appreciable activation energy barrier that inhibits conversion of vacancy clusters between planar and three-dimensional morphologies). The most interesting aspect of the calculations presented in Fig. 8.7 is that void formation is not expected to occur for any vacancy cluster size in pure copper.

Elastic continuum equations are not strictly valid for very small defect clusters,[46] and it would be more appropriate to use atomistic calculations to determine the most stable morphology at cluster sizes where void nucleation is expected to occur ($\lesssim$ 100 vacancies). Unfortunately, the interatomic potentials of most metals are not known at sufficient accuracy to allow this type of calculation to be performed. Atomistic calculations have recently been conducted on the stability of small vacancy clusters in pure copper.[54,55] Both investigations found that the vacancy loop[54,55] and SFT[55] (planar configurations) are more stable than the void, in agreement with the continuum predictions (Fig. 8.7).

There have been several reported observations of SFT in irradiated or quenched copper and copper alloys (see, e.g., Refs. 56-60),

as predicted from Fig. 8.7. This general agreement between theory (Fig. 8.7) and experiment indicates that continuum theory may be at least qualitatively correct in its stability predictions at small cluster sizes. However, a review of the literature reveals that void formation is also commonly observed in quenched or irradiated copper.[30,60,61] These experimental findings are in conflict with the elastic continuum calculations. In order to remedy this discrepancy between theory and experiment, it is necessary to examine the effect of impurities on the relative energies of vacancy clusters. A model is developed in the following sections that addresses the effect of oxygen and helium on the vacancy cluster energies. Calculations are performed for the case of irradiated copper.

VIII.D.2 Role of Oxygen on Void Formation in Copper

It is well known that surface-active species such as oxygen or sulfur may chemisorb onto clean surfaces of metals and cause a reduction in the surface energy.[62-66] If the reduction in surface energy is sufficiently large, then void formation may become energetically favorable. The change in surface energy due to the chemisorption of oxygen at a constant temperature is given by the Gibbs adsorption isotherm:[65,66]

$$\frac{d\Gamma}{d \ln X} = - \frac{RT \, \theta_{sat}}{A_{cu}} \tag{8.9}$$

where θ_{sat} is the saturated fractional surface coverage, X is the mole fraction of oxygen in solution and A_{cu} is the molar surface area

of copper. The value of A_{cu} depends upon crystallographic orientation and is 3.40 x 10^4 m^2/g-mol for the (111) close packed plane.[53] Experimental measurements of the surface energy[65-67] have found that the surface of copper becomes saturated with oxygen at a coverage level of $\theta_{sat} \simeq 0.25$. In the presence of higher partial pressures of oxygen, an oxide layer forms.[66,67] These findings on the oxidation sequence are in good agreement with surface studies of chemisorption and oxidation in copper.[68] However, Habraken et al.[68] reported that $\theta_{sat} \simeq 0.5$ for oxygen chemisorption on copper.

The Langmuir-McLean isotherm[63,69] may be used to determine the temperature-dependent relationship between oxygen in solution in the matrix and the degree of surface coverage (θ) on a void.

$$\frac{\theta}{1-\theta} = x \exp\left(\frac{G_B - G_s}{RT}\right) = (X_o - X_{cs}) \exp \frac{G_B - G_s}{RT} \qquad (8.10)$$

where X_o is the mole fraction of oxygen initially present in the matrix, X_{cs} is the mole fraction of oxygen chemisorbed onto void surfaces, and G_B and G_s are the Gibbs free energies for oxygen in the bulk and on the surface, respectively, relative to a single oxygen atom in vacuum. If entropy terms are neglected, then $G_B \simeq (H_u + E_D)/2$ and $G_s \simeq (H_{cs} + E_D)/2$ where E_D is the dissociation energy of molecular oxygen and H_u and H_{cs} are the heat of solution and chemisorption for molecular oxygen. Using E_D = 498.4 kJ/mol,[70] H_u = -47 kJ/mol[71] and H_{cs} = -167 kJ/mol[63] yields the result, $G_B \simeq 226$ kJ/mol and $G_s \simeq 166$ kJ/mol. This approach implies that there is no

effect of oxygen coverage on the heat of chemisorption. It is known that the magnitude of H_{cs} becomes appreciably smaller at high coverage levels.[63,72,73] However, it appears that there is little change in H_{cs} for coverage levels up to $\theta = 0.25$, which corresponds to the range of interest in the present case.

The change in surface energy due to oxygen chemisorption may be calculated using the method of Gallois and Lupis[65]

$$\Gamma - \Gamma(\theta) = \frac{RT}{A_{cu}} \left[\frac{\theta}{1-4\theta} + \frac{g\,\theta^2}{RT}\right] \qquad (8.11)$$

where g corresponds to an interaction energy between neighboring adsorbed oxygen atoms. It has been empirically observed that g is negative,[65] but its exact value is uncertain. In the following, we will neglect interaction effects (i.e., $g = 0$). This will lead to an overestimate of the effectiveness of oxygen in lowering the surface energy. Simple calculations indicate that the magnitude of the error introduced by setting $g = 0$ is expected to be $\lesssim 20\%$ for surface coverage levels of $\theta \gtrsim 0.22$ (also see Fig. 7 of Ref. 65).

An evaluation of the energetics of vacancy cluster formation indicates that a surface energy of $\Gamma \lesssim 1.0$ J/m^2 is required in order for void formation to occur in copper (Fig. 8.8). Using Eq. (8.11), this corresponds to a surface coverage of $\theta \gtrsim 0.22$. This value is then inserted into Eq. (8.10) in order to compute the requisite matrix oxygen concentration. The amount of oxygen that is chemisorbed onto void surfaces, X_{cs}, depends on the average void size and

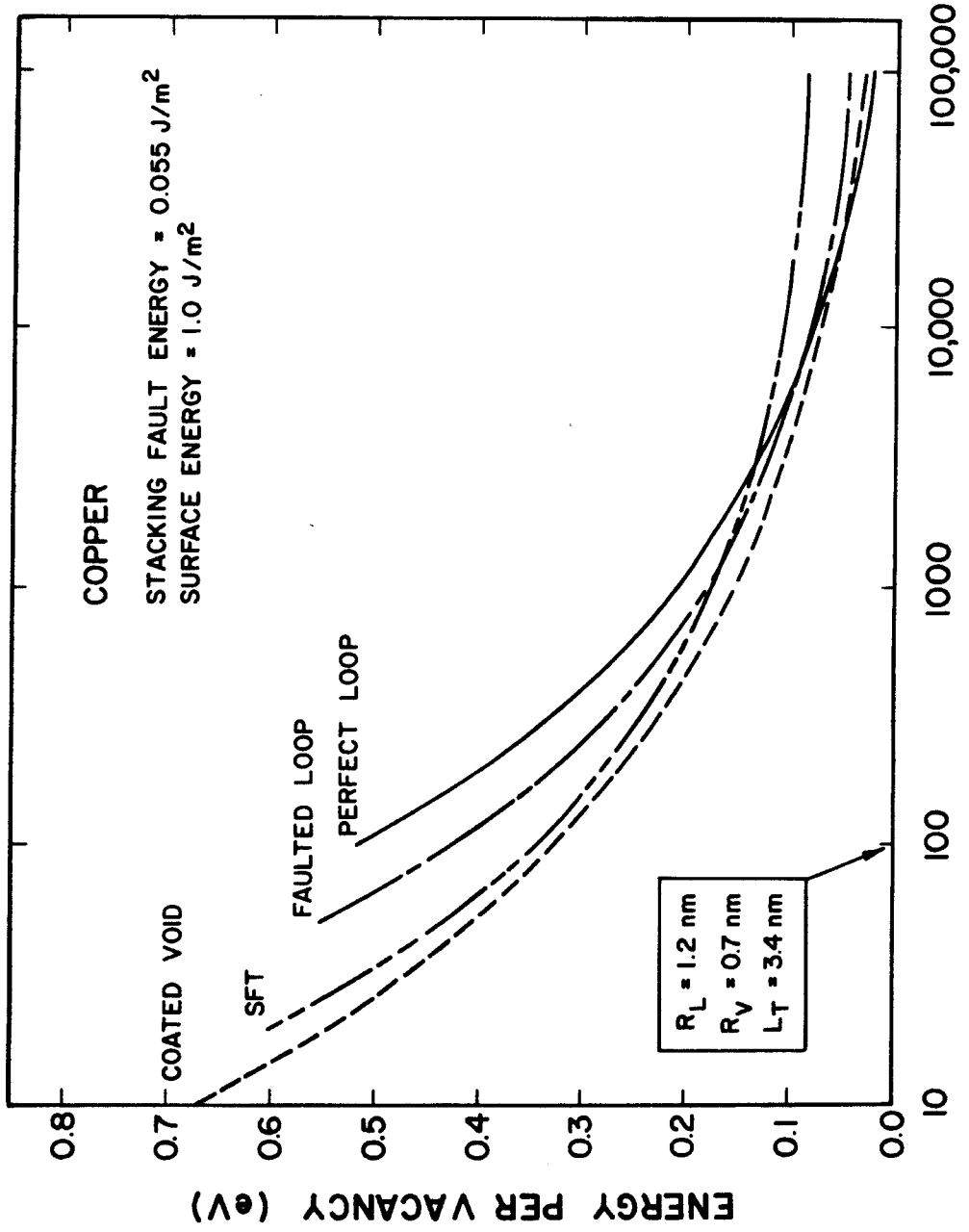

Fig. 8.8. Vacancy cluster energies in pure copper with a surface energy of $\Gamma = 1.0$ J/m^2.

density (n_v):

$$X_{cs} = \frac{4\pi R_v^2 N_A \theta n_v}{A_{Cu} n_{Cu}} \qquad (8.12)$$

where N_A is Avogadro's number and n_{cu} is the atom density of copper. Since we are interested in the stability of clusters at sizes where void nucleation occurs, it is appropriate to use values of n_v and R_v obtained from nucleation theory. Wehner and Wolfer[74,75] have recently developed a dynamic void nucleation theory based on a Fokker-Planck description that is in good agreement with experimental results. Table 8.3 lists the calculated temperature-dependent values of n_v and R_v obtained from their analysis of copper.

The calculated initial matrix oxygen content required to reduce the surface energy of voids in copper to 1.0 J/m^2 is plotted in Fig. 8.9. This oxygen concentration corresponds to the minimum amount of oxygen that is required to stabilize as voids all of the vacancy clusters that are nucleated during irradiation (Table 8.3). A lower oxygen concentration could result in partial stabilization of the void nuclei population. The critical oxygen concentration depends strongly on temperature, and exhibits a minimum value for intermediate temperatures. Larger amounts of oxygen are needed in order to stabilize void formation at low temperatures because of the high vacancy cluster density that is nucleated (Table 8.3). Large oxygen concentrations are also necessary at high temperatures because there

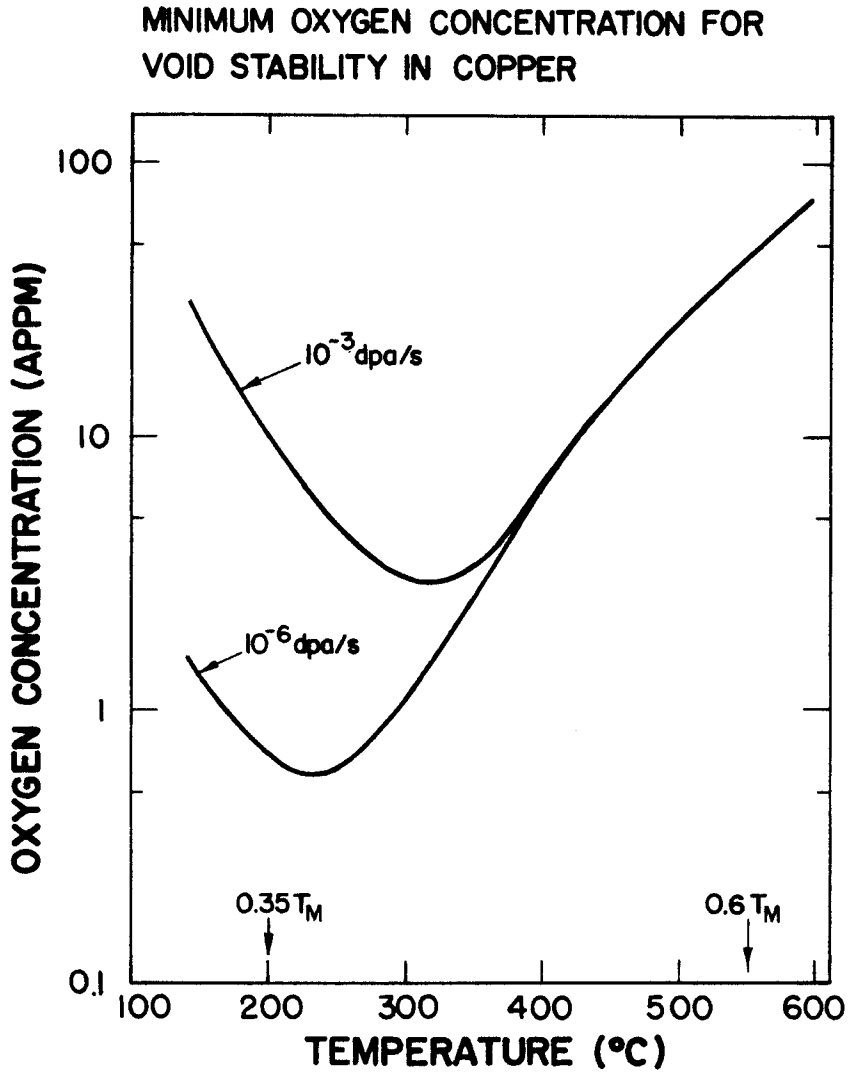

Fig. 8.9. Minimum matrix oxygen content required for void stability in pure copper.

Table 8.3. Calculated Critical Void Size and Density in Copper as a Function of Irradiation Temperature (from Ref. 75)

	Void Density (m^{-3})		Critical Void
Temperature (°C)	10^{-3} dpa/s	10^{-6} dpa/s	Radius (nm)
100	5×10^{23}	2×10^{22}	0.6
200	5×10^{22}	3×10^{21}	0.6
250	2.5×10^{22}	1.5×10^{21}	0.6
300	9×10^{21}	2.5×10^{20}	0.6
400	2.5×10^{21}		0.6
450	1×10^{20}		0.6

is a lowered driving force for oxygen to come out of solution and chemisorb onto void embryo surfaces.

The interpretation of Fig. 8.9 is as follows: Charged particle irradiation at 1×10^{-3} dpa/s of pure copper containing less then 3 appm oxygen (e.g., OFHC copper)[76] should not cause any substantial void formation at any temperature. On the other hand, irradiation of copper containing greater than 50 appm oxygen should result in void formation throughout the entire swelling temperature regime (0.3-0.6 T_M). At intermediate oxygen concentrations, void formation should occur over a limited temperature regime centered around 325° (0.45 T_M). In particular, void swelling will not occur at high temperatures and the void swelling regime will be restricted to the lower temperature range for partially outgassed copper. Neutron irradi-

ation of copper (1×10^{-6} dpa/s) is more complicated than indicated in Fig. 8.9 because helium generated during irradiation greatly enhances void stability in addition to the oxygen stability effects (see following section). It should be noted that regular "high purity" copper that has not been deoxidized often contains $\gtrsim$ 200 appm oxygen.[76] In addition, electropolishing of metal foils prior to their irradiation may result in the introduction of oxygen into the foil.[77]

The predicted values of oxygen concentration required to stabilize void formation in copper at a given temperature are not expected to be exact due to the various approximations that were used to obtain the final result. For example, the assumption of $g = 0$ in Eq. (8.11) results in an underestimation of the critical matrix oxygen concentration necessary for void stability. Nevertheless, it is pleasing to note that the predictions are in good agreement with the limited amount of irradiation data that is available on copper containing known amounts of oxygen.[30] It was reported in Section VII.D that 14-MeV Cu ion irradiation of high-purity copper containing < 5 ppm oxygen at a damage rate of 2×10^{-3} dpa/s did not result in any significant void formation over the temperature range of 100-400°C. A previous investigation at the University of Wisconsin[40] using the same lot of annealed copper foils and similar ion irradiation conditions found that there was no observable void formation at irradiation temperatures of 400, 450 or 500°C. Therefore, there does not appear to be an appreciable void formation in ion-irradiated pure

copper over the temperature range where void swelling normally occurs (0.28-0.6 T_M). A very limited number of voids ($n_v \simeq 10^{17}/m^3$) were observed at one temperature, 400°C (Section VII.D). There was no observable void formation at 300 or 450°C. Glowinski and coworkers found that copper containing 50 wt.ppm oxygen (~ 200 appm O) formed voids easily following electron[78] and ion[79-81] irradiation. Outgassing of the foils in a high-vacuum furnace prior to irradiation shifted the swelling peak to lower temperatures and completely eliminated high-temperature void swelling. As noted earlier, Fig. 8.9 predicts that partial deoxidation of copper will preferentially eliminate void formation at the high temperature end of the void swelling regime. Sindelar et al.[82] have recently observed a similar temperature shift in ion-irradiated stainless steels which they attributed to oxygen effects.

The effect of oxygen gas existing in the void interior was neglected in the preceding analysis of void stability. Application of Sievert's Law data[71] at 400°C shows that 10 appm oxygen in solution is in equilibrium with a partial pressure of 2.6×10^{-6} atm. The contribution to void stability for these pressures is negligible. We have also neglected to include the oxygen atoms residing in the void interior in the oxygen mass balance. This contribution can also be shown to insignificant, i.e. $X \simeq X_o - X_{cs}$. It may be stated that void stabilization in copper in the presence of oxygen is solely due to the chemical surface interaction between oxygen and copper.

VIII.D.3 Role of Helium in Void Formation in Copper

Unlike oxygen, inert gases such as helium have no effect on the macroscopic surface energy of copper.[64] There have been several investigations of the energetics of cavities in the presence of helium (see, e.g., Refs. 83, 84). However, the derived energy equations contain several terms whose values are not well known. A simplistic estimate of the stability of vacancy clusters in the presence of helium may be obtained from the following:

$$E_v \simeq E_v^o - \left[\sum_{i=1}^{m} (E_{He}^B)_i - pV\right] \tag{8.13}$$

$$E_x \simeq E_x^o - m\, E_{He-D}^B \tag{8.14}$$

where E_v^o is the energy of a void in the absence of helium, E_x^o is the energy of a vacancy loop or SFT in the absence of helium, m is the number of helium atoms associated with the vacancy cluster, $E_{He}^B)_i$ is the binding energy of the ith helium atom to the cavity, and E_{He-D}^B is the binding energy of interstitial helium to a dislocation. In a sufficiently dilute system, (helium/vacancy << 1) the binding energies of helium atoms in a helium-vacancy cluster can be approximated by the formation energy of interstitial helium, E_{He}^F.

$$\sum_{i=1}^{m} (E_{He}^B)_i \lesssim m\, E_{He}^F$$

This approximation breaks down for concentrated helium-vacancy

clusters (see, e.g., Table 6.53 in Ref. 85). The value of E^B_{He}/E^F_{He} decreases to about 0.5 as the helium to vacancy ratio approaches 1. The last term in Eq. (8.13) can be represented by the helium equation of state, pV = zmkT. The compressibility factor, z, is on the order of unity[86] for all cases considered in this paper. Therefore, $zkT \lesssim 0.1$ eV for temperatures in the void swelling regime. This factor is negligible compared to the uncertainties in E^F_{He}. From the above considerations, Eq. (8.13) may be approximated by

$$E_v \gtrsim E^o_v - m\, E^F_{He} \,. \tag{8.15}$$

The inequality sign serves as a reminder that the simplifications used to obtain Eq. (8.15) may result in an underestimation of the actual void energy, especially for high helium per vacancy ratios.

The values of E^F_{He} and E^B_{He-D} apparently have not yet been accurately determined for copper. Calculations of E^F_{He} for copper[87] indicate that it should be ~ 3 to 4 eV. The binding energy of helium to a dislocation is taken to be[88] $E^B_{He-D} \approx 0.3$ eV, which is the calculated value for nickel.

Figure 8.10 shows the calculated energy per vacancy of voids and stacking fault tetrahedra in copper in the presence of 3.5 and 35 He/vacancy cluster. This is equivalent to a helium concentration of 0.1 and 1 appm, respectively, for ion-irradiated copper at 400°C (Table 8.3) assuming that all of the helium initially present in the matrix is contained in the vacancy clusters. The presence of helium

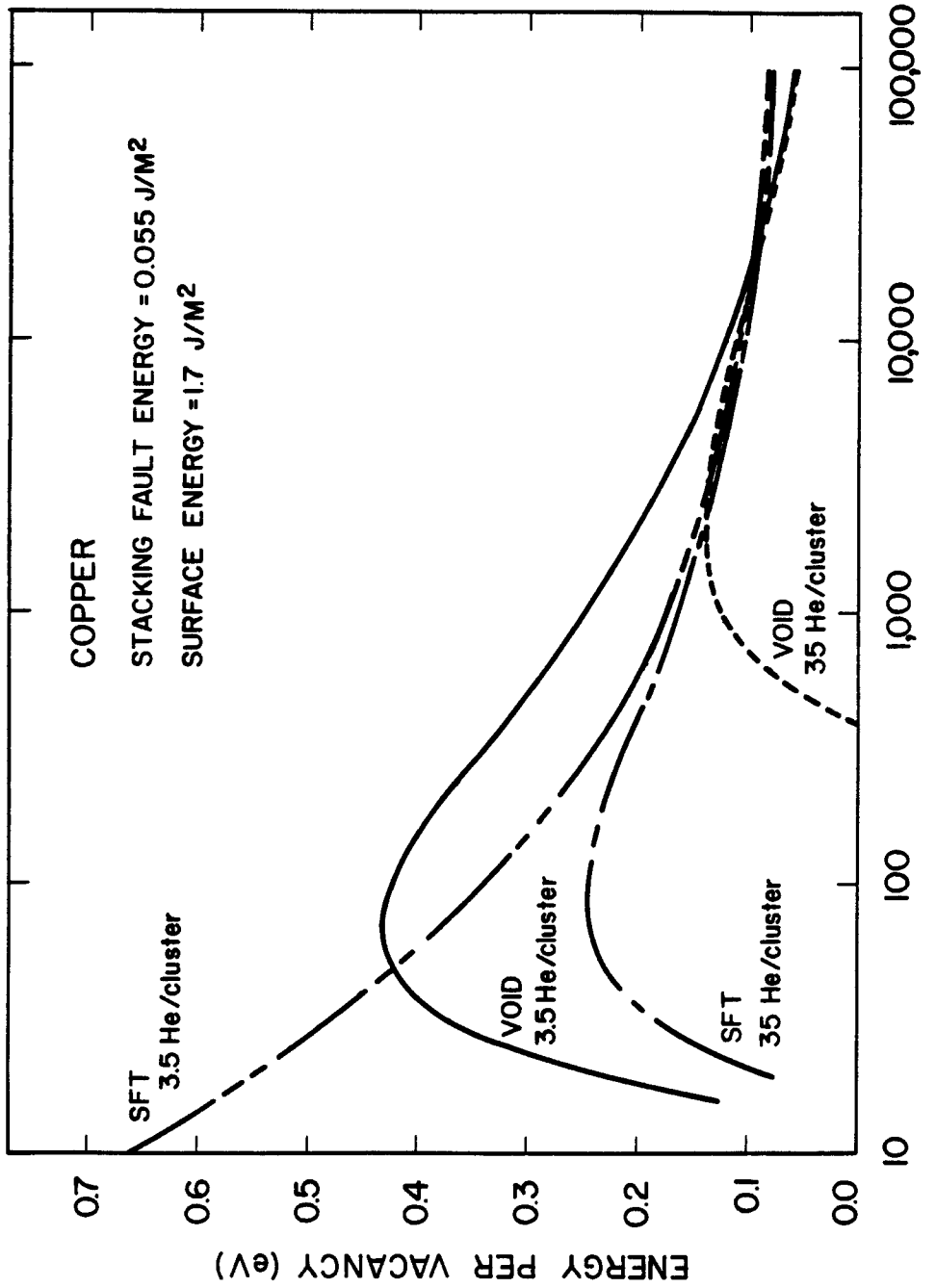

Fig. 8.10. SFT and void energies in the presence of helium.

causes the void to be the most stable type of vacancy cluster for small cluster sizes. Previous atomistic calculations reached a similar conclusion -- addition of helium to copper causes the void to be energetically favorable compared to planar defect clusters.[54] Increasing concentrations of helium further enhance the stability of the void relative to the other vacancy cluster morphologies. The critical amount of helium required to make the void energetically stable compared to the stacking fault tetrahedron is given by

$$m_{crit} \simeq \frac{E_V - E_T}{E^F_{He} - E^B_{He-D}} \tag{8.16}$$

where E_V and E_T are given by Eqs. (8.7) and (8.8) and depend on the cluster size. Table 8.4 gives the values of m_{crit} for two different void sizes that are appropriate for void nucleation. Values are tabulated for E^F_{He} = 2 eV and 4 eV, which represents the lower and upper estimates for this quantity. The helium per vacancy ratio is << 1 for a critical sized void nucleus, indicating that Eq. (8.15) may be a reasonable approximation.

Figure 8.11 gives the minimum helium concentration required for void stability during irradiation as a function of temperature, assuming that all of the helium initially present in the matrix precipitates into the vacancy clusters. Values relevant for neutron (1×10^{-6} dpa/s) and ion or electron irradiation (1×10^{-3} dpa/s) of copper were obtained from the data in Tables 8.3 and 8.4. The minimum helium concentration for void stability decreases rapidly with

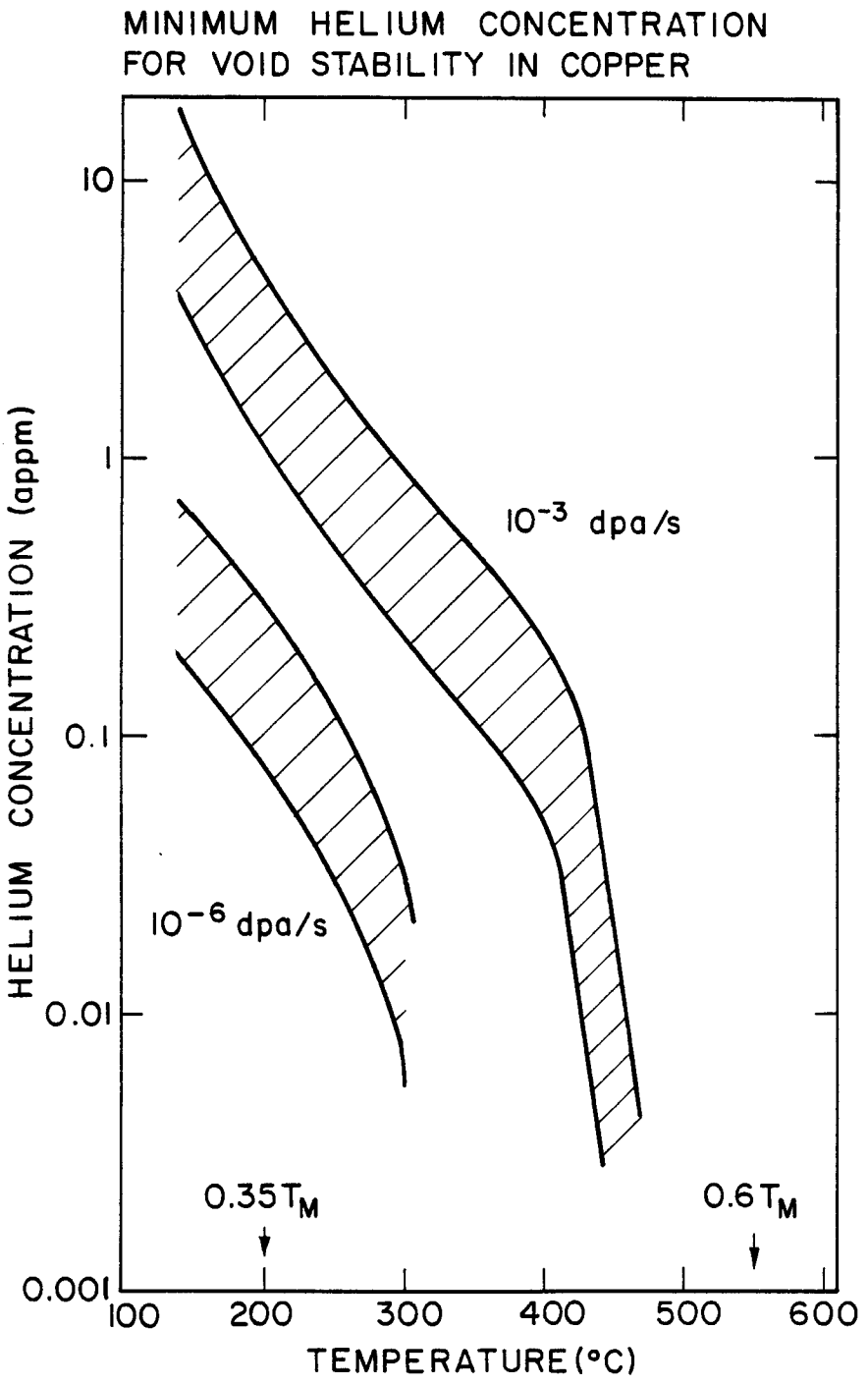

Fig. 8.11. Minimum He content required for void stability in pure copper.

Table 8.4. Minimum Helium Concentration for Void Stability in Copper

	R_v = 0.6 nm		R_v = 1.0 nm	
	m_{crit}	He/vacancy	m_{crit}	He/vacancy
E^B_{He} = 2 eV	4.3	0.056	8.2	0.023
E^B_{He} = 4 eV	2.0	0.026	3.8	0.01

increasing temperature. Figure 8.11 predicts that less than 0.1 appm He will cause the void to be the most stable vacancy cluster morphology during neutron irradiation at all void swelling temperatures (0.35-0.6 T_M). Irradiation at a higher displacement rates requires a higher helium concentration. Small amounts of helium should greatly enhance the stability of voids at high temperatures, and may "shift" the void swelling temperature regime to higher temperatures. Such a shift has been observed in irradiated copper,[81] stainless steel[89] and nickel[90].

Figure 8.11 is in good agreement with the limited amount of experimental data on helium effects in copper -- no voids were observed in degassed copper following ion irradiation at 450°C. However, implantation of 1-100 appm He prior to irradiation resulted in void formation.[81] McLaurin[49] observed that high-purity aluminum irradiated with 9-MeV Al ions at 50°C (0.35 T_M) did not form voids,

whereas preimplantation of as little as 0.1 appm He resulted in significant void swelling with a void concentration of $1 \times 10^{21}/m^3$. The corresponding He concentration per void in this case is $m_{He} \simeq 6$, assuming that all of the implanted helium is contained in the voids. Application of Eq. (8.16) to the vacancy cluster energetics data for aluminum[91] results in a calculated void stability criterion of $m_{crit} \lesssim 5$ He atoms per void. The preceding calculation used $E^F_{He} - E^B_{He-D} = 3.7$ eV and an average void nucleus size of 200 vacancies ($R_v = 0.7$ nm). Therefore, void formation is predicted to be stable in aluminum for implanted helium concentrations ~ 0.1 appm He, in agreement with the observations of McLaurin.[44]

The model developed to describe helium effects in metals contains several assumptions that may limit its applicability. First, it is assumed that all of the helium that was initially in the matrix migrates to the void embryos where it is equally partitioned. Helium has a relatively high mobility in most metals and tends to cluster at vacancies or other high-order vacancy clusters.[92,93] Therefore, the above assumption should be valid in the experimental cases where helium initially exists as isolated atoms in a metal containing vacancy clusters (neutron irradiation or subthreshold coimplantation studies). The case of helium preimplantation by ion bombardment prior to irradiation is not accurately modeled here -- the implanted helium tends to spontaneously cluster at the implantation-produced vacancies (forming He_6V clusters in copper),[93] and becomes relatively immobile. Also, the nucleation code used in the present

treatment does not account for heterogeneous nucleation at helium clusters. The results may therefore be inappropriate for most pre-implantation studies. However, Makin[94] found that the observed void density in irradiated stainless steel was not strongly affected by a 10 ppm He preinjection at room temperature. It is possible that the results obtained in this paper concerning helium effects may be valid for preinjection studies if low helium concentrations are involved (< 10 appm He).

VIII.D.4 Activation Energy for the Collapse of a Void

At very large sizes, the perfect loop is always the most energetically stable type of vacancy cluster. Therefore, voids which may have been energetically stable at small sizes may become unstable once they have grown larger than a critical size. It is important to determine what the probability is that a void of a given size will collapse into a planar defect cluster. An activation energy barrier exists that inhibits conversion of a void to a dislocation loop. An upper limit to this activation energy barrier is obtained by comparing the energy difference between a sphere and a disk (of thickness b) that are of equal volume.

$$\Delta E = E_V \left[\frac{2 R_V}{3b} - 1\right] \qquad (8.17)$$

A more realistic estimate of the activation energy is obtained by comparing the energies between a sphere and an oblate spheroid (a "squashed" sphere).[95] The oblate spheroid accurately represents

the geometry of a void that is in the process of collapsing to a planar configuration. The energy difference is given by

$$\Delta E = C \cdot E_v \tag{8.18}$$

where C is a constant that depends on the eccentricity of the spheroid. Values of C are given in Table 8.5 for various ratios of major to minor axis along with calculated activation energies for the collapse of a "typical" small void. A rule-of-thumb in void nucleation calculations is that energy barriers up to 30 kT may occasionally be surmounted by thermal energy processes. For temperatures applicable to void swelling in metals, this indicates that energy barriers $\gtrsim$ 2 eV will not allow void collapse to occur. Since the activation energy barrier is proportional to R_v^2, it is apparent from Table 8.5 that void collapse will not occur except possibly for voids that have just nucleated and are, therefore, very small, $R_v \lesssim 2$ nm).

Continuum calculations predict that void formation is energetically unstable in copper (Fig. 8.7) along with several other metals.[91] Incorporation of the effects of oxygen and helium on the stability of vacancy clusters modifies the relative energies of the cluster so as to favor void formation. The gas effects models presented in this section appear to be in good agreement with the experimental data that is available on oxygen and helium. Small amounts of oxygen in copper tend to stabilize voids at low irradiation temperatures whereas small helium concentrations preferentially

Table 8.5. Energy Barrier for Collapse of a Void

	Oblate Spheroid			
	a/c = 2	a/c = 4	a/c = 6	Disk
Energy Barrier Constant, C*	0.095	0.43	0.88	$\frac{2R_v}{3b} - 1$
Activation Energy**	1 eV	4.4 eV	9.1 eV	24 eV

a/c = ratio of major/minor axis
*In terms of the initial void energy
** Assuming R_v = 5 b (1.8 nm) and Γ = 1 J/m^2

stabilize voids at high temperatures. The combination of minute quantities of oxygen and helium can stabilize void formation in copper at all temperatures relevant to void swelling. Figure 8.12 shows the minimum combined gas content that is needed to stabilize void formation in copper irradiated at a damage rate of 10^{-3} dpa/s. The combination of 10 appm oxygen and 0.01 appm helium in solution in the matrix is predicted to result in void stabilization at all temperatures in the void swelling regime. Even lower gas levels are sufficient for void stability in copper during neutron irradiation (1×10^{-6} dpa/s).

The continuum calculations presented here (Section VIII.D.1) and elsewhere[91] predict that void formation should not occur in aluminum, copper or austenitic stainless steel unless suitable impurities (such as gas atoms) are present. Previous researchers have similarly

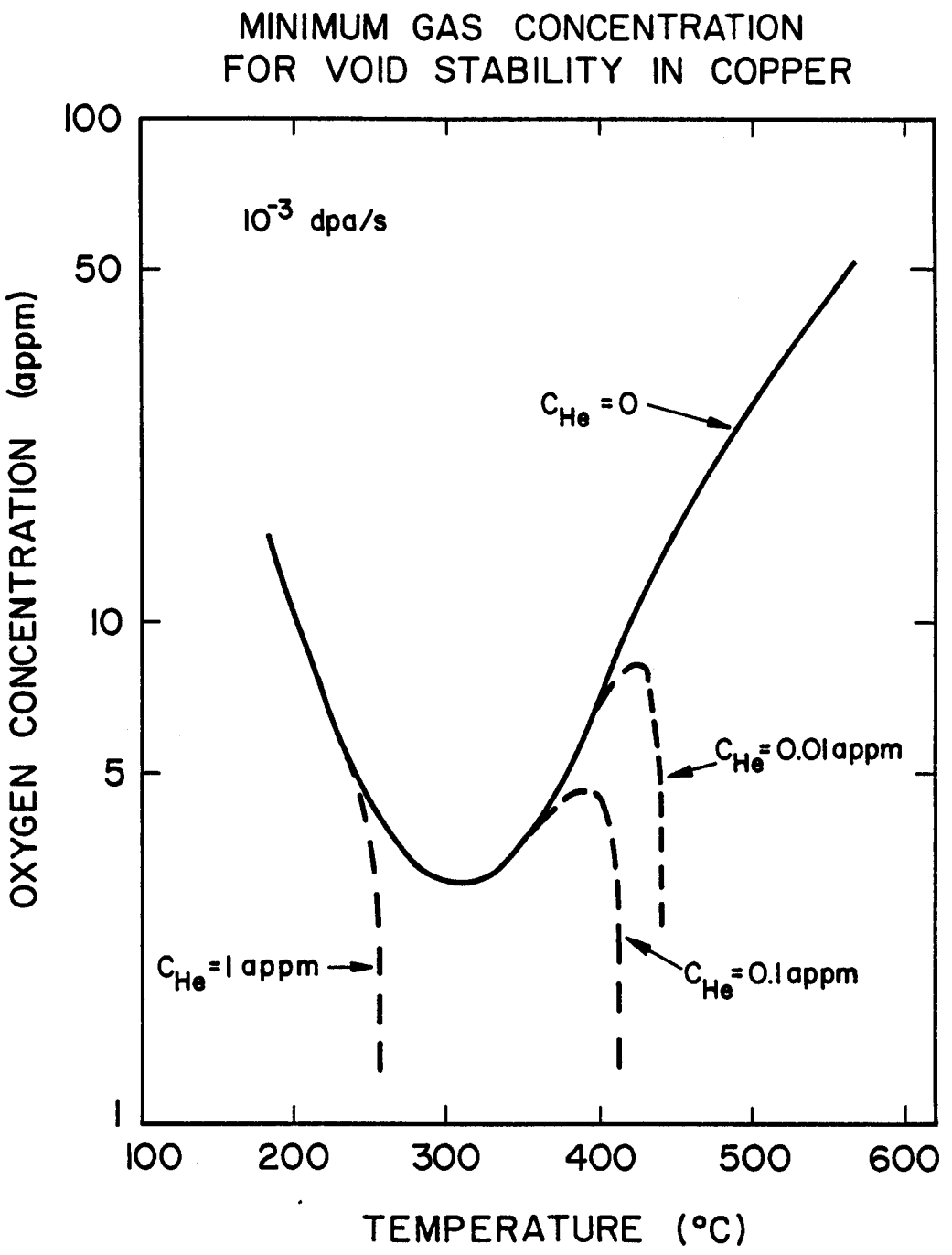

Fig. 8.12. Minimum oxygen content required for void stability in copper containing various amounts of helium.

concluded that gas is necessary for void formation (see, e.g., Ref. 96). Recent experimental studies on high-purity aluminum[44] and copper (Section VII.D and Ref. 40) have shown that these two metals do not exhibit any significant void formation following self-ion irradiation to high doses. In addition, ion irradiation of a "low-oxygen" (200 appm O) austenitic stainless steel resulted in greatly reduced swelling (and no observable void formation at high temperatures) compared to a "high-oxygen" (1000 appm O) alloy.[82] It is not known whether stainless steel has ever been irradiated in a very low oxygen form (< 5 appm). The presence of voids following irradiation of the annealed AMZIRC specimen at 300°C (Fig. 7.25) may be due to oxygen effects. This specimen was given a preirradiation electropolish at a higher temperature (-20°C) than other specimens (-50°C), which may have introduced oxygen into the foil.[77]

There have been many reported observations of void formation in high-purity aluminum and copper following irradiation with charged particles. For example there are more than twenty known reports of void formation in copper following electron or ion irradiation.[30] From the preceding discussion, it appears that some type of gas must have been present in the foil during the irradiation. Significant oxygen levels can be found in high-purity copper unless special deoxidation steps are taken.[76] Unfortunately, irradiation studies to date on copper have not kept close control of their oxygen content. It appears that all of the preceding charged particle irradiation studies on aluminum and copper that reported void formation should be

reevaluated with respect to gas effects. These gas effects may have masked or distorted the effects of other irradiation parameters that were being studied.

The conclusion that gas is necessary for void formation is currently known to be valid only for aluminum and copper. However, it seems likely that many other metals may also be resistant to void formation in the absence of impurities (gaseous and otherwise). Future irradiation studies should be performed only on foils with a well-characterized and preferably low gas concentration.

From a metallurgical point of view, the theoretical prediction (and experimental confirmation) that voids are not inherently stable in metals such as Al and Cu during irradiation raises hopes that alloy development research may be able to prevent deleterious levels of void swelling. At least two conditions are needed to minimize void swelling. First, the base metal should be oxygen-free ($\lesssim$ 1 appm O). A second consideration is that helium generated during neutron irradiation cannot be allowed to freely interact with the embryonic vacancy clusters. Significant advances in this area have recently been made using microstructural tailoring of precipitates, etc. that directs the helium into a rather benign role.[97]

VIII.E. Comparison of Theoretical and Experimental Ion Damage Range

Irradiation of copper and the two copper alloys (AMZIRC, AMAX-MZC) with 14-MeV Cu ions produced damage which generally extended to depths greater than expected from BRICE code calculations (Fig. 2.2). In the cold-worked plus aged alloys, signs of radiation-enhanced re-

covery and recrystallization were observed to depths of ~ 4 μm. The BRICE code predicts that the damage range for 14-MeV Cu ions incident on copper should be $\lesssim$ 2.8 μm. More direct observations of the extent of the displacement damage could be made on the pure copper and solution annealed plus aged copper alloys that were irradiated at low temperatures (100-300°C). In these cases, black spot damage profiles gave a clear measurement of the distribution and range of the cumulative displacement process. The maximum range of 14-MeV Cu ions incident on copper was determined to be 2.7-4.4 μm from black spot damage measurements. There were no obvious differences in the measured damage ranges in copper versus the copper alloys. Measurements were made on over 25 cross-section specimens that were irradiated at low temperatures. There was no apparent temperature dependence of the damage range within the scatter of the data.

The rather large variation in the experimentally measured damage range may be due to several different sources. The lower values of the damage range were obtained on specimens where the foil-plating interface was not intact. Although attempts were made to ensure that the edge of the foil coincided with the original interface, it is possible that as much as 0.2-0.3 μm of the foil may have been missing. The cross-section foils were always placed in the electron microscope with the foil-plating interface parallel to the tilt axis. Translation along the interface provided a check on whether a substantial portion of the original foil surface had been removed during the electrothinning process (estimated accuracy limit ≈ 0.2 μm). All

cross-section measurements were corrected for the tilt angle in the microscope. The higher values of the measured damage range may possibly be due to channeling effects. A previous ion irradiation study of copper has found that displacement damage in channeling directions occurred up to 16 times the projected range.[98] Since polycrystalline samples were used in the present study, there was no way to orient the foil to preclude the possibility of channeling in some grains (apart from "rocking" the incident beam).

Previous cross-section studies of ion-irradiated metals by other researchers have also found that the measured damage range exceeds the calculated value by a significant amount.[99-105] Knoll[40] observed evidence of displacement damage (loss of coherence of precipitates) to depths of 3.4-4.3 μm in copper alloys irradiated with 14-MeV Cu ions. This extended damage observation is in good agreement with the present results, although Knoll postulated that the observed effects may simply be due to long-range migration of interstitials. The occurrence of ion displacement damage beyond the calculated end of range has generally been attributed to diffusional spreading effects[103,105] and stopping power errors.[99-102,104]

The calculated ion damage range depends on a somewhat arbitrary choice of the available electronic stopping powers.[100]. Figure 8.13 shows the calculated depth-dependent displacement damage profiles for 14 MeV Cu incident on a copper target using LSS[106] and Firsov[107] electronic stopping power (esp) values. The use of Firsov's esp values leads to a broadened damage distribution and a

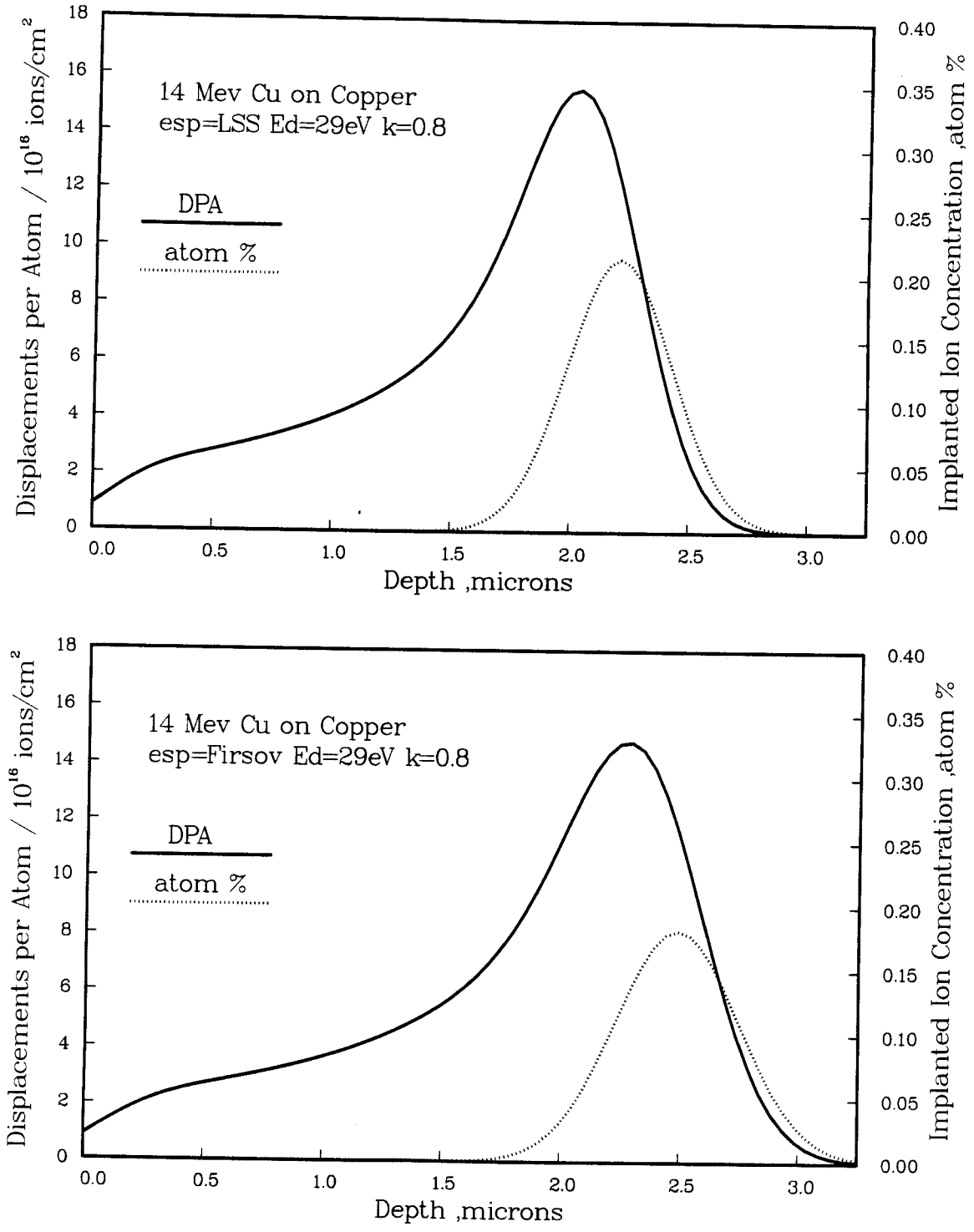

Fig. 8.13. Ion damage profiles using LSS and Firsov elecronic stopping power values (courtesy of D.L. Plumton).

deeper ion damage range as compared to LSS, in agreement with the present experimental results. However, the predicted damage range is still significantly less than the observed maximum range. Narayan et al.[100] and others[108,109] have found that modifications of the electronic stopping power result in calculated ion ranges that are in good agreement with experimental findings.

Farrell et al.[103] have proposed that the discrepancy between observed and calculated damage profiles in ion irradiated metals is primarily due to the neglect of diffusional spreading effects in the calculations. However, Whitley[101] concluded that diffusional spreading alone could not cause the observed deeper damage range. In general, the high dose levels of the irradiated cross-section specimens in the present study do not allow a distinct determination of damage level versus depth to be made -- there are no distinguishable depth-dependent changes in defect cluster density. However, the irradiated microstructure at 100°C did exhibit a different end of range behavior (Figs. 7.27, 7.30, 7.32, 7.39). It seems reasonable to associate this end of range (EOR) microstructure with the peak damage and/or injected ion region. The "coarse" EOR microstructure extended from a depth of 2.8 μm to 3.6 μm for both ion-irradiated copper and AMAX-MZC. If diffusion spreading was by itself responsible for the observed extended damage depth in ion-irradiated copper and copper alloys, then the coarse EOR microstructure should begin at $\lesssim$ 2 μm (corresponding to the calculated EOR damage) and extend out to the maximum observed damage depth (~ 3.6 μm). The fact that the coarse

EOR microstructure is not observed at the calculated peak damage region indicates that the damage range calculations (electronic stopping power) are underestimating the actual mean ion range. It is possible that diffusional spreading may be further enhancing this discrepancy, but by itself it cannot account for the experimental observations.

In summary, it appears that the difference between the observed and calculated ion displacement damage profiles may be attributed to the use of too large an electronic stopping power in the calculations, along with diffusion spreading and possible ion channeling effects. Failure to take into account this difference between the calculated and actual damage profile can result in wrong dose values. In particular the extended ion damage range means that at a given depth the actual displacement damage is slightly less than the calculated value on the near-surface side of the damage peak. This may be one contributing source to the well-known difference[30,110] between ion and neutron void swelling rates.

References for Chapter VIII

1. R.E. Reed-Hill, Physical Metallurgy Principles, 2nd Ed. (Brooks/Cole, 1973) 286-288.

2. E.A. Wilson, Worked Examples in the Kinetics and Thermodynamics of Phase Transformations, Inst. Metallurgists Monograph No. 7 (Chameleon Press, London).

3. F.W. Wiffen and R.E. Gold (Eds.), Copper and Copper Alloys for Fusion Reactor Applications, DOE-OFE Workshop Proceedings (Oak Ridge National Laboratory, CONF-830466, June 1984).

4. G. Gottstein and U.F. Kocks, Acta Metall. 31 (1983) 175.

5. C. Logan, Lawrence Livermore National Laboratory, private communication (1984).

6. R.W. Siegel, in Positron Annihilation, P.G. Coleman et al. (Eds.), (North-Holland, 1982) 351-368.

7. J.R. Cahoon et al., Met. Trans. 2 (1971) 1979.

8. J.G. Tweedale, Mechanical Properties of Metals, (Elsevier, 1964) 162-166.

9. S.J. Zinkle and G.L. Kulcinski, in Symp. on Use of Nonstandard Subsized Specimens for Irradiated Testing, Albuquerque, NM, Sept. 1983, ASTM STP 888 (1985).

10. J.J. Gilman, in The Science of Hardness Testing and Its Research Applications, J.H. Westbrook and H. Conrad (Eds.), (ASM, 1973) 55.

11. J.A. Spitznagel and J.W. Davis, "Response of Selected High Strength, High Conductivity Copper Alloys to Simulated Fusion Irradiation and Temperature Conditions," ADIP Semi-Annual Progress Report, Fall 1984.

12. W. Christ, K. Gschwendtner and F. Haessner, Phys. Stat. Sol. 10 (1965) 337.

13. K.R. Williams, S.B. Fisher and I.R. McLauchlin, Rad. Effects 7 (1971) 203.

14. V.V. Klyushin et al., Phys. Metals and Metallogr. 34, No. 5 (1972) 205.

15. F. Haessner and H.P. Holzer, Acta Met. 22 (1974) 695.

16. G. Das and T.E. Mitchell, Scripta Met. 8 (1974) 1135.

17. W.V. Vaidya and K. Ehrlich, J. Nucl. Mater. 113 (1983) 149.

18. H. Gleiter and B. Chalmers, High Angle Grain Boundaries, Prog. in Mat. Sci. series, Vol. 16, B. Chalmers et al. (Eds.), (Pergamon Press, 1972) 127-178.

19. R.V. Hesketh, J. Nucl. Mater. 35 (1970) 253.

20. F.R.N. Nabarro, R. Bullough and J.R. Matthews, Acta Met. 30 (1982) 1761.

21. H.W. King, J. Mater. Sci. 1 (1966) 79-90.

22. P. Niessen and W.C. Winegard, J. Inst. Met. 92 (1963/64) 300.

23. H.R. Brager, H.L. Heinisch and F.A. Garner, "Effects of Neutron Irradiation at 450°C and 16 dpa on the Properties of Various Commercial Copper Alloys," 1st Intern. Conf. on Fusion Reactor Materials, Tokyo, Dec. 1984.

24. R.J. Livak and F.W. Clinard, Jr., "High Dose Neutron Radiation Damage Study of Copper Alloys for the CRFPR First Wall," presented at EPRI, Palo Alto, Ca, Feb. 1985; also to be presented at the ANS Annual Meeting, Boston, June 9-14, 1985.

25. M. Baron, in Phase Stability During Irradiation, J.R. Holland et al. (Eds.), Pittsburgh, 1980 (TMS-AIME, 1981) 63.

26. G.R. Piercy, J. Phys. Chem. Solids 23 (1962) 463.

27. P. Chou and N.M. Ghoniem, J. Nucl. Mater. 117 (1983) 55-63.

28. N.M. Ghoniem et al., in 11th Intern. Symp. on Effects of Radiation on Materials, M.R. Brager and J.S. Perrin (Eds.), ASTM STP 782 (1982) 1054.

29. H.G. Mohamed et al., Trans. Indian Inst. Metals 36 (1982) 258-262.

30. S.J. Zinkle and R.W. Knoll, "A Literature Review of Radiation Damage Data for Copper and Copper Alloys," UWFDM-578, June 1984.

31. A.J. Perry, Thin Solid Films 78 (1977) 81.

32. C.A. Brooks, Phil. Mag. A 43 (1981) 529-543.

33. M.J. Makin, in Radiation Effects, Met. Soc. Conf. 37, Asheville, NC, W.F. Sheely (Ed.), (Gordon and Breach, 1967) 627.

34. T. Nai-Yong, "High Temperature Deformation and Fracture of Cu-Cr Type Alloys," Ph.D. Thesis, University of Waterloo (1983).

35. V.A. Phillips, Metallography 7 (1974) 137.

36. P. Forey et al., C.R. Acad. Sci. Paris, Serie C 291 (1980) 177.

37. L. Bsenko, J. Less-Common Metals 40 (1975) 365.

38. J-P. Gabathuler et al., Acta Cryst. 31 (1975) 608.

39. K.W. Andrews et al., Interpretation of Electron Diffraction Patterns, (Adam Hilger Ltd., London, 1971).

40. R.W. Knoll, "Effects of Heavy Ion Irradiation on the Phase Stability of Several Copper-Base Alloys", Ph.D. Thesis, Nuclear Engineering Department, University of Wisconsin-Madison (1981), UWFDM-436.

41. K. Farrell, Rad. Effects 53 (1980) 175-194.

42. W.G. Wolfer, J. Nucl. Mater. 122 & 123 (1984) 367-378.

43. D.B. Bullen, G.L. Kulcinski and R.A. Dodd, "Effect of Hydrogen on Void Production in Nickel", 1st Intern. Conf. on Fusion Reactor Materials (ICFRM-1) Tokyo (Dec. 1984); to be publ. in J. Nucl. Mater.

44. S.K. McLaurin, "Radiation Damage from Heavy Ion Bombardment in High Purity Aluminum", Ph.D. Thesis, Nuclear Engineering Department, University of Wisconsin-Madison (Jan. 1984). Also see S.K. McLaurin et al., J. Nucl. Mater. 117 (1983) 208.

45. J.A. Sigler and D. Kuhlmann-Wilsdorf, in The Nature of Small Defect Clusters, Vol. 1 (Consultants Symp.), M.J. Makin (Ed.), Harwell Report AERE R5269, July 1966, 125-143.

46. R.J.C. Cotterill, in The Nature of Small Defect Clusters, Vol. 1 (Consultants Symp.), M.J. Makin (Ed.), Harwell Report AERE R5269, July 1966, 144-172.

47. F. Kroupa, Czech J. Phys. 10B (1960) 284.

48. M. Abramowitz and I.A. Stegun, Handbook of Mathematical Functions, Dover Publications, Inc., New York, 1972, 591-592.

49. T. Jossang and J.P. Hirth, Phil. Mag. 13 (1966) 657.

50. A. Si-Ahmed and W.G. Wolfer, in Effects of Radiation on Materials: 11th Conf., ASTM STP 782, H.R. Brager and J.S. Perrin (Eds.), (1982) 1008.

51. G.W.C. Kaye and T.H. Laby, Tables of Physical and Chemical Constants, 14th Ed., (Longman Group, Ltd., London, 1973) p. 31, and Mark's Standard Handbook for Mechanical Engineers, T. Baumeister et al. (Eds.), (McGraw-Hill) p. 5-5.

52. P.C.J. Gallagher, Met. Trans. 1 (1970) 2429.

53. W.R. Tyson, Can. Metall. Quart 14, 4 (1975) 307.

54. M.I. Baskes, Trans ANS 27 (1977) 320.

55. N.V. Doan, in Point Defects and Defect Interactions in Metals, J-I. Takamura, M. Doyama and M. Kiritani (Eds.), (Univ. of Tokyo Press, 1982) 722.

56. J.W. Muncie et al., "Low-Dose Neutron Irradiation Damage in Copper, Parts I and II," AERE Report R11223 and R11224, to be published in Phil. Mag. (1985).

57. N. Yoshida, et al., J. Nucl. Mater. 122/123 (1984) 664-8; also see Y. Shimomura, et al., "Electron Microscopic Studies of Damage Evolution in Fission Neutron Irradiated Metals", and N. Yoshida et al., "Effect of Cascade Damage by 14 MeV Neutrons on Microstructure Evolution", 1st Intern. Conf. on Fusion Reactor Materials, Tokyo (Dec. 1984).

58. A.Y. Stathopoulos et al., Phil. Mag. A 44 (1981) 309-322.

59. H. Fujita, T. Sakata and H. Fukuyo, Jap. J. Appl. Phys. 21 (1981) L235-6.

60. B.L. Eyre, J. Phys. F: Metal Phys. 3, 2, (1973) 422-470.

61. H.G. Bowden and R.W. Ballufi, Phil. Mag. 19 (1969) 1001.

62. N. Eustathopoulos and J-C Joud, "Interfacial Tension and Adsorption of Metallic Systems", in Current Topics in Materials Science, Vol. 4, E. Kaldis (Ed.), (North-Holland, 1980) Chpt. 6, 281-360.

63. G.A. Somorjai, Chemistry in Two Dimensions: Surfaces (Cornell Univ. Press, 1981) Chpts. 3,6.

64. M.F. Felsen and P. Regnier, Surf. Sci. 68 (1977) 410-418.

65. B. Gallois and C.H.P. Lupis, Met. Trans. 12B (1981) 549.

66. C.E. Bauer, R. Speiser and J.P. Hirth, Met. Trans. 7A (1976) 75.

67. M. McLean and E.D. Hondros, J. Mater. Sci. 8 (1973) 349.

68. F.H.P.M. Habraken et al., Surf. Sci. 97 (1980) 264.

69. R.H. Jones and W.G. Wolfer, J. Nucl. Mater. 122/123 (1984) 379.

70. R.C. Weast (Ed.), CRC Handbook of Chemistry and Physics, 59th Ed. (CRC Press, 1978-79) p. F-236.

71. W. Dürrschnabel and H. Vosskühler, in Gase und Kohlenstoff in Metallen, E. Fromm and E. Gebhardt (Eds.), (Springer-Verlag, 1976) 657-678.

72. D.O. Hayword, in Chemisorption and Reactions on Metallic Films, J.R. Anderson (Ed.), (Academic Press, 1971) 225-326.

73. K-I. Tanaka and K. Tamaru, J. Catalysis 2 (1963) 366-370.

74. M.F. Wehner and W.G. Wolfer, "Vacancy Cluster Evolution in Metals under Irradiation", to be publ. in Phil. Mag. A (1985); also UWFDM-590.

75. W.G. Wolfer, M.F. Wehner and J.W. Davis, "Resistivity Contribution of Vacancy Clusters and Voids in Irradiated Copper", to be submitted to ADIP Progress Report DOE/ER-0045/15 (Sept. 1985).

76. Oxygen free copper designation requires an oxygen concentration of less than 10 ppm (40 appm) -- see ASTM Standard specification for oxygen-free electrolytic copper, 1983 ASTM standards Vol. 2.01, copper and copper alloys, B170-82. Electrolytic tough pitch copper has < 50 ppm total metallic impurities (99.995% Cu + O) but generally contains 200-400 ppm O (ASM Metals Handbook, Vol. 2, "Properties and Selection: Nonferrous Alloys and Pure Metals", 9th Ed., ASM, Metals Park, OH).

77. R.L. Sindelar, R.A. Dodd and G.L. Kulcinski, "A Note on Reactive Gas Charging During Pre-Irradiation Specimen Preparation," DAFS Quarterly Progress Report DOE/ER-0046/21 (April 15, 1985)

78. L.D. Glowinski, J. Nucl. Mater. 61 (1976) 8-21.

79. L.D. Glowinski, C. Fiche and M. Lott, J. Nucl. Mater. 47 (1973) 295-310.

80. L.D. Glowinski and C. Fiche, J. Nucl. Mater. 61 (1976) 22-28.

81. L.D. Glowinski and C. Fiche, J. Nucl. Mater. 61 (1976) 29-40.

82. R.L. Sindelar, G.L. Kulcinski and R.A. Dodd, "Heterogeneous Void Formation in 14-MeV Nickel Ion Irradiated 316 SS", 1st Intern. Conf. on Fusion Reactor Materials, Tokyo (Dec. 1984).

83. M.W. Finnis et al., Rad. Eff. 78 (1983) 121-132.

84. H. Trinkaus, Rad. Eff. 78 (1983) 189-211.

85. J.R. Beeler, Jr., Radiation Effects Computer Experiments, Vol. 13 of the series Defects in Solids, S. Amelinckx et al. (Eds.), (North-Holland, 1983).

86. B.B. Glasgow and W.G. Wolfer, DAFS Quarterly Progress Report DOE/ER-0046/16 (Feb. 1984) p. 68.

87. M.I. Baskes and C.F. Melius, Phys. Rev. B 20 (Oct. 1979) 3197.

88. H. Ullmaier, Nucl. Fusion 24 (1984) 1039.

89. N.H. Packan and K. Farrell, Nucl. Tech./Fusion 3 (1983) 392; also K. Farrell and N.H. Packan, J. Nucl. Mater. 85/86 (1979) 683-7.

90. N.H. Packan, K. Farrell and J.O. Stiegler, J. Nucl. Mater. 78 (1978) 143-155.

91. S.J. Zinkle, L.E. Seitzman and W.G. Wolfer, "Stability of Vacancy Clusters in Copper and Other Metals," DAFS Quarterly Progress Report DOE/ER-0046/21 (April 15, 1985).

92. W.D. Wilson, C.L. Bisson and M.I. Baskes, Phys. Rev. B 24 (1981) 5616.

93. M.I. Baskes and W.D. Wilson, J. Nucl. Mater. 63 (1976) 126-131.

94. M.J. Makin, J. Nucl. Mater. 107 (1982) 133-147.

95. CRC Standard Mathematical Tables, 25th Ed., W.H. Bleyer (Ed.), (CRC Press, 1978) p. 149.

96. J.M. Lanore, et al., in Fundamental Aspects of Radiation Damage in Metals, Vol. 2, M.T. Robinson and F.W. Young (Eds.), Gatlinburg, TN (1975) CONF 751006-P2, 1169-1179.

97. P.J. Maziasz, J. Nucl. Mater. 122/123 (1984) 472-486.

98. D.K. Sood and G. Dearnaly, J. Vac. Sci. and Tech. 12 (1975) 463.

99. J. Narayan et al., in Fund. Aspects of Rad. Damage in Metals, Vol. I, M.T. Robinson and F.W. Young (Eds.), Gatlinburg, TN, Oct. 1975, CONF-751006-P1, p. 90.

100. J. Narayan et al., J. Nucl. Mater. 71 (1977) 160.

101. J.B. Whitley, Ph.D. Thesis, University of Wisconsin-Madison (1978).

102. G. Fenske et al., J. Nucl. Mater. 85/86 (1979) 707.

103. K. Farrell et al., Rad. Effects 62 (1982) 39.

104. D.B. Bullen, Ph.D. Thesis, University of Wisconsin-Madison (1984).

105. C.H. Henager et al., Rad. Effects 36 (1978) 49.

106. J. Lindhard, M. Scharff and H.E. Schiott, Kgl. Dansk. Videns. Selsk., Mag.-Fys. Medd. 33 (1963) 1.

107. O.B. Firsov, Soviet Phys. JETP 36 (1959) 1076.

108. G. Fenske et al., J. Appl. Phys. 52 (1981) 3618.

109. H. Attaya, Ph.D. Thesis, University of Wisconsin-Madison (1981).

110. F.A. Garner, J. Nucl. Mater. 117 (1983) 177.

CHAPTER IX. CONCLUSIONS

The main conclusions resulting from this thesis study are listed below. Suggested topics that need further study are given at the end of this chapter.

IX.A. As-Received and Thermal Annealed Alloys

1. AMZIRC (Cu-0.15% Zr) exhibits negligible precipitation hardening, whereas the strength of solution annealed AMAX-MZC (Cu-0.8% Cr-0.15% Zr-0.04% Mg) increases by a factor of two when aged at suitable conditions. Cold-working of AMZIRC and AMAX-MZC prior to aging has no measurable effect on the electrical conductivity, while it increases the yield strength of these alloys by a factor of 2 to 3 compared to the solution annealed plus aged condition. AMZIRC exhibits a higher electrical conductivity than AMAX-MZC at all conditions. On the other hand, AMAX-MZC is capable of a larger yield strength than AMZIRC at a given operating temperature.
2. The recrystallization temperature of both AMZIRC and AMAX-MZC is about 480°C for a 1 hour anneal. The activation energy for recrystallization of these alloys is 3.0 eV. The estimated recrystallization temperature for AMZIRC and AMAX-MZC for a 2 year anneal is about 340°C in the absence of stress or irradiation effects. The strength of both alloys decreases to values similar to pure copper following recrystallization. This lack of intrin-

sic high-temperature strength may make these alloys unsuitable for some fusion reactor applications.

3. A linear correlation exists between yield strength and Vickers microhardness over a wide range of thermomechanical conditions for AMZIRC and AMAX-MZC. The relationship for both alloys is given by σ_y (MPa) = 3.0 VHN.
4. The electrical conductivity of AMZIRC and AMAX-MZC is controlled mainly by the character of their alloying elements, i.e. the relative partitioning of solute between precipitates and solid solution. The best combination of strength and conductivity for magnet applications is obtained by aging the alloys at conditions slightly below that required for recrystallization. The resultant optimum yield strength and electrical conductivity values are (400 MPa, 90% IACS) for AMZIRC and (425 MPa, 85% IACS) for AMAX-MZC.

IX.B. Irradiated Copper and Copper Alloys

1. There was no significant amount of void formation in either pure copper or in AMZIRC or AMAX-MZC following single ion irradiation up to a peak damage level of 40 dpa over the temperature range of 100-550°C (0.28-0.61 T_M). Instead, stacking fault tetrahedra were observed. This is in contrast to many previous irradiation studies performed on copper and copper alloys where substantial void formation was observed after doses as low as 10^{-4} dpa. The absence of voids following irradiation is proposed to be due to

the low oxygen content of the copper and copper alloy foils (< 5 ppm).

2. A model has been developed that predicts the most stable vacancy cluster morphology in copper and other metals. Stacking fault tetrahedra (SFT) are predicted to be the most stable configuration of vacancy clusters in the absence of gas, in agreement with the experimental findings of this thesis. Small amounts (0.01-10 appm) of helium and oxygen are predicted to alter the vacancy cluster energies so as to cause void formation to preferentially occur over SFT formation.

3. Indications of radiation-enhanced recrystallization were observed in the irradiated cold-worked plus aged copper alloys. The recrystallization temperature of ion-irradiated AMZIRC and AMAX-MZC decreased to 300-400°C. A simple model based on radiation-enhanced diffusion gives reasonable agreement with the experimental measurements. AMAX-MZC exhibited a sluggish recrystallization response during irradiation when compared to AMZIRC. This is attributed to Cr and Mg solute atoms retarding the grain boundary mobility. The radiation-enhanced diffusion model predicts a recrystallization temperature of ~ 150°C for AMZIRC and AMAX-MZC for a long term (2 year) neutron irradiation. This may severely limit the applicability of these and other cold-worked plus aged high-strength, high-conductivity copper alloys since much of their strength is lost when recrystallization occurs.

4. Evidence of displacement damage in the form of "black spot" defect clusters was observed at depths well beyond that expected from ion damage range calculations (BRICE code). The discrepancy between the observed and calculated damage profile is most likely due to the use of too large of an electronic stopping power function in the calculation, but diffusional spreading and ion channeling effects may also be playing a role.
5. There was no definitive evidence of precipitate coarsening or dissolution as a result of 14-MeV Cu ion irradiation. However, the Cr precipitates contained in AMAX-MZC which were initially semicoherent apparently became incoherent following ion irradiation. A small matrix precipitate that exhibited parallel moiré fringe contrast was visible in irradiated and nonirradiated regions of AMZIRC and AMAX-MZC.

IX.C. Suggestions for Future Work

1. The voids/no voids discrepancy between previous irradiation studies on copper and the present investigation highlights the need for a detailed study of the effect of gas on void formation. A thorough experimental investigation should be initiated on high-purity copper foils which contain very low ($\lesssim$ 1 appm) concentrations of oxygen and other gases. Low-level oxygen preinjection or co-implantation irradiation experiments should be performed to determine what is the minimum amount of oxygen required to stabilize void formation in copper as a function of temperature. A similar experiment should be initiated to deter-

mine the amount of helium required for void stability. These experimental findings could then be compared to the predictions of the model presented in this thesis in order to determine its quantitative value.

2. The potential applications of the scratch hardness technique as applied to irradiated cross-section specimens should be studied in further detail. The experimental arrangement that was used in this thesis is of limited usefulness due to its poor reproducibility. Either a commercial miniature scratch hardness tester or perhaps modifications to an instrument such as the Dektak step height recorder should be suitable. Scratch hardness is a potentially powerful technique because it can give a direct qualitative measure of radiation hardening or radiation softening in ion-irradiated cross-section specimens. Scratch hardness is also a nondestructive testing technique, so it therefore allows other experimental data (e.g., TEM) to be subsequently extracted from the same specimen.
3. Additional theoretical work is needed to bring the calculated ion displacement damage profile into accord with experimental observations. Further experimental data is also needed to separate the relative contributions of electronic stopping power errors, diffusional spreading and ion channeling effects in the observed damage profile.
4. Future irradiation studies on high-strength, high-conductivity copper alloys should concentrate on materials which maintain

their strength at elevated temperatures (i.e., dispersion-hardened alloys such as Cu-Al_2O_3). Limited studies should also be continued on the most attractive cold-worked plus aged (precipitation hardened) copper alloys such as Cu-Be-Ni and also possibly AMAX-MZC. Studies on less attractive alloys such as AMZIRC should be confined to fundamental investigations of basic irradiation effects such as radiation induced precipitation, precipitate dissolution, etc.